INTERFACIAL CHEMISTRY AT THE SURFACES OF ENGINEERED AND NATURAL NANOMATERIALS

A Dissertation

by

THEODORE EMMANUEL GATMAITAN ALIVIO

Submitted to the Office of Graduate and Professional Studies of
Texas A&M University
in partial fulfillment of the requirements for the degree of

DOCTOR OF PHILOSOPHY

Chair of Committee,	Sarbajit Banerjee
Committee Members,	Donald J. Darensbourg
	Hongcai Zhou
	Micah J. Green
Head of Department,	Simon W. North

May 2019

Major Subject: Chemistry

ABSTRACT

The central theme of my research seeks to understand the interfacial chemistry of engineered and natural nanomaterials. Manipulation of the surface chemistry of nanostructures is an important tool in tuning their properties for various applications, given that these properties are greatly influenced by the high abundance of defects and dangling bonds on the surface. When an ad-atom, molecule, or periodic solid interacts with the surface of a material, the interaction can be classified as either physisorptive or chemisorptive. Herein, I present three disparate areas of research, which explore interfacial interactions at nanostructured surfaces.

Emphasis on the chemisorption and physisorption on engineered nanomaterials is provided in the **first** and **third projects**. The **first project** illustrates that graphene oxide is partially reduced when used as a substrate for the atomic layer deposition (ALD) of amorphous HfO_2. Understanding the interfacial chemistry between graphene oxide and HfO_2 provides new knowledge on designing graphene-based field effect transistors and semiconductor heterostructures for catalysis. In the **third project**, a novel *ex situ* doping technique for modulating the metal—insulator transition (T_{MIT}) of VO_2 has been developed. Initial deposition of the molecular boron precursor 2-allyl-4,4,5,5-tetramethyl-1,3,2-dioxaborolane on the surface of VO_2 nanowires allows for the subsequent incorporation of B atoms in the tetrahedral interstitial sites of VO_2 upon rapid thermal annealing, which results in the stabilization of the rutile phase in greater proximity to room

temperature. The diffusive annealing process can be tuned to program the T_{MIT} of VO_2 for applications such as thermochromic fenestration and the design of memory devices.

The **second project** is focused on natural nanomaterials, wherein the interactions of Ag-Au bimetallic alloy nanoparticles in aquatic media have been investigated. The growth of these alloy nanoparticles is mediated by dissolved organic matter (DOMs) such as fulvic and humic acids, with or without photoillumination from natural sunlight. In the absence of natural sunlight, Ag- and Au-ions are first complexed with Lewis basic groups (carbonyls, carboxyls, thiols) on the DOM; subsequently, alloy formation is facilitated by galvanic replacement. Under visible light irradiation, Ag, Au, and Ag-Au bimetallic alloy nanocrystals are grown *via* a plasmon-induced mechanism.

The study of the interfacial chemistry at the surfaces of these nanomaterials paves way for the rational design of various architectures which can be used for various applications such as catalysis, environmental remediation, and thermochromic fenestration.

DEDICATION

To my godson and nephew/cousin once removed, Konnor A. P. Gatmaitan, who made my past two Christmas celebrations memorable, I look forward to the day you wear your own Aggie ring. To my maternal grandfather, Abelardo C. Gatmaitan, who never even saw me graduate college, this one's for you. To my parents, Norma C. Gatmaitan-Alivio and Manuel Y. Alivio, and my "fun" sister, M. Louise G. Alivio, thank you for being extremely patient with me. Finally, to my 91 years young maternal grandmother, Segundina S.C. Cervantes-Gatmaitan—you have always wanted to be a teacher but young romance took your dreams away. I promise that I will chase and fulfill those dreams of yours for you.

ACKNOWLEDGMENTS

This research would have not been possible without the various mentors I have met throughout my PhD education.

Most importantly, I would like to thank my advisor, Professor Sarbajit Banerjee, for his unparalleled patience and mentorship. The road to where I am right now was not a smooth ride, but I am grateful that you never gave up on me. I will always treasure every lesson I have learned from you, whether it is research-related or not. Your enthusiasm in the sciences has fueled the same passion I have to teaching chemistry at a collegiate level. You have given me remarkable work with other collaborators, and helped develop important relationships with them.

I would also like to recognize Dr. Diane Sellers, who has been my "second research mentor." Her ingenuity has always challenged me to do better and approach science with a more critical eye. Her vibrant and cheerful personality has made working with her such a delightful encounter.

I would also like to thank the other members of my advisory committee, Professor Donald Darensbourg, Professor Hongcai Zhou, and Professor Micah Green, for their guidance and support, most especially during the latter half of my research.

I would also like to thank both past and present members of the Banerjee Group. I have learned so much through our collaborations and camaraderie. I will be forever grateful to the times I have shared with you. I would like to give my special thanks to Dr. Luis De Jesus, my batchmate and my first friend in the Banerjee Group, and to Nathan

Fleer, Abhishek Parija, Wasif Zaheer, and Aayushi Bajpayee who have been my closest friends in the lab. While it makes me really sad to accept the fact that we will now walk our separate ways, I am still grateful that I have shared a few years of my life with all of you.

I would also like to extend my gratitude to my teaching mentors, Dr. Stephanie McCartney and Dr. Soon-Mi Lim. I have learned a lot about collegiate-level teaching from both of you. Your passion and dedication to chemical education has challenged me to be as innovative in how I relay science to future scientists.

I am also appreciative of my non-chemistry best friends, Dr. Abigail Peralta and Dr. Butch Bataller. We shared a lot of ups and downs but we got each other's back.

I would also like to acknowledge all others who I have been fortunate enough to establish close friendships with.

Finally, I would like to thank my mom, my dad, and my sister for being extremely supportive of my goals and endeavors. I would also like to extend my gratitude to my other family members across the United States.

CONTRIBUTORS AND FUNDING SOURCES

Contributors

This work was supervised by a dissertation committee consisting of Professor Sarbajit Banerjee and Professors Donald J. Darensbourg and Hongcai Zhou of the Department of Chemistry and Professor Micah J. Green of the Department of Chemical Engineering.

All work for the dissertation was completed by the student, in collaboration with Professor Virender K. Sharma of the TAMHSC School of Public Health, Professor Patrick Shamberger of the Department of Materials Science and Engineering, and Professor Raymundo Arróyave of the Department of Mechanical Engineering. External collaborators outside TAMU include: Professor Uttam Singisetti of the Department of Electrical Engineering, State University of New York at Buffalo; Professor Shahbazian-Yassar of Department of Physics, University of Illinois at Chicago and the Department of Mechanical Engineering, Michigan Technological University; Drs. Daniel Fisher and Cherno Jaye of Brookhaven National Laboratory; and Dr. Lucia Zuin of the Canadian Light Source.

Funding Sources

Work in Chapter II was made possible in part by partial support from the New York State Pollution Prevention Institute and through a Scialog Award from the Research Corporation for Science Advancement.

Work in Chapter V was primarily supported by the National Science Foundation under DMR 1504702.

TABLE OF CONTENTS

Page

LIST OF FIGURES

Page

LIST OF TABLES

Page

CHAPTER I

INTRODUCTION AND MOTIVATION

1.1 Interactions on Surfaces

Nanomaterials behave significantly differently from their bulk counterparts as a result of their high surface-area-to-volume ratio, which profoundly alters their physical and chemical properties. While defects such as terraces, steps, vacancies, adatoms,[1] and dangling bonds are present on the surfaces of materials, they exert a greater influence on the properties of nanometer-sized materials given their higher abundance. Scaling materials to finite size gives rise to novel properties not accessible in the bulk such as the stabilization of metastable polymorphs, as seen in a) the synthesis of ultrasmall (4 nm) tetragonal HfO_2,[2] metallic 1T-MoS_2 nanosheets upon the exfoliation of its semiconducting 2H polymorph;[3,4] b) the tunability of electronic and optical properties, as observed in the quantum confinement of CdSe quantum dots;[5] and c) improved catalytic activity, as demonstrated by mesoporous CeO_2 nanotubes.[6] Understanding the interfaces of nanomaterials serves as a powerful tool in rationally designing and developing architectures for specific applications.

In general, the modes in which foreign atoms and molecules (adsorbates) interact with the surface of a material (substrate) can be classified into two categories, based on the ease of overcoming the energy potential needed to desorb the two species bound to each other. Physisorption arises from weak van der Waals' interactions between the adsorbate and substrate. Given that these interactions are due to the polarization of both

the adsorbate and substrate, only a minimal energy is needed to desorb the former from the latter. On the other hand, chemisorption is brought about by the formation of actual chemical bonds between the adsorbate and the substrate. The potential needed to break a bond is much greater for chemisorbed species and therefore requires a greater amount of energy to initiate desorption. **Figure 1.1** shows a Lennard—Jones plot of how the two processes differ from each other in terms of energetics.

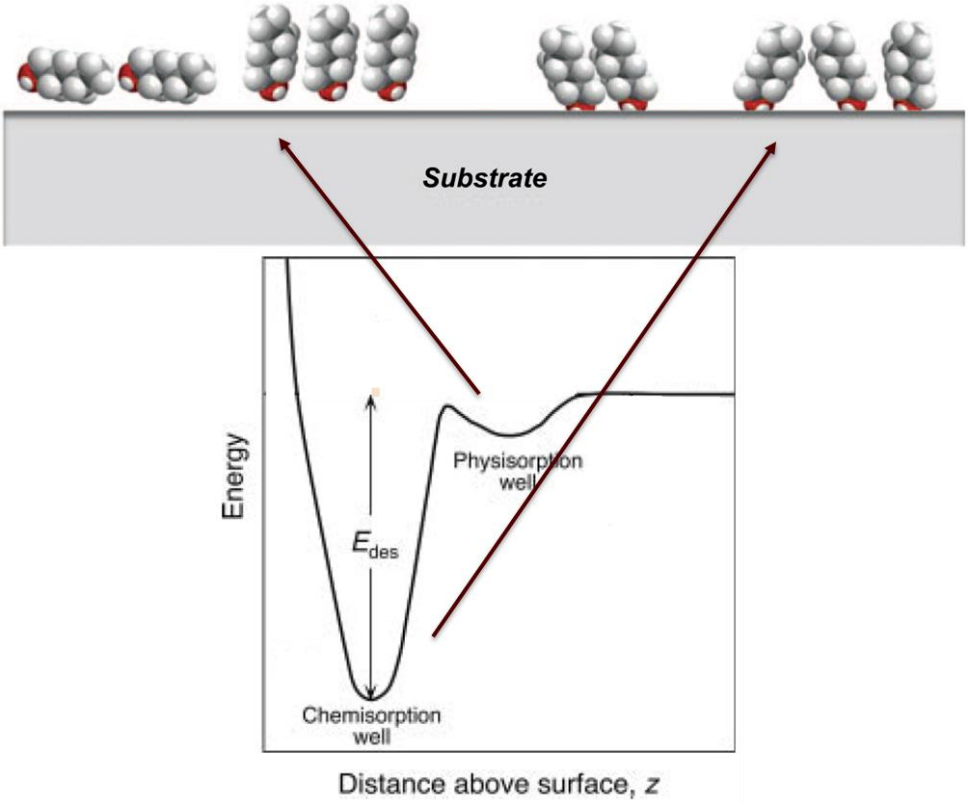

Figure 1.1: Lennard—Jones potential energy curve for physisorption and chemisorption of an adsorbate molecule on a substrate. A minimal amount of energy is needed to overcome the physisorption well, whereas a greater amount of energy is needed to desorb a chemisorbed adsorbate from the substrate. The image is adapted from references 1 and 7. Lennard—Jones potential energy curve reprinted with permission from reference 1. Copyright 2012 John Wiley & Sons, Ltd. The substrate—adsorbate cartoon is reprinted with permission from reference 7. Copyright 2016 The Royal Society of Chemistry.

An example of a physisorption process is the deposition of alkanes on metals such as Ag, Au, and Cu, and metal oxides such as Al_2O_3 and MgO. Tait *et al.* note that longer-chain alkanes introduce more methylene-group interactions with MgO, thereby increasing the amount of energy needed to initiate desorption (*i.e.*, a higher desorption temperature).[8] Smaller molecules are able to migrate easier across the surface of MgO, whereas larger alkanes are trapped in a metastable configuration, which makes them harder to desorb from the MgO surface.[8]

On the other hand, a popular model of chemisorption is the formation of self-assembled monolayers (SAMs) on substrates. This process involves an organic ligand with a polar headgroup that has a high affinity for the substrate. For example, when *n*-alkanethiols bind on metals such as Au, the thiol group of these organic molecules have a high affinity for the surface of the substrate.[9] Chemisorption is accomplished when the S atom from the ligand covalently bonds with Au, expelling H_2 in the process.[10] In general, alkanethiols are initially physisorbed on the surface of Au(111)[10,11] and then react with surface Au atoms as follows:[9]

$$R–SH\ (l) + 2Au\ (s) \rightarrow 2R–S–Au\ (s) + H_2\ (g) \qquad \textbf{Eq. 1.1}$$

Another chemisorptive process, which finds applications in the semiconductor industry is atomic layer deposition (ALD). ALD is a thin-film growth process in which metal oxides are grown on a substrate by the subsequent introduction and reaction of at least two gaseous precursors. These two precursors react with the dangling bonds of the substrate (and with each other) to mediate the formation of metal oxides on the surface.

The most common precursors used are water and metal amides, the latter being reactive with hydroxylated substrates.[12] **Figure 1.2** depicts the mechanism of growth of HfO_2 on substrates, using *tetrakis*(dimethylamido)hafnium(IV) (TDMH) as a metal precursor. While other thin film growth techniques such as physical vapor deposition methods are available, the advantage of ALD over these processes is precise control of film thickness. A cycle is repeated until the desired thin film thickness is achieved. In contrast to chemical vapor deposition (CVD), another thin film growth process, ALD enables thickness control to be achieved at lower processing temperatures.[12]

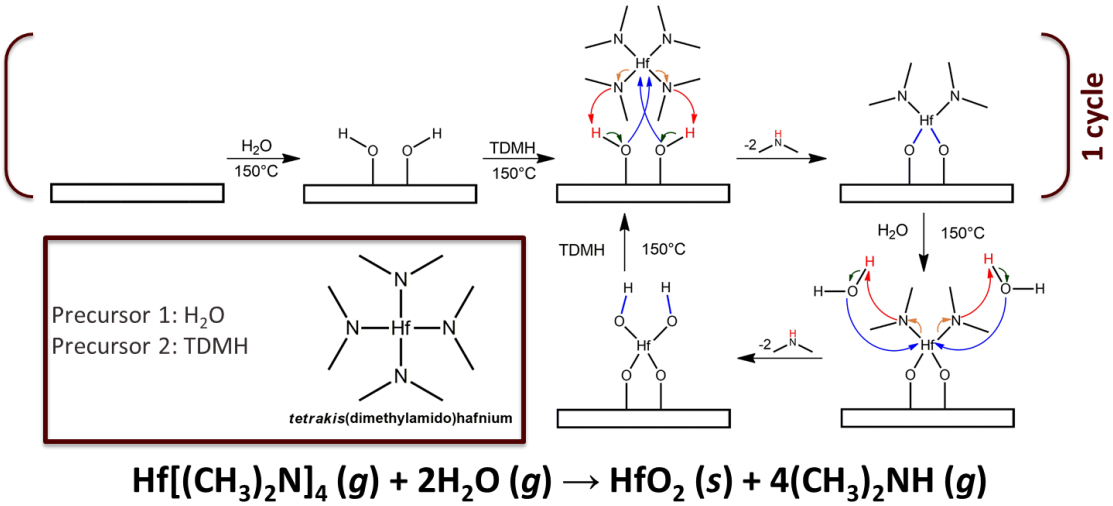

Figure 1.2: Atomic layer deposition of HfO_2 on a substrate using water and *tetrakis*(dimethylamido)hafnium(IV) as precursors. Water reacts with the surface of the substrate to introduce dangling hydroxyl bonds, which in turn react with TDMH to initiate the formation of HfO_2. The mechanism and image are adapted from reference 12.

It is the goal of this dissertation to understand these surficial interactions on nanomaterials to address three different areas of interest. **Chapter II** examines interfacial interactions upon ALD growth of HfO_2 on graphene oxide. We note that the initial dosage

of water promotes partial defunctionalization of graphene oxide *via* the expulsion of gaseous CO_2; the subsequent introduction of TDMH mediates the growth of amorphous HfO_2 on pendant carboxylic acid groups on the surface of graphene oxide.[13] **Chapter III** explores the mechanistic growth of bimetallic Ag-Au nanocrystals in the presence of dissolved organic matter (DOMs) in aqueous media. The bimetallic alloys are formed *via* a galvanic replacement reaction and are stabilized by interactions of the surfaces of the alloy nanoparticles with the functional groups of the DOMs.[14] Moreover, Au→Ag back charge transfer in turn helps in impeding the oxidation of surficial Ag-atoms (as observed in the absence of oxidized Ag species). The Ag-Au bimetallic alloy nanoparticles are stable in solution because the DOMs also serve as passivating ligands and surfactants. **Chapter IV** further explores more natural conditions in which Ag-Au bimetallic alloy nanocrystals are stabilized by DOMs with natural sunlight accelerating the growth of these alloy nanoparticles. **Chapter V** discusses a novel two-step surface-limiting technique we have developed for introducing dopants into theVO_2 lattice.[15] Given that VO_2 undergoes a reversible metal—insulator phase transition at 67°C,[16] modification of its phase diagram *via* dopant incorporation allows for the tuning of the transition temperature (T_{MIT}) the said material for highly specific applications. For B dopant atoms in particular, we note a concentration-dependent decrease in the T_{MIT} of VO_2 that leads to the stabilization of its rutile phase at near-room temperature values. The introduction of B atoms in tetrahedral interstitial sites of VO_2 results to the stabilization of the VO_2(R) by a) hampering the dimerization of [VO_6] octahedra during the R→M_1 transition, and b) increasing the metallicity of VO_2 as a consequence of the formation of B–O bonds and subsequent

decrease in the covalency of V–O bonds. While these topics may be seemingly disconnected and different from each other, the central theme revolving around these three studies is that understanding the interfacial chemistry of nanomaterials allows for better understanding of their behavior in nature, as well as tailoring them for more practical and more specific applications. **Chapters II**, **III**, and **IV** describe chemisorptive processes whereas **Chapter V** introduces an initial physisorption step. The succeeding sections in this *Introduction* will further discuss the motivation behind each project, the rationale in studying them, and future directions given the findings we note.

1.2 Graphene—Dielectric Interfaces

Graphene can be best described as a single-layer of sp^2-hybdridized C atoms arranged in a honeycomb lattice. As a 2D material, graphene is synthesized by exfoliation of a single sheet of graphite. The first successful synthesis of graphene was achieved by the traditional "Scotch Tape™ method" reported by Geim and co-workers.[17] The many remarkable electronic properties of graphene such as high thermal conductivity (5000 $Wm^{-1}K^{-1}$) and high intrinsic mobility (200,000 $cm^2V^{-1}s^{-1}$) opens up opportunities for interfacing graphene with other materials including metals and dielectrics.[18] Examples of those applications are high-speed electronics, single-molecule detection, plasmonic devices, and broadband photodectectors, to name a few.[18,19]

The actual synthesis of graphene itself is dependent on interactions with the surface. Aside from mechanical exfoliation, substrates such as SiC and transition metals including Cu and Ni are used to promote the deposition of carbon atoms at extremely

elevated temperatures, thereby initiating the growth of graphene on such substrates.[18,19] Graphene can furthermore be prepared by the sublimation of Si at extremely high temperatures (*ca.* 1,700°C) from either a Si-rich or a C-rich phase of SiC, leaving behind a network of C atoms, which eventually forms the graphene network. Fisher and coworkers note that the Si-face of SiC gives rise to single-layer graphene, whereas the C-face of SiC provides multilayers of graphene, where 3D islands can initially be observed.[20] On the other hand, graphene can also be grown by CVD on the surfaces of transition metal substrates such as Cu and Ni. In this process, a gaseous carbon precursor such as methane[21,22] or acetylene[23] is used under mildly reducing conditions.

Before discussing the interface of HfO_2 and graphene oxide, it is imperative to consider previously reported literature on graphene interfaces. The interaction of graphene with metals, metal oxides, organic compounds, and even gases can either be *via* physisorption or chemisorption, both of which alter the electronic structure of graphene to some extent. The adsorption of NO_2 for example, introduces holes into graphene, with the degree of p-doping (as much as 0.8 eV was reported) being a function of gas coverage.[24] Organic compounds such as tetrafluorotetracyanoquinodimethane (F4-TCNQ) also mediate p-doping of graphene (*ca.* 0.3 electrons withdrawn from graphene), as determined by density functional theory (DFT) calculations,[25] and as verified experimentally (by evaporating F4-TCNQ onto CVD-grown single layer graphene on Cu).[26] Similar to F4-TCNQ, tetracyanoethylene (TCNE) is predicted to be a p-type dopant, withdrawing *ca.* 0.3—0.4 electrons from graphene as F4-TCNQ.[27] On the other hand, tetrathiafulvalene

(TTF), owing to its chemical structure, behaves as an electron donor (*ca.* 0.1—0.3 electrons are predicted to be transferred to graphene).[28]

The introduction of transition metal ad-atoms onto graphene also promotes either physisorption or chemisorption, depending on the number of d-electrons and the size of their orbitals. Strong orbital mixing, which results in chemisorption, is observed for transition metals with partially filled orbitals, including Ni, Co, Pd, Ru, and Ti.[19,29] These metals transfer electrons into graphene. The metal-to-graphene charge transfer also imparts a diminution in the magnetization of ferromagnetic materials such as Ni and Co.[30] On the other hand, metals with nearly-filled or half-filled orbitals such as Ag, Al, Au, Cd, Cu, Cr, and Pt are only weakly physisorbed on graphene but still have an influence on its electronic structure.[19] For example, it has been noted that as the interlayer distance between Cu and graphene increases, graphene is n-doped instead of being p-doped.[31] Interfacing graphene with metal oxides has also been extensively studied for assembly into electronic devices such as field-effect transistors (FETs).[32] In previous work, ZrO_2, HfO_2, and TiO_2 were sputtered onto graphene/300 nm SiO_2/Si thin films by plasma vapor deposition (PVD). It was observed that HfO_2 promotes p-doping in graphene. The observed charge redistribution was less pronounced with ZrO_2 and TiO_2.[33] These graphene/metal and graphene/dielectric interfaces show that the manipulation of the surface chemistry of graphene is indeed key to tune its electronic structure.

While our group has previously conducted deposition of dielectrics on graphene *via* PVD, the lack of functional groups in unfunctionalized graphene makes the nucleation of such dielectrics difficult.[13] Various strategies have been developed in order to overcome

this fundamental issue, such as the utilization of seed layers.[34,35] Another route to overcome this challenge is to introduce functional groups to graphene, which is commonly done by simultaneous oxidation and exfoliation of graphite into graphene oxide (such as using Hummers' method).[36] Unlike graphene, graphene oxide has a band gap as a result of the introduction of functional groups,[37] rendering graphene oxide insulating. **Figure 1.3** shows the functional group distribution in graphene oxide. In previous work, experimental data from scanning transmission microscopy (STXM) and near edge X-ray fine structure (NEXAFS) spectroscopy obtained were in strong agreement with the Lerf—Klinowski model: carbonyl and carboxylic acid groups decorate the edge sites of graphene oxide, whereas epoxide and hydroxyl groups are prominent on its basal planes.[38,39] The abundance of functional groups in graphene oxide thus provides anchoring points in the nucleation and growth of dielectrics by serving as complexation sites for metal oxide precursors. Indeed, previous studies have noted the complexation of metals with functional groups, such as carboxylic acids on polymeric matrices.[40] For example, Ju *et al.* report that Ca forms Ca-carboxylate complexes with carboxylic acid groups on poly(methyl methacrylate) (PMMA). Identifying these surficial interactions is important in intelligently assembling metal oxide/graphene heterostructures for complex applications.

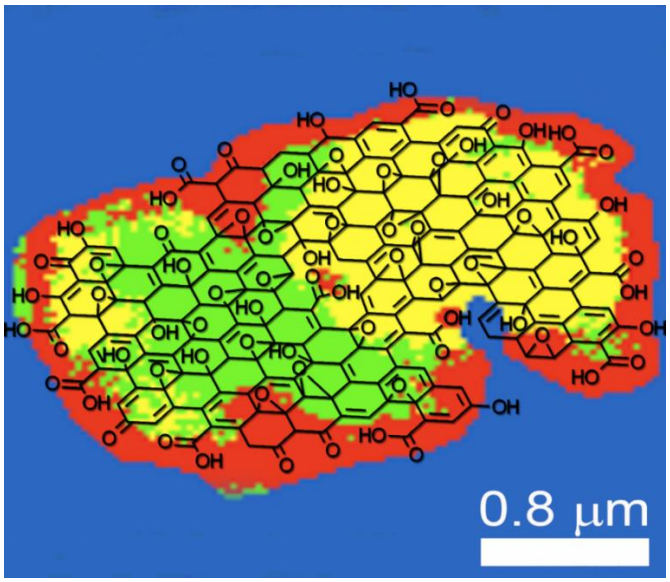

Figure 1.3: The structure of graphene oxide, based on the Lerf—Klinowski model which our group has verified by NEXAFS spectroscopy and STXM.[39]

Keeping problems identified in previous research in mind, we have conducted an ALD study that opens up new synthetic routes for the design of graphene-based heterostructures for various applications in catalysis and optoelectronics. While it has been previously mentioned that the introduction of functional groups on graphene is a more attractive alternative in integrating dielectrics on its surface *versus* using a seed layer, the tradeoff to the oxidation of graphene is the loss of its semimetallic characteristics. In **Chapter II**, we outline how this issue, along with the nucleation of dielectrics, is addressed in the ALD of HfO_2 on a graphene oxide substrate. At 150°C, water, the first ALD precursor, reacts with basal hydroxyl and epoxide groups. These hydroxyl and epoxide groups subsequently react with mobile epoxide groups to liberate CO_2, thereby promoting the partial restoration of the π-conjugated network of graphene. Hunt *et al.* have demonstrated that this thermal reduction reaction with water lowers the band gap of

graphene oxide to the same extent when graphene oxide is reduced with hydrazine.[37] The introduction of the second ALD precursor, TDMH, facilitates the growth of amorphous HfO_2 on pendant carboxylic acids groups on the surface of graphene at the same low processing temperatures. The Hf-carboxylate complexes are stabilized as a result of the sharing of electron density from the carboxylic acid groups of graphene oxide to Hf^{4+}. It is important to note that p-doping of graphene, which was noted upon PVD of HfO_2 was not observed as a result of ALD treatment. This highlights the importance of surface-modification in materials, especially how various processes give rise to different changes in properties (for this case electronic), thereby providing synthetic options for designing heterostructures such as field-effect transistors (FETs) and photocatalysts.

In 2008, IBM designed a graphene-based FET with a cutoff frequency of 26 GHz,[32] utilizing the ability of graphene to exhibit ballistic conduction at room temperature (up to 300 nm mean free paths).[17] This pioneering work has led to the production of a graphene-based FET which operates with a cutoff frequency as high as 100 GHz,[41] thereby showing the previously mentioned potential of using graphene as a channel material to overcome the fundamental limitations of conventional Si-based FETs.[41,42] However, because pristine graphene has no band gap, such FETs would have no "off switch," and therefore it is imperative to interface graphene with high-κ gate dielectrics. Again, the nucleation of these dielectrics on graphene is a challenge. The ALD of high-κ dielectrics on graphene oxide therefore serves as an attractive alternative to designing such graphene-based FETs. Another rudimentary issue in the conventional construction of graphene-based FETs is the need to separately grow pristine graphene on metal substrates such as

Ni and Cu, which is followed by a mandatory transfer onto another substrate using a thin polymer film such as PMMA or polyisobutylene (PIB).[43] This transfer process, however, leaves behind undesired and irremovable residues on the surface of graphene, severely altering its desired properties.[43,44] The ALD procedure we report in **Chapter II** offers a one-step route to restore the properties of graphene lost upon oxidation and to interface the said material with dielectrics, effectively eliminating the necessity to transfer graphene from one substrate to another.

Another application of interfacing graphene oxide and metal oxides is in the heterogeneous photocatalytic degradation of persistent organic compounds (POPs). Transition metal oxides are mostly used as catalysts in which, under ultraviolet radiation, an electron and a hole are photogenerated. These charged carriers then participate in reductive and oxidative reactions (electrons and holes, respectively) directly and/or indirectly, promoting the decomposition of organic compounds. Most photodegradation reactions occur by oxidation of the organic compound, either directly with the photogenerated holes, or indirectly *via* the formation of hydroxyl radicals by holes trapped on the semiconductor surface (the photogenerated electron is scavenged by an oxidant in solution, typically H^+, or gets trapped on the surface of the metal oxide surface).[45,46] A major challenge lies in the process of rapid recombination of these charged species, which occurs at a very fast time scale. Interfacing graphene with semiconductors[47,48] can serve as an efficient assembly in separating photogenerated electrons and holes. Using reduced graphene oxide as a 2D catalyst support for both TiO_2 and Ag^+, Kamat and coworkers have noted that owing to its large surface area (2,630 m^2g^{-1}),[49] graphene behaves as an

electron shuttle, thereby preventing the very rapid and exothermic process of electron-hole recombination.[50]

1.3 Growth of Silver—Gold Alloy Nanoparticles in Natural Aqueous Media

Understanding surficial interactions is key to designing nanomaterials with specific morphologies, and for certain crystals, preferred growth orientations. For example, in the synthesis of quantum dots such as CdSe, tri-*n*-octyl phosphine oxide (TOPO) is used as a growth-directing ligand, together with surfactants like tri-*n*-octyl phosphine (TOP), hexadecylamine, and stearic acid.[51] Precise size control of quantum dots is achieved by modifying various parameters such as reaction temperature and precursor concentration,[52] which underscores the importance of these surficial interactions. Aside from introducing efficient passivation, *via* surface-capping ligands, size control provides a knob to modify the band gap of quantum dots, and in some studies, improve their fluorescence yield.[52,53] In a similar vein, layer thickness of methylammonium lead bromide nanoplatelets can be controlled by varying the chain length of the added alkylamine.[54] Capping ligands can also play a non-innocent role in the reaction mixture. For example, this is observed in the control of oxidation state of dopant ions as shown in the incorporation of Eu-ions in LaOCl nanocrystals, wherein Eu^{2+} is alloyed when oleylamine is used,[55] but not when tri-*n*-octylphosphine is used, in which case Eu^{3+} is preferred.[56] These observations underscore the specific roles of surficial functional groups on how these growth mechanisms proceed. In a related study, Wang and coworkers were able to control the growth of anatase TiO_2 using functionalized glass substrates. The authors note that amine-terminated glass grows

octahedron-shaped anatase TiO_2 nanocrystals, which are *ca.* 90—150 nm wide, whereas agglomerated crystals were observed to form on the surface of carboxylic acid-terminated glass. Interestingly, the authors note that the addition of alcohol during the synthesis promotes preferred growth along the [001] direction.[57]

In these examples above, organic molecules serve as surfactants and passivating ligands in the growth of nanoparticles. Correspondingly, this phenomenon extends to more practical situations such as environmental pollution, in particular on the growth and stabilization of metallic nanoparticles in the presence of dissolved organic compounds in natural aquatic systems. As technology has advanced, alarming concentrations of precious metals and their ions have been measured in water streams near sewage facilities. Concerning numbers include 1,890,000 μg/L Au detected in Nagano Prefecture, Japan in 2009 and 602,000 μg/L Pt and 710,000 μg/L Pd from sewage ash from incinerators in the United Kingdom in 2012.[58] Aside from the significant emphasis that has been raised on the toxicity they pose in the environment, focus on their fate and transport in environmental systems has likewise been given attention.[59] Most of these precious metal ions are known to reduce into their metallic forms, and these zerovalent metals can likewise be re-oxidized into their cationic form in the presence of mild oxidants such as dissolved O_2.[60] The reduction of these metal cations into their zerovalent nanoparticles is usually mediated by DOMs. DOMs are defined to be particulate (below 450 nm[61]) organic mixtures of macromolecules produced by the microbial decomposition of animals and plants.[62] DOMs, such as Suwanee River fulvic and humic acids, are comprised of a mixture of polysaccharides, proteins, carbohydrates, and amino acids in aqueous

media.[60,63,64] While the exact structures of fulvic and humic acids are difficult to describe, it is known that the former are of lower molar mass and are water-soluble over a wide range of pH, whereas the former are of higher molar mass and are water-soluble only at non-acidic pH.[60] Some metal cations, including Cu^{2+}, have been reported to form complexes with DOMs in aqueous media.[65] For other precious metal ions, especially those with high reduction potentials, such as Ag^{+} and Au^{3+}, DOMs serve as reducing agents and surface-passivating ligands, mediating the formation and stabilization of Ag^{0} and Au^{0}.[64,66,67] Various mechanisms on the reduction of these precious metals have been proposed—the most common of which involves an initial complexation with Lewis basic groups in fulvic and humic acids followed by single-electron transfer events from redox-active quinone, hydroquinone, and semiquinone groups.[14,68,69] Jiang and coworkers further emphasize that these hydroquinone (and phenolic) groups in fulvic and humic acid are photooxidized in the presence of sunlight (**Eq. 1.2**), leading to the formation of superoxide anion radicals from dissolved O_2 in water (**Eq. 1.3**),

$$HA\ (aq.) + h\nu \rightarrow HA^{+}\ (aq.) + e^{-} \qquad \textbf{Eq. 1.2}$$

$$O_2\ (aq.) + e^{-} \rightarrow O_2^{\bullet -}\ (aq.) \qquad \textbf{Eq. 1.3}$$

which are then responsible for the reduction of Ag^{+} and Au^{3+} into Ag^{0} and Au^{0}, respectively.[70]

An autocatalytic reaction mechanism has also been proposed for the formation of Ag nanoparticles, which involves the initial generation of Ag_2O at basic pH followed by the deposition of stable Ag^{+} clusters on the surface of colloidal Ag_2O. The Ag^{+} clusters are then reduced by DOMs in aqueous solution.[66] The importance of studying the

formation and stabilization of precious metal nanoparticles allows one to understand the potential ecotoxicity, transport, and stability of these nanoparticles[59] in aquatic systems. **Figure 1.4** shows a diagram of how Ag^+ in aqueous media can be reduced into its metallic form with DOMs as reducing agents, and how Ag nanoparticles can be oxidized back into Ag^+ in the presence of oxidizing agents, such as O_2, under acidic conditions.[71]

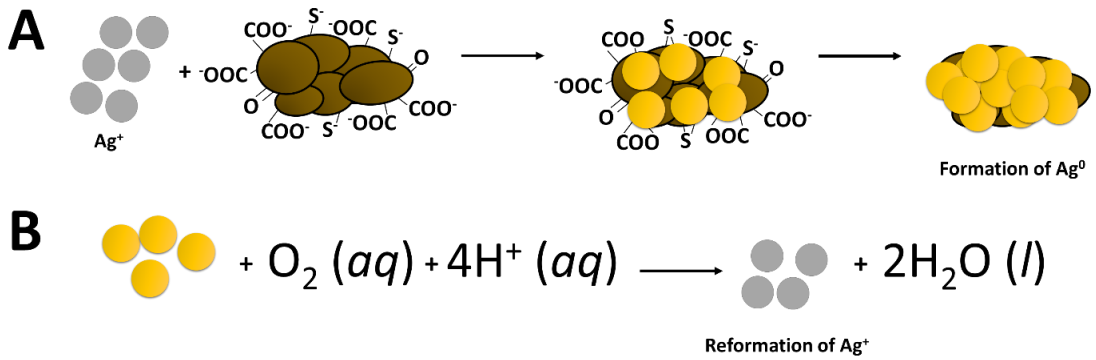

Figure 1.4: Schematic of the reduction of Ag^+ (A) and oxidation of Ag^0 in aqueous media (B). Dissolved organic matter such as fulvic and humic acids promote the reduction by an initial complexation of Ag^+ with Lewis basic groups, followed by single-electron transfer reactions from quinone, hydroquinone, and semiquinone groups. Under acidic conditions and in the presence of O_2, Ag^0 can be oxidized back to Ag^+. The images from **Figure 1.4A** and **1.4B** are adapted from references 14 and 71.

In past work, our group, in collaboration with the group of Prof. Virender Sharma, extensively studied the growth of Ag nanoparticles in the presence of fulvic and humic acids at pH values emulative of natural aquatic conditions. It has been noted that Ag^+ can be reduced into Ag^0 in aqueous media in the presence of fulvic and humic acids with such reductants serving as electron donors in the redox process.[67] The formation of Ag nanoparticles is further accelerated by an increase in alkalinity and temperature of the

reaction.[66] The temperature increase is still environmentally relevant given that the U.S. Environmental Protection Agency (EPA) has detected an average of 43,000 μg/L of Ag^+ in hot springs across the country.[72] Aside from these, other studies on the formation of Au nanoparticles by the reduction of Au^{3+} in the presence of DOMs have likewise been thoroughly investigated.[70,73] The mechanism of Au nanoparticle formation does not deviate significantly from Ag nanoparticle formation.

These studies, however, have only focused on the mechanistic growth of a single metallic species. While various studies do note that their findings can also be generalized to other precious metals, what this assumption fails to account for is the fact that the possibility of metal alloy formation exists, given that various metals and metal ions are continuously released into water streams from processing plants. However, no studies investigating the mechanistic growth of metallic alloy nanoparticles in natural aquatic systems have been attempted. Silver and gold, for example, both have the same face-centered cubic (fcc) crystal structure (with lattice constants which are in close proximity to each other, a_{Ag} = 4.086Å and a_{Au} = 4.079Å), and can therefore form Ag-Au alloys. Various studies on the synthesis of Ag-Au alloys have been conducted (the common route to which is the co-reduction of $HAuCl_4$ and $AgNO_3$), owing to the fact that the plasmonic properties of this alloy are tunable as a function of Ag and Au composition, thereby finding attractive applications in biosensing and catalysis, among many others.[74–76] In the area of environmental remediation, however, these alloys may possibly exhibit toxic properties which are different to what has already been determined for individual Ag and Au nanoparticles.

Aside from the surface properties of the monometallic and alloyed nanocrystals, natural aquatic parameters, including pH and ionic strength, contribute to their fate, transport, and toxicity.[60] Elucidating the mechanism underpinning the natural formation of Ag-Au bimetallic alloy nanoparticles and understanding the surficial interactions which promote their stability in aqueous media are keys to determining the fate, transport, and toxicity of these nanomaterials. In **Chapter III**, we verify that Ag-Au bimetallic alloy nanoparticles can be grown and stabilized in aqueous media in the presence of DOMs. In general, a higher yield of Ag-Au bimetallic alloy nanoparticles is noted with increasing pH. Surficial interactions, particularly complexation with Lewis basic groups (carbonyls, carboxyls, thiols, *etc.*) in fulvic and humic acids, initiate the reduction of Ag- and Au-ions with redox-active quinone, hydroquinone, and semiquinone groups *via* single-electron transfer events. The Ag-Au bimetallic alloy NPs are eventually formed as a result of galvanic replacement. An observed charge-transfer from Au to Ag is noted to help in mitigating the oxidation of Ag on the surface of Ag-Au bimetallic alloy NPs.[14] Preferential incorporation of Au over Ag is observed, since Au^{3+} has a greater/more positive reduction potential over Ag^{+} (1.50 V *vs.* SHE for Au^{3+}, 0.80 V *vs.* SHE for Ag^{+}).[14] Ag-Au bimetallic alloy nanoparticles grown in the presence of humic acids appeared to be more agglomerated than those synthesized with fulvic acids, given that humic acids have higher molar mass (and thus have more functional groups than fulvic acids). In **Chapter IV**, we take a step further into a more realistic scenario in which natural sunlight plays a role in the formation of Ag-Au bimetallic alloy nanoparticles. Jiang and coworkers suggest that the presence of sunlight promotes the photooxidation of DOMs, mediating the formation

of superoxide anion radicals which then ultimately act as reducing agents for Ag^{+} and Au^{3+}. However, it is important to note that another possible mechanism, in particular, a plasmon-induced pathway, can lead to the photoreduction of Ag- and Au-ions in solution. Brus and coworkers have shown that plasmon-excitation of Ag seeds played a catalytic role in the formation of Ag nanoparticles. Upon the photogeneration of electrons and holes on the surface of the metal, holes oxidize the capping ligand, in their case trisodium citrate dihydrate, leaving behind electrons to reduce Ag^{+}.[77,78] The size and morphology of the Ag nanoparticles were tuned by adjusting the concentration of the citrate.[77,79] In our work, we anticipate fulvic and humic acids to behave as hole acceptors, leaving behind plasmon-generated electrons to mediate the formation of Ag-Au bimetallic alloy nanoparticles. **Chapter IV** outlines our efforts to derive which of these two mechanisms dominate the sunlight-activated and DOM-mediated formation of Ag-Au bimetallic alloy nanoparticles. **Figure 1.5** illustrates the difference between these two mechanisms. We note a minimal initial contribution of superoxide anion radicals in the formation of Ag, Au, and Ag-Au bimetallic alloy nanoparticles. After the formation of Ag and Au seeds, the plasmon-mediated pathway is the more dominant mechanism for the formation of the nanoparticles. Badirredy *et al.* have deduced the same mechanism with Ag nanoparticles grown with either DOMs or extracellular polymeric substances (EPS) as reducing agent.[80] On the other hand, Au and Ag-Au bimetallic alloy nanoparticles have the same size whether the reaction is conducted under an LED lamp or in the dark. The same surficial interactions present in Ag-Au bimetallic alloy nanoparticles grown without exposure to sunlight, which are, a) complexation with Lewis basic groups of DOMs and b) Au to Ag charge-

transfer are also observed with the sunlight-grown Ag-Au bimetallic alloy nanoparticles. Unlike our results outlined in **Chapter III**, preferential incorporation of Ag over Au is observed. This observation is suggestive of an accelerated DOM-mediated growth of Ag nanoparticles over Au nanoparticles.

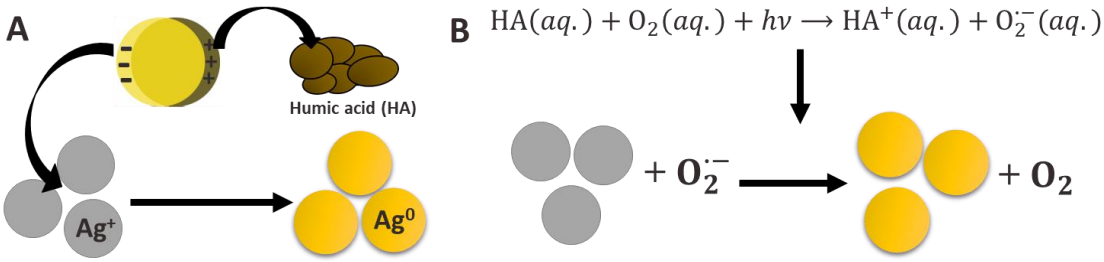

Figure 1.5: Two possible mechanisms underpinning the formation of Ag nanoparticles in natural aquatic media, in the presence of humic acid and sunlight. A) The first mechanism is plasmon-induced, in which plasmon-generated holes oxidize the humic acid, leaving behind plasmon-generated electrons to reduce remaining Ag^{+} into Ag^{0}. B) Sunlight activates the humic acid, which undergoes a redox reaction (*via* its phenol groups) with dissolved O_2 to form superoxide anion radicals. These superoxide anion radicals subsequently reduce Ag^{+} into Ag^{0} to regenerate O_2. The mechanism for **Figure 1.5B** is adapted from reference 70.

Our work in **Chapters III** and **IV** underscores the importance of surficial interactions in the DOM-mediated reduction of Ag, Au, and Ag-Au NPs in natural aquatic media, which are mediated by complexation of Lewis acid groups of DOM's to cationic precursors. We have shown that at room temperature conditions (*i.e.*, without the introduction of external heat), it is still possible to grow Ag-Au bimetallic alloy nanoparticles, albeit it requires an extensive period of time.[14] Nonetheless, this highlights the natural generation of Ag-Au bimetallic alloy nanoparticles from Ag- and Au-ions released in aquatic systems. The formation of Ag-Au bimetallic alloy nanoparticles also extends to other mineralization processes which can produce other alloys from other

precious metal ions which are likewise released in aquatic systems. Moreover, knowing the underpinning mechanisms behind the surface-mediated growth will aid in designing preventive protocols in the remediation of these nanoparticles in the environment. ElBishlawi and Jaffe have noted that the complexation of metals with Lewis basic groups of DOMs promotes the mobilization of metallic nanoparticles in aquatic systems.[81] In previous work, our group has noted that Ag nanoparticles tend to agglomerate and segregate in hard water systems faster than in freshwater streams owing to competing interactions of salt cations such as Na^+, K^+, Mg^{2+}, and Ca^{2+} with fulvic and humic acids.[64] Additionally, for Ag-Au bimetallic alloys, only a few toxicity studies have been conducted.[82,83] Our work shows that similar to engineered nanomaterials, various experimental conditions (such as pH and molar mass of the DOM) dictate the growth of natural nanoparticles. Studies on Ag and Au nanoparticles note that toxicity is a function of size and the surface-capping ligand. In general, the toxicity of a metallic nanoparticle increases as its size decreases as a result of the increased surface-area-to-volume ratio.[84] In an article published by Bishnoi and coworkers, it was observed that the toxicity of Ag-Au bimetallic alloy nanoparticles is a function of the composition of Ag and Au in the alloy.[82] Other studies have reported antimicrobial[85] and germicidal[83] properties of Ag-Au bimetallic alloy nanoparticles.

1.4 Interstitial Boron-Doping of Vanadium(IV) Oxide

In a technologically advancing world, thermal comfort has become an important necessity in everyday function, thereby increasing energy costs for cooling and/or heating

maintenance in both commercial and residential buildings. Around 19% of global energy consumption is from the United States alone.[86] The Department of Energy (DoE) reports that in the country, the biggest contributor to energy consumption in the past decade has been the buildings sector, accounting for around 40% of total consumption (98.2×10^{15} BTU, accounting to a global 7% contribution), followed by the industrial (*ca.* 33%) and transportation (*ca.* 28%) sectors.[86] The DoE further reports that around 30% of energy spent to cool and/or heat commercial and residential buildings is wasted with average traditional windows,[87] given that their glazings frequently permit excessive transmittance of thermal radiation (corresponding to the 700 to 2,500 nm range of the electromagnetic spectrum).[88] The imminent challenge therefore is to modify the fenestration (windows, doors, skylights, roofs, etc.)[89] of buildings in order to minimize, if not eliminate, costs on excessive cooling and/or heating buildings.

In terms of "smart windows," the use of thermochromic materials as window glazings has attracted much research interest. As the name implies, these materials undergo a spectral change in response to external temperature. As fenestration elements, these materials can be used to control solar heat gain, without the external application of a voltage, in response to external temperatures. At warmer temperatures, the thermochromic glazing modulates infrared radiation, thereby reducing cooling costs in the summer, but at colder outside temperatures, the material permits the transmittance of infrared radiation, thus minimizing heating expenditures in the winter. **Figure 1.6** shows a cartoon depiction of how a smart window is envisioned to work. Regardless of outside temperature, visible light transmission should not be compromised. The prime candidates

for thermochromic coatings are transition metal oxides, which undergo a reversible metal—insulator transition upon the application of heat.[90–92] For smart windows, however, VO_2 is perhaps the most practical to use as a thermochromic film, given that its T_{MIT} is 67°C, a value which is reasonably close to room temperature.[16] Below 67°C, VO_2 is infrared-transparent and exists in its monoclinic (M_1) phase ($P2_1/c$) with a band gap of *ca.* 0.8 eV. Above 67°C, VO_2 transforms at a timescale faster than *ca.* 307 fs into its infrared-blocking, metallic tetragonal/rutile (R) phase ($P4_2/mnm$).[16,93–97] The M_1 phase of VO_2 has alternating V—V bond lengths of 2.65Å and 3.12Å (along the crystallographic *a* axis) which adopt a canted, zigzag configuration. On the other hand, the R phase is more symmetric and more linear in configuration, with uniform V—V bond lengths of 2.85Å (along the *c* axis).[16,93,98,99] This phase transition from M_1 to R is depicted in **Figure 1.7**. Infrared radiation is transmitted in the low-temperature M_1 phase, whereas infrared radiation is absorbed (as a result of localized surface plasmon resonance[97]) in the high-temperature R phase (for both cases, the visible-region transmittance is not compromised).[16]

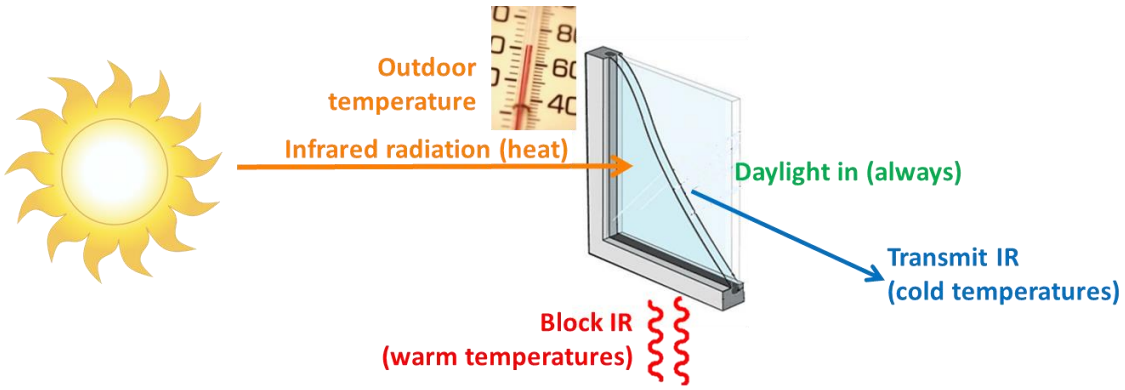

Figure 1.6: Cartoon depiction of a "smart window." When outside temperatures are high, the thermochromic coating blocks infrared radiation *via* the formation of a localized surface plasmon. When outside temperatures are low, the thermochromic coating blocks infrared radiation. Regardless of outside temperature, the glazing should transmit visible light. The image is adapted from references 89 and 97.

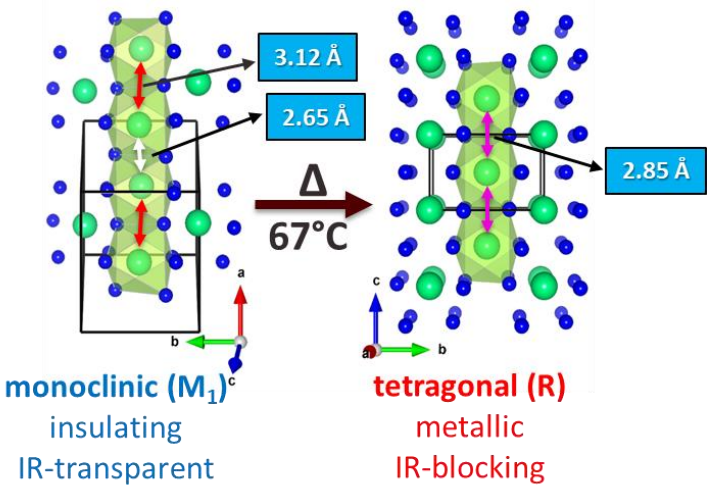

Figure 1.7: Schematic depiction of the metal—insulator transition of VO_2 at 67°C. Green spheres represent V atoms whereas blue spheres depict O atoms. The M_1 phase has alternating V—V bond lengths along the crystallographic *a* axis whereas the R phase has uniform V—V bond lengths along the crystallographic *c* axis. The image is adapted from reference 98.

Despite the remarkable efforts invested in dispersion of VO_2 nanocrystals within polymeric matrices,[100] it is equally important to modulate the T_{MIT} from 67°C to a value within the room temperature range (20—30°C).[16,101,102] One way to achieve this goal is by

scaling to finite size. In previous work, our group has demonstrated the solvothermal synthesis of VO_2 nanobelts and nanosheets by the intercalation, cleavage, and exfoliation of bulk V_2O_4 by small aliphatic alcohols. A drop of the metal→insulator transition (cooling transition) to as low as 32°C using 1,3-butanediol as a structure-directing agent was observed.[103] Another route is to introduce oxygen vacancies into VO_2 *via* electrochemical reactions with ionic liquids.[104] However, the most studied route to the modulation of the metal—insulator transition is the introduction of metal cations as dopants, such as Mg^{2+}, Ti^{4+}, Nb^{5+}, Mo^{5+}, and W^{6+} into the VO_2 lattice. In particular, most of these metal cations serve as substitutional dopants in V sites.[98,105–108] For example, at 0.9 at.% of W, W-doped VO_2 transitions at *ca.* 34°C,[98] whereas 1.45 at.% Mo-doped VO_2 transitions at *ca.* 26°C.[108] **Figure 1.8** shows the dependence of T_{MIT} with at.% of either W^{6+} or Mo^{5+}. Both heating and cooling transitions are depressed to lower temperatures with increasing dopant concentration. The modulation of T_{MIT} is brought about by a) the introduction of a localized strain on the $(12\bar{2})$ plane of M_1 VO_2 which accelerates the metal→insulator transition[109] and b) Mo and W donating one and two electrons, respectively, per dopant atom to the band structure of VO_2.[98,108] Long and coworkers have likewise studied introducing lanthanides into the VO_2 lattice, with each dopant substituting in a V site. The greatest drop in average T_{MIT} was observed for 4 at.% Eu-doped VO_2, at 48°C.[110] On the other hand, slight modulation of average T_{MIT} to 63°C was observed for both 4 at.% La-doped VO_2[111] and Tb-doped VO_2.[112]. It has been reported that the same strain arguments with W^{6+} and Mo^{5+} dopants also hold correct when these lanthanides substitute in a V site.[110–112] On the other hand, some dopants, give rise to an *increase* in

transition temperature of VO_2 upon introduction, such as Al^{3+} (83°C)[113] and Ga^{3+} (80°C).[114] Aside from increasing the transition temperature, these trivalent dopants, along with Cr^{3+} and Fe^{3+}, stabilize the metastable M_2 phase of VO_2.[115] The M_2 phase is three times more insulating than the M_1 phase and is not useful for thermochromic coatings.[116] Various methods of doping VO_2 have been reported in literature including hydrothermal synthesis,[98,106,108,117] chemical vapor deposition,[107,118,119] ion implantation,[120] sol-gel synthesis,[121–123] solid-state reaction,[124] sputtering,[105,125,126] and thermolysis.[127]

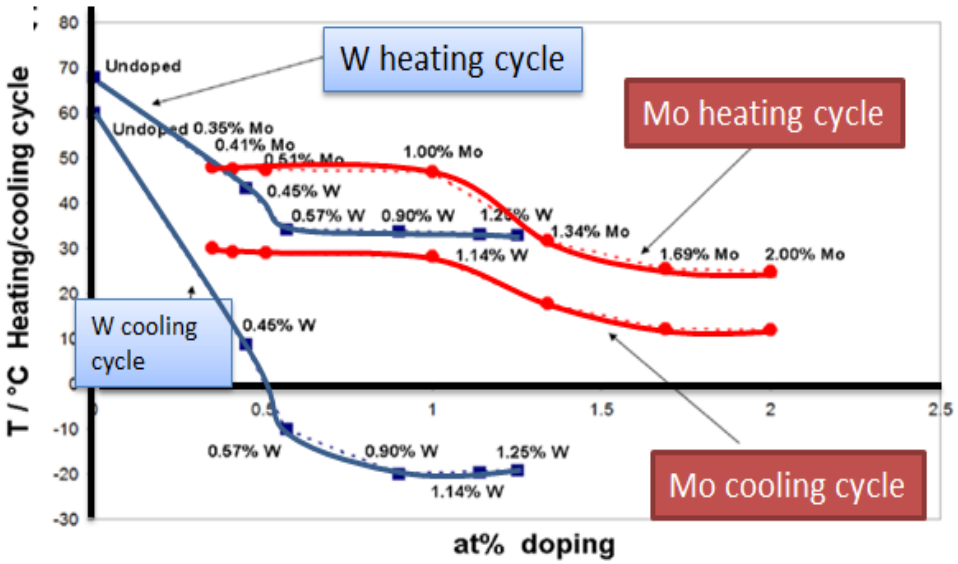

Figure 1.8: Relationship between metal—insulator transition temperature *versus* dopant concentration (W^{6+} or Mo^{5+}) in $M_xV_{1-x}O_2$ nanowires (where M = W or Mo). Greater dopant incorporation results in a lower T_{MIT}. The image is adapted from reference 16.

Dopants are introduced into freestanding VO_2 during synthesis. The process for introducing W^{6+} and Mo^{5+} into VO_2 involves a one-pot hydrothermal synthesis in which the dopant precursor is introduced along with the starting material, usually V_2O_5. In the

presence of reducing agents, such as aliphatic alcohols and ketones, V_2O_5 is hydrothermally reduced into VO_2.[98,128] The strain introduced along the crystallographic columns of VO_2 (normal to the $(12\bar{2})$ plane) as a consequence of W and Mo substituting for a V atom results in the depression of the T_{MIT} of VO_2. **Figure 1.9** shows a high-angle annular dark field (HAADF) atomic resolution image of W-doped VO_2. Aside from the possibility of inhomogeneous doping,[109] the success or failure of *in situ* doping is highly sensitive to subtle changes in experimental variables. These issues, originally encountered in the silicon-doping industry, are mitigated by *ex situ* doping. *Ex situ* doping involves a facile and robust two-step process in which dopants are introduced after the target substrate (in this case, VO_2) is synthesized. Aside from the additional procedural flexibility, *ex situ* doping techniques offer greater control of dopant incorporation into the substrate.[129] *Ex situ* doping of VO_2 has been relatively underexplored due to its close-packed crystal structure. Intriguingly, Pan and coworkers have calculated that as a diffusive interstitial dopant, B atoms can reduce the T_{MIT} of VO_2 by as much as 83 K/at. B% (thrice the value for W-doping). The main advantage of the *ex situ* doping process over its conventional one-pot *in situ* counterpart is the capability to first synthesize high-quality VO_2 prior to introducing a dopant, allowing for a more programmable route for "dialing in" the T_{MIT} of VO_2.

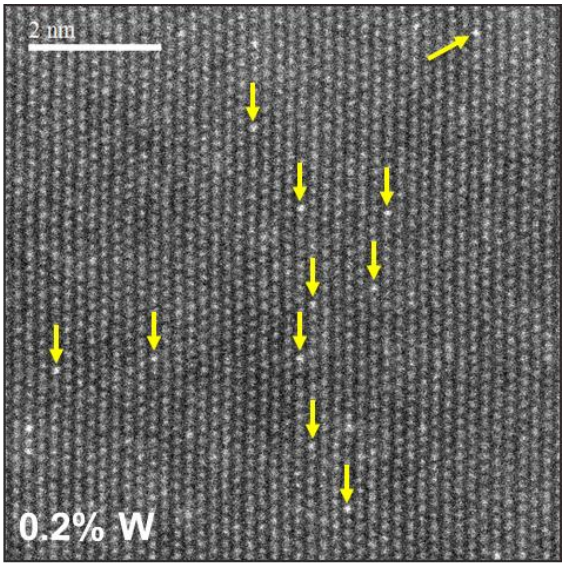

Figure 1.9: High-angle annular dark field atomic resolution image of 0.2% W-doped VO_2. The brighter spots (marked with yellow arrows) observed are W atoms which substitute for V sites. The image is adapted from reference 109.

In **Chapter V** we report a novel two-step surface-limiting *ex situ* diffusive doping technique for introducing B atoms into the interstitial sites of the VO_2 lattice. The first step is the initial physisorption of the molecular precursor, 2-allyl-4,4,5,5-tetramethyl-1,3,2-dioxaborolane onto previously-prepared freestanding VO_2 nanowires. After physisorption is achieved, the reaction mixture is annealed at 900—950°C in the second step, promoting the simultaneous thermal decomposition of the boron precursor and the diffusion of B atoms into VO_2.[15] This technique we have developed is a modification from a previous work which involved monolayer doping of B atoms into Si.[130] The doping process we developed is schematically illustrated in **Figure 1.10**. We note a linear correlation between dopant concentration and T_{MIT}; a greater modulation of T_{MIT} is observed with increasing B atom incorporation, thereby stabilizing the R-phase at lower temperatures. For example, at 3.8 at.% B incorporation, B-doped VO_2 transitions from the

M_1 to the R phase at a temperature as low as 23°C.[15] More B atoms are incorporated into VO_2 nanowires as particle size decreases as a result of the increased surface-area-to-volume ratio. The B atoms reside in the tetrahedral interstitial sites of VO_2, and their incorporation results to the formation of B–O bonds, resulting in a decreased covalency of V–O bonds and increased V–V overlap along the crystallographic *c* axis, thereby rendering VO_2 more metallic.

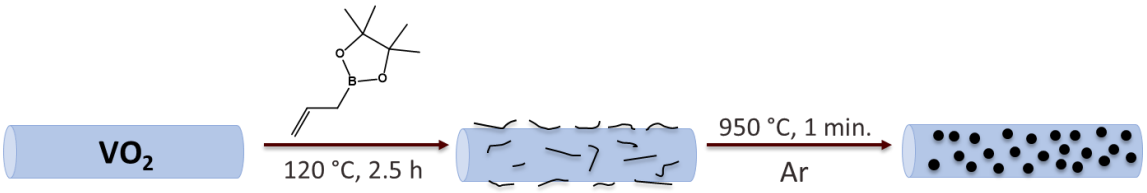

Figure 1.10: Schematic of the *ex situ* introduction of VO_2 *via* diffusive annealing. The molecular precursor, 2-allyl-4,4,5,5-tetramethyl-1,3,2-dioxaborolane (depicted as crooked lines) is first physisorbed onto VO_2 nanobeams at 120°C, after which the assembly is heated in an inert atmosphere at 900—950°C to simultaneously promote the decomposition of the molecular precursor and the introduction of B atoms (depicted as black spheres). The image is adapted from reference 15.

Our results for *ex situ* B-doping opens up an alternative route for introducing dopant atoms into VO_2. Aside from B atoms, atomic H is another diffusive dopant which has been reported to be introduced in the interstitial sites of VO_2 through a catalytic spillover method. The incorporation of H atoms in VO_2, especially at high concentrations, stabilizes two orthorhombic phases of VO_2: O1 and O2. However, annealing H-doped VO_2 at 130°C causes the diffusion of H atoms out of the VO_2 lattice.[131,132] The introduction of B atoms in VO_2 using our *ex situ* diffusive doping process suggests that unlike H-incorporation, our process is not reversible at relatively low temperatures, given that our

annealing temperatures were mostly held at 900—950°C. Our doping method offers a more precise way for selectively tuning the T_{MIT} of VO_2 by simply changing the annealing temperature. The particle size of VO_2 also dictates how much B atoms are incorporated into the lattice, given that smaller nanowires have a higher surface-area-to-volume ratio, as previously mentioned. For *in situ* doping procedures, adjusting the T_{MIT} of VO_2 to a desired value is rigorously done by careful adjustment of dopant precursor concentration. Therefore, the *ex situ* diffusive annealing method allows for easier tuning of the T_{MIT} for temperature-specific applications. For example, as used in thermochromic coatings, *ex situ* doping can provide a wide selection of T_{MIT} values, since different geographic locations around the world will require values specific for their climate. Moreover, given the pronounced hysteresis that the B-doped VO_2 samples (*ca.* 19—23°C) show *versus* undoped VO_2 (*ca.* 5°C), this material can also be useful in other applications such as hybrid memory devices.[133,134] A large hysteresis is necessary to retain the nonvolatile state triggered upon the application of an external stimulus on a material once said stimulus is removed.[135] Understanding the mechanism of B-incorporation, which is commenced by an initial physisorption step, is key to further exploiting this technique to introduce other diffusive dopants into the VO_2 lattice. Indeed, this initial physisorption step makes our process starkly different from a one-step, one-pot *in situ* hydrothermal method. Until now, interstitial doping of VO_2 has not been provided much attention, given that the said transition metal oxide is a close-packed structure. Aside from B atoms, calculations by Pan and coworkers predict that other diffusive atoms, such as Be, can also be introduced into VO_2 and have the same effects of modulating the T_{MIT}.[136] **Chapter V** highlights the

promising results of our novel *ex situ* diffusive doping process in the hopes that this surface-limiting technique finds use in tuning the properties of other close-packed systems[137] by introduction of diffusive dopants.

1.5 References

(1) Kolasinski, K. W. *Surface Science: Foundations of Catalysis and Nanoscience*, 3rd ed.; John Wiley & Sons: West Chester, PA, 2012.

(2) Waetzig, G. R.; Depner, S. W.; Asayesh-Ardakani, H.; Cultrara, N. D.; Shahbazian-Yassar, R.; Banerjee, S. Stabilizing Metastable Tetragonal HfO_2 Using a Non-Hydrolytic Solution-Phase Route: Ligand Exchange as a Means of Controlling Particle Size. *Chem. Sci.* **2016**, *7*, 4930–4939.

(3) Lukowski, M. A.; Daniel, A. S.; Meng, F.; Forticaux, A.; Li, L.; Jin, S. Enhanced Hydrogen Evolution Catalysis from Chemically Exfoliated Metallic MoS_2 Nanosheets. *J. Am. Chem. Soc.* **2013**, *135*, 10274–10277.

(4) Ambrosi, A.; Sofer, Z.; Pumera, M. Lithium Intercalation Compound Dramatically Influences the Electrochemical Properties of Exfoliated MoS_2. *Small* **2014**, *11*, 605–612.

(5) Medintz, I. L.; Uyeda, H. T.; Goldman, E. R.; Mattoussi, H. Quantum Dot Bioconjugates for Imaging, Labelling and Sensing. *Nat. Mater.* **2005**, *4*, 435–446.

(6) Hua, G.; Zhang, L.; Fei, G.; Fang, M. Enhanced Catalytic Activity Induced by Defects in Mesoporous Ceria Nanotubes. *J. Mater. Chem.* **2012**, *22*, 6851–6855.

(7) Amabilino, D. B. Surfaces for Supramolecular Systems. In *Supramolecular*

Chemistry at Surfaces; Royal Society of Chemistry: Cambridge, England, 2016; Vol. 2016, pp 1–54.

(8) Tait, S. L.; Dohnálek, Z.; Campbell, C. T.; Kay, B. D. *n*-Alkanes on Pt(111) and on C(0001) Pt(111): Chain Length Dependence of Kinetic Desorption Parameters. *J. Chem. Phys.* **2006**, *125*, 24308/1–15.

(9) Love, J. C.; Estroff, L. A.; Kriebel, J. K.; Nuzzo, R. G.; Whitesides, G. M. Self-Assembled Monolayers of Thiolates on Metals as a Form of Nanotechnology. *Chem. Rev.* **2005**, *105*, 1103–1169, .

(10) Vericat, C.; Vela, M. E.; Corthey, G.; Pensa, E.; Cortés, E.; Fonticelli, M. H.; Ibañez, F.; Benitez, G. E.; Carro, P.; Salvarezza, R. C. Self-Assembled Monolayers of Thiolates on Metals: A Review Article on Sulfur-Metal Chemistry and Surface Structures. *RSC Adv.* **2014**, *4*, 27730–27754.

(11) Shon, Y.-S.; Lee, T. R. Chelating Self-Assembled Monolayers on Gold Generated from Spiroalkanedithiols. *Langmuir* **1999**, *15*, 1136–1140.

(12) Hausmann, D. M.; Kim, E.; Becker, J.; Gordon, R. G. Atomic Layer Deposition of Hafnium and Zirconium Oxides Using Metal Amide Precursors. *Chem. Mater.* **2002**, *14*, 4350–4358.

(13) Alivio, T. E. G.; De Jesus, L. R.; Dennis, R. V.; Jia, Y.; Jaye, C.; Fischer, D. A.; Singisetti, U.; Banerjee, S. Atomic Layer Deposition of Hafnium(IV) Oxide on Graphene Oxide: Probing Interfacial Chemistry and Nucleation by Using X-Ray Absorption and Photoelectron Spectroscopies. *ChemPhysChem* **2015**, *16*, 2842 – 2848.

(14) Alivio, T. E. G.; Fleer, N. A.; Singh, J.; Nadadur, G.; Feng, M.; Banerjee, S.; Sharma, V. K. Stabilization of Ag-Au Bimetallic Nanocrystals in Aquatic Environments Mediated by Dissolved Organic Matter: A Mechanistic Perspective. *Environ. Sci. Technol.* **2018**, *52*, 7269–7278.

(15) Alivio, T. E. G.; Sellers, D. G.; Asayesh-Ardakani, H.; Braham, E. J.; Horrocks, G. A.; Pelcher, K. E.; Villareal, R.; Zuin, L.; Shamberger, P. J.; Arroyave, R.; Shahazian-Yassar, R.; Banerjee, S.. Postsynthetic Route for Modifying the Metal—Insulator Transition of VO_2 by Interstitial Dopant Incorporation. *Chem. Mater.* **2017**, *29*, 5401–5412.

(16) Whittaker, L.; Patridge, C. J.; Banerjee, S. Microscopic and Nanoscale Perspective of the Metal-Insulator Phase Transitions of VO_2: Some New Twists to an Old Tale. *J. Phys. Chem. Lett.* **2011**, *2*, 745–758.

(17) Geim, A. K.; Novoselov, K. S. The Rise of Graphene. *Nat. Mater.* **2007**, *6*, 183–191.

(18) Allen, M. J.; Tung, V. C.; Kaner, R. B. Honeycomb Carbon: A Review of Graphene. *Chem. Rev.* **2010**, *110*, 132–145.

(19) Schultz, B. J.; Dennis, R. V.; Lee, V.; Banerjee, S. An Electronic Structure Perspective of Graphene Interfaces. *Nanoscale* **2014**, *6*, 3444–3466.

(20) Luxmi; Srivastava, N.; He, G.; Feenstra, R. M.; Fisher, P. J. Comparison of Graphene Formation on C-Face and Si-Face SiC {0001} Surfaces. *Phys. Rev. B* **2010**, *82*, 1–11.

(21) Vlassiouk, I.; Regmi, M.; Fulvio, P.; Dai, S.; Datskos, P.; Eres, G.; Smirnov, S.

Role of Hydrogen in Chemical Vapor Deposition Growth of Large Single-Crystal Graphene. *ACS Nano* **2011**, *5*, 6069–6076.

(22) Li, X.; Cai, W.; An, J.; Kim, S.; Nah, J.; Yang, D.; Piner, R.; Velamakanni, A.; Jung, I.; Tutuc, E.; Banerjee, S. K.; Colombo, L.; Ruoff, R. S.. Large-Area Synthesis of High-Quality and Uniform Graphene Films on Copper Foils. *Science* **2009**, *324*, 1312–1314.

(23) Qi, M.; Ren, Z.; Jiao, Y.; Zhou, Y. Hydrogen Kinetics on Scalable Graphene Growth by Atmospheric Pressure Chemical Vapor Deposition with Acetylene Hydrogen Kinetics on Scalable Graphene Growth by Atmospheric Pressure Chemical Vapor Deposition with Acetylene. *J. Phys. Chem. C* **2013**, *117*, 14348–14353.

(24) Zhou, S. Y.; Siegel, D. A.; Fedorov, A. V.; Lanzara, A. Metal to Insulator Transition in Epitaxial Graphene Induced by Molecular Doping. *Phys. Rev. Lett.* **2008**, *101*, 1–4.

(25) Chen, W.; Chen, S.; Dong, C. Q.; Xing, Y. G.; Wee, A. T. S. Surface Transfer p-Type Doping of Epitaxial Graphene. *J. Am. Chem. Soc.* **2007**, *129*, 10418–10422.

(26) Tsai, H. Z.; Omrani, A. A.; Coh, S.; Oh, H.; Wickenburg, S.; Son, Y. W.; Wong, D.; Riss, A.; Jung, H. S.; Nguyen, G. D.; Rodgers, G. F.; Aikawa, A. S.; Taniguchi, T.; Watanabe, K. Zettl, A.; Louie, S.G.; Lu,J.; Cohen,M. L.; Crommie, M. F.. Molecular Self-Assembly in a Poorly Screened Environment: F4-TCNQ on Graphene/BN. *ACS Nano* **2015**, *9*, 12168–12173.

(27) Lu, Y. H.; Chen, W.; Feng, Y. P.; He, P. M. Tuning the Electronic Structure of

Graphene by an Organic Molecule. *J. Phys. Chem. B* **2009**, *113*, 2–5.

(28) Zhang, Y.-H.; Zhou, K.-G.; Xie, K.-F.; Zeng, J.; Zhang, H.-L.; Peng, Y. Tuning the Electronic Structure and Transport Properties of Graphene by Noncovalent Functionalization: Effects of Organic Donor, Acceptor and Metal Atoms. *Nanotechnology* **2010**, *21*, 065201/1–7.

(29) Dahal, A.; Batzill, M. Graphene-Nickel Interfaces: A Review. *Nanoscale* **2014**, *6*, 2548–2562.

(30) Dedkov, Y. S.; Fonin, M.; Rüdiger, U.; Laubschat, C. Rashba Effect in the Graphene/Ni(111) System. *Phys. Rev. Lett.* **2008**, *100*, 1–4.

(31) Giovannetti, G.; Khomyakov, P. A.; Brocks, G.; Karpan, V. M.; Van Den Brink, J.; Kelly, P. J. Doping Graphene with Metal Contacts. *Phys. Rev. Lett.* **2008**, *101*, 4–7.

(32) Lin, Y.-M.; Jenkins, K. A.; Valdes-Garcia, A.; Small, J. P.; Farmer, D. B.; Avouris, P. Operation of Graphene Transistors at Gigahertz Frequencies. *Nano Lett.* **2009**, *9*, 422–426.

(33) Schultz, B. J.; Lee, V.; Price, J.; Jaye, C.; Lysaght, P. S.; Fischer, D. A.; Prendergast, D.; Banerjee, S. Near-Edge X-Ray Absorption Fine Structure Spectroscopy Studies of Charge Redistribution at Graphene/Dielectric Interfaces. *J. Vac. Sci. Technol. B Microelectron. Nanom. Struct.* **2012**, *30*, 041205/1–6.

(34) Wang, X.; Tabakman, S.; Dai, H. Atomic Layer Deposition of Metal Oxides on Pristine and Functionalized Graphene. *J. Am. Chem. Soc.* **2008**, *130*, 8152–8153.

(35) Hollander, M. J.; Labella, M.; Hughes, Z. R.; Zhu, M.; Trumbull, K. A.; Cavalero,

R.; Snyder, D. W.; Wang, X.; Hwang, E.; Datta, S.; Robinson, J. A. Enhanced Transport and Transistor Performance with Oxide Seeded High-κ Gate Dielectrics on Wafer-Scale Epitaxial Graphene. *Nano Lett.* **2011**, *11*, 3601–3607.

(36) Hummers, W. S.; Offeman, R. E. Preparation of Graphitic Oxide. *J. Am. Chem. Soc*. **1958**, *80*, 1339.

(37) Hunt, A.; Kurmaev, E. Z.; Moewes, A. Band Gap Engineering of Graphene Oxide by Chemical Modification. *Carbon* **2014**, *75*, 366–371.

(38) Lerf, A.; He, H.; Forster, M.; Klinowski, J. Structure of Graphite Oxide Revisited. *J. Phys. Chem. B* **1998**, *102*, 4477–4482.

(39) De Jesus, L. R.; Dennis, R. V.; Depner, S. W.; Jaye, C.; Fischer, D. A.; Banerjee, S. Inside and Outside: X-Ray Absorption Spectroscopy Mapping of Chemical Domains in Graphene Oxide. *J. Phys. Chem. Lett.* **2013**, *4*, 3144–3151.

(40) Ju, H.; Feng, X.; Ye, Y.; Zhang, L.; Pan, H.; Campbell, C. T.; Zhu, J. Ca Carboxylate Formation at the Calcium/Poly(Methyl Methacrylate) Interface. *J. Phys. Chem. C* **2012**, *116*, 20465–20471.

(41) Lin, Y.-M.; Dimitrakopoulos, C.; Jenkins, K. A.; Farmer, D. B.; Chiu, H.; Grill, A.; Avouris, P. 100-GHz Transistors From. *Science* **2010**, *327*, 100.

(42) Lin, Y.-M.; Valedes-Garcia, A.; Han, S.-J.; Farmer, D. B.; Meric, I.; Sun, Y.; Wu, Y.; Dimitrakopoulos, C.; Grill, A.; Avouris, P.; Jenkins, K. A. Wafer-Scale Graphene Integrated Circuit. **2011**, *Science 332*, 1294–1298.

(43) Song, J.; Kam, F. Y.; Png, R. Q.; Seah, W. L.; Zhuo, J. M.; Lim, G. K.; Ho, P. K. H.; Chua, L. L. A General Method for Transferring Graphene onto Soft Surfaces.

Nat. Nanotechnol. **2013**, *8*, 356–362.

(44) Schultz, B. J.; Patridge, C. J.; Lee, V.; Jaye, C.; Lysaght, P. S.; Smith, C.; Barnett, J.; Fischer, D. A.; Prendergast, D.; Banerjee, S. Imaging Local Electronic Corrugations and Doped Regions in Graphene. *Nat. Commun.* **2011**, *2*, 372/1–7.

(45) Hoffmann, M. R.; Martin, S.; Choi, W.; Bahnemann, D. W. Environmental Applications of Semiconductor Photocatalysis. *Chem. Rev.* **1995**, *95*, 69–96.

(46) Wu, W.; Jiang, C.; Roy, V. A. L. Recent Progress in Magnetic Iron Oxide Semiconductor Composite Nanomaterials as Promising Photocatalysts. *Nanoscale* **2014**, 38–58.

(47) Machado, B. F.; Serp, P. Graphene-Based Materials for Catalysis. *Catal. Sci. Technol.* **2012**, *2*, 54–75.

(48) Cheng, Y.; Fan, Y.; Pei, Y.; Qiao, M. Graphene-Supported Metal/Metal Oxide Nanohybrids: Synthesis and Applications in Heterogeneous Catalysis. *Catal. Sci. Technol.* **2015**, *5*, 3903–3916.

(49) Zhu, Y.; Murali, S.; Cai, W.; Li, X.; Suk, J. W.; Potts, J. R.; Ruoff, R. S. Graphene and Graphene Oxide: Synthesis, Properties, and Applications. *Adv. Mater.* **2010**, *22*, 3906–3924.

(50) Lightcap, I. V.; Kosel, T. H.; Kamat, P. V. Anchoring Semiconductor and Metal Nanoparticles on a Two-Dimensional Catalyst Mat. Storing and Shuttling Electrons with Reduced Graphene Oxide. *Nano Lett.* **2010**, *10*, 577–583.

(51) Murray, C. B.; Norris, D. J.; Bawendi, M. G. Synthesis and Characterization of Nearly Monodisperse CdE (E = S, Se, Te) Semiconductor Nanocrystallites. *J. Am.*

Chem. Soc. **1993**, *115*, 8706–8715.

(52) Bailey, R. E.; Smith, A. M.; Nie, S. Quantum Dots in Biology and Medicine. *Phys. E* **2004**, *25*, 1–12.

(53) Peng, X.; Schlamp, M. C.; Kadavanich, A. V; Alivisatos, A. P. Epitaxial Growth of Highly Luminescent CdSe/CdS Core/Shell Nanocrystals with Photostability and Electronic Accessibility. *J. Am. Chem. Soc.* **1997**, *7863*, 7019–7029.

(54) Cho, J.; Choi, Y. H.; O'Loughlin, T. E.; De Jesus, L.; Banerjee, S. Ligand-Mediated Modulation of Layer Thicknesses of Perovskite Methylammonium Lead Bromide Nanoplatelets. *Chem. Mater.* **2016**, *28*, 6909–6916.

(55) Waetzig, G. R.; Horrocks, G. A.; Jude, J. W.; Villalpando, G. V.; Zuin, L.; Banerjee, S. Ligand-Mediated Control of Dopant Oxidation State and X-Ray Excited Optical Luminescence in Eu-Doped LaOCl. *Inorg. Chem.* **2018**, *57*, 5842–5849.

(56) Waetzig, G. R.; Horrocks, G. A.; Davidson, R. D.; Jude, J. W.; Villalpando, G. V.; Zuin, L.; Banerjee, S. In a Different Light: Deciphering Optical and X-Ray Sensitization Mechanisms in an Expanded Palette of LaOCl Phosphors. *J. Phys. Chem. C* **2018**, *122*, 16412–16423.

(57) Wang, D.; Liu, J.; Huo, Q.; Nie, Z.; Lu, W.; Williford, R. E.; Jiang, Y. B. Surface-Mediated Growth of Transparent, Oriented, and Well-Defined Nanocrystalline Anatase Titania Films. *J. Am. Chem. Soc.* **2006**, *128*, 13670–13671.

(58) Prichard, H. M.; Wedin, F.; Sampson, J.; Jackson, M. T.; Fisher, P. C. Precious Metals in Urban Waste. *Water Environ. J.* **2016**, *30*, 151–156.

(59) Holden, P. A.; Nisbet, R. M.; Lenihan, H. S.; Miller, R. J.; Cherr, G. N.; Schimel, J. P.; Gardea-Torresdey, J. L. Ecological Nanotoxicology: Integrating Nanomaterial Hazard Considerations across the Subcellular, Population, Community, and Ecosystems Levels. *Acc. Chem. Res.* **2013**, *46*, 813–822.

(60) Sharma, V. K.; Filip, J.; Zboril, R.; Varma, R. S. Natural Inorganic Nanoparticles-Formation, Fate, and Toxicity in the Environment. *Chem. Soc. Rev.* **2015**, *44*, 8410–8423.

(61) Zsolnay, Á. Dissolved Organic Matter: Artefacts, Definitions, and Functions. *Geoderma* **2003**, *113*, 187–209.

(62) Dubas, S. T.; Pimpan, V. Humic Acid Assisted Synthesis of Silver Nanoparticles and Its Application to Herbicide Detection. *Mater. Lett.* **2008**, *62*, 2661–2663.

(63) Aiken, G. R.; Hsu-Kim, H.; Ryan, J. N. Influence of Dissolved Organic Matter on the Environmental Fate of Metals, Nanoparticles, and Colloids. *Environ. Sci. Technol.* **2011**, *45*, 3196–3201.

(64) Akaighe, N.; Depner, S. W.; Banerjee, S.; Sharma, V. K.; Sohn, M. The Effects of Monovalent and Divalent Cations on the Stability of Silver Nanoparticles Formed from Direct Reduction of Silver Ions by Suwannee River Humic Acid/Natural Organic Matter. *Sci. Total Environ.* **2012**, *441*, 277–289.

(65) Craven, A. M.; Aiken, G. R.; Ryan, J. N. Copper(II) Binding by Dissolved Organic Matter: Importance of the Copper-to-Dissolved Organic Matter Ratio and Implications for the Biotic Ligand Model. *Environ. Sci. Technol.* **2012**, *46*, 9948–9954.

(66) Adegboyega, N. F.; Sharma, V. K.; Siskova, K.; Zbořil, R.; Sohn, M.; Schultz, B. J.; Banerjee, S. Interactions of Aqueous Ag+ with Fulvic Acids: Mechanisms of Silver Nanoparticle Formation and Investigation of Stability. *Environ. Sci. Technol.* **2013**, *47*, 757–764.

(67) Akaighe, N.; MacCuspie, R. I.; Navarro, D. A.; Aga, D. S.; Banerjee, S.; Sohn, M.; Sharma, V. K. Humic Acid-Induced Silver Nanoparticle Formation under Environmentally Relevant Conditions. *Environ. Sci. Technol.* **2011**, *45*, 3895–3901.

(68) Zhou, S.; Chen, S.; Yuan, Y.; Lu, Q. Influence of Humic Acid Complexation with Metal Ions on Extracellular Electron Transfer Activity. *Sci. Rep.* **2015**, *5*, 1–9.

(69) Ratasuk, N.; Nanny, M. A. Characterization and Quantification of Reversible Redox Sites in Humic Substances. *Environ. Sci. Technol.* **2007**, *41*, 7844–7850.

(70) Yin, Y.; Liu, J.; Jiang, G. Sunlight-Induced Reduction of Ionic Ag and Au to Metallic Nanoparticles by Dissolved Organic Matter. *ACS Nano* **2012**, *6*, 7910–7919.

(71) Liu, J. Y.; Hurt, R. H. Ion Release Kinetics and Particle Persistance in Aqueous Nano-Silver Colloids. *Environ. Sci. Technol.* **2010**, *44*, 2169–2175.

(72) United States Environmental Protection Agency, Ambient Water Quality Criteria for Silver. https://nepis.epa.gov (accessed Sep 1, 2018).

(73) Yin, Y.; Yu, S.; Liu, J.; Jiang, G. Thermal and Photoinduced Reduction of Ionic Au(III) to Elemental Au Nanoparticles by Dissolved Organic Matter in Water: Possible Source of Naturally Occurring Au Nanoparticles. *Environ. Sci. Technol.*

2014, *48*, 2671–2679.

(74) Csapó, E.; Oszkó, A.; Varga, E.; Juhász, Á.; Buzás, N.; Korösi, L.; Majzik, A.; Dékány, I. Synthesis and Characterization of Ag/Au Alloy and Core(Ag)-Shell(Au) Nanoparticles. *Colloids Surfaces A Physicochem. Eng. Asp.* **2012**, *415*, 281–287.

(75) Liu, R.; Guo, J.; Ma, G.; Jiang, P.; Zhang, D.; Li, D.; Chen, L.; Guo, Y.; Ge, G. Alloyed Crystalline Au-Ag Hollow Nanostructures with High Chemical Stability and Catalytic Performance. *ACS Appl. Mater. Interfaces* **2016**, *8*, 16833–16844.

(76) Zhang, Z. S.; Yang, Z. J.; Liu, X. L.; Li, M.; Zhou, L. Multiple Plasmon Resonances of Au/Ag Alloyed Hollow Nanoshells. *Scr. Mater.* **2010**, *63*, 1193–1196.

(77) Thrall, E. S.; Steinberg, A. P.; Wu, X.; Brus, L. E. The Role of Photon Energy and Semiconductor Substrate in the Plasmon-Mediated Photooxidation of Citrate by Silver Nanoparticles. *J. Phys. Chem. C* **2013**, *117*, 26238–26247.

(78) Maillard, M.; Huang, P.; Brus, L. Silver Nanodisk Growth by Surface Plasmon Enhanced Photoreduction of Adsorbed [Ag^+]. *Nano Lett.* **2003**, *3*, 1611–1615.

(79) Brongersma, M. L.; Halas, N. J.; Nordlander, P. Plasmon-Induced Hot Carrier Science and Technology. *Nat. Nanotechnol.* **2015**, *10*, 25–34.

(80) Badireddy, A. R.; Farner Budarz, J.; Marinakos, S. M.; Chellam, S.; Wiesner, M. R. Formation of Silver Nanoparticles in Visible Light-Illuminated Waters: Mechanism and Possible Impacts on the Persistence of AgNPs and Bacterial Lysis. *Environ. Eng. Sci.* **2014**, *31*, 338–349.

(81) ElBishlawi, H.; Jaffe, P. R. Characterization of Dissolved Organic Matter from a Restored Urban Marsh and Its Role in the Mobilization of Trace Metals.

Chemosphere **2015**, *127*, 144–151.

(82) Li, T.; Albee, B.; Alemayehu, M.; Diaz, R.; Ingham, L.; Kamal, S.; Rodriguez, M.; Whaley Bishnoi, S. Comparative Toxicity Study of Ag, Au, and Ag-Au Bimetallic Nanoparticles on *Daphnia magna*. *Anal. Bioanal. Chem.* **2010**, *398*, 689–700.

(83) Taylor, U.; Tiedemann, D.; Rehbock, C.; Kues, W. A.; Barcikowski, S.; Rath, D. Influence of Gold, Silver and Gold-Silver Alloy Nanoparticles on Germ Cell Function and Embryo Development. *Beilstein J. Nanotechnol.* **2015**, *6*, 651–664.

(84) Moreno-Garrido, I.; Pérez, S.; Blasco, J. Toxicity of Silver and Gold Nanoparticles on Marine Microalgae. *Mar. Environ. Res.* **2015**, *111*, 60–73.

(85) Ramakritinan, C. M.; Kaarunya, E.; Shankar, S.; Kumaraguru, A. K. Antibacterial Effects of Ag, Au and Bimetallic (Ag-Au) Nanoparticles Synthesized from Red Algae. *Solid State Phenom.* **2013**, *201*, 211–230.

(86) United States Department of Energy. Buildings Sector. In *2011 Buildings Energy Data Book*; Washington, DC, 2012.

(87) Risser, R. Making Smart Windows Smarter https://energy.gov/articles/making-smart-windows-smarter (accessed Sep 1, 2018).

(88) Sellers, D. G.; Alivio, T. E. G.; Banerjee, S. Adaptive Homes. In *Physics World Discovery*; IOP Publishing: Bristol, England, 2018; manuscript in preparation.

(89) Farley, K. E. Electron-Phonon Coupling and Structural Phase Transitions in Early Transition Metal Oxides and Chalcogenides. Ph.D. Thesis, University at Buffalo: The State University of New York, Buffalo, New York, United States, 2016.

(90) Kanu, S. S.; Binions, R. Thin Films for Solar Control Applications. *Proc. R. Soc. A*

Math. Phys. Eng. Sci. **2010**, *466*, 19–44.

(91) Wang, Y.; Runnerstrom, E. L.; Milliron, D. J. Switchable Materials for Smart Windows. *Annu. Rev. Chem. Biomol. Eng.* **2016**, *7*, 283–304.

(92) Marley, P. M.; Horrocks, G. A.; Pelcher, K. E.; Banerjee, S. Transformers: The Changing Phases of Low-Dimensional Vanadium Oxide Bronzes. *Chem. Commun.* **2015**, *51*, 5181–5198.

(93) Goodenough, J. B. The Two Components of the Crystallographic Transition in VO_2. *J. Solid State Chem.* **1971**, *3*, 490–500.

(94) Wei, J.; Wang, Z.; Chen, W.; Cobden, D. H. New Aspects of the Metal-Insulator Transition in Single-Domain Vanadium Dioxide Nanobeams. *Nat. Nanotechnol.* **2009**, *4*, 420–424.

(95) Baum, P.; Yang, D.-S.; Zewail, A. H. 4D Visualization of Transitional Structures in Phase Transformations by Electron Diffraction. *Science* **2007**, *318*, 788–792.

(96) Schilbe, P. Raman Scattering in VO_2. *Phys. B.* **2002**, *316–317*, 600–602.

(97) Fleer, N. A.; Pelcher, K. E.; Nieto, K.; Braham, E. J.; Zou, J.; Horrocks, G. A.; Naoi, Y.; Depner, S. W.; Schultz, B. J.; Amano, J.; Sellers D. G; Banerjee, S. Elucidating the Crystallite Size Dependence of the Thermochromic Properties of Nanocomposite VO_2 Thin Films. *ACS Omega* **2018**, *3*, 14280–14293.

(98) Whittaker, L.; Wu, T.-L.; Patridge, C. J.; Sambandamurthy, G.; Banerjee, S. Distinctive Finite Size Effects on the Phase Diagram and Metal–Insulator Transitions of Tungsten-Doped Vanadium(IV) Oxide. *J. Mater. Chem.* **2011**, *21*, 5580–5592.

(99) Pelcher, K. E.; Crawley, M. R.; Banerjee, S. Silica-Shell Encapsulation and Adhesion of VO_2 Nanowires to Glass Substrates: Integrating Solution-Derived VO_2 Nanowires within Thermally Responsive Coatings. *Mater. Res. Express* **2014**, *1*, 035014/1–12.

(100) Fleer, N. A.; Pelcher, K. E.; Zou, J.; Nieto, K.; Douglas, L. D.; Sellers, D. G.; Banerjee, S. Hybrid Nanocomposite Films Comprising Dispersed VO2Nanocrystals: A Scalable Aqueous-Phase Route to Thermochromic Fenestration. *ACS Appl. Mater. Interfaces* **2017**, *9*, 38887–38900.

(101) Saeli, M.; Piccirillo, C.; Parkin, I. P.; Binions, R.; Ridley, I. Energy Modelling Studies of Thermochromic Glazing. *Energy Build.* **2010**, *42*, 1666–1673.

(102) Wang, S.; Liu, M.; Kong, L.; Long, Y.; Jiang, X.; Yu, A. Recent Progress in VO_2 Smart Coatings: Strategies to Improve the Thermochromic Properties. *Prog. Mater. Sci.* **2016**, *81*, 1–54.

(103) Whittaker, L.; Jaye, C.; Fu, Z.; Fischer, D. A.; Banerjee, S. Depressed Phase Transition in Solution-Grown VO_2 Nanostructures. *J. Am. Chem. Soc.* **2009**, *131*, 8884–8894.

(104) Singh, S.; Abtew, T. A.; Horrocks, G. A.; Kilcoyne, C.; Marley, P. M.; Stabile, A. A.; Banerjee, S.; Zhang, P.; Sambandamurthy, G. Selective Electrochemical Reactivity of Rutile VO_2 Towards the Suppression of Metal-Insulator Transition. *Phys. Rev. B* **2016**, *93*, 125132/1-8.

(105) Mlyuka, N. R.; Niklasson, G. A.; Granqvist, C. G. Mg Doping of Thermochromic VO_2 Films Enhances the Optical Transmittance and Decreases the Metal-Insulator

Transition Temperature. *Appl. Phys. Lett.* **2009**, *95*, 171909/1–3.

(106) Wu, Y.; Fan, L.; Liu, Q.; Chen, S.; Huang, W.; Chen, F.; Liao, G.; Zou, C.; Wu, Z. Decoupling the Lattice Distortion and Charge Doping Effects on the Phase Transition Behavior of VO_2 by Titanium (Ti^{4+}) Doping. *Sci. Rep.* **2015**, *5*, 9328/1–8.

(107) Manning, T. D.; Parkin, I. P.; Blackman, C.; Qureshi, U. APCVD of Thermochromic Vanadium Dioxide Thin Films - Solid Solutions $V_{2-x}M_xO_2$ (M = Mo, Nb) or Composites VO_2: SnO_2. *J. Mater. Chem.* **2005**, *15*, 4560–4566.

(108) Patridge, C. J.; Whittaker, L.; Ravel, B.; Banerjee, S. Elucidating the Influence of Local Structure Perturbations on the Metal-Insulator Transitions of $V_{1-x}Mo_xO_2$ Nanowires: Mechanistic Insights from an X-Ray Absorption Spectroscopy Study. *J. Phys. Chem. C* **2012**, *116*, 3728–3736.

(109) Asayesh-Ardakani, H.; Nie, A.; Marley, P. M.; Zhu, Y.; Phillips, P. J.; Singh, S.; Mashayek, F.; Sambandamurthy, G.; Low, K.; Klie, R. F.; Banerjee, S.; Odegard, G. M.; Shahbazian-Yassar, R. Atomic Origins of Monoclinic-Tetragonal (Rutile) Phase Transition in Doped VO_2 Nanowires. *Nano Lett.* **2015**, *15*, 7179–7188.

(110) Cao, X.; Wang, N.; Magdassi, S.; Mandler, D.; Long, Y. Europium Doped Vanadium Dioxide Material: Reduced Phase Transition Temperature, Enhanced Luminous Transmittance and Solar Modulation. *Sci. Adv. Mater.* **2014**, *6*, 558–561.

(111) Wang, N.; Chew Shun, N. T.; Duchamp, M.; Dunin-Borkowski, R. E.; Li, Z.; Long, Y. Effect of Lanthanum Doping on Modulating the Thermochromic Properties of VO_2 Thin Films. *RSC Adv.* **2016**, *6*, 48455–48461.

(112) Wang, N.; Duchamp, M.; E. Dunin-Borkowski, R.; Liu, S.; Ting Zeng, X.; Cao, X.; Long, Y. Terbium-Doped VO_2 Thin Films: Reduced Phase Transition Temperature and Largely Enhanced Luminous Transmittance. *Langmuir* **2016**, *32*, 759–764.

(113) Strelcov, E.; Tselev, A.; Ivanov, I.; Budai, J. D.; Zhang, J.; Tischler, J. Z.; Kravchenko, I.; Kalinin, S. V.; Kolmakov, A. Doping-Based Stabilization of the M2 Phase in Free-Standing VO_2 Nanostructures at Room Temperature. *Nano Lett.* **2012**, *12*, 6198–6205.

(114) Brückner, W.; Gerlach, U.; Moldenhauer, W.; Brückner, H. P.; Mattern, N.; Oppermann, H.; Wolf, E. Phase Transitions and Semiconductor-Metal Transition in $V_{1-x}Ga_xO_2$ Single Crystals. *Phys. Status Solidi* **1976**, *38*, 93–102.

(115) Marezio, M.; McWhan, D. B.; Remeika, J. P.; Dernier, P. D. Structural Aspects of the Metal-Insulator Transitions in Cr-Doped VO_2. *Phys. Rev. B* **1972**, *5*, 2541–2551.

(116) Tselev, A.; Luk'yanchuk, I. A.; Ivanov, I. N.; Budai, J. D.; Tischler, J. Z.; Strelcov, E.; Kolmakov, A.; Kalinin, S. V. Symmetry Relationship and Strain-Induced Transitions between Insulating M1 and M2 and Metallic R Phases of Vanadium Dioxide. *Nano Lett.* **2010**, *10*, 4409–4416.

(117) Zhou, J.; Gao, Y.; Liu, X.; Chen, Z.; Dai, L.; Cao, C.; Luo, H.; Kanahira, M.; Sun, C.; Yan, L. Mg-Doped VO_2 Nanoparticles: Hydrothermal Synthesis, Enhanced Visible Transmittance and Decreased Metal-Insulator Transition Temperature. *Phys. Chem. Chem. Phys.* **2013**, *15*, 7505–7511.

(118) Lee, S.; Cheng, C.; Guo, H.; Hippalgaonkar, K.; Wang, K.; Suh, J.; Liu, K.; Wu, J.

Axially Engineered Metal-Insulator Phase Transition by Graded Doping VO_2 Nanowires. *J. Am. Chem. Soc.* **2013**, *135*, 4850–4855.

(119) Manning, T. D.; Parkin, I. P.; Pemble, M. E.; Sheel, D.; Vernardou, D. Intelligent Window Coatings: Atmospheric Pressure Chemical Vapor Deposition of Tungsten-Doped Vanadium Dioxide. *Chem. Mater.* **2004**, *16*, 744–749.

(120) Lopez, R.; Boatner, L. A.; Haynes, T. E.; Feldman, L. C.; Haglund, R. F. Synthesis and Characterization of Size-Controlled Vanadium Dioxide Nanocrystals in a Fused Silica Matrix. *J. Appl. Phys.* **2002**, *92*, 4031–4036.

(121) Mai, L. Q.; Hu, B.; Hu, T.; Chen, W.; Gu, E. D. Electrical Property of Mo-Doped VO_2 Nanowire Array Film by Melting-Quenching Sol-Gel Method. *J. Phys. Chem. B* **2006**, *110*, 19083–19086.

(122) Du, J.; Gao, Y.; Luo, H.; Kang, L.; Zhang, Z.; Chen, Z.; Cao, C. Significant Changes in Phase-Transition Hysteresis for Ti-Doped VO_2 Films Prepared by Polymer-Assisted Deposition. *Sol. Energy Mater. Sol. Cells* **2011**, *95*, 469–475.

(123) Wang, N.; Duchamp, M.; Xue, C.; Dunin-Borkowski, R. E.; Liu, G.; Long, Y. Single-Crystalline W-Doped VO_2 Nanobeams with Highly Reversible Electrical and Plasmonic Responses Near Room Temperature. *Adv. Mater. Interfaces* **2016**, *3*, 1600164/1-9.

(124) Tang, C.; Georgopoulos, M.; Fine, M. E.; Cohen, J. B. Local Atomic and Electronic Arrangements in $W_xV_{1-x}O_2$. *Phys. Rev. B* **1985**, *31*, 1000–1011.

(125) Burkhardt, W.; Christmann, T.; Meyer, B. K.; Niessner, W.; Schalch, D.; Scharmann, A. W-and F-Doped VO_2 Films Studied by Photoelectron Spectrometry.

Thin Solid Films **1999**, *345*, 229–235.

(126) Li, S. Y.; Niklasson, G. A.; Granqvist, C. G. Thermochromic Undoped and Mg-Doped VO_2 Thin Films and Nanoparticles: Optical Properties and Performance Limits for Energy Efficient Windows. *J. Appl. Phys.* **2014**, *115*, 053513/1–10.

(127) Peng, Z.; Jiang, W.; Liu, H. Synthesis and Electrical Properties of Tungsten-Doped Vanadium Dioxide Nanopowders by Thermolysis. *J. Phys. Chem. C.* **2007**, *111*, 1119–1122.

(128) Horrocks, G. A.; Singh, S.; Likely, M. F.; Sambandamurthy, G.; Banerjee, S. Scalable Hydrothermal Synthesis of Free-Standing VO_2 Nanowires in the M1 Phase. *ACS Appl. Mater. Interfaces*. **2014**, *6*, 15726–15732.

(129) Ingole, S.; Aella, P.; Manandhar, P.; Chikkannanavar, S. B.; Akhadov, E. A.; Smith, D. J.; Picraux, S. T. Ex Situ Doping of Silicon Nanowires with Boron. *J. Appl. Phys.* **2008**, *103*, 104302/1–8.

(130) Ho, J. C.; Yerushalmi, R.; Jacobson, Z. A.; Fan, Z.; Alley, R. L.; Javey, A. Controlled Nanoscale Doping of Semiconductors via Molecular Monolayers. *Nat. Mater.* **2008**, *7*, 62–67.

(131) Filinchuk, Y.; Tumanov, N. A.; Ban, V.; Ji, H.; Wei, J.; Swift, M. W.; Nevidomskyy, A. H.; Natelson, D. In Situ Diffraction Study of Catalytic Hydrogenation of VO_2: Stable Phases and Origins of Metallicity. *J. Am. Chem. Soc.* **2014**, *136*, 8100–8109.

(132) Yoon, H.; Choi, M.; Lim, T. W.; Kwon, H.; Ihm, K.; Kim, J. K.; Choi, S. Y.; Son, J. Reversible Phase Modulation and Hydrogen Storage in Multivalent VO_2

Epitaxial Thin Films. *Nat. Mater.* **2016**, *15*, 1113–1119.

(133) Driscoll, T.; Kim, H.-T.; Chae, B.-G.; Kim, B.-J.; Lee, Y.-W.; Jokerst, N. M.; Palit, S.; Smith, D. R.; Di Ventra, M.; Basov, D. N. Memory Metamaterials. *Science* **2009**, *325*, 1518–1521.

(134) Memory with a Spin. *Nat. Nanotechnol.* **2015**, *10*, 185.

(135) Pershin, Y. V.; Di Ventra, M. Memory Effects in Complex Materials and Nanoscale Systems. *Adv. Phys.* **2011**, *60*, 145–227.

(136) Zhang, J.; He, H.; Xie, Y.; Pan, B. Giant Reduction of the Phase Transition Temperature for Beryllium Doped VO_2. *Phys. Chem. Chem. Phys.* **2013**, *15*, 4687–4690.

(137) Quesada-González, M.; Boscher, N. D.; Carmalt, C. J.; Parkin, I. P. Interstitial Boron-Doped TiO_2 Thin Films: The Significant Effect of Boron on TiO_2 Coatings Grown by Atmospheric Pressure Chemical Vapor Deposition. *ACS Appl. Mater. Interfaces* **2016**, *8*, 25024–25029.

CHAPTER II

ATOMIC LAYER DEPOSITION OF HAFNIUM(IV) OXIDE ON GRAPHENE OXIDE: PROBING INTERFACIAL CHEMISTRY AND NUCLEATION BY USING X-RAY ABSORPTION AND PHOTOELECTRON SPECTROSCOPIES[*]

2.1 Summary

Interfacing graphene with metal oxides is of considerable technological importance for modulating carrier density through electrostatic gating as well as for the design of earth-abundant electrocatalysts. Herein, we probe the early stages of the atomic layer deposition (ALD) of HfO_2 on graphene oxide using a combination of C and O K-edge near-edge X-ray absorption fine structure spectroscopies and X-ray photoelectron spectroscopy. Dosing with water is observed to promote defunctionalization of graphene oxide as a result of the reaction between water and –hydroxyl/epoxide species, which yields carbonyl groups that further react with migratory epoxide species to release CO_2. The carboxylates formed by the reaction of carbonyl and epoxide species facilitate binding of Hf precursors to graphene oxide surfaces. The ALD process is accompanied by recovery of the π-conjugated framework of graphene. The delineation of binding modes provides a means to rationally assemble 2D heterostructures.

---

[*] Reprinted with permission from "Atomic Layer Deposition of Hafnium(IV) Oxide on Graphene Oxide: Probing Interfacial Chemistry and Nucleation by using X-ray Absorption and Photoelectron Spectroscopies" by Alivio, T. E. G.; De Jesus, L. R.; Dennis, R. V.; Jia, Y.; Jaye, C.; Fischer, D. A.; Singisetti, U.; Banerjee, S. *ChemPhysChem.* **2015**, *16*, 2482-2848.

2.2 Introduction

Interfacing metals, semiconductors, and dielectrics with graphene has assumed great significance as a means of modulating the electronic structure of this remarkable 2D material while further providing a route to integrate graphene within functional architectures.[1–7] Interfacial interactions can profoundly modify the electronic structure of graphene by inducing charge redistribution, opening a bandgap at the Fermi level, establishing an interfacial dipole, or even entirely disrupting the conical dispersion of bands such as in the case of covalent hybridization.[2,8] Obtaining high-quality interfaces of disparate materials is non-trivial given the long-range warping, electronic structure inhomogeneities, relative inertness of the sp^2-hybridized basal planes of graphene, and the distinctive reactivity of edge sites in this material. For functionalized graphene, the specific surface functional groups additionally play a critical role in mediating the precise nature of the interface.[1,9–12] In this work, we probe the reactivity of surface functional groups of graphene oxide upon the atomic layer deposition of HfO_2 to examine their role as nucleation sites for the deposition of high-κ dielectric layers. Beyond the fundamental imperative of understanding the reactivity of functional groups on graphene oxide towards binding transition metals, the atomic layer deposition of oxide dielectrics onto graphene surfaces is technologically relevant to two broad classes of applications. First, high-κ dielectrics are necessary to overcome fundamental limitations of conventional Si/SiO_2 in metal-oxide semiconductor field-effect transistors based on graphene as the active element, particularly in the high-frequency regime above 100 GHz.[13–15] Second, there is

considerable interest in graphene/transition-metal-oxide hybrid architectures as earth-abundant substitutes for platinum-group-metals within electrocatalytic systems.[11,16,17]

Considerable interest has focused on atomic layer deposition (ALD) as a saturative and self-limiting route for the deposition of ultra-thin conformal dielectric layers on graphene.[14,18–20] However, given the sp^2-hybridized honeycomb-like lattice of graphene, it can be difficult to initiate nucleation of HfO_2 on unfunctionalized graphene surfaces and indeed under typical ALD conditions, HfO_2 growth is confined to edge sites and defects.[14,18–20] The growth of pinhole-free conformal dielectric films on graphene has been facilitated by the increased curvature-induced reactivity of graphene upon transfer to a substrate different from the growth substrate, direct surface functionalization, or the utilization of a seed layer.[12,15,21] However, the atomistic details of nucleation processes within these systems remain mostly unknown. Given the abundance of functional groups in graphene oxide,[9,22] this material is an excellent model system for examining the nucleation of oxide growth during sequential atomic layer deposition reactions as mediated by surface functionalization. In this work, we probe the evolution of interfacial chemistry during the initial stages of the atomic layer deposition process using a combination of *ex situ* near-edge X-ray absorption fine structure (NEXAFS) and X-ray photoelectron spectroscopies (XPS).

XPS involves the ejection of a core-level electron upon photon irradiation; the binding energy of the electron provides a sensitive and quantitative measure of the specific surface species. In the context of graphene oxide, XPS allows for semi-quantitative evaluation of the functional group distribution and dopant incorporation. In contrast,

NEXAFS spectroscopy involves the excitation of core electrons to partially occupied or unoccupied states and serves as a sensitive element-specific probe of surface chemistry, electronic structure, interfacial bonding, dopant incorporation, substrate alignment, and steric orientation of functional groups in graphene and functionalized graphene[1,7,16,23–29] as well as carbon nanotubes.[30–32] In past work, we have derived a spatially resolved scanning transmission X-ray microscopy map of graphene oxide indicating that carboxylic acid groups are localized on the periphery of graphene oxide flakes whereas epoxide and keto functional groups decorate the basal planes, consistent with the Lerf—Klinowski model of the structure of graphene oxide.[25,33] The presence of these functional groups provides an abundance of reactive sites that can serve to anchor ALD precursors to initiate deposition of an amorphous HfO_2 overlayer. The mediation of functional groups of graphene oxide in ALD growth stands in stark contrast to HfO_2 deposition by the plasma vapor deposition of Hf metal followed by air oxidation, wherein NEXAFS spectroscopy results corroborated density functional theory predictions of charge redistribution and hole doping of graphene.[8,34]

2.3 Methods

2.3.1 Materials

Graphene oxide was produced using a modified Hummer's method as described in previous work.[23–25,35] Freestanding graphene oxide paper was prepared by filtering an aqueous solution of 0.5 mg/mL graphene oxide through a Millipore "V" series nitrocellulose membrane.

HfO_2 was deposited onto graphene oxide by thermal ALD at 150°C in a Cambridge Nanotech Savannah S100 system using TDMH and water precursors. The ALD chamber was first purged with 20 sccm N_2 with the outer heater kept at 150°C and the inner heater at 150°C.[36] The system was then equilibrated for 60 s. Each ALD cycle comprises the following steps: an initial exposure of water in the chamber for a pulse period of 0.015 s, 20 s of purge with N_2 gas, pulsed exposure of TDMH for a period of 0.15 s, followed finally by equilibration for 20 s under N_2 gas to complete the cycle. Five and ten cycles are contrasted for the different graphene oxide samples corresponding to approximately 0.5 and 1 nm depositions of HfO_2, respectively.[37] All spectroscopy results correspond to *ex situ* experiments performed on samples stored at room temperature within a dry environment.

2.3.1 NEXAFS

NEXAFS experiments were performed at the National Institute of Standards and Technology (NIST) beamline U7A of the National Synchrotron Light Source (NSLS) at Brookhaven National Laboratory (BNL). A toroidal spherical grating monochromator with 600 lines/mm was used to acquire the C K-edge spectra, yielding an energy step size of approximately 0.08 eV. The slits were maintained at 30 μm x 30 μm. All spectra were acquired in partial electron yield (PEY) mode using a channeltron electron multiplier as the detector with the entrance grid bias set at -150 V. Charge compensation was facilitated with the aid of an electron flood gun to mitigate surface charging of the samples. All PEY signals were normalized using the incident beam intensity obtained from the

photoemission yield of a clean Au grid with 90% transmittance placed along the path of the incident X-ray beam. C K-edge spectra were calibrated against an amorphous carbon mesh with a π* transition at 285.1 eV. All C K-edge data presented herein were pre- and post-edge normalized using the Athena suite of programs.

2.3.2 XPS

XPS analyses were performed on an Omicron XPS/UPS system with an Argus detector using Mg Kα X-rays (source energy of 1253.6 eV) and with charge neutralization of the samples (using a CN10 electron flood source). The instrument resolution was at approximately 0.8 eV. All high-resolution spectra were collected at a pass energy of 20 eV (at constant analyzer energy (CAE) mode) and at an energy step size of -0.05 eV. All spectra were calibrated against the C 1s line at 284.8 eV. Peak assignments are referenced to previously reported literature and the NIST XPS spectra database. Atomic concentration calculations were performed with the CasaXPS 2.3.16 software, using the Marquardt-Levenberg optimization algorithm.

2.4 Results and Discussion

To examine the interface between graphene oxide and the ALD-grown HfO_2 overlayer, we have examined samples with sub-monolayer coverage representing the beginnings of HfO_2 deposition. Specifically, we contrast 5 and 10 cycles of alternating exposures to water and *tetrakis*(dimethylamido)hafnium (TDMH) precursors. Given the elevated temperature of the ALD process and to deconvolute the reactivity of graphene oxide

towards TDMH from changes resulting from reactions with water and thermally induced defunctionalization,[24,26] we contrast the sub-monolayer results with data for graphene oxide subjected to the same sequence of processes during ALD growth except for dosing with TDMH. The latter samples are denoted hereinafter as control samples.

Table 2.1 depicts the atomic concentrations of carbon, oxygen, and hafnium deduced from the integration of C 1s, O 1s, and Hf 4f intensities measured in high-resolution XPS scans (**Figure 2.1**, indicates survey scans). An important caveat to this analysis is that sensitivity factors used to convert peak areas to concentrations have not been derived for the specific matrix of interest (and instead global parameters have been used). Nevertheless, the spectra provide a good measure of the relative differences in functional group distribution induced upon ALD processing. Graphene oxide prepared by Hummers' method has about 30 at.% oxygen content, which is consistent with previous observations.[38] Subjecting graphene oxide to ALD results in substantial incorporation of hafnium (3 at.% and 6 at.% for 5 and 10 cycles, respectively).

Table 2.1: Atomic concentrations deduced from XPS high-resolution scans (at 95% confidence level)

Sample	Carbon (at.%)	Oxygen (at.%)	Hafnium (at.%)
Graphene oxide	70±1	30±0	0
Graphene oxide 5 cycles control	64±1	36±1	0
Graphene oxide + 5 cycles HfO_2	69±1	28±0	3±0
Graphene oxide 10 cycles control	59±1	41±0	0
Graphene oxide + 10 cycles HfO_2	62±2	32±1	6±0

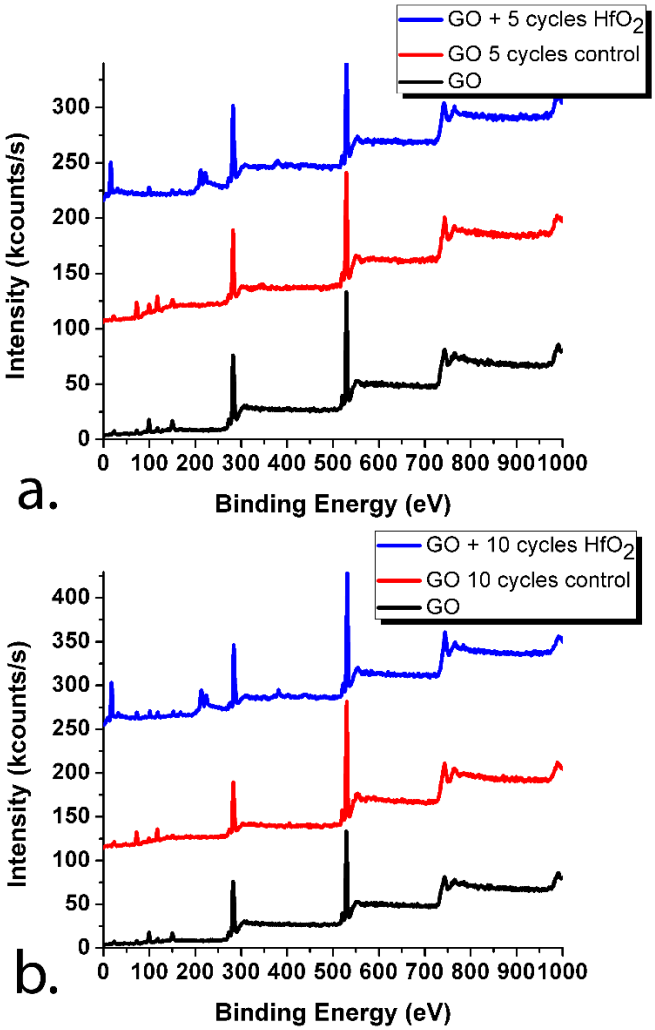

Figure 2.1: XPS survey spectra for graphene oxide contrasted to graphene oxide subjected to ALD deposition for (a) 5 cycles and (b) 10 cycles of sequential water and TDMH exposures. Spectra for associated control experiments wherein the graphene oxide undergoes the same set of cycles but without exposure to TDMH are plotted alongside in each case.

The high-resolution Hf 4f XPS spectra in **Figure 2.2** for samples exposed to 5 and 10 cycles of TDMH show overlapping couplets attributed to Hf $4f_{7/2}$ and Hf $4f_{5/2}$ lines at 17.80 and 19.30 eV, respectively, consistent with the predominant stabilization of Hf^{4+} species on the surface of graphene oxide.[39] The spin-orbit coupling of 1.5 eV is also consistent with the value reported for HfO_2.[40] The broad lineshapes do indicate

heterogeneity in the specific chemical environments of Hf^{4+}, which is not surprising considering the diversity of binding sites in graphene oxide as discussed in more detail below. Characteristic peaks of monoclinic or tetragonal HfO_2 are not observed by Raman spectroscopy suggesting the amorphous nature of the deposited species. Approximating a Hf:O stoichiometry ratio of 1:2 consistent with formation of HfO_2 and assigning the remaining oxygen content to functional groups on the surface of graphene oxide, the ratio of carbon to oxygen is deduced to be around 76:24 for graphene oxide both after 5 and 10 cycles. These numbers suggest that ~6% of the functional groups are eliminated during the ALD process. The increased oxygen content in the control samples arises from dosing with water and the substantially greater amounts of entrapped water in these samples.

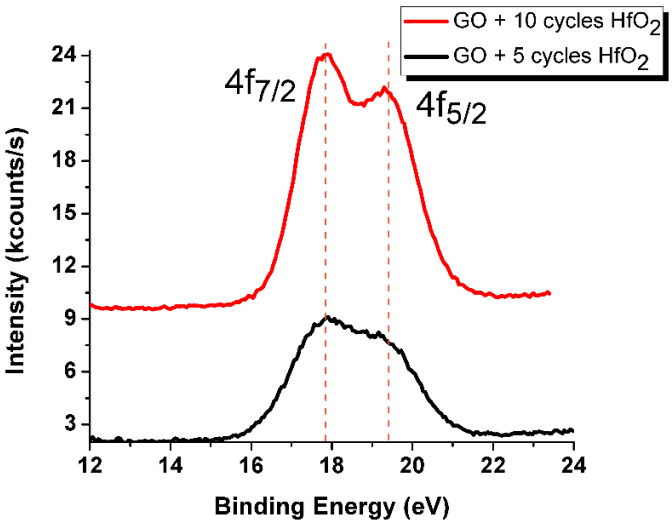

Figure 2.2: High-resolution Hf 4f XPS spectra of graphene oxide samples after 5 and 10 cycles of ALD deposition of HfO_2.

Figure 2.3 juxtaposes high-resolution C1s XPS spectra acquired for free-standing graphene oxide, graphene oxide subjected to 5 and 10 ALD cycles and the associated

controls where the TDMH dosing was omitted. The XPS spectra have been fitted using three components centered at 284.8, 286.8, and 289.0 eV corresponding to aromatic C=C, C—O, and O—C=O moieties, respectively.[41–43] The C1s spectrum of GO reveals a characteristic double-peaked lineshape resulting from the extensive disruption of the π-conjugated framework of graphene.[38,44] This double-peaked lineshape arises from the pronounced contributions to the C—O spectral component derived from epoxide and alcohol groups pendant from the basal planes of graphene oxide. The control samples without TDMH dosing indicate a diminished contribution from the C—O component suggesting partial defunctionalization even at the relatively low processing temperature of 150°C. Past work on thermal defunctionalization has verified that epoxide and alcohol groups are not substantially eliminated from the basal planes of graphene oxide at this temperature.[24,26] The defunctionalization observed here can thus be ascribed to the reaction of functional groups with water to form CO_2, which has been found to substantially diminish the bandgap of graphene oxide.[45,46] Indeed, Acik *et al.* have determined that the thermal defunctionalization of exfoliated single-layered graphene oxide is quite distinct from the thermal defunctionalization of multilayered graphene oxide as a result of the intercalated water molecules trapped in the galleries of the latter.[46] The water molecules react with epoxide and alcohol groups to yield carbonyl moieties, which subsequently react with mobile epoxide groups to release CO_2 and leave behind defect sites.[46,47] Interestingly, the C—O feature is greatly diminished relative to the π-conjugated component at 284.8 eV after 5 and 10 cycles of ALD with respect to the control sample suggesting that the reaction of TDMH and the nucleation of HfO_2 on graphene oxide

facilitates restoration of the π-conjugated structure of graphene by defunctionalization of functional groups on the basal planes. In contrast, we note a pronounced increase in the intensity of the O—C=O feature suggesting a role for carboxylic acids/carboxylates and potentially carbonates in binding Hf at the interface.

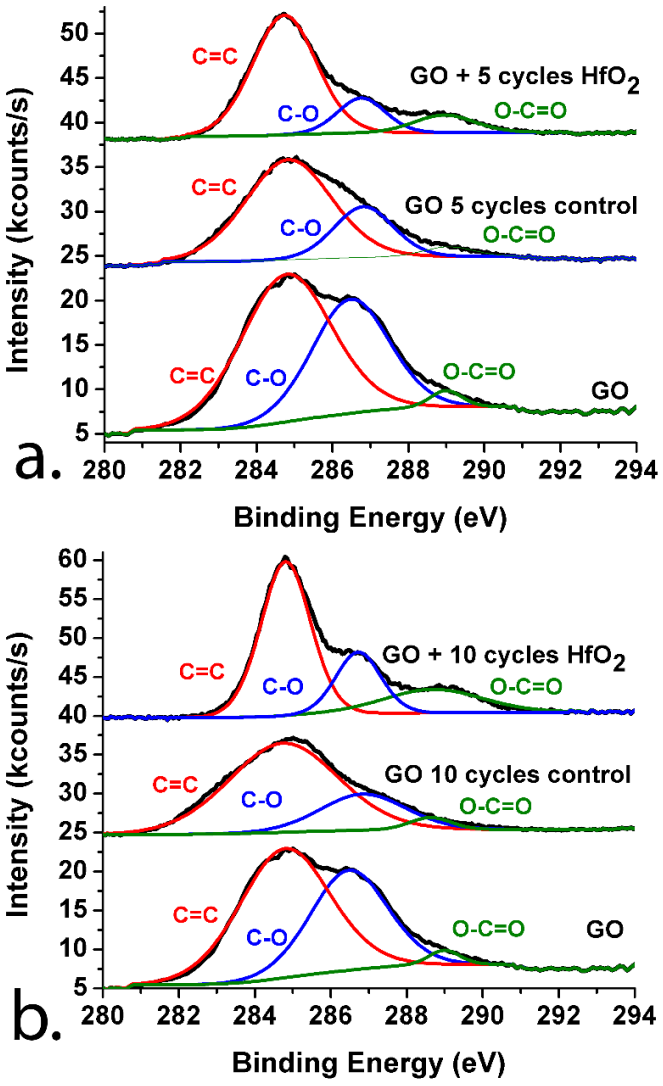

Figure 2.3: High-resolution C 1s XPS spectra for graphene oxide samples upon a) 5 cycles and b) 10 cycles of HfO_2 treatment. Spectra for associated control experiments wherein the graphene oxide undergoes the same set of cycles but without exposure to TDMH are plotted alongside in each case.

The evolution of functional groups of graphene oxide with TDMH treatment is captured with greater sensitivity in C K-edge NEXAFS spectra of the same samples depicted in **Figure 2.4**. All spectra have been collected at 54.7° (magic angle) incidence of the X-ray beam where the intensities of the NEXAFS resonances are independent of the angular dependences of the transition matrix elements.[48] Given that NEXAFS uses linearly polarized light and involves classical dipolar transitions with minimal quadrupolar contributions, the absorption cross section of a powder sample transforms into a second-order Cartesian tensor, derived by Pettifer *et al.* as follows:[48]

$$\sigma(\hat{\varepsilon}) = \sigma_a \sin^2\theta + \sigma_b \cos^2\theta \qquad \textbf{Eq. 2.1}$$

where $\sigma(\hat{\varepsilon})$ is the tensor for the polarization dependent absorption cross section derived from Fermi's Golden rule, σ_a and σ_b are distribution functions of crystallite orientations, and θ is the angle between the polarization vector and the sample normal.[48] When θ = 54.7° (corresponding to $\cos^2\theta = 1/3$), the isotropic average can be calculated from **Eq. 2.2** as follows:[48]

$$\sigma(\theta) = \frac{2\sigma_a + \sigma_b}{3} \qquad \textbf{Eq. 2.2}$$

and thus specific texturation effects are substantially mitigated at this angle.

The lowest-energy resonance at ~285.5 eV (labeled π*) can be assigned to the transition of C 1s core-level electrons into states of π* symmetry in proximity to the M and L points of the graphene Brillouin zone;[1,26,49–51] the resonance at ~293.4 eV (labeled σ*) can be attributed to the excitation of C 1s core-level electrons into unoccupied states of σ* symmetry. In the intermediate energy range between the π* and σ* resonances, four

additional features can be resolved and are labeled *a*—*d* in **Figure 2.4**; these features arise from the functional groups decorating the edges and basal planes of graphene oxide. Based on literature precedence, measurements of gas-phase model compounds in the McMaster NEXAFS database,[52] and trends calculated from density functional theory, feature *a* can be assigned to transitions from C 1s core levels to π* states of C−O bonds of hydroxyl groups, *b* to the transition of C 1s core-level electrons to σ* C−O states of epoxides, *c* to the excitation of C 1s core-level electrons to π* states of carbonyl (C=O) bonds, and *d* to transitions to π* states of C=O bonds from carboxylic acid groups.[25,26,53,54] Peak *d* furthermore overlaps with the transitions of C 1s electrons in $–CO_3^{2-}$ groups to π* O—C=O states.[7,45,55] **Table 2.2** presents a summary of the peak assignments.[25]

Table 2.2: Functional group assignments of spectral features in NEXAFS C K-Edge spectra.

Label	Incident Photon Energy (eV)	Functional Group
π*	288.5	π* C=C
a	286.8	π* C—OH
b	288.0	σ* C—O (epoxide)
c'	288.5—288.9	π* C=O (carboxylate)
c	289.2	π* C=O
d	290.3	π* O=C—O, π* $-CO_3^{2-}$
σ*	293.4	σ* C—C

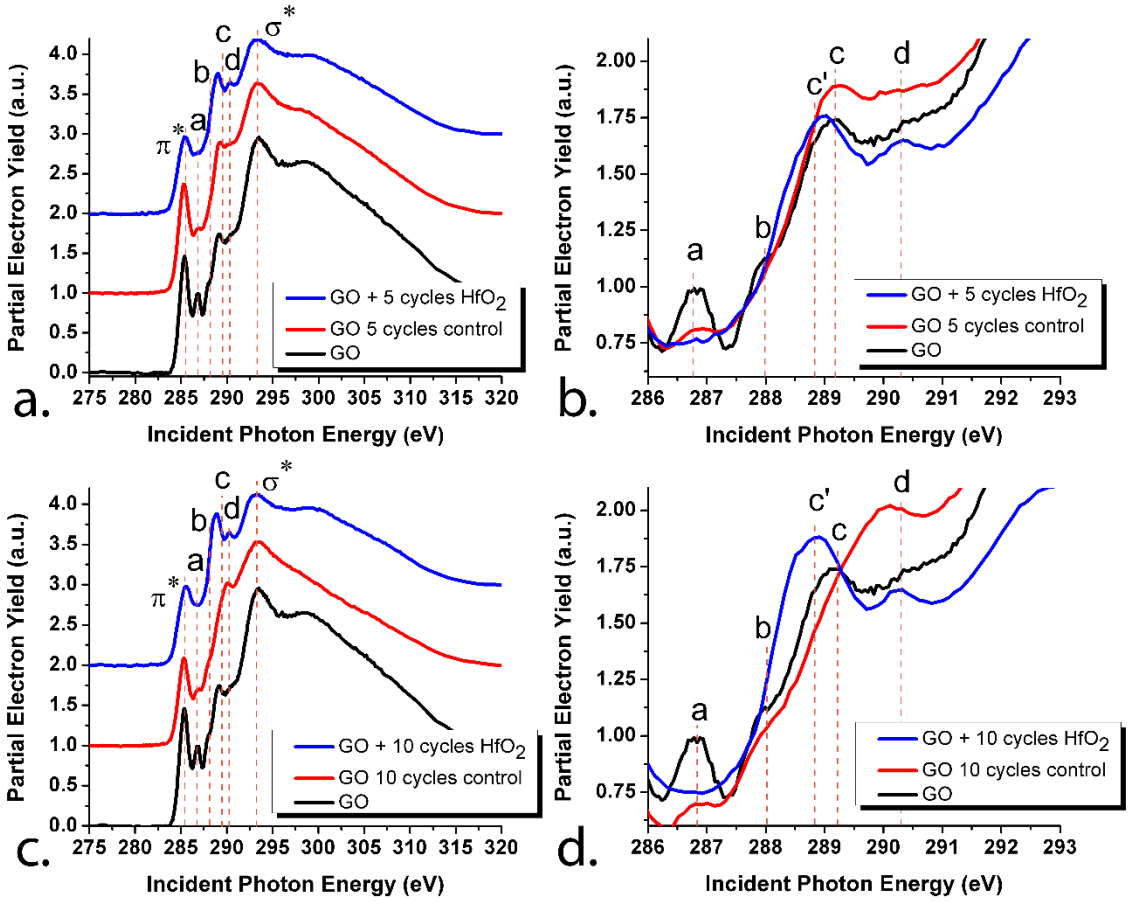

Figure 2.4: C K-edge NEXAFS spectra, acquired at 54.7° (magic angle) incidence of the X-ray beam for graphene oxide samples after a) 5 cycles and c) 10 cycles of ALD deposition of HfO_2. (b) and (d) show a magnified view of the energy range between 286 and 293 eV between the π* and σ* resonances. Spectra for associated control experiments wherein the graphene oxide undergoes the same set of ALD cycles but without exposure to TDMH are plotted alongside in each case.

Figures 2.4b and **d** illustrate three significant changes to NEXAFS resonances in the intermediate energy region between the π* and σ* features. First, the resonance labeled *a*, attributed to localized absorptions for carbon atoms attached to hydroxyl groups is clearly discernible for graphene oxide but is greatly diminished for the control sample and appears to have been completely eliminated upon ALD deposition of HfO_2. Next, the resonance labeled *d*, attributed to transitions of C 1s electrons into π* O—C=O states

becomes well defined upon ALD deposition but is not observed for the control samples. Finally, the most prominent feature *c* attributed to transitions of C 1s electrons to π* C=O states in ketone and carboxylic acid moieties is diminished in intensity at the expense of a red-shifted feature labeled *c*' that is centered in the 288.7-288.9 eV range. This shift to lower energy allows for better resolution of feature *d* upon HfO_2 deposition. These spectral shifts are further clearly discernible in **Figure 2.5**, which shows C K-edge data acquired at 25° incidence of the X-ray beams to the sample wherein the electric field vector of the X-rays has a large projection aligned with along the p_z orbitals that constitute the π* bands in graphene as schematically illustrated in the inset to **Figure 2.5b**. As the angle of incidence is increased from 25°, the intensity due to the π* resonance decreases while that of the σ* resonance increases as the electric field vector has a larger projection aligned with the basal planes. The diminution in the intensity of the hydroxyl resonances can be attributed to the reaction between –OH groups at edge holes with water molecules impinged onto graphene oxide during the ALD process, which leads to the stabilization of carbonyl groups. The presence of water is known to result in much more effective dehydroxylation at lower temperatures as compared to thermal defunctionalization under "dry" conditions.[24,45,46] The well-defined π* O=C—O resonance observed at ca. 290.3 eV (*d*) suggests a Hf-carboxylate or Hf-carbonate interaction as the primary binding mode at the interface. Indeed, this notion is further corroborated by the appearance of the red-shifted feature at *c*'. Binding of metal ions to carboxylic acids is known to induce a diminution of the π* C=O resonance accompanied by the growth of a red-shifted broad absorption feature as illustrated by experimental data on humic acids and polyacrylic acid

as well as quantum chemical calculations; the shift in energy is roughly proportional to the charge on the metal cation[56,57] for the same binding mode. The spectral shift (which also allows for better resolution of the high-energy O—C=O feature) arises from structural changes to the carboxylate ions at the interface.

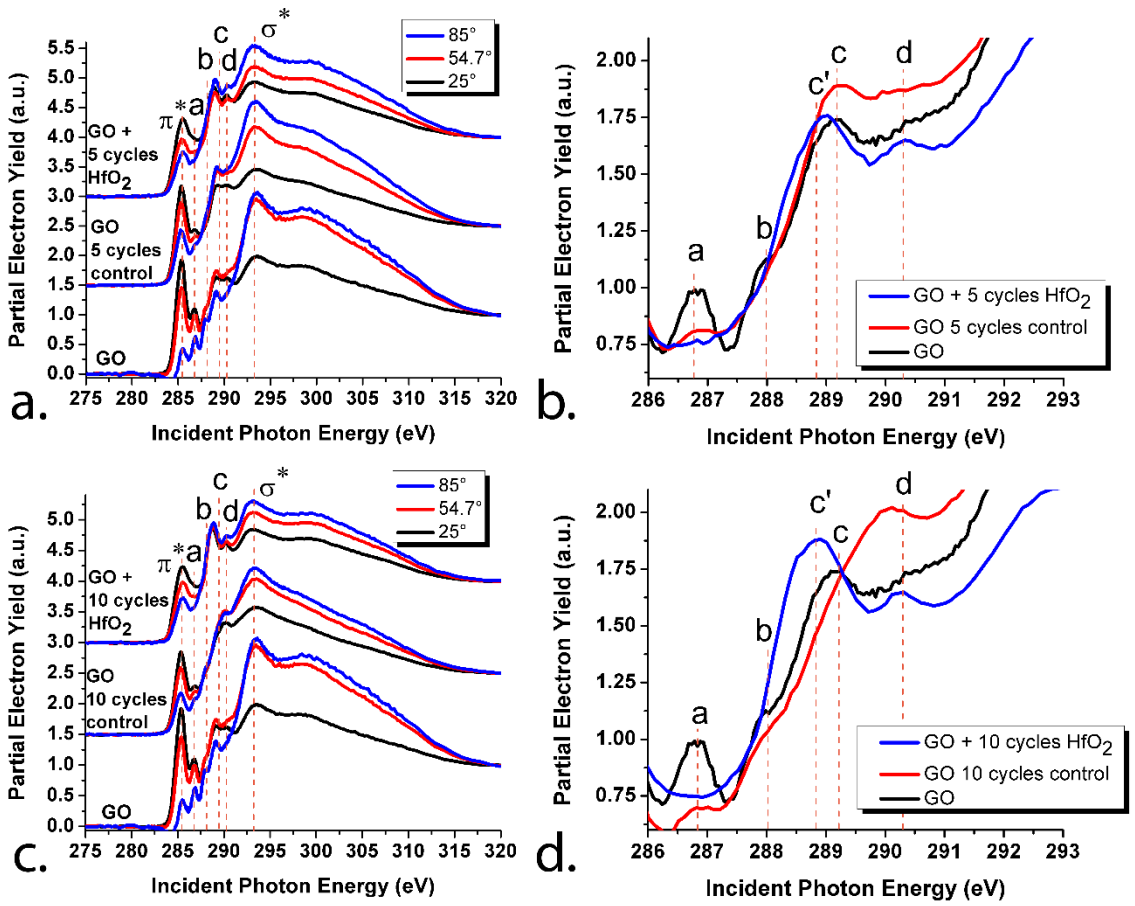

Figure 2.5: C K-edge NEXAFS spectra, acquired at 25°, 54.7°, and 85° incidence of the X-ray beam for graphene oxide samples after a) 5 cycles and c) 10 cycles of ALD deposition of HfO_2. (b) and (d) show a magnified view of the energy range between 286 and 293 eV between the π* and σ* resonances for the spectra corresponding to 25°. The inset in (b) illustrates that at 25° incidence of the X-ray beam, the intensity from the π* bands of graphene are most pronounced. Spectra for associated control experiments wherein the graphene oxide undergoes the same set of ALD cycles but without exposure to TDMH are plotted alongside in each case.

Figures 2.6 and **2.7** depict magic-angle O K-edge NEXAFS spectra acquired for the graphene oxide samples with and without exposure to TDMH along with the fitted resonances. In the graphene oxide O K-edge NEXAFS spectrum, the resonance at 531.0 eV (labeled *a*) can be ascribed to transitions from O1s core levels of oxygen atoms in C=O groups to π* C=O states localized on carbonyl and carboxylic acid moieties, The broad absorption feature centered at ca. 545.4 eV (labeled *b*) is attributed to transitions from O 1s core levels to σ* states derived from O—H, C=O, and C—O single bonds in the different oxygen-containing functional groups of graphene oxide.[25,26,53] The control sample dosed with water and heated to 150°C shows a pronounced and well-defined π* resonance that is substantially increased in relative intensity as compared to the graphene oxide precursor. This observation corroborates the hypothesis based on XPS and C K-edge NEXAFS data advanced above that the hydroxyl and epoxide groups react with water during the initial ALD wetting step and are converted to carbonyl species, as has been suggested by previous infrared spectroscopy and NEXAFS studies of multilayered graphene oxide intercalating water.[45,46] Upon subsequent exposure to TDMH, the π* intensity is greatly diminished. Complexation of metal ions to carboxylic acid moieties is known to bring about a diminution and a shift to higher energies of the π* resonance as a result of electron density being shared with the metal ion.[58] The results here are thus consistent with a carboxylate group mediating the interaction with Hf species at the graphene/HfO_2 interface.

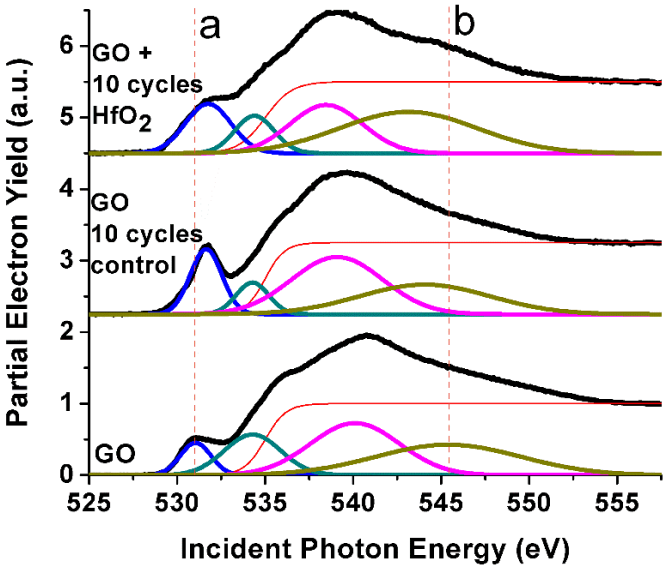

Figure 2.6: Normalized O K-edge NEXAFS spectra, acquired at 54.7° incidence of the X-ray beam for graphene oxide samples after 10 cycles of ALD deposition of HfO_2.

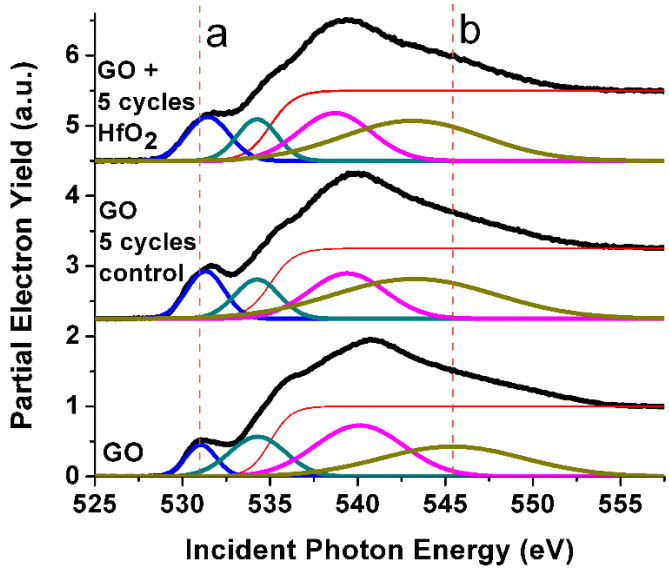

Figure 2.7: Normalized O K-edge NEXAFS spectra, acquired at 54.7° incidence of the X-ray beam for graphene oxide samples after 5 cycles of ALD deposition of HfO_2.

Based on the XPS and NEXAFS spectra, the picture that emerges is that the initial dosing of water at 150°C strongly modifies the functional group distribution of graphene

oxide. Specifically, hydroxyl and epoxide groups react with the water molecules and are converted to carbonyl groups even at the relatively low temperature of 150°C. Epoxide groups dotting the basal planes of graphene oxide are fairly mobile and can react with the incipient carbonyl groups to form carboxylate species that can subsequently be eliminated to release CO_2. The partial recovery of the π-conjugated structure of graphene oxide is discernible in both C 1s XPS and C K-edge NEXAFS spectra, which also corroborate the loss of epoxide and increasing concentration of carbonyl moieties upon dosing with water at 150°C. Exposure to TDMH results in the binding of the transition metal precursors to form hafnium carboxylates, as indicated by the clear appearance of a 290.3 eV resonance in the C K-edge NEXAFS spectrum, increased spectral weight of the O—C=O feature in the XPS spectrum, and the diminution in the intensity of π* resonance in the O K-edge spectrum. The carboxylate groups thus likely serve as the initial nucleation sites for HfO_2 deposition. Partial decarboxylation likely further accompanies the deposition of HfO_2 bringing about additional restoration of the π-conjugated framework of graphene oxide as evident from the XPS spectra.

2.5 Conclusions

The atomic layer deposition of high-κ dielectrics onto graphene to constitute high-quality interfaces continues to be an important technological challenge. However, little is known about the atomistic details of the nucleation of dielectric oxides on graphene surfaces and indeed the role of functional groups in graphene oxide in mediating interfacial interactions with oxide dielectrics remains entirely unexplored. In this work, we have used X-ray

photoelectron spectroscopy in conjunction with C and O K-edge NEXAFS spectroscopy to examine the initial stages of the ALD growth of HfO_2 on graphene oxide. NEXAFS spectra in particular serve as a sensitive probe of the evolution of functional groups during the ALD process. The significance of this study is two-fold: First it provides a mechanistic understanding of how the functional groups in grapehene oxide evolve during ALD processing and delineates the specific mode for tethering of HfO_2. Second, this establishes a route for selective patterning of high-κ dielectrics onto graphene oxide. Treatment of graphene oxide with water in the initial ALD step is observed to greatly modify the functional group distribution; the water molecules react with epoxide and hydroxyl groups of graphene oxide to form carbonyl moieties with partial restoration of the π-conjugated framework. The carbonyl moieties further condense with mobile epoxide species to form carboxylate groups that mediate the binding of Hf precursors upon exposure to TDMH. The formation of Hf carboxylates on the surface of graphene oxide thus precedes the nucleation of amorphous HfO_2. These results suggest a functionalization strategy for obtaining uniform coverage of HfO_2 on 2D material surfaces and further underlines the potential for using specific molecular interactions to constitute 2D heterostructures. Future work will focus on correlating the nature of graphene/metal-oxide interfaces to their catalytic activity.

2.6 References

(1) Schultz, B. J.; Dennis, R. V.; Lee, V.; Banerjee, S. An Electronic Structure Perspective of Graphene Interfaces. *Nanoscale* **2014**, *6*, 3444–3466.

(2) Sarkar, S.; Bekyarova, E.; Haddon, R. C. Chemistry at the Dirac Point: Diels-Alder Reactivity of Graphene. *Acc. Chem. Res.* **2012**, *45*, 673–682.

(3) Park, H.; Chang, S.; Smith, M.; Gradečak, S.; Kong, J. Interface Engineering of Graphene for Universal Applications as Both Anode and Cathode in Organic Photovoltaics. *Sci. Rep.* **2013**, *3*, 1581/1–8.

(4) Grigorenko, A. N.; Polini, M.; Novoselov, K. S. Graphene Plasmonics. *Nat. Photonics* **2012**, *6*, 749 – 758.

(5) Wintterlin, J.; Bocquet, M. L. Graphene on Metal Surfaces. *Surf. Sci.* **2009**, *603*, 1841–1852.

(6) Hong, G.; Wu, Q. H.; Ren, J.; Wang, C.; Zhang, W.; Lee, S. T. Recent Progress in Organic Molecule/Graphene Interfaces. *Nano Today* **2013**, *8*, 388–402.

(7) Schultz, B. J.; Jaye, C.; Lysaght, P. S.; Fischer, D. A.; Prendergast, D.; Banerjee, S. On Chemical Bonding and Electronic Structure of Graphene–metal Contacts. *Chem. Sci.* **2013**, 494–502.

(8) Schultz, B. J.; Lee, V.; Price, J.; Jaye, C.; Lysaght, P. S.; Fischer, D. A.; Prendergast, D.; Banerjee, S. Near-Edge x-Ray Absorption Fine Structure Spectroscopy Studies of Charge Redistribution at Graphene/Dielectric Interfaces. *J. Vac. Sci. Technol. B Microelectron. Nanom. Struct.* **2012**, *30*, 041205/1–6.

(9) Dreyer, D. R.; Park, S.; Bielawski, C. W.; Ruoff, R. S. The Chemistry of Graphene Oxide. *Chem. Soc. Rev.* **2010**, *39*, 228–240.

(10) Lee, B.; Park, S.-Y.; Kim, H.-C.; Cho, K.; Vogel, E. M.; Kim, M. J.; Wallace, R. M.; Kim, J. Conformal Al_2O_3 Dielectric Layer Deposited by Atomic Layer

Deposition for Graphene-Based Nanoelectronics. *Appl. Phys. Lett.* **2008**, *92*, 203102.

(11) Chisaka, M.; Sasaki, H.; Muramoto, H. Monoclinic Hafnium Oxynitride Supported on Reduced Graphene Oxide to Catalyse the Oxygen Reduction Reaction in Acidic Media. *Phys. Chem. Chem. Phys.* **2014**, *16*, 20415–20419.

(12) Wang, X.; Tabakman, S.; Dai, H. Atomic Layer Deposition of Metal Oxides on Pristine and Functionalized Graphene. *J. Am. Chem. Soc.* **2008**, *130*, 8152–8153.

(13) Lin, Y.-M.; Dimitrakopoulos, C.; Jenkins, K. A.; Farmer, D. B.; Chiu, H.; Grill, A.; Avouris, P. 100-GHz Transistors From. *Science* **2010**, *327*, 100.

(14) Robinson, J. A.; Labella, M.; Trumbull, K. A.; Weng, X.; Cavelero, R.; Daniels, T.; Hughes, Z.; Hollander, M.; Fanton, M.; Snyder, D. Epitaxial Graphene Materials Integration: Effects of Dielectric Overlayers on Structural and Electronic Properties. *ACS Nano* **2010**, *4*, 2667–2672.

(15) Zou, K.; Hong, X.; Keefer, D.; Zhu, J. Deposition of High-Quality HfO_2 on Graphene and the Effect of Remote Oxide Phonon Scattering. *Phys. Rev. Lett.* **2010**, *105*, 126601/1–4.

(16) Liang, Y.; Li, Y.; Wang, H.; Zhou, J.; Wang, J.; Regier, T.; Dai, H. Co_3O_4 Nanocrystals on Graphene as a Synergistic Catalyst for Oxygen Reduction Reaction. *Nat. Mater.* **2011**, *10*, 780–786.

(17) Liang, Y.; Wang, H.; Zhou, J.; Li, Y.; Wang, J.; Regier, T.; Dai, H. Covalent Hybrid of Spinel Manganese-Cobalt Oxide and Graphene as Advanced Oxygen Reduction Electrocatalysts. *J. Am. Chem. Soc.* **2012**, *134*, 3517–3523.

(18) George, S. M. Atomic Layer Deposition: An Overview. *Chem. Rev.* **2010**, *110*, 111–131.

(19) Zheng, L.; Cheng, X.; Cao, D.; Wang, Z.; Xu, D.; Xia, C.; Shen, L.; Yu, Y. Effects of Rapid Thermal Annealing on Properties of HfAlO Films Directly Deposited by ALD on Graphene. *Mater. Lett.* **2014**, *137*, 200–202.

(20) Xuan, Y.; Wu, Y. Q.; Shen, T.; Qi, M.; Capano, M. A.; Cooper, J. A.; Ye, P. D. Atomic-Layer-Deposited Nanostructures for Graphene-Based Nanoelectronics. *Appl. Phys. Lett.* **2008**, *92*, 013101/1–4.

(21) Hollander, M. J.; Labella, M.; Hughes, Z. R.; Zhu, M.; Trumbull, K. A.; Cavalero, R.; Snyder, D. W.; Wang, X.; Hwang, E.; Datta, S.; Robinson, J. Enhanced Transport and Transistor Performance with Oxide Seeded High-κ Gate Dielectrics on Wafer-Scale Epitaxial Graphene. *Nano Lett.* **2011**, *11*, 3601–3607.

(22) Loh, K. P.; Bao, Q.; Eda, G.; Chhowalla, M. Graphene Oxide as a Chemically Tunable Platform for Optical Applications. *Nat. Chem.* **2010**, *2*, 1015–1024.

(23) Lee, V.; Dennis, R. V.; Schultz, B. J.; Jaye, C.; Fischer, D. A.; Banerjee, S. Soft X-Ray Absorption Spectroscopy Studies of the Electronic Structure Recovery of Graphene Oxide upon Chemical Defunctionalization. *J. Phys. Chem. C* **2012**, *116*, 20591–20599.

(24) Lee, V.; Dennis, R. V.; Jaye, C.; Wang, X.; Fischer, D. A.; Cartwright, A. N.; Banerjee, S. In Situ Near-Edge x-Ray Absorption Fine Structure Spectroscopy Investigation of the Thermal Defunctionalization of Graphene Oxide. *J. Vac. Sci. Technol. B Microelectron. Nanom. Struct.* **2012**, *30*, 061206/1–8.

(25) De Jesus, L. R.; Dennis, R. V.; Depner, S. W.; Jaye, C.; Fischer, D. A.; Banerjee, S. Inside and Outside: X-Ray Absorption Spectroscopy Mapping of Chemical Domains in Graphene Oxide. *J. Phys. Chem. Lett.* **2013**, *4*, 3144–3151.

(26) Ganguly, A.; Sharma, S.; Papakonstantinou, P.; Hamilton, J. Probing the Thermal Deoxygenation of Graphene Oxide Using High-Resolution In Situ X-Ray-Based Spectroscopies. *J. Phys. Chem. C* **2011**, *115*, 17009–17019.

(27) Hunt, A.; Dikin, D. A.; Kurmaev, E. Z.; Boyko, T. D.; Bazylewski, P.; Chang, G. S.; Moewes, A. Epoxide Speciation and Functional Group Distribution in Graphene Oxide Paper-like Materials. *Adv. Funct. Mater.* **2012**, *22*, 3950–3957.

(28) Hunt, A.; Kurmaev, E. Z.; Moewes, A. A Re-Evaluation of How Functional Groups Modify the Electronic Structure of Graphene Oxide. *Adv. Mater.* **2014**, *26*, 4870–4874.

(29) Zhou, C.; Wang, J.; Szpunar, J. a. X-Ray Chemical Imaging and the Electronic Structure of a Single Nanoplatelet Ni/Graphene Composite. *Chem. Commun.*. **2014**, *50*, 2282–2285.

(30) Hemraj-Benny, T.; Banerjee, S.; Sambasivan, S.; Balasubramanian, M.; Fischer, D. A.; Eres, G.; Puretzky, A. A.; Geohegan, D. B.; Lowndes, D. H.; Han, W.; Misewich, J. A.; Wong, S. S. Near-Edge X-Ray Absorption Fine Structure Spectroscopy as a Tool for Investigating Nanomaterials. *Small* **2006**, *2*, 26–35.

(31) Winter, A. D.; Larios, E.; Alamgir, F. M.; Jaye, C.; Fischer, D. A.; Campo, E. M. Thermo-Active Behavior of Ethylene-Vinyl Acetate | Multiwall Carbon Nanotube Composites Examined by in Situ near-Edge X-Ray Absorption Fine-Structure

Spectroscopy. *J. Phys. Chem. C* **2014**, *118*, 3733–3741.

(32) Winter, A. D.; Jaye, C.; Fischer, D.; Omastová, M.; Campo, E. M.; Omastová, M.; Campo, E. M. Prestrain Relaxation in Non-Covalently Modified Ethylene-Vinyl Acetate | PyChol | Multiwall Carbon Nanotube Nanocomposites. *APL Mater.* **2014**, *2*, 066105/1–8.

(33) Lerf, A.; He, H.; Forster, M.; Klinowski, J. Structure of Graphite Oxide Revisited. *J. Phys. Chem. B* **1998**, *102*, 4477–4482.

(34) Kamiya, K.; Umezawa, N.; Okada, S. Energetics and Electronic Structure of Graphene Adsorbed on HfO_2(111): Density Functional Theory Calculations. *Phys. Rev. B* **2011**, *83*, 1–4.

(35) Hummers, W. S.; Offeman, R. E. Preparation of Graphitic Oxide. *J. Am. Chem. Soc.* **1958**, *80*, 1339.

(36) Hausmann, D. M.; Kim, E.; Becker, J.; Gordon, R. G. Atomic Layer Deposition of Hafnium and Zirconium Oxides Using Metal Amide Precursors. *Chem. Mater.* **2002**, *14*, 4350–4358.

(37) Ho, M.-T.; Wang, Y.; Brewer, R. T.; Wielunski, L. S.; Chabal, Y. J.; Moumen, N.; Boleslawski, M. In Situ Infrared Spectroscopy of Hafnium Oxide Growth on Hydrogen-Terminated Silicon Surfaces by Atomic Layer Deposition. *Appl. Phys. Lett.* **2005**, *87*, 133103/1–3.

(38) Dennis, R. V.; Schultz, B. J.; Jaye, C.; Wang, X.; Fischer, D. A.; Cartwright, A. N.; Banerjee, S. Near-Edge x-Ray Absorption Fine Structure Spectroscopy Study of Nitrogen Incorporation in Chemically Reduced Graphene Oxide. *J. Vac. Sci.*

Technol. B Microelectron. Nanom. Struct. **2013**, *31*, 041204/1–9.

(39) Morant, C.; Galán, L.; Sanz, J. M. An XPS Study of the Initial Stages of Oxidation of Hafnium. *Surf. Interface Anal.* **1990**, *16*, 304–308.

(40) Barreca, D.; Milanov, A.; Fischer, R. a.; Devi, A.; Tondello, E. Hafnium Oxide Thin Film Grown by ALD: An XPS Study. *Surf. Sci. Spectra* **2007**, *14*, 34/1–8.

(41) Schultz, B. J.; Dennis, R. V.; Aldinger, J. P.; Jaye, C.; Wang, X.; Fischer, D. A; Cartwright, A. N.; Banerjee, S. X-Ray Absorption Spectroscopy Studies of Electronic Structure Recovery and Nitrogen Local Structure upon Thermal Reduction of Graphene Oxide in an Ammonia Environment. *RSC Adv.* **2014**, *4*, 634–644.

(42) Kovtyukhova, N. I.; Mallouk, T. E.; Pan, L.; Dickey, E. C. Individual Single-Walled Nanotubes and Hydrogels Made by Oxidative Exfoliation of Carbon Nanotube Ropes. *J. Am. Chem. Soc.* **2003**, *125*, 9761–9769.

(43) NIST X-Ray Photoelectron Spectroscopy Database http://srdata.nist.gov/xps/. (accessed Feb 1, 2015).

(44) Becerril, H. A.; Mao, J.; Liu, Z.; Stoltenberg, R. M.; Bao, Z.; Chen, Y. Evaluation of Solution-Processed Reduced Graphene Oxide Films as Transparent Conductors. *ACS Nano* **2008**, *2*, 463–470.

(45) Hunt, A.; Kurmaev, E. Z.; Moewes, A. Band Gap Engineering of Graphene Oxide by Chemical Modification. *Carbon.* **2014**, *75*, 366–371.

(46) Acik, M.; Mattevi, C.; Gong, C.; Lee, G.; Cho, K.; Chhowalla, M.; Chabal, Y. J. The Role of Intercalated Water in Multilayered Graphene Oxide. *ACS Nano.* **2010**,

4, 5861–5868.

(47) Radovic, L. R. Active Sites in Graphene and the Mechanism of CO_2 Formation in Carbon Oxidation. *J. Am. Chem. Soc.* **2009**, *131*, 17166–17175.

(48) Pettifer, R. F.; Brouder, C.; Benfatto, M.; Natoli, C. R.; Hermes, C.; Ruiz Lpez, M. F. Magic-Angle Theorem in Powder x-Ray-Absorption Spectroscopy. *Phys. Rev. B* **1990**, *42*, 37–42.

(49) Pacilé, D.; Papagno, M.; Rodríguez, A.; Grioni, M.; Papagno, L.; Girit, Ç.; Meyer, J.; Begtrup, G.; Zettl, A. Near-Edge X-Ray Absorption Fine-Structure Investigation of Graphene. *Phys. Rev. Lett.* **2008**, *101*, 066806/1–4.

(50) Fischer, D. A.; Wentzcovitch, R. M.; Carr, R. G.; Continenza, A.; Freeman, A. J. Graphitic Interlayer States: A Carbon *K* Near-Edge X-Ray-Absorption Fine-Structure Study. *Phys. Rev. B* **1991**, *44*, 1427–1429.

(51) Lee, V.; Park, C.; Jaye, C.; Fischer, D. A.; Yu, Q.; Wu, W.; Liu, Z.; Bao, J.; Pei, S.-S.; Smith, C.; Lysaght, P.; Banerjee, S. Substrate Hybridization and Rippling of Graphene Evidenced by Near-Edge X-Ray Absorption Fine Structure Spectroscopy. *J. Phys. Chem. Lett.* **2010**, *1*, 1247–1253.

(52) Gas Phase Core Excitation Database http://unicorn.mcmaster.ca/corex/cedb-title.html. (accessed Feb 1, 2015).

(53) Jeong, H.-K.; Colakerol, L.; Jin, M. H.; Glans, P.-A.; Smith, K. E.; Lee, Y. H. Unoccupied Electronic States in Graphite Oxides. *Chem. Phys. Lett.* **2008**, *460*, 499–502.

(54) Jeong, H.-K.; Noh, H.-J.; Kim, J.-Y.; Jin, M. H.; Park, C. Y.; Lee, Y. H. X-Ray

Absorption Spectroscopy of Graphite Oxide. *Europhysics Lett.* **2008**, *82*, 67004/1–5.

(55) Freund, H.-J.; Roberts, M. W. Surface Chemistry of Carbon Dioxide. *Surf. Sci. Rep.* **1996**, *25*, 225–273.

(56) Plaschke, M.; Rothe, J.; Altmaier, M.; Denecke, M. A.; Fanghänel, T. Near Edge X-Ray Absorption Fine Structure (NEXAFS) of Model Compounds for the Humic Acid/Actinide Ion Interaction. *J. Electron Spectros. Relat. Phenomena* **2005**, *148*, 151–157.

(57) Armbruster, M. K.; Schimmelpfennig, B.; Plaschke, M.; Rothe, J.; Denecke, M. A.; Klenze, R. Metal-Ion Complexation Effects in C 1s-NEXAFS Spectra of Carboxylic Acids-Evidence by Quantum Chemical Calculations. *J. Electron Spectros. Relat. Phenomena.* **2009**, *169*, 51–56.

(58) Ju, H.; Feng, X.; Ye, Y.; Zhang, L.; Pan, H.; Campbell, C. T.; Zhu, J. Ca Carboxylate Formation at the Calcium/Poly(Methyl Methacrylate) Interface. *J. Phys. Chem. C* **2012**, *116*, 20465–20471.

CHAPTER III

STABILIZATION OF Ag-Au BIMETALLIC NANOCRYSTALS IN AQUATIC ENVIRONMENTS MEDIATED BY DISSOLVED ORGANIC MATTER: A MECHANISTIC PERSPECTIVE[*]

3.1 Summary

Gold and silver nanoparticles can be stabilized endogenously within aquatic environments from dissolved ionic species as a result of mineralization induced by dissolved organic matter. However, the ability of fulvic and humic acids to stabilize bimetallic nanoparticles is entirely unexplored. Elucidating the formation of such particles is imperative given their potential ecological toxicity. Herein, we demonstrate the nucleation, growth, and stabilization of bimetallic Ag-Au nanocrystals from the interactions of Ag^{+} and Au^{3+} with Suwannee River fulvic and humic acids. The mechanisms underpinning the stabilization of Ag-Au alloy NPs at different pH (6.0 – 9.0) values are studied by UV-vis spectrophotometry, X-ray photoelectron spectroscopy (XPS), high-resolution transmission electron microscopy (HRTEM), and selected area electron diffraction (SAED). Complexation of free Ag^{+} and Au^{3+} ions with the Lewis basic groups (carbonyls, carboxyls, and thiols) of FA and HA, followed by electron-transfer from redox-active moieties present in dissolved organic matter initiates the nucleation of the NPs. Alloy

[*] Reprinted with permission from "Stabilization of Ag–Au Bimetallic Nanocrystals in Aquatic Environments Mediated by Dissolved Organic Matter: A Mechanistic Perspective" by Alivio, T. E. G.; Fleer, N. A.; Singh, J.; Nadadur, J.; Feng, M.; Banerjee, S.; Sharma, V. K. *Environ. Sci. Technol*. **2018**, *52*, 7269-7278.

formation and interdiffusion of Au and Ag atoms are further facilitated by a galvanic replacement reaction between $AuCl_4^-$ and Ag. Charge-transfer from Au to Ag stabilizes the formed bimetallic NPs. A more pronounced agglomeration of the Ag-Au NPs is observed when HA is used compared to FA as the reducing agent. The bimetallic NPs are stable for greater than four months, which suggests the possible persistence and dispersion of these materials in aquatic environments. The mechanistic ideas have broad generalizability to reductive mineralization processes mediated by dissolved organic matter.

3.2 Introduction

Silver nanoparticles (Ag NPs) exhibit antimicrobial properties and have therefore found extensive use in consumer and healthcare products. For instance, such nanoparticles have been incorporated within dietary supplements, embedded within clothing, and utilized as coatings for medical implements.[1] Some estimates suggest that more than 20% of the *ca.* 1,800 commercial products that explicitly claim to incorporate nanomaterials contain Ag NPs.[2] The unintentional release of Ag NPs into the environment has raised concerns regarding their accumulation as well as potential toxicity to humans and ecosystems.[1,3,4] In a similar vein, significant recent attention has focused on gold nanoparticles (Au NPs); Au NPs are finding widespread applications in catalysis, chemical/biological sensing, photovoltaics, electronics, and cancer theranostics.[5,6] Increasing adoption of Ag and Au NPs, particularly in consumer products where oversight of responsible disposal is almost

entirely absent, portends their inevitable release into the aquatic environment wherein they show worrying indications of ecological toxicity.[7–10]

The fate (and transport) of engineered nanoparticles is determined by their surface properties, as well as the parameters of the aquatic system wherein they are released (such as pH, dissolved organic content, and ionic strength).[8,11,12] Both types of NPs can be oxidized by chlorine and ozone in various treatment processes to generate free ions in water.[13–15] In addition to the dissolution of engineered nanoparticles, high concentrations of Ag-ions in aqueous media can be derived from industrial effluent streams such as from the electroplating, mining, mineral processing, photovoltaics, and legacy photoprocessing industries.[16–18] For instance, the occurrence of high concentrations of radioactive Ag nuclides in nuclear waste streams, derived from decommissioning of control rods typically constituted from Ag-In-Cd alloys,[19,20] represents a major concern. The environmental fate and sequestration of such ions are largely unexplored. Some intriguing studies suggest that in the presence of dissolved organic matter (DOM), free Ag- and Au-ions are reconstituted (under sunlight) to yield Ag and Au NPs, respectively.[21–24] However, the mechanisms of crystal growth remain to be elucidated and such studies have thus far been limited to single ionic species, either Ag^{+} or Au^{3+}. In this article, we present a systematic mechanistic evaluation of the alloying and crystallization of bimetallic Ag-Au nanocrystals mediated by the DOM reduction of precursor ions in aquatic environments.

Aqueous concentrations of Ag- and Au-ions can reach high values in specific waste streams and in proximity to mineral deposits.[25–30] For instance, the concentration of Ag-ions in legacy photoprocessing wastewater samples can reach up to 300 μg/L.[30] As

much as 1,890,000 µg/L of Au has likewise been measured from sludge from the Suwa Manufacturing Facility.[25,26] There is considerable evidence that geological deposits of Au and Ag are co-localized and thus the coexistence of both types of ions in mineral processing streams is unavoidable.[31–34] Mixtures of both ions can further be derived from dissolution of engineered bimetallic nanomaterials since Ag-Au alloy NPs are finding increasing use in catalysis, biomedicine, and chemical sensing.[35] While our past research[23,24,36,37] has led to the intriguing finding that DOM mediates the crystallization of Ag NPs and Au NPs, serving as both a reductant and a passivating ligand, the stabilization of bimetallic Ag-Au NPs under environmentally relevant conditions has not hitherto been examined.

In this article, we present a systematic evaluation of the stabilization of bimetallic Ag-Au NPs in aquatic environments in the presence of DOM. In particular, Suwannee River fulvic (FA) and humic acids (HA) are examined for their ability to reduce Ag^{+} and Au^{3+} ions at pH values that are emulative of environmental conditions. The systems are examined at temperatures approaching 90°C in order to mimic aqueous media in areas at naturally-elevated temperatures, such as hot springs.[36] The US Environmental Protection Agency (EPA) notes a silver content up to 43,000 µg/L in some hot springs.[27] The formation of Ag, Au, and Ag-Au NPs is evaluated using ultraviolet-visible (UV-vis) spectrophotometry. X-ray photoelectron spectroscopy (XPS) is further used to examine the chemical speciation of Ag and Au in the samples and to elucidate the nature of the surficial interactions with FA and HA. High-resolution transmission electron microscopy (HRTEM) is used to evaluate the morphology of the stabilized particles as well as to obtain

insight into crystal growth mechanisms. Together, these techniques provide mechanistic understanding of the stabilization of bimetallic Ag-Au NPs mediated by DOM and have broad generalizability to reductive mineralization processes in aquatic environments.

3.3 Methods

3.3.1 Materials

$AgNO_3$ (> 99.0 %) and $AuCl_3$ (> 99.9 %) were purchased from Sigma Aldrich (St. Louis, MO) and used as received without further purification. Suwannee River FA and HA were acquired from the International Humic Substances Society (IHSS, St. Paul, MN). All pieces of glassware in the study were acid-washed before use. Solutions were prepared with deionized water that had been distilled and passed through a Milli-Q water purification system yielding a conductivity of 18 MΩ/cm. Solutions of Ag- and Au-ions were prepared by dissolving the respective salts in water at concentrations of 2.0×10^{-4} M. Solutions of FA and HA at 25 mg/L were prepared by dissolving the solids in a 1.0×10^{-3} M 2-(*N*-morpholino)ethanesulfonic acid (MES) buffer (Sigma Aldrich; St. Louis, MO) by stirring for 24 h; the dispersions were subsequently filtered through previously dried 0.45 μm filters.[23] The pH of the solution was adjusted to the desired range by adding an appropriate amount of aqueous 0.1 M NaOH. pH measurements were performed using an Orion pH/ISEmeter, model 710A instrument (Thermo Fisher Scientific, Waltham, MA).

3.3.2 Stabilization of Monometallic and Alloy Nanoparticles

Bimetallic Ag-Au NPs were prepared by adding a mixture of Ag- and Au-ions to HA or FA solutions at different pH (6.0—9.0) values. The solutions were subsequently heated to 90±1°C for 1 h. Mixtures with varying molar ratios of Ag- and Au-ions (maintaining a total concentration of 1.0×10^{-4} M) were evaluated while holding the concentration of DOM (HA or FA) constant at 12.5 mg/L. Molar ratios of ions ranged from $x_{Ag} = 1.0$ to $x_{Au} = 1.0$. The total volume of the mixed solutions was kept at 2.0 mL with illumination from laboratory fluorescent lighting in capped clear glass tubes. Monometallic Ag NPs and Au NPs were prepared at the extremes of the molar ratios ($x_{Ag} = 1.0$ and $x_{Au} = 1.0$).

3.3.3 Characterization of Nanoparticles

The nucleation and growth of NPs were evaluated using a DR-5000 UV-visible spectrophotometer (Hach Company, Loveland, CO). Quartz cuvettes with a 1 cm optical path length were used for absorption spectroscopy measurements. The samples were cooled to room temperature prior to acquiring spectra. Blank measurements were acquired using a MES buffer solution without FA or HA. Prior to analyses by XPS and HRTEM, the samples were dehydrated, which was accomplished by centrifugation at 6,000 rpm for 30 min using an Avanti J-E centrifuge (Beckman Coulter, Inc., Palo Alto, CA), dispersion in methanol, and further centrifugation under the same conditions to remove the unreacted reagents. The solvent was decanted and the samples were washed thrice with methanol in order to obtain solid samples for further analysis. The samples were then freeze-dried for

48 h using a Labconco Freezone 12 Freeze Dry System (Labconco Corp., Kansas City, MO).

All XPS measurements were performed using an Omicron XPS/UPS system with a 128-channel micro-channelplate Argus detector, using Mg Kα X-rays (source energy of 1253.6 eV). The spectral resolution of the instrument was *ca.* 0.8 eV. Charge neutralization was accomplished using a CN10 electron flood source. High-resolution spectra were collected in constant analyzer energy (CAE) mode at a pass energy of 20 eV and an energy step size of 0.05 eV. All spectra were calibrated using the C 1s line of adventitious carbon at 284.8 eV. Relative atomic concentrations for the bimetallic samples were determined by fitting the spectra to mixed Gaussian—Lorentzian (7:3) lineshapes using the CasaXPS 2.3.16 software by the application of a Marquart-Levenberg optimization algorithm.

The morphologies of the prepared monometallic and bimetallic NPs were assessed by electron microscopy using a FEI Tecnai G2 F20 ST field-emission TEM. Briefly, samples were dispersed in 2-propanol (Fisher, Fair Lawn, NJ), drop-cast onto 400-mesh holey-carbon films supported by copper grids (Electron Microscopy Sciences, Hatfield, PA), and air-dried at room temperature prior to imaging. Images were acquired at an operating voltage of 200 kV.

3.4 Results and Discussion

Figure 3.1 shows UV-vis absorption spectra of monometallic and bimetallic Ag-Au NPs obtained by mixing solutions of varying mole fractions of Ag^{+} and Au^{3+} ions (χ_{Ag} = 0.0—

1.0) with FA at different pH values. At χ_{Ag} = 0.0 (i.e., with only Au^{3+} precursor ions), a pronounced absorption band is observed centered at *ca.* 520 nm, corresponding to the surface plasmon resonance (SPR) of Au NPs. In contrast, when only Ag-ions are present in solution with FA (i.e., χ_{Ag} = 1.0), a yellowish coloration is observed with a SPR at *ca.* 390 nm. In other words, FA is able to mediate the reduction of the precursor ions to metallic nanocrystals. The DOM-mediated stabilization of Au and Ag NPs have been extensively documented in our previous work.[21–24,38]

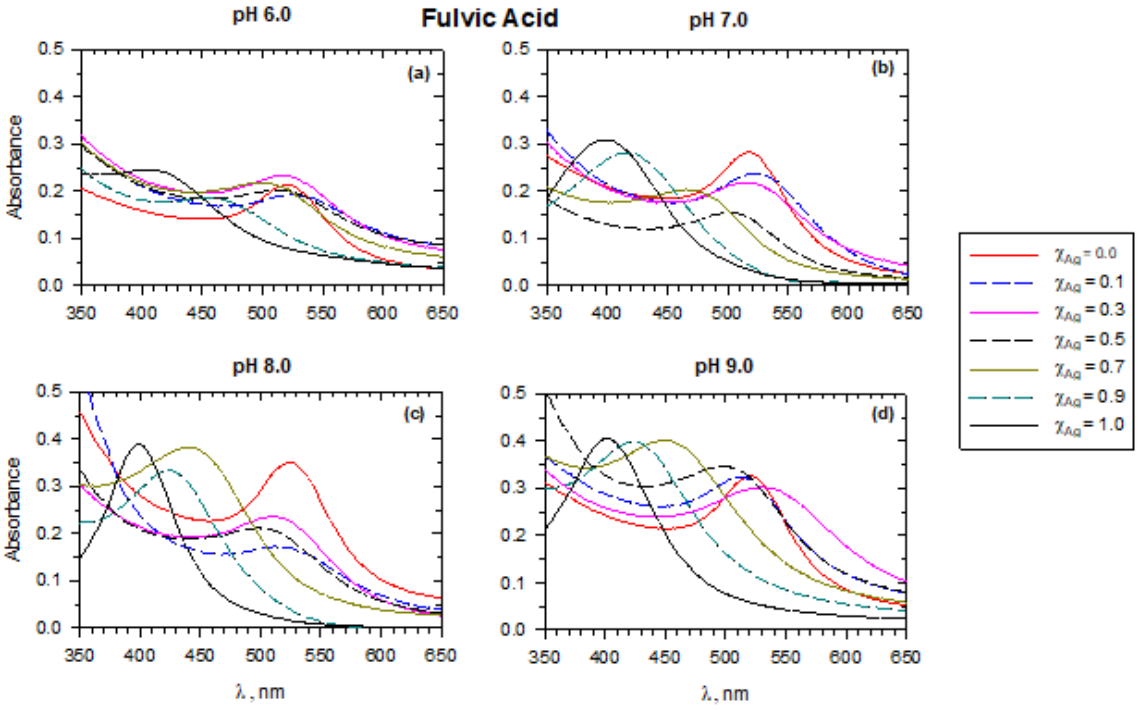

Figure 3.1: UV-vis absorbance spectra of bimetallic Ag-Au NPs at different mole fractions of Ag^{+} ions (χ_{Ag}) in mixed solutions of Ag^{+}-Au^{3+}-FA at pH a of (a) 6.0, (b) 7.0, (c) 8.0, and (d) 9.0. (Experimental conditions: $[Ag^{+}] + [Au^{3+}] = 1.0\times10^{-4}$ M, [FA] = 12.5 mg/L, reaction time = 1 h; temperature = 90°C)

Figure 3.1 shows that the formation of Ag NPs mediated by FA is facilitated by increasing pH (the absorbance at *ca.* 390 nm increases monotonically from 0.25 to 0.40 as the pH is increased from 6.0 to 9.0). The reduction of monovalent Ag-ions to zero-valent Ag by FA can be rationalized based on the differential in reduction potentials. The Ag^{+}/Ag reduction potential is 0.7994 V (*vs.* NHE), whereas the reduction potential for FA (FA^{-} + H^{+})/FA-H is estimated to be 0.5 V (*vs.* NHE).[39] The oxidation of FA has been observed to be accompanied by the consumption of protons.[39] A higher pH value shifts the equilibrium towards the reduced form of FA, increasing the concentration of deprotonated FA, facilitating more effective reduction of the precursor ions and thereby providing a higher yield of Ag NPs.

In the case of monometallic Au NPs, **Figure 3.1** shows a similar increase in the formation of Au NPs as the pH of the solution is increased from 6.0 to 8.0, denoted by an increase in absorbance at *ca*. 520 nm from 0.21 to 0.35. Interestingly, upon increasing the pH to 9.0, a decrease of the absorbance at *ca*. 520 nm is observed (to 0.33), indicating a slight decrease in the formation of Au NPs under such conditions. This observation can be explained by considering changes in the speciation and reduction potentials of FA and Au^{3+} ions as a function of the solution pH. The reduction potential of organic matter decreases with increasing pH;[22,40,41] consequently, the thermodynamic driving force for reduction of Au^{3+} is enhanced with increasing pH. However, as a result of hydrolysis reactions, the solution-phase speciation of the Au-ions is also altered as a function of pH. At a pH below 5.25, $AuCl_3$ in aqueous media is predominantly speciated as $AuCl_2OH{\cdot}H_2O$; increasing the solution pH results in the preferential stabilization of

$AuCl_3OH^-$ and $Au(OH)_4^-$.[42] The reduction potential of these species decrease with solution pH (**Table 3.1**), rendering reduction less favorable under highly alkaline conditions.[42] In other words, the observed pH dependence of the stabilization of Au NPs reflects the cumulative effects of the speciation of Au and the pH dependence of the FA reduction potential; a pH of 8.0 corresponds to greatest differential in reduction potentials between FA and the precursor ions, resulting in the highest yield of Au NPs.

Table 3.1: Standard reduction potentials of Au species *versus* the standard hydrogen electrode (SHE).[42]

Reduction half-reaction	E^0 **(V)**
$AuCl_4^-$ (*aq.*) + $3e^-$ ⇄ Au^0 (*s*) + $4Cl^-$ (*aq.*)	+1.00
$AuCl_2OH{\cdot}H_2O^0$ (*aq.*) + $3e^-$ ⇄ Au^0 (*s*) + $2Cl^-$ (*aq.*) + OH^- (*aq.*) + H_2O (*l*)	+0.94
$AuCl(OH)_3^-$ (*aq.*) + $3e^-$ ⇄ Au^0 (*s*) + Cl^- (*aq.*) + $3OH^-$ (*aq.*)	+0.69
$Au(OH)_4^-$ (*aq.*) + $3e^-$ ⇄ Au^0 (*s*) + $4OH^-$ (*aq.*)	+0.60

In solutions with χ_{Ag} = 0.1—0.9, only one SPR band is observed, as shown in **Figure 3.1** and **Figure 3.2**, suggesting the formation of alloy NPs instead of a heterogeneous mixture of monometallic Ag and Au NPs. Significantly, a mixture of equal molar fractions of precursor ions (χ_{Ag} = 0.5 and χ_{Au} = 0.5) in just MES buffer solution (i.e., without FA or HA) showed no apparent SPR band (**Figure 3.3**); clearly delineating the role of FA and HA as reducing agents in facilitating the electroless nucleation of bimetallic NPs. Spectral measurements of mixtures containing equal molar fractions of precursor ions (χ_{Ag} = 0.5 and χ_{Au} = 0.5) with FA and MES buffer were likewise conducted as a function of time for 60 min (**Figure 3.4**). The growth of plasmon band for mixed fractions in FA with time appears to be weighted towards the Au SPR band indicative of the preferential incorporation of Au, which can be rationalized based on its higher reduction

potential (1.5 V *vs.* SHE). A notable pH dependence is observed for the position of the SPR band for FA-mediated reduction, which is predominantly reflective of the non-monotonic changes in Au incorporation as a result of the pH dependence of the reduction potential differentials between Au precursor species and FA. It is worth noting that initially formed Ag^0 clusters can further react with $AuCl_4^-$ in solution *via* a galvanic replacement reaction as per:[43]

$$3Ag\ (s) + AuCl_4^-\ (aq.) \rightarrow 3Ag^+\ (aq.) + Au\ (s) + 4Cl^-\ (aq.) \qquad \textbf{Eq. 3.1}$$

thereby resulting in preferential incorporation of Au in the alloy NPs. The precipitated Au^0 clusters are then subsequently alloyed with unreacted Ag^0 to yield Ag-Au alloy NPs. Both Ag and Au crystallize in the same face-centered cubic (fcc) crystal structure with well-matched lattice constants (a_{Ag} = 4.086Å and a_{Au} = 4.079Å); alloy-formation by galvanic replacement appears to be the likely mechanism underpinning the observed variation of alloy composition as a function of the amount of $AuCl_4^-$.[44]

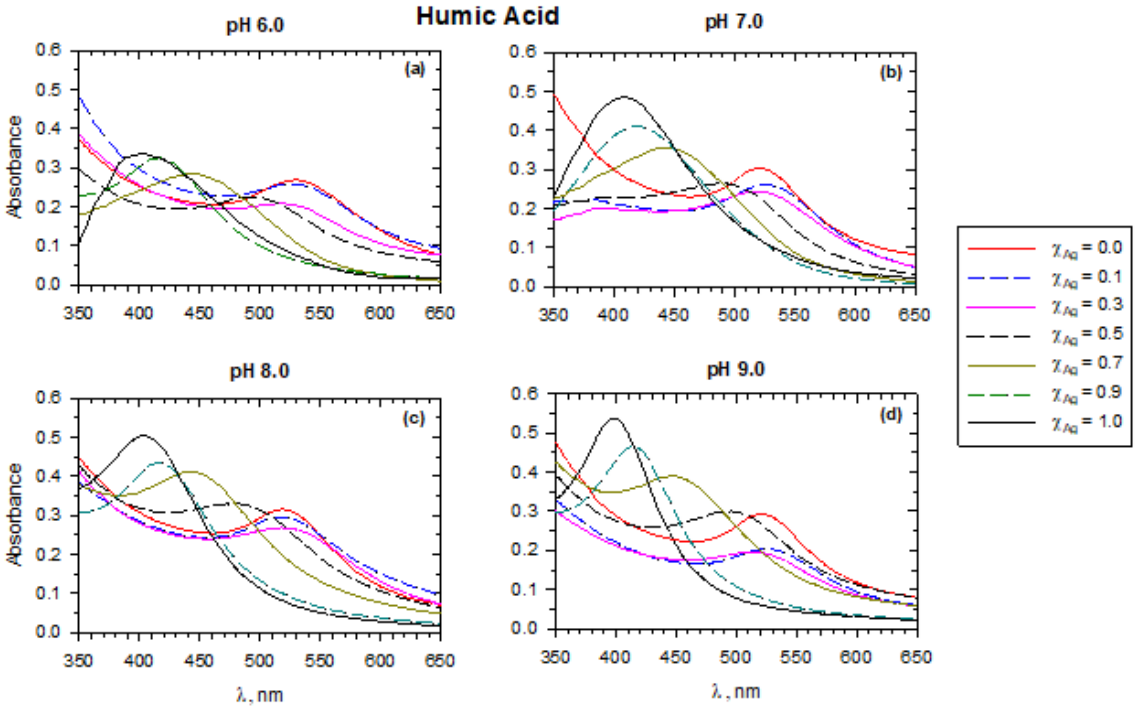

Figure 3.2: UV-vis absorbance spectra of bimetallic Ag-Au NPs at different mole fractions of Ag^{+} ions (χ_{Ag}) in aqueous solutions of Ag^{+}, Au^{3+}, and HA at pH of (a) 6.0; (b) 7.0; (c) 8.0; and (d) 9.0. (Experimental conditions: $[Ag^{+}] + [Au^{3+}] = 1.0\times10^{-4}$ M, [HA] = 12.5 mg/L, reaction time = 1 h, temperature = 90±1°C)

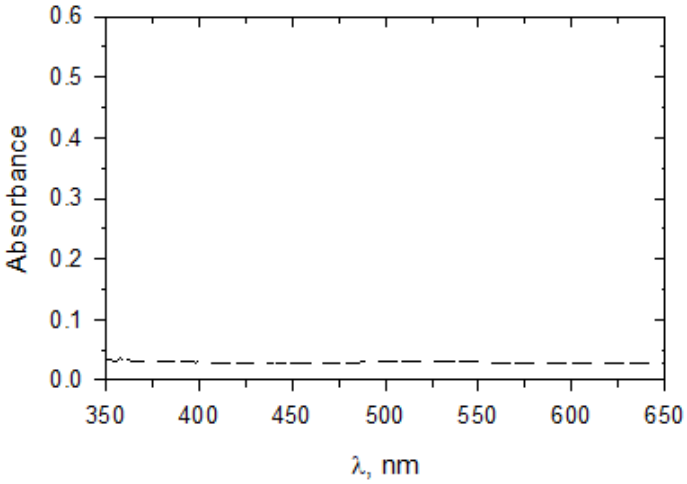

Figure 3.3: UV-vis absorbance spectra obtained in aqueous solutions of Ag^{+}, Au^{3+}, and MES buffer at pH 8.0. (Experimental conditions: $[Ag^{+}] + [Au^{3+}] = 1.0\times10^{-4}$ M, reaction time = 2 h, and temperature = 90±1°C)

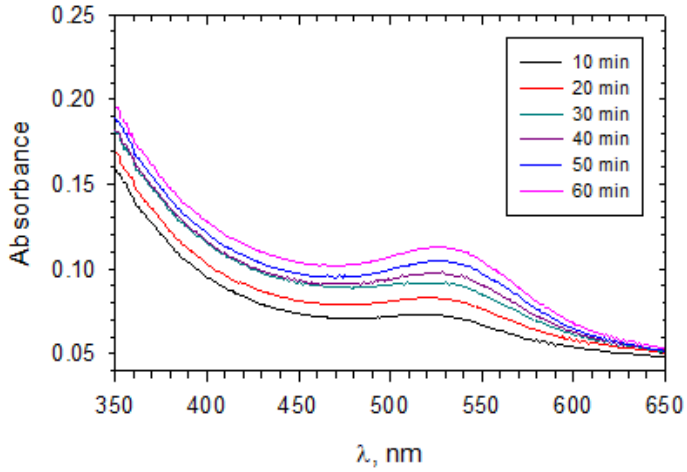

Figure 3.4: UV-vis absorbance spectra obtained at different time in aqueous solutions of Ag^{+}, Au^{3+}, and MES buffer at pH 8.0. (Experimental conditions: $[Ag^{+}] + [Au^{3+}] = 0.5\times10^{-4}$ M, [FA] = 12.5 mg/L, and temperature = 90±1°C)

Similar formation of bimetallic Ag-Au NPs is observed in solutions of Ag^{+}/Au^{3+} mixed with HA at different pH values (**Figure 3.2**). Comparing the plots depicted in

Figure 3.1 with those in **Figure 3.2**, no significant difference in the alloy composition is observed, whether FA or HA is used as the reducing agent. **Figure 3.5** indicates that when $\chi_{Ag} \geq 0.3$, a linear relationship between λ_{max} and χ_{Ag} is observed ($r^2 = 0.98$), reflective of a proportional increase of Ag content within the bimetallic nanocrystals as a function of the Ag precursor concentration. Both FA and HA serve as electron donors to Ag^+ and Au^{3+} ions, which are reduced to Ag^0 and Au^0, respectively. The ability of FA and HA to bind metal ions and mediate the formation of NPs can be attributed to the abundance of Lewis basic sites such as carbonyl, carboxyl, nitrogen-containing, and sulfur-containing groups that are able to complex metal cations.[45] The role of HAs as electron transfer shuttles is thought to derive in large measure from their abundant redox-active quinone moieties that are transformed between quinone, semiquinone, and hydroquinone through facile single-electron transfer reactions.[46,47] Indeed, the use of hydroquinone as a selective reducing agent for Ag^+ has been reported.[48] It is likely that reduced quinone moieties within the DOM are primed to facilitate Ag^+ and Au^{3+} reduction to elemental Ag and Au, respectively.[23] It is interesting to note that the pH dependence noted for FA is not observed for reduction by HA (**Figures 3.2** and **3.5**). HA has a higher molar mass than FA, which is reflected in a larger number of functional groups per oligomer and thereby allows for buffering of the proton concentration over a broad range. In other words, the reduced form of HA is not the limiting reagent, and consequently changes in solution pH over this range do not appreciably alter the thermodynamic driving force for the reduction of precursor ions to metallic nanocrystals. FA being the limiting reagent is corroborated by examining the electron donating capacity (EDC) of FA and HA. At a pH of 7 and a redox potential

of 0.73 V (*vs.* SHE), HA has an EDC of 3684±66 mmol of electrons per gram of HA whereas the corresponding value for FA is 2848±85 mmol electrons per gram FA.[41] This further clarifies the origins of accelerated NP formation at higher pH values as reduction of the acid moiety in a basic environment increases the EDC.[41]

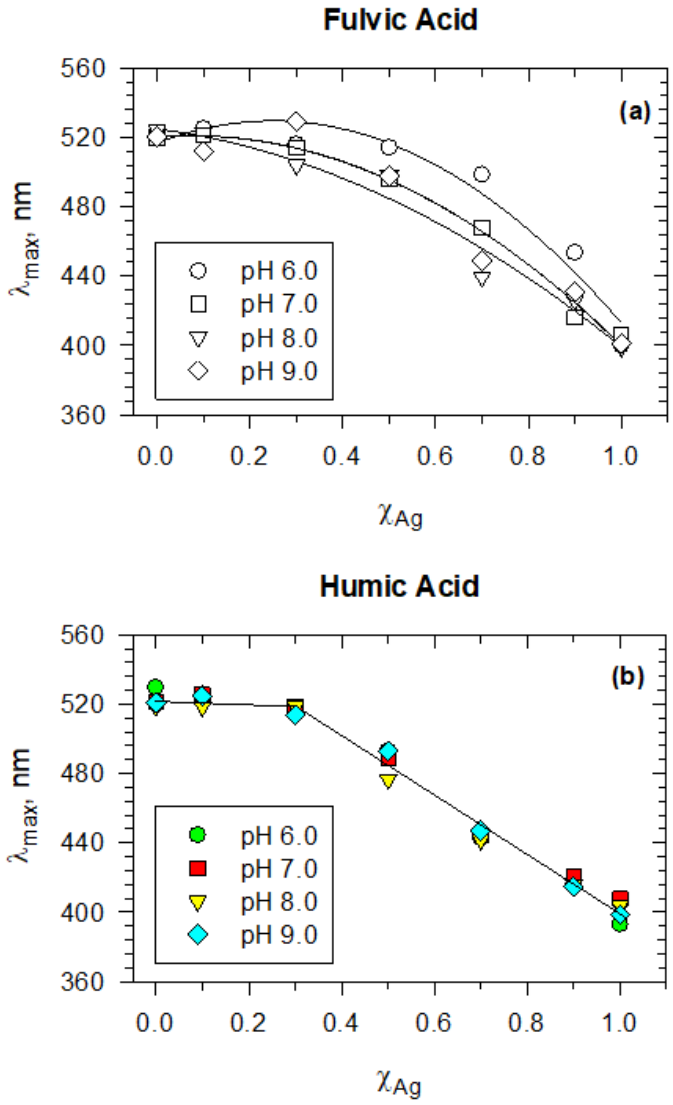

Figure 3.5: Plots of plasmon maximum (λ_{max}) of the bimetallic Ag-Au NPs grown in (a) FA and (b) HA *versus* χ_{Ag} at different pH values.

The formation of bimetallic Ag-Au NPs was also investigated at low concentrations by mixing Ag^{+} and Au^{3+} ($[Ag^{+}] + [Au^{3+}] = 2.0\times10^{-5}$ mol/L; $\chi_{Ag} = 0.5$) with 12.5 mg/L HA at pH 8.0. The optical absorption spectrum of the solution after heating for 1 h at 90°C is shown in **Figure 3.6**. The expected SPR peak of the Ag-Au bimetallic alloy is observed, but is less pronounced compared to the observed peak at higher concentrations of Ag^{+} and Au^{3+} (**Figure 3.4** *vs.* **Figure 3.1**). The stabilization of bimetallic Ag-Au NPs at low levels of precursors ions is thus established to be viable.

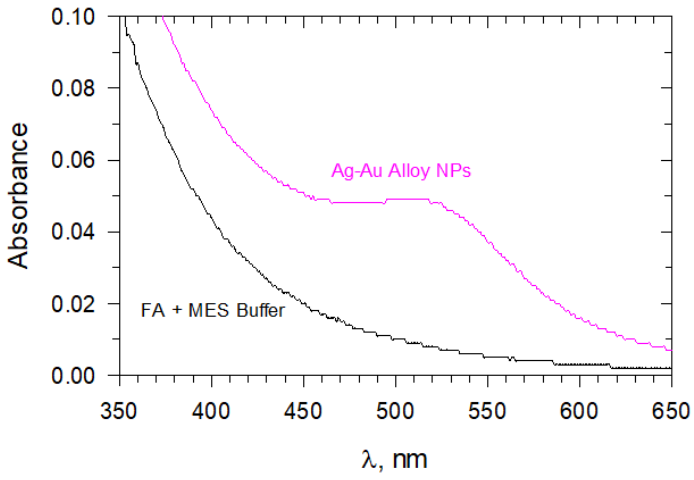

Figure 3.6: UV-vis absorbance spectrum obtained in aqueous solutions of Ag^{+}, Au^{3+}, and MES buffer at pH 8.0. (Experimental conditions: $[Ag^{+}] + [Au^{3+}] = 2.0\times10^{-5}$ M, [HA] = 12.5 mg/L, reaction time = 1 h, temperature = 90±1°C) The black curve shows the spectrum of an FA+MES buffer solution without any ionic precursors, for comparison.

Finally, the formation of bimetallic Ag-Au NPs was also explored at room temperature (22°C). **Figure 3.7** shows that Ag-Au bimetallic NPs are indeed formed, albeit after a relatively longer incubation time extending to several days. The diminished kinetics of crystal growth result in broader SPR bands. At low temperatures, initially

formed molecular Ag-Au precursors are bound to HA moieties as small clusters, which are ultimately coalesced to form nanoparticles. Nevertheless, these results illustrate that the higher temperatures examined here are a reasonable accelerated proxy for processes expected at room temperature.

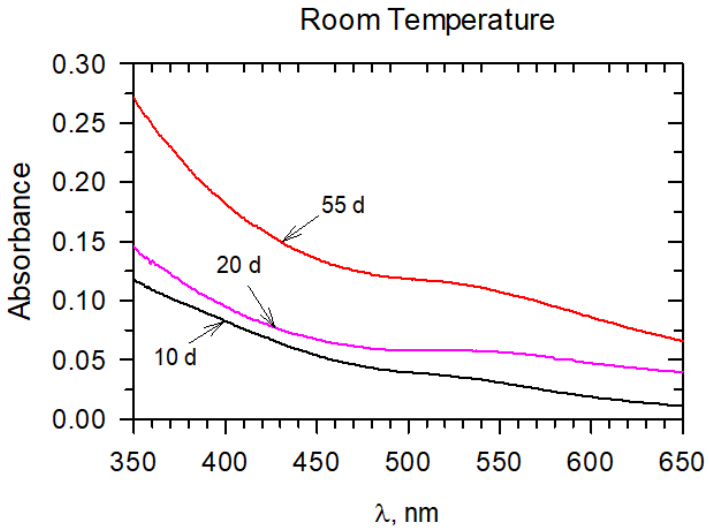

Figure 3.7: UV-vis absorbance spectra obtained in aqueous solutions of Ag^{+}, Au^{3+}, and MES buffer at pH 8.0. (Experimental conditions: $[Ag^{+}] + [Au^{3+}] = 1.0\times10^{-4}$ M, [HA] = 12.5 mg/L, temperature = 22°C)

Bimetallic NPs, prepared with χ_{Ag} = 0.5 and 0.8 (at pH = 8.0), have been characterized by XPS for both FA and HA reduction. **Table 3.2** notes the relative atomic concentrations of Ag and Au for these samples, deduced from integrating the areas of the respective spectral features in high-resolution Ag 3d and Au 4f XPS spectra. Consistent with the discussion of optical spectra above and the higher driving forces for Au reduction, for χ_{Ag} = 0.8 and both FA and HA as reducing agents, more Au is incorporated on the surface of the Ag-Au NPs than expected from the precursor concentration (ca. 35 at.% as

compared to the added concentration of ca. 20 at.%). **Figures 3.8A—B** and **3.8C—D** exhibit high-resolution Ag 3d and Au 4f XPS spectra of these samples, respectively. A spin-orbit coupling of 6.0 eV is observed between the Ag $3d_{5/2}$ and $3d_{3/2}$ peaks, whereas the splitting between the Au $4f_{5/2}$ and $4f_{7/2}$ peaks is 3.7 eV. Both values are consistent with the reported literature for elemental Ag and Au.[49–51] For Ag NPs synthesized using either FA or HA, the Ag $3d_{5/2}$ component is centered at 368.0 eV, whereas the $3d_{3/2}$ component is centered at 374.0 eV; these values are also concordant with an assignment to zero-valent silver.[52,53] For Au NPs synthesized using either FA or HA, the Au $4f_{7/2}$ feature is centered at 83.9 eV, whereas the $4f_{5/2}$ feature is centered at 87.6 eV, which are furthermore concordant with the reported literature for zero-valent Au.[54]

Table 3.2: Atomic concentrations as deduced from integration of characteristic XPS spectral signatures (at the 95% confidence level).

	Ag at.%	**Au at.%**
χ_{Ag} = 0.5, fulvic acid	52±8	48±6
χ_{Ag} = 0.5, humic acid	56±3	44±2
χ_{Ag} = 0.8, fulvic acid	65±3	35±2
χ_{Ag} = 0.8, humic acid	65±5	35±3

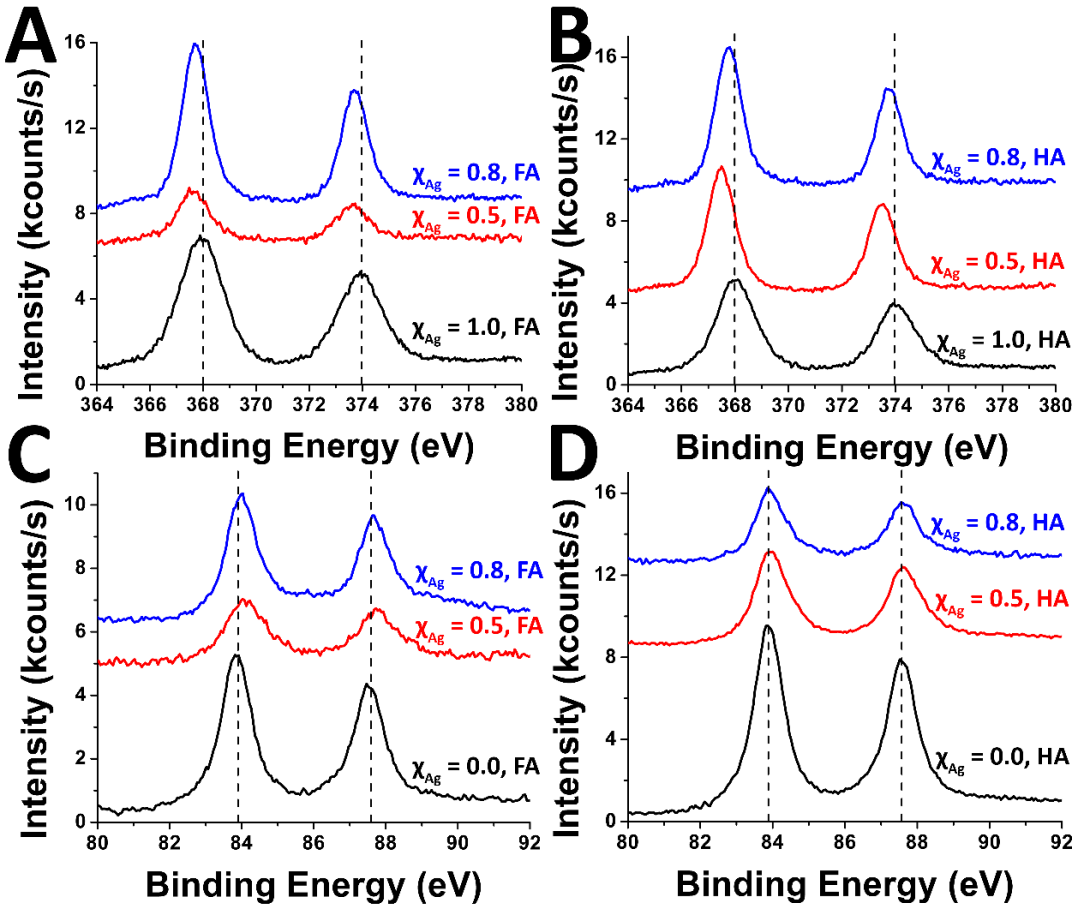

Figure 3.8: (A, B) Ag 3d and (C, D) Au 4f high-resolution XPS spectra of the nanoparticle samples synthesized in FA (A, C) and HA (B, D) solutions. Ag 3d spectra show a shift to lower binding energies for the bimetallic samples (*ca.* 0.3—0.5 eV), indicating charge transfer from Au to Ag. No shift in binding energies is seen for the Au 4f spectra.

Interestingly, when Ag is mixed with Au in bimetallic NP samples, a decrease of the Ag 3d binding energy by *ca.* 0.3—0.5 eV is observed. Conversely, the Au 4f spectra show a modest shift of ca. 0.1 eV to higher energies. The red-shift of the Ag 3d peak and the blue-shift of the Au 4f peak can be attributed to electron transfer from Au to Ag as a result of a charge compensation mechanism that increases the density of 5d holes of Au upon interfacing with Ag.[53] The charge compensation mechanism derives from the differential in the Pauling electronegativities of these two elements (2.54 and 1.93 for Au

and Ag, respectively).[55] Electron injection from Ag into the 5d and 6sp states of Au results in extensive back-donation in order to maintain charge balance. The back-donation of electron density increases the hole density of Au 5d states while further depleting the Au 4f states of electrons.[56] The resulting charge transfer has been observed to inhibit oxidation of surficial Ag-atoms.

In addition to the distinct observation of charge transfer suggestive of interfacing of Ag and Au within the same nanocrystals, minor contributions are observed in Ag 3d spectra at 368.8 eV (Ag $3d_{5/2}$) and 374.8 eV (Ag $3d_{3/2}$) (**Figures 3.9A—B**), which can be attributed to monovalent Ag with an electronic structure analogous to silver carboxylates and provides insight into a possible interfacial interaction between functional groups of the DOM and the surfaces of the NPs.[57,58] Indeed, features at centered *ca.* 288.2 eV and *ca.* 531.6 eV are observed in C 1s and O 1s high-resolution spectra (**Figure 3.10**) of bimetallic samples, both of which are consistent with the presence of metal carboxylates. The observation of monovalent Ag with carboxylate interactions does not rule out interactions with other functional groups on HA and FA such as thiols, which furthermore have a high affinity for binding monovalent Ag species.[59,60]

Considering the Au 4f XPS spectra of bimetallic NPs, distinctive contributions at *ca.* 84.6—84.8 eV and 88.5—88.7 eV can be deconvoluted (**Figures 3.9C—D**), which can be attributed to the Au $4f_{7/2}$ and $4f_{5/2}$ binding energies of a more oxidized Au species. While precise speciation is not possible based on XPS alone, the observed binding energy values are concordant with monovalent Au such as observed for Au(I)-thiolate complexes.[54,61,62] The characteristic spectral signatures of oxidized Ag and Au species

point to the existence of surficial interactions between HA and FA functional groups and the coordinatively unsaturated surfaces of the bimetallic NPs. These functional groups likely complex the metal ions and hold them in close proximity to redox-active (e.g., quinone) sites of FA and HA, which further facilitate their reduction while being concomitantly oxidized in the process. The nucleation of nanocrystalline seeds is subsequently followed by monomer addition with the DOM buffering the extent of local supersaturation of the monomers.[63]

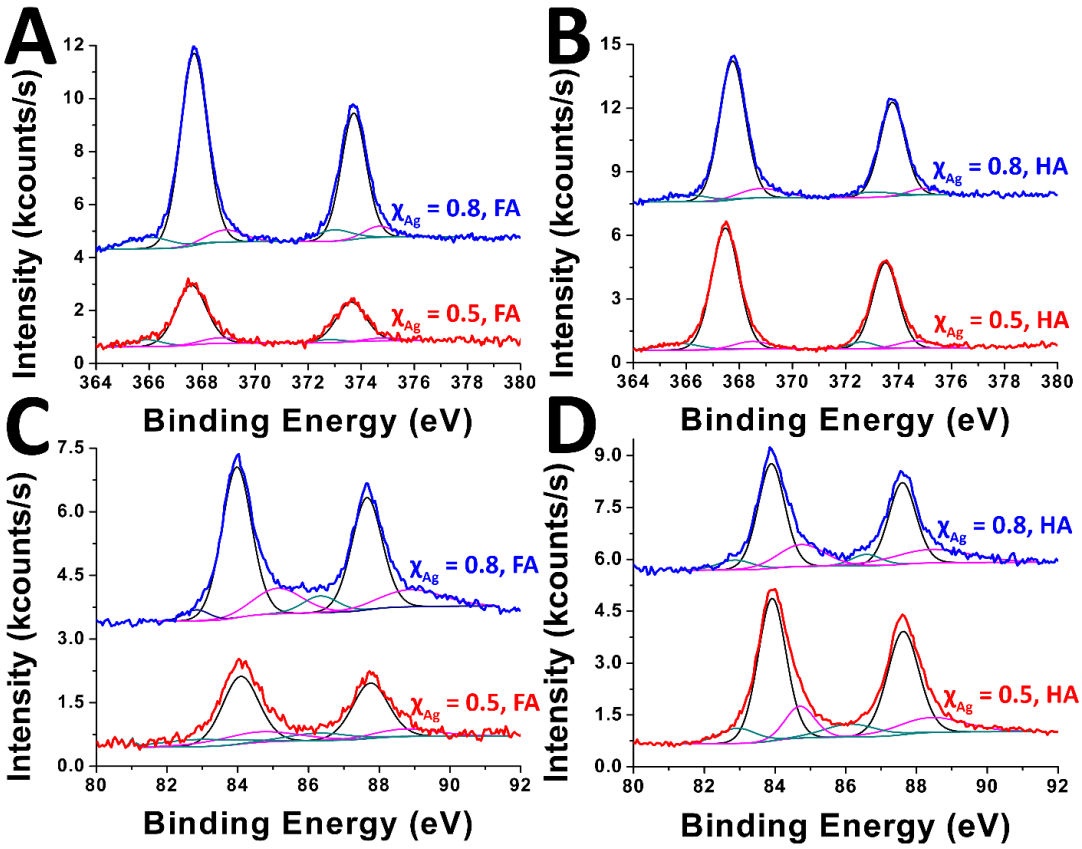

Figure 3.9: Deconvoluted (A, B) Ag 3d and (C, D) Au 4f high-resolution XPS spectra of bimetallic Ag-Au NPs synthesized in (A, C) FA and (B, D) HA solutions.

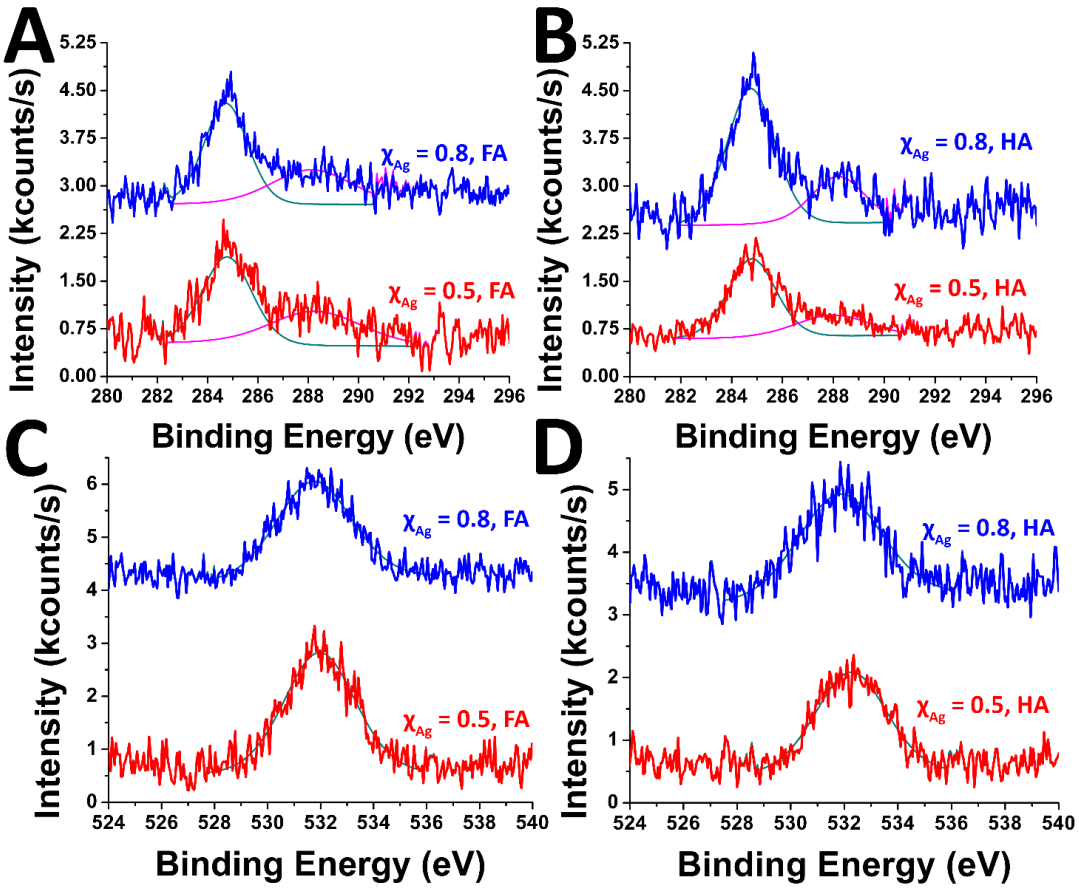

Figure 3.10: (A, B) C 1s and (C, D) O 1s high-resolution XPS spectra of the nanoparticle samples synthesized in FA (A, C) and HA (B, D) solutions.

Figures 3.11A—D show low-magnification TEM images of Ag and Au NPs synthesized using FA and HA as the reducing agents. Individual particles can be distinguished and have morphologies ranging from quasi-spherical to distorted irregular rods. The particles range in size from *ca.* 20 to 30 nm. The contours of individual nanoparticles can readily be distinguished with the exception of some agglomeration observed for the HA-reduced Au NP sample in **Figure 3.11D**. For monometallic nanocrystals, individual particles appear to be stabilized through classical nucleation and

growth schemes mediated by complexation of metal ions to functional groups followed by subsequent reduction and monomer addition. The particles adopt energy minimized Wulff constructions. **Figures 3.11E—F** show low-magnification TEM images of bimetallic Ag-Au NPs (χ_{Ag} = 0.5 and 0.8). The particles are relatively larger as compared to the monometallic NPs with lengths of *ca.* 40 nm and demonstrate both irregular morphologies and extensive agglomeration. The presence of extended defects, discernible as variations in electron density contrast, and branching is evident even at low magnification. Comparing the two reducing agents, bimetallic Ag-Au NPs grown in the presence of HA are observed to be agglomerated to a much greater extent as compared to NPs stabilized by FA. Given the greater abundance of functional groups on HA as compared to FA, the former likely has a larger number of nucleation sites; multiple nucleation events likely yield irregularly shaped aggregates of crystalline domains. The greater abundance of functional groups on HA furthermore translates to increased complexation of cations and a higher local supersaturation, thereby resulting in accelerated kinetics of crystal growth.

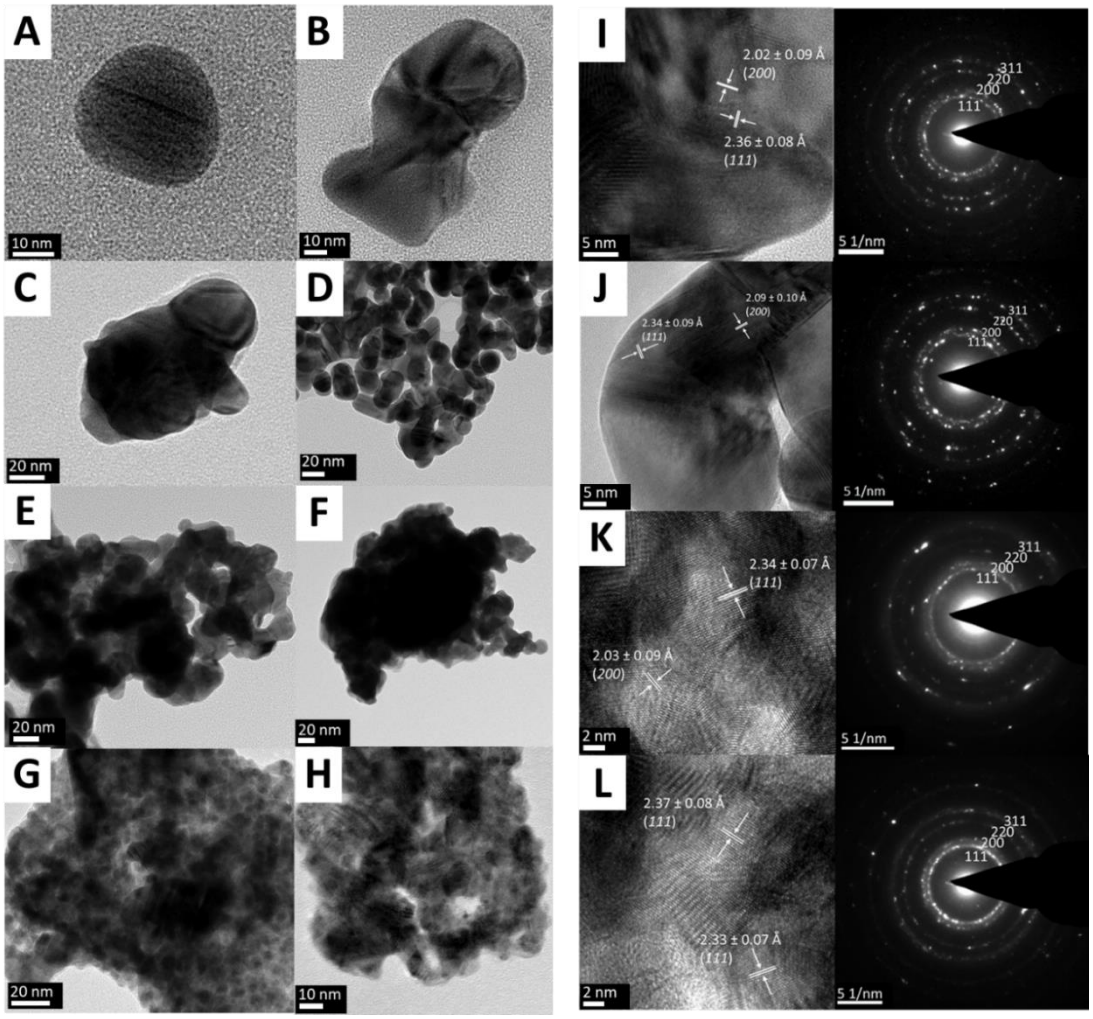

Figure 3.11: Low-magnification TEM image of AgNPs synthesized using (A) FA and (B) HA. Individual particles are easily discernable. Low-magnification TEM image of AuNPs synthesized using (C) FA and (D) HA are also presented. Again, individual particles are prevalent. (E) shows $\chi_{Ag} = 0.5$ bimetallic NPs synthesized in FA and (D) shows an identical reaction using HA in place of FA, both samples form large agglomerations with varying particle shapes and sizes. (G) and (H) show $\chi_{Ag} = 0.8$ bimetallic NPs synthesized using FA and HA respectively. Both show a high degree of branching and highly random particle shapes and sizes. (I) High-resolution TEM image of $\chi_{Ag} = 0.5$ NPs synthesized using FA and their SAED pattern. The diffraction pattern was indexed to the fcc phases of both Ag and Au. Twinning in this sample has become much more pronounced. (J) High-resolution TEM image of $\chi_{Ag} = 0.5$ NPs synthesized using HA and the corresponding SAED pattern. The diffraction pattern was indexed to the fcc phases of both Ag and Au. Pronounced twinning is likewise observed. (K) High-resolution TEM image of $\chi_{Ag} = 0.8$ NPs synthesized using FA and their SAED pattern. The diffraction pattern was indexed to the fcc phases of Ag and Au. Twinning has become highly random and disordered. (L) High-resolution TEM image of $\chi_{Ag} = 0.8$ NPs synthesized using HA and their SAED pattern. The diffraction pattern was indexed to the fcc phases of both Ag and Au. Twinning remains highly random and disordered.

Figure 3.12 shows lattice-resolved HRTEM images and indexed selected area electron diffraction (SAED) patterns of individual Ag and Au NPs prepared using FA and HA as the reducing agents. The SAED patterns can be indexed to the fcc phases of Ag and Au (Joint Committee on Powder Diffraction Standards (JCPDS) 04-0783 and 04-0784, respectively), allowing for unequivocal phase identification. Extended crystalline domains and well-defined lattice spacings are observed for NPs stabilized by both reducing agents. The NPs stabilized using HA show some evidence for stacking faults separating nanocrystalline domains. For instance, **Figure 3.12B** shows pairs of diffraction spots characteristic of twinning;[64] indeed, coherent twin boundaries can be resolved within individual particles. No evidence for crystalline oxides of silver and gold is discernible in lattice-resolved imaging of the NPs (or for that matter from X-ray diffraction measurements).

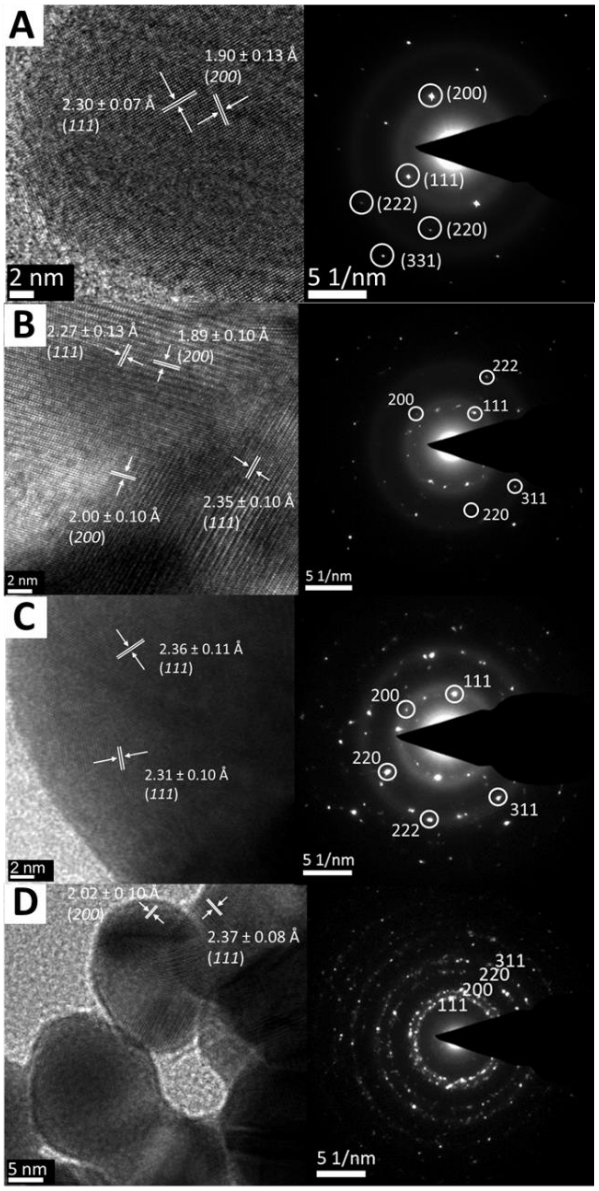

Figure 3.12: (A) High-resolution TEM image of Ag NPs synthesized using FA alongside the corresponding indexed SAED pattern. The diffraction pattern is indexed to the fcc phase of Ag. (B) High-resolution TEM image of Ag NPs synthesized using HA and the corresponding indexed SAED pattern. The image shows evidence of some twinning. The diffraction pattern is indexed to the fcc phase of Ag. (C) High-resolution TEM image of Au NPs synthesized using FA; the indexed SAED pattern acquired for the imaged region is shown in the right panel. The diffraction pattern is indexed to the fcc phase of Au. The presence of rings indicates the stabilization of multiple nanocrystalline domains. (D) High-resolution TEM image of Au NPs synthesized using HA alongside the corresponding indexed SAED pattern. The pattern indexes to the fcc phase of Au with well-defined rings characteristic of multiple nanocrystalline domains.

Figures 3.11I—L shows HRTEM images and SAED patterns of bimetallic Ag-Au NPs prepared using FA and HA as reducing agents. The SAED patterns are indexed to a fcc structure (Ag and Au exhibit comparable values of lattice constants) and the imaged lattice spacings are similarly assigned to interplanar separations in fcc Au and Ag. The NPs show a high density of stacking faults, substantially increased over the monometallic NPs. The manifestation of five-fold twinning has been reported for both Au and Ag NPs.[65,66] Such five-fold twinning is thought to be thermodynamically favorable for noble metal NPs that are less than 20 nm in size given their low stacking fault energies and imposes specific surface energy constraints resulting in the adoption of energy minimized Wulff constructions in multiply twinned particles[67,68] that differ substantially from particles without twin planes. Twinning along the high density (111) plane can serve as a means to compensate for strain energy of defects in five-fold symmetry particles, and imposes specific thermodynamic constraints on the particle morphology for particles with dimensions less than 20 nm.[65] In contrast, multiple twin planes in larger particles tend to reflect kinetic effects during early stages of crystal growth. As a literature precedent, Au colloids grown by slow addition of chloroauric acid to a solution containing poly(diallyl dimethyl ammonium chloride) (PDDA) at a rate of 0.375 mL/min have been reported to crystallize as polycrystalline agglomerates with micron-sized dimensions, whereas addition at a rate of 0.1875 mL/min stabilizes well-defined faceted, triangular and hexagonal platelets.[65] The irregular morphologies, extensive agglomeration, and relatively larger particle dimensions (as compared to monometallic NPs) observed in **Figures 3.11I—L** suggest much accelerated rates of crystal growth and a kinetically controlled

regime for the bimetallic NPs. In this regime, growth occurs from atomically rough surfaces and is diffusion-controlled, reflecting the local supersaturation and thereby yielding rounded and poorly defined facets.[69] Since the overall concentrations of precursor ions and DOM are held constant, the accelerated growth kinetics for the bimetallic particles points to the importance of the galvanic replacement reaction in **Eq. 3.1**, which accelerates the incorporation of zero-valent Au. The defects observed in the TEM images corroborate the manifestation of this diffusion-controlled regime. The stacking faults likely reflect the oriented attachment of multiple nuclei growing rapidly under conditions of high local supersaturation mediated by complexation of precursor cations at the different functional groups of HA and FA.

Figure 3.13 presents a schematic illustration of the DOM-mediated reduction and crystallization of bimetallic Ag-Au NPs. In this picture, Ag^{+} and Au^{3+} are individually reduced to Ag NPs and Au NPs in the presence of either FA or HA (**Figure 3.13A**). The Lewis basic groups of these DOMs (e.g., carbonyls, carboxylates, thiols, etc.) can complex the precursor ions, whereas electro-active species such as quinone moieties bring about reduction through single-electron transfer events. The formation of alloys (**Figure 3.13B**) is initiated by the galvanic reaction between $AuCl_4^{-}$ and Ag^0, as noted by **Eq. 3.1**. The reaction deposits Au^0 atoms and releases Ag^{+} ions back into solution.[44] The Ag-Au alloy is eventually formed (**Figure 3.13B**) given the close proximity of the lattice constants of Ag and Au. This takes place when the deposited Au^0 are interdiffused with Ag^0, which have not participated in the galvanic reaction. The formed alloys are stabilized by electron transfer from Au to Ag.[53–56] On a microscopic level, agglomeration is observed the

greatest for the bimetallic samples, especially for χ_{Ag} = 0.8, synthesized in HA owing to its greater abundance of sites that can complex the precursor ions, allowing for facile nucleation and high local supersaturation.

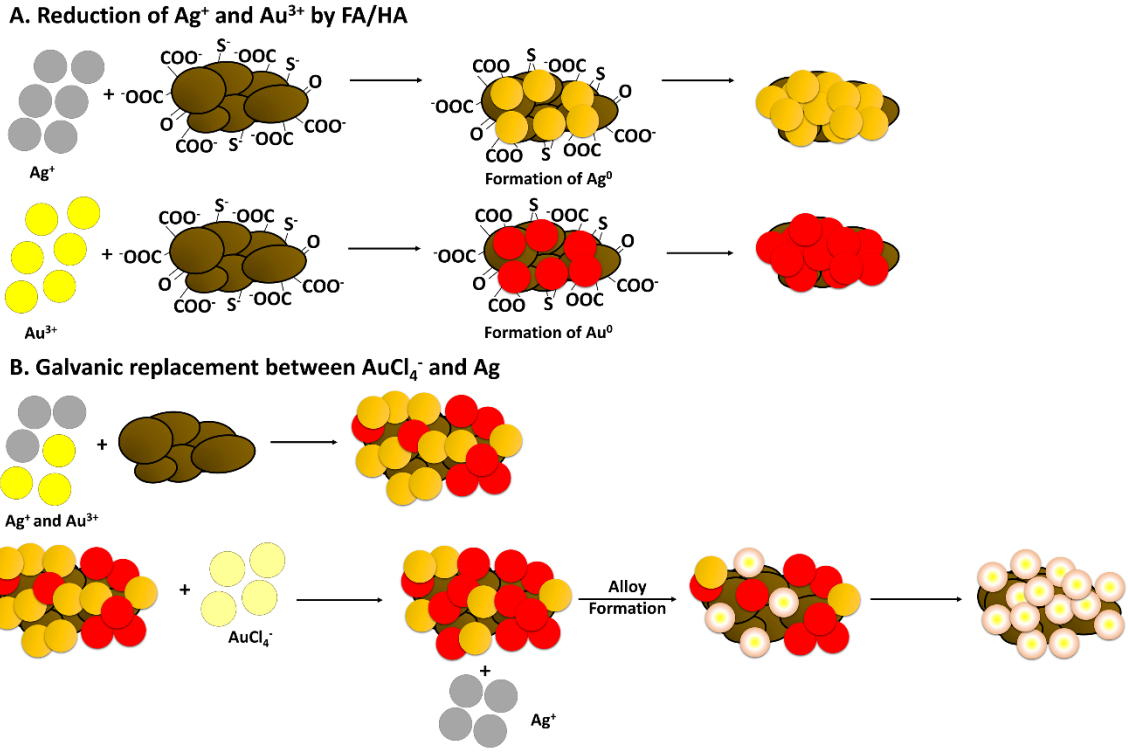

Figure 3.13: Schematic representation of the formation of Ag-Au alloy NPs in the presence of DOMs.

3.5 Conclusions and Environmental Significance

The results presented herein demonstrate the formation of bimetallic Ag-Au alloy NPs when both Ag^+ and Au^{3+} interact with DOM at environmentally relevant pH values. The complexation of the functional groups of DOM with Ag, Au, and bimetallic Ag-Au can promote their mobilization.[70] Given the co-localization of Au and Ag in geological

deposits, high concentrations of Ag^{+}/Au^{3+} and organic matter are expected in mineral processing and mining waste streams and can potentially speciate as Ag-Au bimetallic NPs. The migration, bioavailability, and toxicity of NPs are a function of their stability.[8] SPR spectra have been monitored for four months to evaluate the stability of bimetallic NPs stabilized using HA (by mixing equal molar ratios of Ag^{+} and Au^{3+} ions ($x_{Ag} = 0.5$ and $x_{Au} = 0.5$) at pH 8.0. UV-vis spectra of the NPs (**Figure 3.14**) do not show a diminution of the characteristic SPR absorbance. HA appears to serve as a passivating group and surfactant, thereby stabilizing the bimetallic NPs and preventing further growth. Indeed, a ζ-potential value of -33 mV has been measured, suggesting that the colloidal particles are electrostatically stabilized in aqueous media. The colloidal stability of the bimetallic NPs suggests the potential for long range transport and dispersion of these materials across aquatic environments. Further studies on the toxicity of Ag-Au bimetallic NPs are likewise warranted. A preliminary study conducted on *Daphnia magna* shows that the toxicity of Ag-Au bimetallic NPs is dependent on the elemental composition of the alloy, and is approximately intermediate between effects of monometallic Ag and Au NPs.[71] Other studies have shown that Ag-Au bimetallic NPs show antibacterial properties[72] and deleteriously influence germ cell function and embryo development.[73]

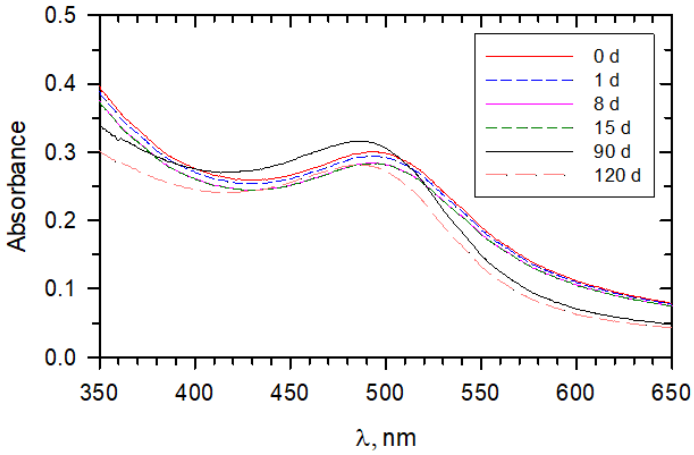

Figure 3.14: Stability of UV-vis absorption spectra of bimetallic Ag-Au alloyed NPs over a period of 120 days (χ_{Ag} = 0.5).

3.6 References

(1) Pourzahedi, L.; Vance, M.; Eckelman, M. J. Life Cycle Assessment and Release Studies for 15 Nanosilver-Enabled Consumer Products: Investigating Hotspots and Patterns of Contribution. *Environ. Sci. Technol.* **2017**, *51*, 7148–7158.

(2) Consumer Products Inventory http://www.nanotechproject.org/cpi/products/ (accessed Sep 1, 2017).

(3) Jia, J.; Li, F.; Zhou, H.; Bai, Y.; Liu, S.; Jiang, Y.; Jiang, G.; Yan, B. Oral Exposure to Silver Nanoparticles or Silver Ions May Aggravate Fatty Liver Disease in Overweight Mice. *Environ. Sci. Technol.* **2017**, *51*, 9334–9343.

(4) Stepka, Z.; Dror, I.; Berkowitz, B. The Effect of Nanoparticles and Humic Acid on Technology Critical Element Concentrations in Aqueous Solutions with Soil and Sand. *Sci. Total Environ.* **2018**, *610–611*, 1083–1091.

(5) Yoo, J.; Lee, E.; Kim, H. Y.; Youn, D. H.; Jung, J.; Kim, H.; Chang, Y.; Lee, W.;

Shin, J.; Baek, S.; Jang, W.; Jun, W.; Kim, S.; Hong, J.; Park, H.-J., Lengner, C. J.; Moh, S. H.; Kwon, Y.; Kim, J. Electromagnetized Gold Nanoparticles Mediate Direct Lineage Reprogramming into Induced Dopamine Neurons in Vivo for Parkinson's Disease Therapy. *Nat. Nanotechnol.* **2017**, *12*, 1006–1014.

(6) Chen, Y.; Xianyu, Y.; Jiang, X. Surface Modification of Gold Nanoparticles with Small Molecules for Biochemical Analysis. *Acc. Chem. Res.* **2017**, *50*, 310–319.

(7) Köser, J.; Engelke, M.; Hoppe, M.; Nogowski, A.; Filser, J.; Thöming, J. Predictability of Silver Nanoparticle Speciation and Toxicity in Ecotoxicological Media. *Environ. Sci. Nano* **2017**, *4*, 1470–1483.

(8) Sharma, V. K.; Filip, J.; Zboril, R.; Varma, R. S. Natural Inorganic Nanoparticles-Formation, Fate, and Toxicity in the Environment. *Chem. Soc. Rev.* **2015**, *44*, 8410–8423.

(9) Yu, S.; Yin, Y.; Zhou, X.; Dong, L.; Liu, J. Transformation Kinetics of Silver Nanoparticles and Silver Ions in Aquatic Environments Revealed by Double Stable Isotope Labeling. *Environ. Sci. Nano* **2016**, *3*, 883–893.

(10) Iswarya, V.; Manivannan, J.; De, A.; Paul, S.; Roy, R.; Johnson, J. B.; Kundu, R.; Chandrasekaran, N.; Mukherjee, A.; Mukherjee, A. Surface Capping and Size-Dependent Toxicity of Gold Nanoparticles on Different Trophic Levels. *Environ. Sci. Pollut. Res.* **2016**, *23*, 4844–4858.

(11) Wagner, S.; Gondikas, A.; Neubauer, E.; Hofmann, T.; Von Der Kammer, F. Spot the Difference: Engineered and Natural Nanoparticles in the Environment-Release, Behavior, and Fate. *Angew. Chemie. Int. Ed.* **2014**, *53*, 12398–12419.

(12) Levard, C.; Mitra, S.; Yang, T.; Jew, A. D.; Badireddy, A. R.; Lowry, G. V.; Brown, G. E. Effect of Chloride on the Dissolution Rate of Silver Nanoparticles and Toxicity to E. Coli. *Environ. Sci. Technol.* **2013**, *47*, 5738–5745.

(13) He, D.; Bligh, M. W.; Waite, T. D. Effects of Aggregate Structure on the Dissolution Kinetics of Citrate-Stabilized Silver Nanoparticles. *Environ. Sci. Technol.* **2013**, *47*, 9148–9156.

(14) Li, L.; Xu, Z.; Wimmer, A.; Tian, Q.; Wang, X. New Insights into the Stability of Silver Sulfide Nanoparticles in Surface Water: Dissolution through Hypochlorite Oxidation. *Environ. Sci. Technol.* **2017**, *51*, 7920–7927.

(15) Thalmann, B.; Voegelin, A.; Von Gunten, U.; Behra, R.; Morgenroth, E.; Kaegi, R. Effect of Ozone Treatment on Nano-Sized Silver Sulfide in Wastewater Effluent. *Environ. Sci. Technol.* **2015**, *49*, 10911–10919.

(16) U. S. Public Health Service. *Toxicological Profile for Silver*; Agency for Toxic Substances and Disease Registry, TP-90–24I, 1990.

(17) Seiler, H. G.; Sigel, H.; Sigel, A. *Handbook on Toxicity of Inorganic Compounds*; Marcel Dekker: New York, NY, 1988.

(18) Purcell, T. W.; Peters, J. J. Sources of Silver in the Environment. *Environ. Toxicol. Chem.* **1998**, *17*, 539–546.

(19) Lepel, E. A.; Pratt, S. L.; Robertson, D. E.; Thomas, C. W.; Haggard, D. L. Radiological Characterization of Spent Control Rod Assemblies. *J. Radioanal. Nucl. Chem.* **1995**, *194*, 81–94.

(20) Scheetz, B. E.; Agrawal, D. K.; Breval, E.; Roy, R. Sodium Zirconium Phosphate

(NZP) as a Host Structure for Nuclear Waste Immobilization: A Review. *Waste Manag.* **1994**, *14*, 489–505.

(21) Yin, Y.; Yu, S.; Liu, J.; Jiang, G. Thermal and Photoinduced Reduction of Ionic Au(III) to Elemental Au Nanoparticles by Dissolved Organic Matter in Water: Possible Source of Naturally Occurring Au Nanoparticles. *Environ. Sci. Technol.* **2014**, *48*, 2671–2679.

(22) Yin, Y.; Liu, J.; Jiang, G. Sunlight-Induced Reduction of Ionic Ag and Au to Metallic Nanoparticles by Dissolved Organic Matter. *ACS Nano* **2012**, *6*, 7910–7919.

(23) Adegboyega, N. F.; Sharma, V. K.; Siskova, K.; Zbořil, R.; Sohn, M.; Schultz, B. J.; Banerjee, S. Interactions of Aqueous Ag^{+} with Fulvic Acids: Mechanisms of Silver Nanoparticle Formation and Investigation of Stability. *Environ. Sci. Technol.* **2013**, *47*, 757–764.

(24) Adegboyega, N. F.; Sharma, V. K.; Cizmas, L.; Sayes, C. M. UV Light Induces Ag Nanoparticle Formation: Roles of Natural Organic Matter, Iron, and Oxygen. *Environ. Chem. Lett.* **2016**, *14*, 353–357.

(25) Prichard, H. M.; Wedin, F.; Sampson, J.; Jackson, M. T.; Fisher, P. C. Precious Metals in Urban Waste. *Water Environ. J.* **2016**, *30*, 151–156.

(26) Yoshikawa, M. Sewage Yields More Gold than Top Mines https://www.reuters.com/article/2009/01/30/us-goldsewage-oddidUSTRE50T56120090130 (accessed Sep 1, 2017).

(27) U. S. Environmental Protection Agency. Ambient Water Quality Criteria for Silver

https://nepis.epa.gov (accessed Jan 1, 2018).

(28) Gulbrandsen, R. A.; Rait, N.; Krier, D. J.; Baedecker, P. A.; Childress, A. Gold, Silver, and Other Resources in the Ash of Incinerated Sewage Sludge at Palo Alto, California − A Preliminary Report. In *Geological Survey Circular*; Department of Interior, 1978; p 784.

(29) Reeves, S. J.; Plimer, I. R.; Foster, D. Exploitation of Gold in a Historic Sewage Sludge Stockpile, Werribee, Australia: Resource Evaluation, Chemical Extraction and Subsequent Utilisation of Sludge. *J. Geochemical Explor.* **1999**, *65*, 141–153.

(30) Howe, P. D.; Dobson, S. *Silver and Silver Compounds: Environmental Aspects*; Concise International Chemical Assessment Document, 2002.

(31) Zaleska-Medynska, A.; Marchelek, M.; Diak, M.; Grabowska, E. Noble Metal-Based Bimetallic Nanoparticles: The Effect of the Structure on the Optical, Catalytic and Photocatalytic Properties. *Adv. Colloid Interface Sci.* **2016**, *229*, 80–107.

(32) Xu, Z.; Liu, Y.; Ren, F.; Yang, F.; Ma, D. Development of Functional Nanostructures and Their Applications in Catalysis and Solar Cells. *Coord. Chem. Rev.* **2016**, *320–321*, 153–180.

(33) Goldfarb, R.; Baker, T.; Dube, B.; Groves, D. I.; Hart, C. J. R.; Gosselin, P. Distribution, Character and Genesis of Gold Deposits in Metamorphic Terranes. In *Distribution, character and genesis of gold deposits in metamorphic terranes, Economic geology 100th Anniversary volume*; Hedenquist, J. W., Thompson, J. F. H., Goldfarb, R. G., Richards, J. P., Eds.; Society of Economic Geologists:

Littleton, CO, 2005; pp 407–450.

(34) Morrison, G. W.; Rose, W. J.; Jaireth, S. Geological and Geochemical Controls on the Silver Content (Fineness) of Gold in Gold-Silver Deposits. *Ore Geol. Rev.* **1991**, *6*, 333–364.

(35) Yin, Z.; Wang, Y.; Song, C.; Zheng, L.; Ma, N.; Liu, X.; Li, S.; Lin, L.; Li, M.; Xu, Y.; Li, W.; Hu, G.; Fang, Z.; Ma, D. Hybrid Au-Ag Nanostructures for Enhanced Plasmon-Driven Catalytic Selective Hydrogenation through Visible Light Irradiation and Surface-Enhanced Raman Scattering. *J. Am. Chem. Soc.* **2018**, *140*, 864–867.

(36) Akaighe, N.; MacCuspie, R. I.; Navarro, D. A.; Aga, D. S.; Banerjee, S.; Sohn, M.; Sharma, V. K. Humic Acid-Induced Silver Nanoparticle Formation under Environmentally Relevant Conditions. *Environ. Sci. Technol.* **2011**, *45*, 3895–3901.

(37) Adegboyega, N. F.; Sharma, V. K.; Siskova, K. M.; Vecerova, R.; Kolar, M.; Zbořil, R.; Gardea-Torresdey, J. L. Enhanced Formation of Silver Nanoparticles in Ag+-NOM-Iron(II, III) Systems and Antibacterial Activity Studies. *Environ. Sci. Technol.* **2014**, *48*, 3228–3235.

(38) Hou, W. C.; Stuart, B.; Howes, R.; Zepp, R. G. Sunlight-Driven Reduction of Silver Ions by Natural Organic Matter: Formation and Transformation of Silver Nanoparticles. *Environ. Sci. Technol.* **2013**, *47*, 7713–7721.

(39) Skogerboe, R. K.; Wilson, S. A. Reduction of Ionic Species by Fulvic Acid. *Anal. Chem.* **1981**, *53*, 228–232.

(40) Shirshova, L. Redox Properties of Humic Acids. *Geochim. Cosmochim. Acta* **1997**, *61*, 4599–4604.

(41) Aeschbacher, M.; Graf, C.; Schwarzenbach, R. P.; Sander, M. Antioxidant Properties of Humic Substances. *Environ. Sci. Technol.* **2012**, *46*, 4916–4925.

(42) Machesky, M. L.; Andrade, W. O.; Rose, A. W. Interactions of Gold (III) Chloride and Elemental Gold with Peat-Derived Humic Substances. *Chem. Geol*. **1992**, *102*, 53–71.

(43) Sun, Y.; Xia, Y. Mechanistic Study on the Replacement Reaction between Silver Nanostructures and Chloroauric Acid in Aqueous Medium. *J. Am. Chem. Soc.* **2004**, *126*, 3892–3901.

(44) Da Silva, A. G. M.; Rodrigues, T. S.; Haigh, S. J.; Camargo, P. H. C. Galvanic Replacement Reaction: Recent Developments for Engineering Metal Nanostructures towards Catalytic Applications. *Chem. Commun.* **2017**, *53*, 7135–7148.

(45) Chen, Z.; Porcher, C.; Campbell, P. G. C.; Fortin, C. Influence of Humic Acid on Algal Uptake and Toxicity of Ionic Silver. *Environ. Sci. Technol.* **2013**, *47*, 8835–8842.

(46) Ratasuk, N.; Nanny, M. A. Characterization and Quantification of Reversible Redox Sites in Humic Substances. *Environ. Sci. Technol.* **2007**, *41*, 7844–7850.

(47) Zhou, S.; Chen, S.; Yuan, Y.; Lu, Q. Influence of Humic Acid Complexation with Metal Ions on Extracellular Electron Transfer Activity. *Sci. Rep.* **2015**, *5*, 1–9.

(48) Gentry, S. T.; Fredericks, S. J.; Krchnavek, R. Controlled Particle Growth of Silver

Sols through the Use of Hydroquinone as a Selective Reducing Agent Controlled Particle Growth of Silver Sols through the Use of Hydroquinone as a Selective Reducing Agent. *Langmuir*. **2009**, *25*, 2613–2621.

(49) Casaletto, M. P.; Longo, A.; Martorana, A.; Prestianni, A.; Venezia, A. M. XPS Study of Supported Gold Catalysts: The Role of Au^0 and $Au^{+\delta}$ Species as Active Sites. *Surf. Interface Anal.* **2006**, *38*, 215–218.

(50) Uznanski, P.; Zakrzewska, J.; Favier, F.; Kazmierski, S.; Bryszewska, E. Synthesis and Characterization of Silver Nanoparticles from (Bis)Alkylamine Silver Carboxylate Precursors. *J. Nanoparticle Res.* **2017**, *19*, 121/1–20.

(51) Moulder, J. F.; Stickle, W. F.; Sobol, P. E.; Bomben, K. D. *Handbook of X-Ray Photoelectron Spectroscopy*; Chastain, J., King, R. C., Jr.: Eden Prairie, MN, 1995.

(52) National Institute of Science and Technology. X-ray Photoelectron Spectroscopy Database Version 3.5 https://srdata.nist.gov/xps/main_search_menu.aspx. (accessed Sep 1, 2017).

(53) Thi Ngoc Anh, D.; Singh, P.; Shankar, C.; Mott, D.; Maenosono, S. Charge-Transfer-Induced Suppression of Galvanic Replacement and Synthesis of (Au@Ag)@Au Double Shell Nanoparticles for Highly Uniform, Robust and Sensitive Bioprobes. *Appl. Phys. Lett.* **2011**, *99*, 4–7.

(54) Alves, L.; Ballesteros, B.; Boronat, M.; Cabrero-Antonino, J. R.; Concepcioén, P.; Corma, A.; Correa-Duarte, M. A.; Mendoza, E. Synthesis and Stabilization of Subnanometric Gold Oxide Nanoparticles on Multiwalled Carbon Nanotubes and Their Catalytic Activity. *J. Am. Chem. Soc.* **2011**, *133*, 10251–10261.

(55) Nishimura, S.; Dao, A. T. N.; Mott, D.; Ebitani, K.; Maenosono, S. X-Ray Absorption Near-Edge Structure and X-Ray Photoelectron Spectroscopy Studies of Interfacial Charge Transfer in Gold–Silver–Gold Double-Shell Nanoparticles. *J. Phys. Chem. C* **2012**, *116*, 4511–4516.

(56) Bzowski, A.; Yiu, Y. M.; Sham, T. K. Charge Redistribution in Au-Metalloid Intermetallics: A Au $L_{2,3}$-Edge X-Ray-Absorption Study. *Phys. Rev. B* **1995**, *51*, 9515−9520.

(57) Dong, T.-Y.; Chen, W.-T.; Wang, C.-W.; Chen, C.-P.; Chen, C.-N.; Lin, M.-C.; Song, J.-M.; Chen, I.-G.; Kao, T.-H. One-Step Synthesis of Uniform Silver Nanoparticles Capped by Saturated Decanoate: Direct Spray Printing Ink to Form Metallic Silver Films. *Phys. Chem. Chem. Phys.* **2009**, *11*, 6269–6275.

(58) Hammond, J. S.; Holubka, J. W.; deVries, J. E.; Dickie, R. A. The Application of X-Ray Photo-Electron Spectroscopy to a Study of Interfacial Composition in Corrosion-Induced Paint de-Adhesion. *Corros. Sci.* **1981**, *21*, 239–253.

(59) Chen, Z.; Campbell, P. G. C.; Fortin, C. Silver Binding by Humic Acid as Determined by Equilibrium Ion-Exchange and Dialysis. *J. Phys. Chem. A* **2012**, *116*, 6532–6539.

(60) Bell, R. A.; Ogden, N.; Kramer, J. R. The Biotic Ligand Model and a Cellular Approach to Class B Metal Aquatic Toxicity. *Comp. Biochem. Physiol. C. Toxicol. Pharmacol.* **2002**, *133*, 175–188.

(61) Pensa, E.; Cortés, E.; Corthey, G.; Carro, P.; Vericat, C.; Fonticelli, M. H.; Benítez, G.; Rubert, A. A.; Salvarezza, R. C. The Chemistry of the Sulfur-Gold Interface: In

Search of a Unified Model. *Acc. Chem. Res.* **2012**, *45*, 1183–1192.

(62) Corthey, G.; Giovanetti, L. J.; Ramallo-López, J. M.; Zelaya, E.; Rubert, A. A.; Benitez, G. A.; Requejo, F. G.; Fonticelli, M. H.; Salvarezza, R. C. Synthesis and Characterization of Gold@gold(I)-Thiomalate Core@shell Nanoparticles. *ACS Nano.* **2010**, *4*, 3413−3421.

(63) Kort, K. R.; Banerjee, S. Ligand-Mediated Control of Dislocation Dynamics and Resulting Particle Morphology of GdOCl Nanocrystals. *Small.* **2015**, *11*, 329–334.

(64) Depner, S. W.; Cultrara, N. D.; Farley, K. E.; Qin, Y.; Banerjee, S. Ferroelastic Domain Organization and Precursor Control of Size in Solution-Grown Hafnium Dioxide Nanorods. *ACS Nano.* **2014**, *8*, 4678–4688.

(65) Elechiguerra, J. L.; Reyes-Gasga, J.; Yacaman, M. J. The Role of Twinning in Shape Evolution of Anisotropic Noble Metal Nanostructures. *J. Mater. Chem.* **2006**, *16*, 3906–3919.

(66) Ino, S.; Ogawa, S. Multiply Twinned Particles at Earlier Stages of Gold Film Formation on Alkalihalide Crystals. *J. Phys. Soc. Japan.* **1967**, *22*, 1365–1374.

(67) Ringe, E.; Van Duyne, R. P.; Marks, L. D. Kinetic and Thermodynamic Modified Wulff Constructions for Twinned Nanoparticles. *J. Phys. Chem. C* **2013**, *117*, 15859–15870.

(68) Marks, L. D. Modified Wulff Constructions for Twinned Particles. *J. Cryst. Growth.* **1983**, *61*, 556–566.

(69) Klapper, H. Generation and Propagation of Defects During Crystal Growth. In *Springer Handbook of Crystal Growth*; Dhanaraj, G., Byrappa, K., Prasad, V.,

Dudley, M., Eds.; Springer: Berlin, Heidelberg, 2010; pp 93–102.

(70) ElBishlawi, H.; Jaffe, P. R. Characterization of Dissolved Organic Matter from a Restored Urban Marsh and Its Role in the Mobilization of Trace Metals. *Chemosphere* **2015**, *127*, 144–151.

(71) Li, T.; Albee, B.; Alemayehu, M.; Diaz, R.; Ingham, L.; Kamal, S.; Rodriguez, M.; Whaley Bishnoi, S. Comparative Toxicity Study of Ag, Au, and Ag-Au Bimetallic Nanoparticles on Daphnia Magna. *Anal. Bioanal. Chem.* **2010**, *398*, 689–700.

(72) Ramakritinan, C. M.; Kaarunya, E.; Shankar, S.; Kumaraguru, A. K. Antibacterial Effects of Ag, Au and Bimetallic (Ag-Au) Nanoparticles Synthesized from Red Algae. *Solid State Phenom.* **2013**, *201*, 211–230.

(73) Taylor, U.; Tiedemann, D.; Rehbock, C.; Kues, W. A.; Barcikowski, S.; Rath, D. Influence of Gold, Silver and Gold-Silver Alloy Nanoparticles on Germ Cell Function and Embryo Development. *Beilstein J. Nanotechnol.* **2015**, *6*, 651–664.

CHAPTER IV

ROLE OF NATURAL SUNLIGHT IN ACCELERATING THE DISSOLVED ORGANIC MATTER-MEDIATED FORMATION OF Ag-Au BIMETALLIC ALLOY NANOPARTICLES IN AQUATIC ENVIRONMENTS

4.1 Summary

The underpinning mechanism of the sunlight-accelerated growth of Ag, Au, and Ag-Au bimetallic alloy nanoparticles (NPs) in the presence of dissolved organic matter (DOMs) has been investigated. Under natural sunlight, two possible mechanisms have been considered to facilitate the growth of Ag and Au nanocrystals: a) reduction of dissolved Ag- and Au-ions *via* plasmon-generated electrons on the surfaces of incipient Ag and Au nuclei or b) photooxidation of phenol and hydroquinone groups in DOMs followed by the reduction of dissolved oxygen into superoxide radicals, which then serve as reducing agents for Ag- and Au-ions. It is noted that natural sunlight accelerates the formation of Ag NPs and Ag-Au bimetallic alloy NPs *via* the plasmon-induced pathway, with relatively minimal contribution of superoxide anion radicals (Ag^{+} and Au^{3+} are co-reduced upon the formation of Ag and Au nuclei). In contrast, no discernible difference is observed between Au NPs grown with or without illumination from sunlight. Transmission electron microscopy (TEM) reveals that Ag and Ag-Au bimetallic alloy NPs grown under photoillumination show a greater degree of polydispersity and polycrystallinity as compared to their dark counterparts, whereas for Au NPs no clear distinctions are discernible for nanocrystals grown in the presence and absence of sunlight. Regardless of

whether the Ag-Au bimetallic alloy NPs were grown in the presence of natural sunlight or not, X-ray photoelectron spectroscopy (XPS) measurements showed that both samples are stabilized by Au→Ag charge-transfer. Elucidating the mechanism of Ag-Au bimetallic alloy NPs in relevant environmental conditions is key to understanding their fate, transport, and toxicity in aquatic environments.

4.2 Introduction

Over the past few decades, considerable research has focused on the syntheses of silver (Ag NPs) and gold nanoparticles (Au NPs), leading to the discovery of several applications. For example, Ag NPs, have been shown to have antimicrobial properties and are embedded in socks and other pieces of clothing.[1,2] Ag NPs have also been used as natural colorimetric and on-site detectors for pollutants, such as sulfurazon-ethyl herbicide.[3] Similarly, Au NPs have also been used for the colorimetric detection of organophosphate pesticides, such as chlorpyrifos, fenamiphos, and phosalone in aquatic systems.[4] The plasmonic properties of Au NPs also introduce attractive applications in biosensing and catalysis,[5,6] to name a few examples. The widespread use of Ag NPs, Au NPs, and other nanomaterials in consumer products, agriculture, and medicine has also raised serious concerns pertaining to their potential toxicity, given their high surface-area-to-volume ratio. While information on the toxicological properties of bulk materials is thoroughly documented, there is a significant gap in knowledge on how the toxicity of nanomaterials differs from their bulk counterparts.[7,8]

The prevalent use of Ag and Au NPs, among other precious metal nanoparticles, has led to their unintentional release into the environment. Ag and Au NPs have been detected in aquatic systems (due to the lack of disposal regulations of consumer products containing these NPs), prompting concerns on their potential toxicity to humans and other biota.[2,9] Similarly, metallic nanoparticles are released as industrial effluents from various metal processing plants. In 2009, Au concentrations as high as 1,890,000 μg/mL were detected in sludge from the Suwa Manufacturing Facility in Japan.[10,11] The U.S. Environmental Protection Agency (EPA) reports an average of 43,000 μg/mL Ag in hot springs across the United States.[12] Research has shown that Ag and Au NPs post a threat to the ecosystem[13–15] which cannot be ignored. Among the most vulnerable are biota in aquatic systems near processing plants. Various studies have identified that the toxicity of metal nanocrystals is a function of both the size and the capping ligand used in synthesis.[7,16]

Ag- and Au-ions released as part of effluent streams can be reduced into their zerovalent species in aquatic systems under relevant conditions. Various natural parameters, such as pH, ionic strength, and dissolved oxygen, play an important role in the reductive formation and long-range transport of these metallic NPs.[17,18] The surficial properties of nanoparticles (most importantly, size) also play a role in their mobility and toxicity.[17] In general, the underlying mechanism involves dissolved organic matter (DOM) such as fulvic (FA) and humic acids (HA) behaving as reducing agents. DOMs are traditionally described as bioorganic particulate macromolecules which pass through a 0.45-μm filter.[19] DOMs are composed of polysaccharides, proteins, carbohydrates, amino

acids,[17,20,21] and other by-products of the biological decay of dead animals and plants.[3] While their exact molecular structure/chemical composition is complex,[22] it is known that FA is water-soluble at all pH values whereas HA is only water-soluble at high pH values. HA is also known to have a higher molar mass than FA, meaning more functional groups decorate the former as compared to the latter. Functional groups in FA and HA include carboxylic acids, phenols, and thiols, among many others. In previous work, we have noted that the reduction of Ag^{+} and Au^{3+} is initiated by complexation of the ions with Lewis basic groups in FA and HA such as thiols, carbonyls, and carboxyls. Reduction subsequently follows *via* single-electron transfer reactions from redox-active quinone, hydroquinone, and semiquinone groups in FA and HA. These DOMs also serve as surface-capping ligands for Ag and Au NPs, imparting colloidal stability to the nanocrystals.[23] In another study, our group postulated that FA and HA reduce Ag^{+} clusters adsorbed onto colloidal Ag_2O.[24] Another proposed DOM-mediated mechanism takes into consideration the contribution of natural sunlight in the mineralization of Ag NPs. This sunlight-mediated pathway involves the photoactivation of phenolic and hydroquinone groups in FA and HA, followed subsequently by release of an electron to reduce dissolved O_2 in water to form superoxide anion radicals:

$$HA\ (aq.) + O_2\ (aq.) + h\upsilon \rightarrow HA^{+}\ (aq.) + O_2^{\bullet -}\ (aq.) \qquad \textbf{Eq. 4.1}$$

These superoxide anion radicals then reduce Ag^{+} into Ag^{0}, as per:[25]

$$Ag^{+}\ (aq.) + O_2^{\bullet -}\ (aq.) \rightarrow Ag\ (s) + O_2\ (aq.) \qquad \textbf{Eq. 4.2}$$

All mechanisms published in literature report a higher production of Ag NPs in mildly alkaline pH.[17] In contrast, in mildly acidic pH, Ag (and Au) NPs are converted into their ionic forms by oxidants such as O_2,[17] O_3,[26] and Cl_2 in aquatic media.

In facilities where multiple precious metals and metal ions are heavily used, the probability of releasing various elements in water streams is high. In **Chapter III,** we reported the DOM-mediated formation of Ag-Au bimetallic alloy NPs from of Ag^+ and Au^{3+}.[23] These alloys are formed by galvanic replacement and are stabilized by a charge-compensation mechanism. The process involves an initial injection of electrons from Ag to the 5d and 6sp states of Au, which subsequently results in an extensive charge back-donation from Au to Ag.[27–29] We note preferential incorporation of Au over Ag given that the former has a more positive redox potential over the latter (E^0, (Au^{3+}) = 1.50 V *vs.* SHE, $E^0(Ag^+)$ = 0.80 V *vs.* SHE).[23] Ag-Au bimetallic alloy NPs themselves have been extensively studied in the hopes of utilizing the synergy of properties between Ag and Au. Applications on biosensing and catalysis have also been identified for Ag-Au alloys, given the tunability of plasmonic properties by adjusting the elemental composition of the mixture.[30,31] However, there is also growing concern on the toxicity of Ag-Au bimetallic alloy NPs. For instance, a previous study on *Daphnia magna* has noted that the toxicity of Ag-Au bimetallic alloy NPs is a function of their elemental composition, greater toxicity is observed with more Ag incorporated in the alloys.[32]

While in our previous study we tried to mimic environmentally-relevant conditions,[23] our NPs were grown in the absence of natural sunlight. As mentioned previously, Jiang and co-workers observed that Ag NPs can be reduced in a two-step

mechanism involving the photooxidation of DOMs.[25] Another mechanism to be considered is a plasmon-induced route. The plasmon-mediated synthesis of metallic nanoparticles was a result of a serendipitous study.[33,34] In general, when light is irradiated on a metal, a plasmon is created, generating energetic charge-carriers on the metal surface.[35–37] In the presence of hole acceptors, such as trisodium citrate dihydrate, the photogenerated hole oxidizes the hole acceptor, leaving behind a negative charge on the metal surface. This in turn reduces metal ions in solution, resulting in the nucleation and growth of NPs. The size as well as the morphology of the NPs can also be controlled in this photoreductive process.[33,38] The morphology and size of NPs are dependent on the concentration of hole-acceptors in the solution.[35,39] It can thus be imagined that these hole-acceptors serve as passivating ligands to the growth of these NPs. Given that FA and HA both serve as reducing agents and capping-ligands in the formation of individual Ag and Au NPs, it is possible that exposure to sunlight will also lead to the formation of NPs, following either the photoactivation of DOMs route, the plasmon-initiated pathway, or some combination of both routes. The generalizability of these mechanisms to the stabilization of Ag-Au bimetallic alloys remain entirely unexplored.

In this work, we have sought to understand the mechanism of DOM-mediated Ag-Au bimetallic alloy NP stabilization under natural sunlight in aqueous media. The presence of a single surface plasmon resonance (SPR) band in UV-vis spectra denotes the formation of Ag-Au bimetallic alloy NPs under various conditions simulating the environment. The plasmon-mediated reduction of Ag- and Au-ions appears to be the dominant mechanism following the initial formation of Ag and/or Au seeds, which can

form from superoxide anion radicals in solution. A more pronounced increase in yield is observed for Ag and Ag-Au bimetallic alloy NPs, whereas for Au NPs, no increase in yield was observed upon exposure to natural sunlight. All DOM-reduced NPs grown under photoillumination are noted to have a higher Ag:Au ratio as compared to the precursor concentrations, which is deduced from UV-vis and X-ray photoelectron (XPS) spectra, indicating that natural sunlight accelerates the single-electron reduction of Ag^{+}. Transmission electron microscopy (TEM) results indicate a more defined morphology of samples grown under photoillumination as compared to samples similarly treated in the dark, especially for Ag and Ag-Au bimetallic alloy NPs. XPS illustrates that surficial complexation with carboxylic acid and thiol groups and Au→Ag charge-transfer are observed for all samples grown under photoillumination, similar to what we have previously[23] reported. Understanding the mechanism underpinning the formation of these NPs in the presence of DOMs and natural sunlight is also imperative for determination of the ecotoxicity of these nanomaterials.

4.3 Methods

4.3.1 Chemicals

$AgNO_3$ (>99.0%), $AuCl_3$ (>99.9%), and superoxide dismutase (SOD, 75,000 units) from bovine erythrocytes were obtained from Sigma-Aldrich (St. Louis, MO) and were used as received. Suwannee River humic acid (HA) and Suwannee River fulvic acid (FA) were purchased from the International Humic Substances Society (IHSS, St. Paul, MN). Deionized (DI) water used to prepare all aqueous solutions was distilled and passed

through a Milli-Q water purification system (conductivity ≈ 18 MΩ/cm). All pieces of glassware were immersed in a 10% aqueous solution of HNO_3 for at least 24 h. Stock solutions of HA and FA solutions (25 mg/L) were stirred for 24 h by dissolution of solid HA and FA in a 1.0×10^{-3} M 2-2-(*N*-morpholino)-ethanesulfonic acid (MES) buffer (Sigma-Aldrich, St. Louis, MO)—undissolved solids were removed using 0.45 μm filters.[24] The pH of the resulting solutions were measured using an Orion pH/ISEmeter (model 710A, Thermo Fisher Scientific, Waltham, MA) and adjusted with aqueous 0.1 M NaOH.

4.3.2 Growth and Stabilization of NPs under Sunlight

Aqueous solutions of 0.2 mM Ag^+ and Au^{3+} were prepared by dissolving their respective solid precursors in DI water. Reaction solutions were prepared by mixing Ag- and Au-ions to a total mixture of 10.0 mL with 10.0 mL DOM (HA or FA) at varying pH values (6.0, 7.0, 8.0, and 9.0) in 40 mL screw cap Tuf-Bond Teflon-fitted glass vials (Fisher Scientific, Hampton, NH). Reaction solutions of varying molar ratios (χ_{Ag} = 0.0, 0.2, 0.5, 0.8, and 1.0) of Ag- and Au-ions (the total concentration was maintained at 1.0×10^{-4} M) were prepared while keeping the concentration of DOM (HA or FA) constant at 12.5 mg/L. Corresponding control experiments were done as follows:

a) **dark** reaction mixtures covered with Al foil and a black polyethylene plastic bag;
b) **no DOM** mixtures exposed to natural sunlight; and
c) **dark**, **no DOM** mixture covered with Al foil and a black polyethylene plastic bag.

The solutions were subsequently exposed under natural sunlight for *ca.* 15 h at total intensity of 2.5×10^4 kJ/m^3 (measured by a Solar Light light meter (PMA 2100, Solarlight, Glenside, PA). A DR-5000 UV−visible spectrophotometer (Hach Company, Loveland, CO) was used to verify and quantify the formation of Ag, Au and Ag-Au bimetallic alloy NPs. The quartz cuvettes have an optical path length of 1 cm.

4.3.3 Superoxide Anion Radical-Quenching Experiments

A stock solution of 1,500 units/mL SOD was prepared with DI water. The pH of the stock solution was adjusted to 8.0. Various 0.2 mM Ag^+ and Au^{3+} solutions were also prepared and adjusted to a pH of 8.0. $AgNO_3$ and $AuCl_3$ solutions at a concentration of 0.2 mM were prepared as follows: a measured amount of individual ion solutions was mixed in 40 mL screw cap Tuf-Bond Teflon-fitted glass vials at a total volume of 5.0 mL, while keeping [HA] = 12.5 mg/L and $[Ag^+] + [Au^{3+}] = 0.1$ mM. Concentrations at 10, 20, 50, 100, 200, and 400 units/mL SOD were added to the solutions accordingly. Molar ratios of $\chi_{Ag} = 0.0$, 0.2, 0.5, 0.8, and 1.0 were prepared. Reactions under natural sunlight were then conducted for *ca.* 12 h at a total sunlight intensity of 2×10^4 kJ/m^3.

4.3.4 Surface Analyses of Samples

Mixtures of Ag- and Au-ions with a total volume of 250.0 mL at target molar ratios of χ_{Ag} = 0.0, 0.2, 0.5, 0.8, and 1.0 were added to 250.0 mL of aqueous 25 mg/L HA solution in a 500 mL amorphous glass conical beaker (Pyrex, Greencastle, PA). All final solutions were adjusted to a pH of 8.0 before exposure to natural sunlight. Total sunlight intensity was

maintained at 1.0×10^5 kJ/m^3. All mixtures were exposed to sunlight for a total of 60 h. Dark control solutions were also prepared in the same manner, but the reaction vessels were covered in Al foil and a black polyethylene bag. After the NPs were generated, the solutions were transferred into Falcon™ 15 mL conical centrifuge tubes (polypropylene, Fisher Scientific, Hampton, NH) and were subsequently centrifuged at 8,000 rotations/min for 30 min using an Avanti J-E centrifuge (Beckman Coulter, Inc., Palo Alto, CA). The supernatant from each solution was decanted from the precipitate, which was then triple-washed with methanol (HPLC grade, ≥99.9%, Fisher Scientific, Hampton, NH) in order to remove unreacted reagents. Prior to analyses by XPS and TEM, the samples were freeze-dried for 48 h using a Labconco Freezone 12 Freeze-Dry System (Labconco Corp., Kansas City, MO).

Morphologies of Ag, Au, and Ag-Au bimetallic alloy NPs were determined using an FEI Tecnai G2 F20 ST field-emission TEM. Samples were dispersed in 2-propanol (Fisher, Fair Lawn, NJ) after which, a small volume was drop-cast onto 400-mesh holey-carbon films supported by Cu grids (Electron Microscopy Sciences, Hatfield, PA). Prior to analyses, all TEM grids were air-dried at room temperature. All TEM micrographs were obtained at an operating voltage of 200 kV.

XPS measurements were performed to assess the surficial interactions of the monometallic and bimetallic NPs.[23] All analyses were conducted with an Omicron XPS/UPS system with a 128-channel micro-channelplate Argus detector (instrument spectral resolution was *ca.* 0.8 eV). Mg Kα X-rays were used as the photon source (1253.6 eV). A CN10 electron flood source was used to for charge neutralization of the samples.

All high-resolution spectra were collected at a pass energy of 20 eV and an energy step size of 0.05 eV (using constant analyzer energy (CAE) mode). All XPS spectra were calibrated against the C 1s line of adventitious carbon at 284.8 eV. The CasaXPS 2.3.16 software was used to determine the relative atomic concentrations of Ag and Au in the bimetallic samples; this was accomplished by fitting the high-resolution spectra to 70% Gausian:30% Lorentzian product lineshapes and using a Marquart—Levenberg optimization algorithm.

4.3.5 Ar-Purged Control Experiments

Samples of χ_{Ag} = 0.0 and 1.0 were prepared at a pH of 8 with HA as the reducing agent were exposed to white light from a commercial digital single lens reflex (DSLR) camera light-emitting diode (LED) lamp (ProLED Video W300, color temperature = 6000 K) for 24 h with and without Ar purging. The purged samples were prepared using the same procedure previously mentioned, after which Ar (>99.9%, Praxair, Bryan, TX) was bubbled into the solution for *ca.* 10 min. The vials were quickly capped afterwards. Experiments without Ar purge were also performed. UV-vis spectra of all samples were collected afterwards.

4.4 Results and Discussion

In our previous work, we elucidated the DOM-mediated mechanism underpinning the formation of Ag, Au, and Ag-Au bimetallic alloy NPs in aqueous media.[23] The formation of Ag-Au bimetallic alloy NPs was observed both in the case of HA and FA as reducing

agents. The yield of Ag-Au bimetallic alloy NPs was noted to be a function of solution pH for FA but not for HA. The higher molar mass per oligomeric unit of HA provides an abundance of functional groups, which enables buffering of proton concentration in solution. For FA, a higher yield of NPs is generally observed at alkaline pH values. These DOM species both serve as reducing agents and surface-capping ligands in the growth of the monometallic and bimetallic NPs. Ag- and Au-ions are thought to be initially complexed by Lewis basic groups (carbonyl, carboxyl, thiols, *etc.*) in either HA or FA. These ions are subsequently reduced into their zerovalent forms by single-electron transfer reactions from quinone, hydroquinone, and semiquinone groups in the DOMs[40,41] (the initial complexation step holds Ag- and Au-ions in close proximity to these redox-active groups). The Ag-Au bimetallic alloy NPs are subsequently formed by galvanic replacement: Ag^0 on the surface of HA or FA react with $AuCl_4^-$ in solution, depositing more Au^0 on the DOM and releasing Ag^+ back into solution as per:[42,43]

$$Ag\ (s) + AuCl_4^-\ (aq.) \rightarrow 3Ag^+\ (aq.) + Au\ (s) + 4Cl^-\ (aq.) + Au\ (E^0 = 0.19\ V) \qquad \textbf{Eq. 4.3}$$

Ag^0 which has not participated in the galvanic replacement is then alloyed with the newly-precipitated Au^0 with subsequent interdiffusion stabilizing alloy particles.[23] The formation of Ag-Au bimetallic alloy NPs is promoted by the close similarity of the crystal structures of Ag and Au, which both have a preference for face-centered cubic (fcc) polymorphs with similar values of lattice constants (a_{Ag} = 4.086Å and a_{Au} = 4.079Å).

This entire process is herein referred to in this report as mechanism ***a***.

Monometallic and bimetallic NPs synthesized with HA showed greater agglomeration in comparison to FA-grown NPs owing to the greater abundance of

functional groups of HA over FA, which provide a higher density of complexation and nucleation sites enabling the growth of Ag, Au, and Ag-Au bimetallic alloy NPs. In either case, the Ag-Au bimetallic alloy NPs are stabilized by Au→Ag charge-transfer, which is a result of extensive back-donation of electrons from Au to Ag in order to maintain charge balance.[29]

Guided by knowledge acquired from our previous work, in this chapter we have sought to understand the role of sunlight in accelerating the DOM-mediated formation of Ag-Au bimetallic alloy NPs. It is hypothesized that natural sunlight can alter the reaction mechanism through the following pathways:

b) promote the photoactivation of phenol and hydroquinone groups in DOMs,[25] or

c) give rise to a surface plasmon band for incipient Ag and Au nuclei in solution.[44]

Mechanism ***b*** involves the reduction of dissolved oxygen by photooxidized phenol and hydroquinone groups to generate superoxide anion radicals in solution which are then oxidized back to O_2 upon reduction of Ag- and Au-ions as per **Eq. 4.1** and **4.2**. Mechanism ***c*** involves the formation of surface plasmons on the surface of Ag and/or Au seeds, followed by the reduction of more Ag^+ and/or Au^{3+} in solution. It is noteworthy to point out, however, that there has been considerable debate regarding the influence of $O_2^{\bullet-}$ in the reduction of metal ions in aqueous media. Recent studies such as those performed by Zepp and coworkers[45] and by Adegboyega *et al.*[46] note that $O_2^{\bullet-}$ derived from dissolved O_2 in aqueous solution does not promote the reduction of Ag NPs. In fact, Adegboyega *et al.* note an increased yield in Ag NP after purging the aqueous solutions in nitrogen compared to unpurged solutions.[46] Similarly, Wiesner and coworkers suggest that Ag-ions

are initially reduced by $O_2^{\bullet-}$ (formed from dissolved O_2 in the presence of DOMs and/or extracellular polymeric substances (EPS)) into Ag^0 nuclei, which subsequently aggregate and grow through Ostwald ripening.[47] The authors note that plasmon-activated Ag NPs covered by DOMs behave as heterogeneous nucleation sites for the further reduction of Ag^+ bound on the surface of Ag NPs.[47,48]

Figure 4.1 shows UV-visible spectra of χ_{Ag} = 0.0, 0.2, 0.5, 0.8, and 1.0 samples reduced with HA in aqueous solution at an external temperature of 31—35°C at various pH values with and without exposure to natural sunlight. As expected, no NPs were grown in the absence of HA, at any χ_{Ag} value and pH, whether or not the samples were exposed to sunlight. In the presence of HA, NP growth was observed in the presence and absence of natural sunlight at all χ_{Ag} values. For mixtures with χ_{Ag} = 0.2, 0.5, 0.8, a single SPR feature was observed, which denotes alloy formation. These results are in good agreement with our previous study in which we deduce the formation of Ag-Au bimetallic alloy NPs in the presence of either HA or FA.[23] For both monometallic and bimetallic NPs synthesized in the dark, there is no apparent trend between absorbance intensity and pH, consistent with our previous findings that HA is not a limiting reagent in the reduction of Ag- and Au-ions. On the other hand, NPs grown under exposure to sunlight do not seem to show any drastic changes in absorbance intensity with increasing pH at any molar ratio except at χ_{Ag} = 1.0, where Ag NP formation is the highest at pH 7.0 and 8.0.

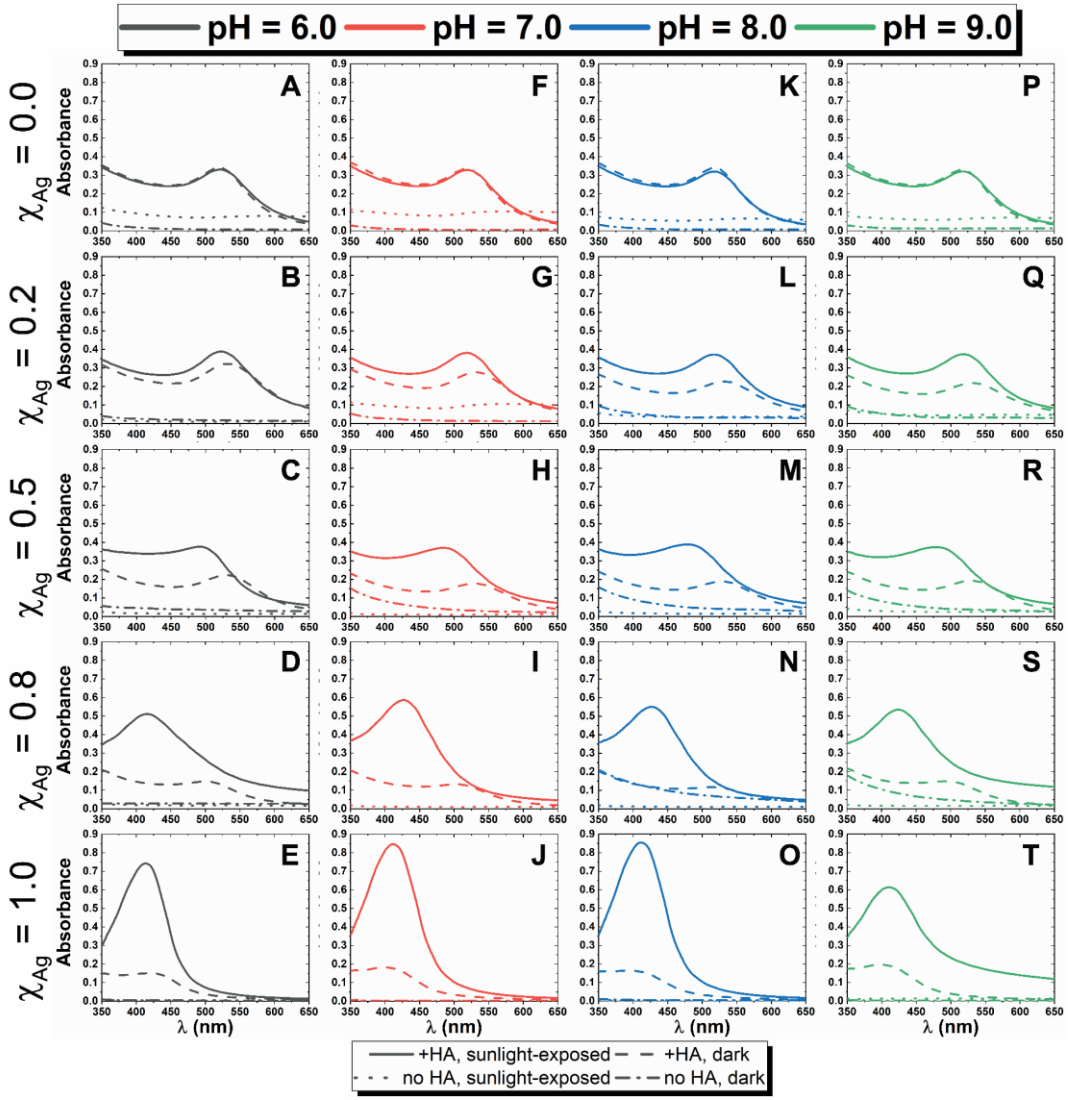

Figure 4.1: UV-vis spectra of χ_{Ag} = 0.0, 0.2, 0.5, 0.8, and 1.0 samples acquired with HA, at pH = 6.0, 7.0, 8.0, and 9.0 after *ca.* 15 h. Solid lines denote experiments performed under natural sunlight with HA, dashed lines denote experiments performed in the dark with HA, dotted lines experiments performed under sunlight but without HA, and dotted-dashed lines denote experiments performed in the dark but without HA.

Interestingly, in the presence of natural sunlight, a dramatic increase in Ag SPR intensity is observed for χ_{Ag} = 1.0, whereas no change in SPR intensity is observed for χ_{Ag} = 0.0. This seems to suggest that the HA-mediated generation of Au NPs is not affected

by additional exposure to natural sunlight—the same amount of Au NPs is produced with and without the presence of sunlight. Clearly, photoreduction by $O_2^{\bullet -}$ therefore does not contribute to a greater yield of Au NPs. Since there was no change in absorbance intensity between Au NP grown under photoillumination and in the dark, it appears the predominant mechanism for Au NP formation is the reduction of Au-ions by redox-active quinone, hydroquinone, and semiquinone groups of HA, as we previously reported.[23] Given the highly positive redox potential of Au^{3+} (1.50 V *vs.* SHE), it is not surprising that the formation of Au NPs is favorable with HA as reducing agent, whether the reaction is exposed to sunlight or not.

On the other hand, natural sunlight appears to accelerate the formation of Ag NPs, as seen by the remarkable increase in SPR intensity from samples grown in the dark to samples exposed under natural sunlight, denoting a dramatic increase in the yield of Ag NPs. The samples grown in the dark also show a broad SPR band, whereas the Ag NPs grown under photoillumination have sharper features at all pH values. Indeed, this suggests a more uniform size distribution for Ag NPs grown under photoillumination over their dark counterparts. The polydispersity in the dark-grown samples can be attributed to Ag NPs in solution being nucleated and grown at different rates because of the abundance of functional groups in HA.

For χ_{Ag} = 0.2, 0.5, and 0.8 NPs, both sunlight- and dark-grown samples show a single SPR band which is indicative of alloy formation. For Ag-Au bimetallic alloy NPs synthesized in the absence of natural sunlight, the SPR absorbance is weighted toward the SPR of Au. These observations are likewise consistent with our previous findings that

there is a preferential incorporation of Au over Ag for Ag-Au bimetallic alloy NPs grown with DOMs in the absence of natural sunlight (and at *ca.* 90°C), given that the reduction of Au^{3+} into Au^0 is thermodynamically more favorable than the reduction of Ag^+ into Ag^0 (E^0, (Au^{3+}) = 1.50 V *vs.* SHE, $E^0(Ag^+)$ = 0.80 V *vs.* SHE).[23].[23] For NPs grown under natural sunlight, there is a noticeable blueshift in the SPR bands with increasing χ_{Ag}. This shift to lower λ_{max} values does not seem to be affected by pH. This is indicative of the preferential incorporation of Ag over Au for the alloys grown under photoillumination. Natural sunlight seems to play a role in accelerating the single-electron reduction of Ag^+ into Ag^0 (whereas three electrons are needed for the reduction of Au^{3+} into Au^0), despite the fact that Au^{3+} has a higher reduction potential than Ag^+. Aside from the shift to lower λ_{max} values, an increase in absorbance intensity is also observed upon exposure to sunlight for the alloyed NPs. The increase in intensity is more apparent for χ_{Ag} = 0.8, which were prepared at higher Ag^+ concentrations. This is indicative of a greater yield of NPs upon exposure to sunlight, with a particular preference for the reduction of Ag-ions.

Figure 4.2 shows plots of λ_{max} as a function of χ_{Ag} for NPs grown with HA in the dark (**Figure 4.2A**) and exposed under natural sunlight (**Figure 4.2B**). In agreement with our previous findings, when HA is used as the reducing agent in the dark, pH does not affect the relative position of λ_{max} at for most χ_{Ag} (χ_{Ag} = 0.8 and 1.0 samples grown in the dark show some pH dependence). The same is true for HA-grown NPs grown under sunlight as well. The shift towards the SPR of Ag is clearly evident for χ_{Ag} = 0.5 and 0.8 in **Figure 4.2B**.

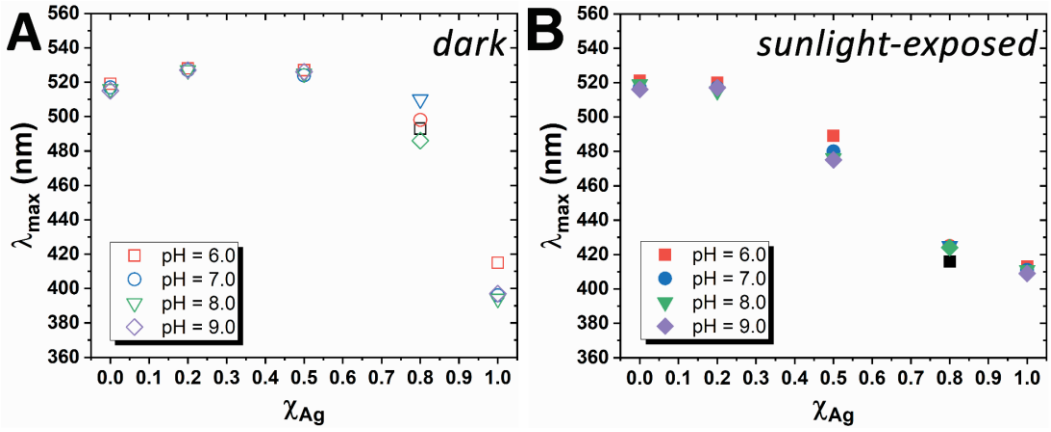

Figure 4.2: Plasmon maximum (λ_{max}) plotted as a function of χ_{Ag} for HA-grown (A) dark and (B) sunlight-exposed nanocrystals.

Figure 4.3 shows UV-vis spectra of sunlight-exposed NPs grown with either HA or FA. All UV-vis spectra of bimetallic samples showed a single SPR band, indicative of Ag-Au bimetallic alloy NP formation. In our past work we derived a pH dependence for the yield of FA-reduced nanocrystals.[23] On the other hand, the NP yield was observed to have no correlation with reaction pH when HA is used as the reducing agent, given that HA has more functional groups, and therefore, a higher electron-donating capacity (EDC) *versus* FA (3684±66 mmol of electrons per gram *versus* HA 2848±85 mmol electrons per gram FA[49]).[23,49] This pH trend was not observed for sunlight-exposed FA-grown NPs. Aside from a few samples (χ_{Ag} = 1.0 at pH of 8 and 9; χ_{Ag} = 0.8 at pH of 9), there was no difference in absorbance intensity between HA and FA, suggestive of independence to solution pH when either DOM is used as a reducing agent in reactions conducted under photoillumination. In mechanism ***c***, HA and FA can behave as hole scavengers upon the reduction of Ag^{+} and Au^{3+} by plasmon-generated electrons.[50] In mechanism ***b***, HA and FA donate an electron to dissolved O_2 in solution.[25] Under alkaline conditions, HA and

FA exist predominantly in their reduced form.[23] Negatively-charged quinone moieties (Q) such as menaquinone, duroquinone, 2,5-dimethyl-*p*-benzoquinone, and *p*-benzoquinone have been reported to have positive reduction potentials when they react with molecular oxygen to produce superoxide anion radicals as defined by the reaction:[51]

$$Q^{-}\,(aq.) + O_2\,(aq.) \rightleftharpoons O_2^{\bullet -}\,(aq.) + Q\,(aq.) \qquad \textbf{Eq. 4.4}$$

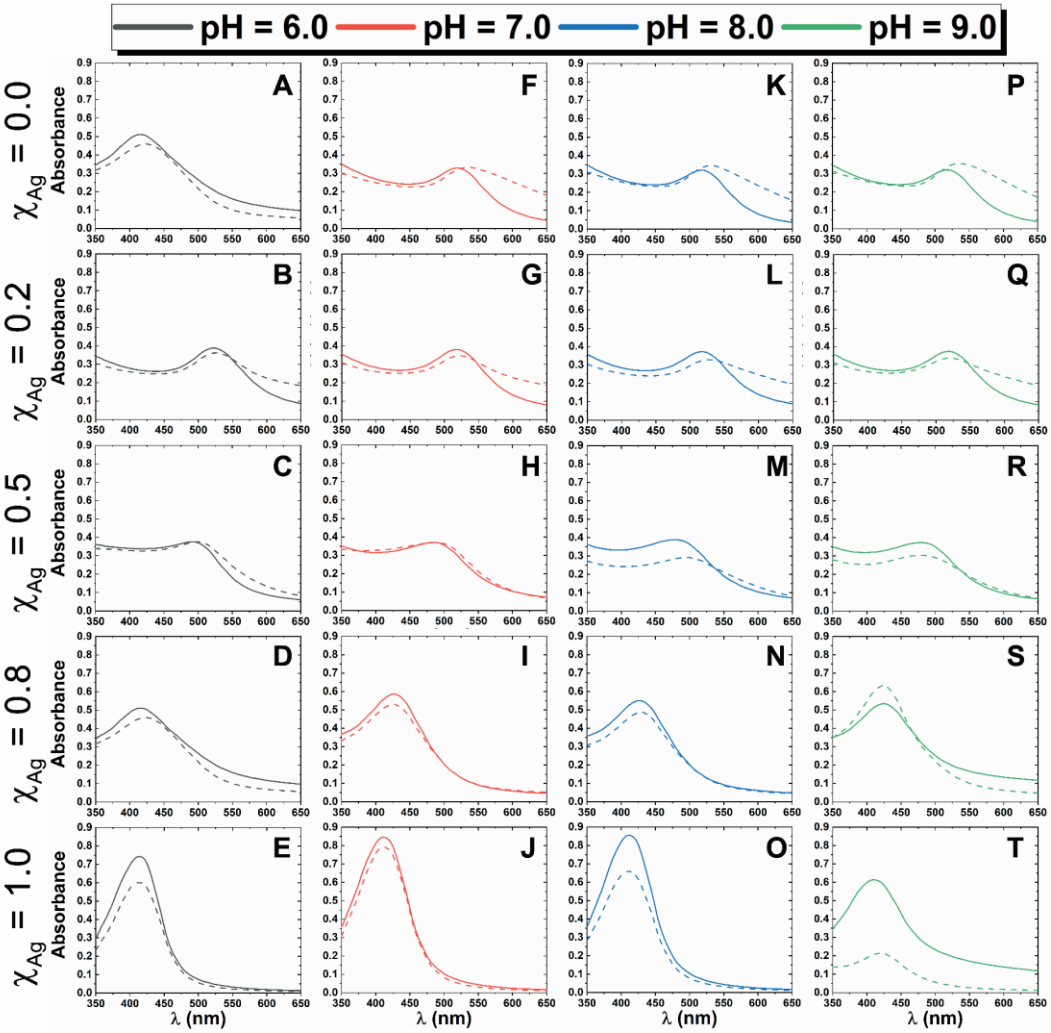

Figure 4.3: UV-vis spectra of sunlight-exposed χ_{Ag} = 0.0, 0.2, 0.5, 0.8, and 1.0 samples acquired with HA and FA, at pH = 6.0, 7.0, 8.0, and 9.0 after *ca.* 15 h. Solid lines denote experiments performed with HA, dashed lines denote experiments performed with FA.

Figure 4.4 shows plots of λ_{max} as a function of χ_{Ag} for NPs grown with FA and under natural sunlight. Similar to sunlight-exposed samples grown with HA (**Figure 4.2A**), most samples do not show a clear pH dependence (χ_{Ag} = 0.5 shows some pH dependence). A shift towards the SPR of Ag is also evident for χ_{Ag} = 0.5 and 0.8, also suggestive of Ag incorporation in Ag-Au bimetallic alloy NPs.

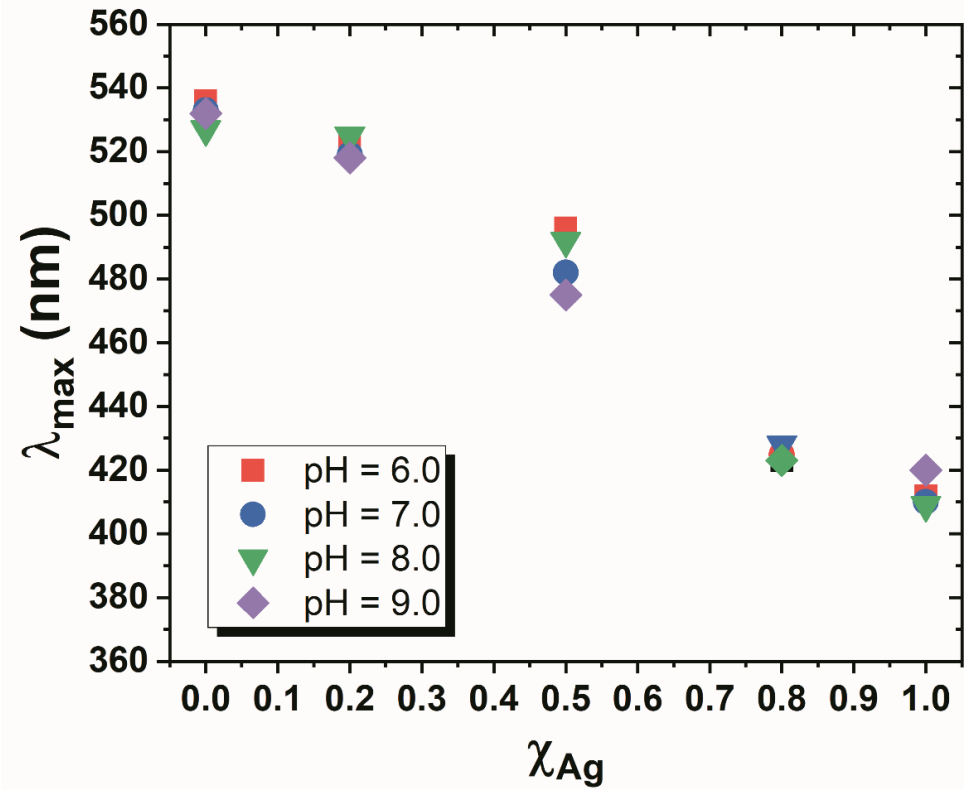

Figure 4.4: Plasmon maximum (λ_{max}) plotted as a function of χ_{Ag} for FA-grown nanocrystals exposed under natural sunlight.

Figures 4.54A, **B**, **C**, and **E** show low-magnification TEM micrographs of individual Au NPs and Ag NPs grown under sunlight (**Figures 4.5A** and **C**) and in the

dark (**Figures 4.54B** and **D**). No obvious differences in morphology and size distribution were observed for Au NPs. Both sunlight-exposed (**Figure 4.54A**) and dark-grown (**Figure 4.54B**) Au NPs show irregularly-shaped nanocrystals with approximate dimensions of 13±2 nm for sunlight-exposed samples and 19±2 nm for samples grown in the dark. These similarities in morphology and size distribution is consistent with UV-vis spectra for Au NPs, which show identical spectral signatures for both sunlight- and dark-grown samples. For Ag, NPs grown in the presence of sunlight (44±16 nm, **Figure 4.5C**) are observed to be relatively monodisperse, whereas those grown in the dark (34±26 nm, **Figure 4.5D**) are more polydisperse. The observed increase in SPR intensity for Ag NPs (**Figure 4.1A**, **E**, **I**, and **M**) can therefore point to individual nucleation events happening in the presence of sunlight as a result of either mechanism ***b***, ***c***, or both. In the dark, the Ag NPs are grown by mechanism ***a*** as we have previously discussed.[23] **Figures 4.54E** and **F** show low-magnification TEM micrographs of χ_{Ag} = 0.8 NPs grown in the presence (20±15 nm) and absence (8±3 nm) of natural sunlight, respectively. The same polydispersity observed for dark-grown Ag NPs is observed for the dark alloy sample, whereas the sunlight-exposed samples more monodisperse.

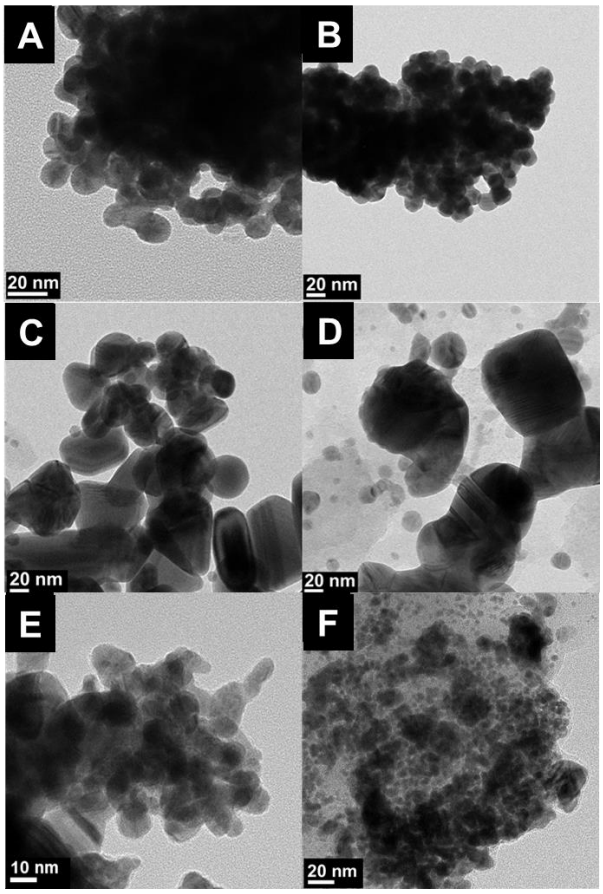

Figure 4.5: Low-magnification TEM images of (A) χ_{Ag} = 0.0 NPs grown in the presence of sunlight and HA and (B) χ_{Ag} = 0.0 NPs grown in the absence of sunlight with HA present. These nanoparticles appear to be relatively unaffected across the two trials with consistent morphology and show a high degree of monodispersity. (C) χ_{Ag} = 1.0 NPs grown in sunlight and HA and (D) χ_{Ag} = 1.0 NPs grown in the absence of sunlight with HA present. The trend of polydispersity and irregular morphology in NPs grown in dark conditions persists in the χ_{Ag} = 1.0 NPs. (E) χ_{Ag} = 0.8 bimetallic NPs grown in sunlight and HA and (F) χ_{Ag} = 0.8 bimetallic NPs grown in the absence of sunlight with HA present. Nanoparticles grown in dark conditions are more polydisperse with inconsistent morphology.

Figures 4.6A, **B**, **C**, and **D** show high-resolution TEM micrographs and SAED patterns of individual Ag NPs and Au NPs grown under sunlight (**Figure 4.6A**, **C**) and in the dark (**Figures 4.6B** and **D**). The nanocrystals can be indexed to the fcc phases of Ag and Au (JCPDS 04-0783 and 04-0784, respectively.) The existence of crystalline oxides

was not noted in any of the samples. Au NPs do not show any difference in crystallinity whether the reaction is exposed to sunlight (**Figure 4.6A**) or not (**Figure 4.6B**). For both χ_{Ag} = 1.0 and 0.8, the SAED patterns of both sunlight-exposed (**Figures 4.6C** and **E**) and dark (**Figures 4.6D** and **F**) samples show a high degree of polycrystallinity.

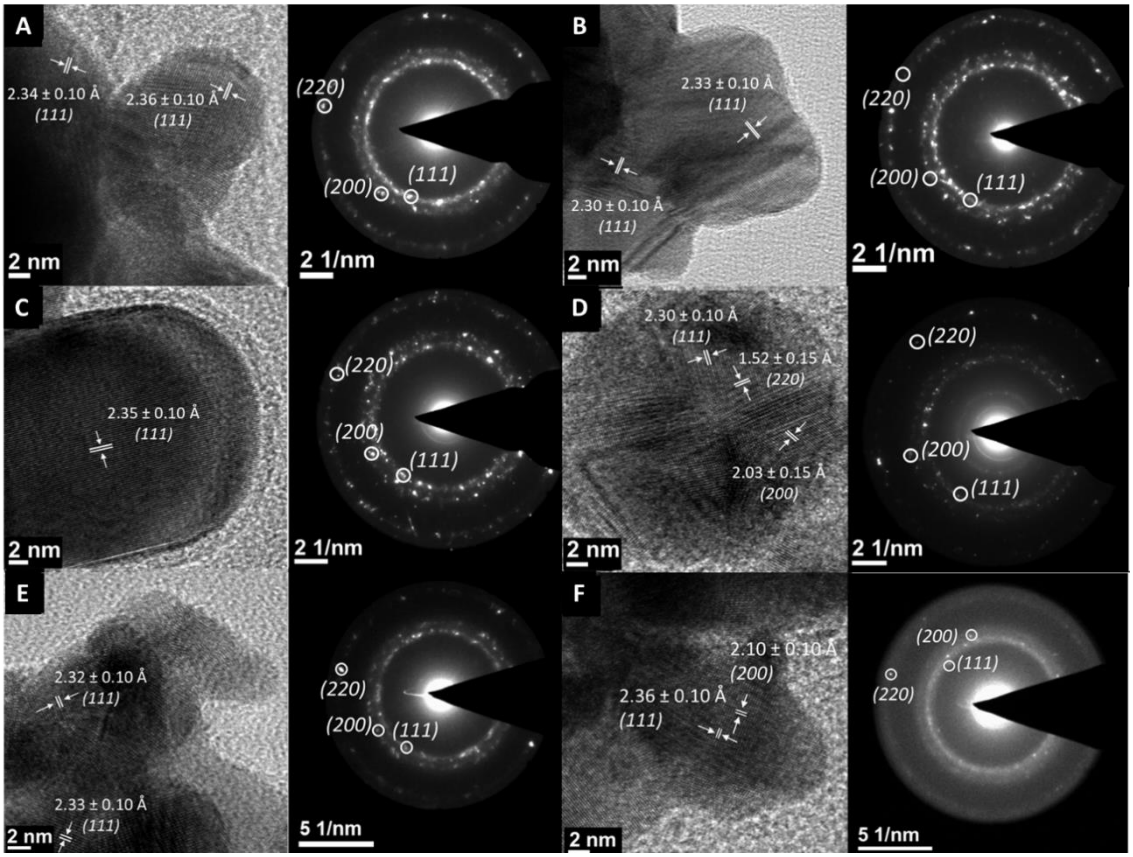

Figure 4.6: High-resolution TEM images and the corresponding SAED of (A) χ_{Ag} = 0.0 NPs grown in the presence of sunlight and HA and (B) χ_{Ag} = 0.0 NPs grown in the absence of sunlight with HA present. High-resolution images and SAED patterns show little to no change between the NPs grown in sunlight and those grown in the absence of sunlight with the SAED displaying the expected fcc Au pattern. (C) χ_{Ag} = 1.0 NPs grown in sunlight and HA and (D) χ_{Ag} = 1.0 NPs grown in the absence of sunlight with HA present. High-resolution images show a higher degree of polycrystallinity. SAED patterns remain consistent with fcc Ag phases. (E) χ_{Ag} = 0.8 bimetallic NPs grown in sunlight and HA and (F) χ_{Ag} = 0.8 bimetallic NPs grown in the absence of sunlight with HA present. The indexed pattern is consistent with that of fcc Ag and Au phases. The SAED pattern is rather diffuse in the NPs grown in dark conditions indicating a high degree of polycrystallinity.

The incorporation of Ag over Au is confirmed by XPS. **Table 4.1** shows the relative elemental composition of sunlight- and dark-grown samples at pH of 8 in the presence of HA. All bimetallic alloy NPs show an increased Ag at.% upon exposure to natural sunlight, which is in good agreement with the observed blueshift in λ_{max} in UV-vis absorbance spectra. **Figure 4.7** shows high-resolution Ag 3d and Au 4f XPS spectra of sunlight- and dark-grown NPs in HA. A spin-orbit splitting value of 6.0 eV is observed for all Ag 3d high-resolution scans, whereas a spin-orbit splitting of 3.7 eV is observed for all Au 4f spectra, both of which are consistent with assignments reported in literature for zerovalent Ag and Au.[52–54] For χ_{Ag} = 1.0 (*i.e.*, monometallic Ag) synthesized in either the presence or absence of sunlight, the Ag $3d_{5/2}$ feature is centered at 368.3 eV, whereas the $3d_{3/2}$ feature is centered at 374.3 eV, which is also consistent with Ag^0 reported in literature.[27,55]

Table 4.1: Ag and Au atomic concentration (at 95% confidence level) in Ag-Au bimetallic alloy NP samples derived by integrating high-resolution Ag 3d and Au 4f XPS spectra.

		Ag at.%	**Au at.%**
Sunlight-exposed, humic acid	**χ_{Ag} = 0.2**	33±2	67±1
	χ_{Ag} = 0.5	63±4	37±2
	χ_{Ag} = 0.8	79±2	21±1
Dark, humic acid	**χ_{Ag} = 0.2**	27±2	73±2
	χ_{Ag} = 0.5	53±2	47±1
	χ_{Ag} = 0.8	63±3	37±2

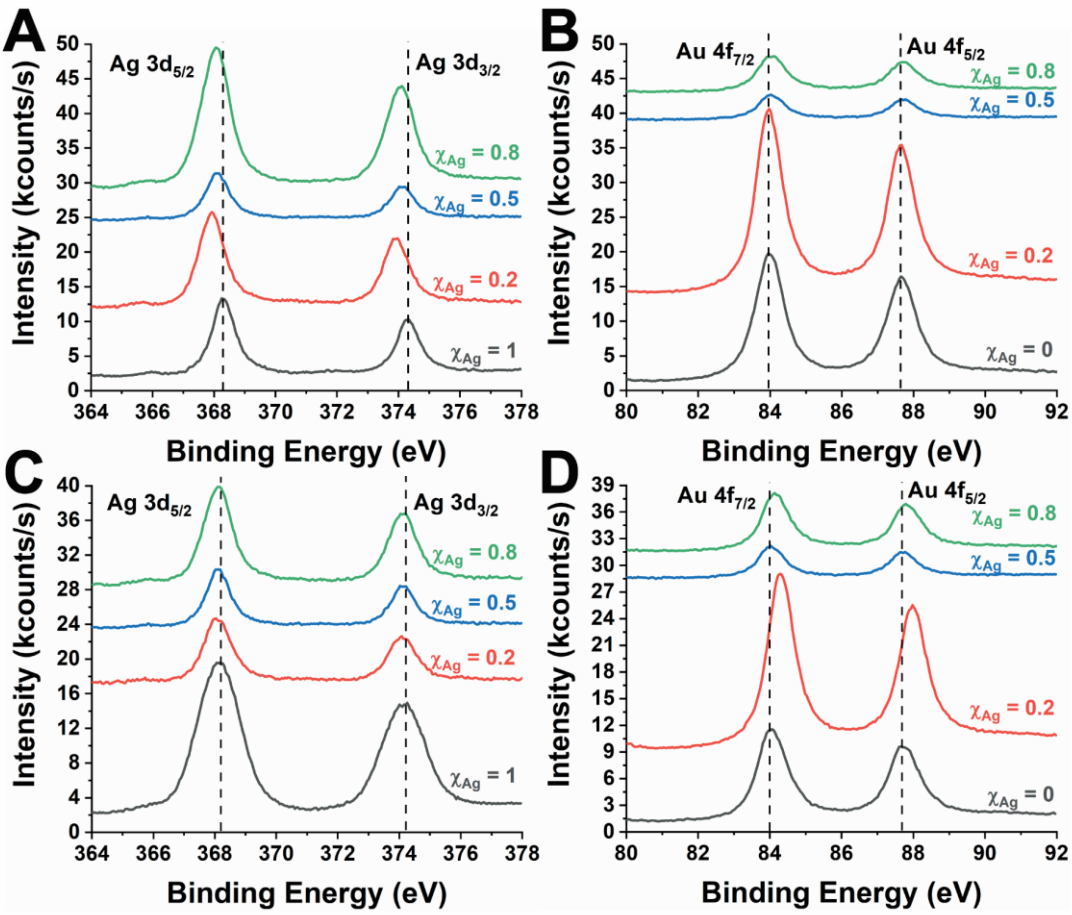

Figure 4.7: Ag 3d (A, C) and Au 4f (B, D) high-resolution spectra of samples ran under sunlight (A, B) and in the dark (C, D), reduced with HA at pH of 8. Au→Ag back-charge transfer is observed for alloyed samples, as denoted by the redshift of Ag 3d features and the blueshift of Au 4f features.

For both sunlight- and dark-grown χ_{Ag} = 0.0 (*i.e.*, monometallic Au), the peak centered at 84.0 eV can be assigned to the Au $4f_{7/2}$, whereas for the peak centered at 87.7 eV can be assigned to the $4f_{5/2}$ feature, which is also in good agreement with reported literature for Au^0.[55,56] In another study with Au NPs, Jiang's group suggested that alcohol, phenol, and aldehyde groups of HA participate in single-electron transfer reactions with Au^{3+}. This was observed for the various species of Au (oxidation states of +1 and +3 were

observed on solid samples aside from the usual zerovalent metal) observed in Au 4f high-resolution XPS, with Au^{3+} being the second most dominant species, next to Au^0.[57] In stark contrast, we note that Au^0 is the predominant species in the $\chi_{Ag} = 0.0$ samples examined in this work.

Figures 4.7C and **D** show high-resolution Ag 3d and Au 4f spectra, respectively, of monometallic and bimetallic NP samples reduced with HA at a pH of 8 without sunlight exposure. Consistent with our previous findings, a back charge-transfer from Au to Ag as a result of charge compensation is observed with $\chi_{Ag} = 0.2$, 0.5, and 0.8, as denoted by a redshift *ca.* 0.3—0.5 eV in Ag 3d spectra with respect to zerovalent Ag ($\chi_{Ag} = 1.0$) and a blueshift of *ca.* 0.1—0.3 eV in Au 4f spectra with respect to zerovalent Au ($\chi_{Ag} = 0.0$). Au is more electronegative than Ag (Pauling electronegativities of 2.54 and 1.93 for Au and Ag, respectively[28]) and this results in the redistribution of electrons from Ag 5d to Au 6sp states. In order to maintain charge balance, electrons from Au 5d and 4f are excessively back donated into Ag.[27–29] This series of electron donations reflects the observed decrease and increase in binding energies in the Ag 3d and Au 4f high-resolution spectra, respectively. **Figures 4.7A** and **B** show high-resolution Ag 3d and Au 4f spectra, respectively, of monometallic and bimetallic NPs reduced with HA at a pH of 8 grown under photoillumination. The same charge-transfer events are noticeable in the high-resolution spectra of the Ag-Au bimetallic alloy NPs, denoting that these alloyed nanocrystals are stabilized by a Au→Ag charge transfer as well. This back-charge transfer mechanism is thought to impede the oxidation of surficial Ag.[23]

Figure 4.8 shows fitted Ag 3d and Au 4f high-resolution spectra of all monometallic and bimetallic NPs. The same surficial interactions we have previously reported were observed, such as the formation of Ag(I)-carboxylates/thiolates[58–60] at 368.7—369.5 eV ($Ag3d_{5/2}$) and 374.7—375.5 eV ($Ag3d_{3/2}$) and the formation of Au(I) thiolates[56,61,62] at 85.0—85.3 eV ($Au4f_{7/2}$) and 88.7—89.0 eV ($Au4f_{5/2}$) eV, and were evident in both sunlight- and dark-grown samples, indicative of the presence of surficial interactions between HA and the metallic nanocrystals. The formation of these complexed species was also observed in C1s and O1s high-resolution spectra[23] (**Figure 4.9**). The existence of metal oxides in all samples was also ruled out by a single O 1s feature in all samples which can all be assigned to the formation of metallic carboxylates and thiolates.[23] The observance of these features not only supports mechanism ***a*** (especially for the samples prepared in the dark), but it also further underlines the role of HA (and likely, FA) as a surfactant and as a surface-capping ligand in the DOM-mediated reduction of Ag, Au, and Ag-Au bimetallic alloy NPs. Similar to samples grown in the dark, HA (and FA) also provides a surface passivating layer to stabilize sunlight-exposed Ag, Au, and Ag-Au bimetallic alloy NPs in aqueous solution. We have previously observed that the Ag-Au bimetallic alloy NPs are stable for at least 120 days, as observed in the negligible diminution of SPR absorbance.[23] The formation of metal complexes also suggests that acceleration of mechanism ***a*** cannot be ruled out upon exposure of the reaction to natural sunlight.

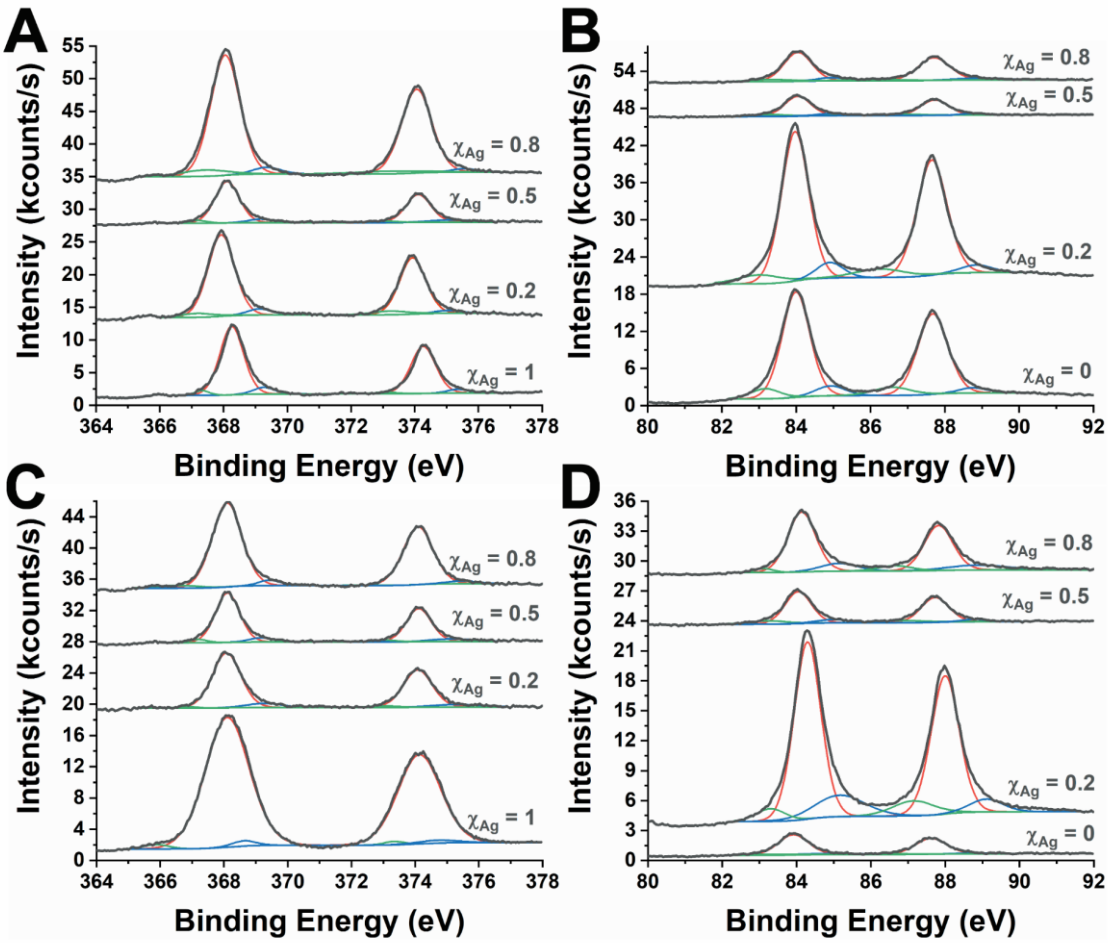

Figure 4.8: Fitted Ag 3d (A, C) and Au 4f (B, D) high-resolution spectra of samples ran under sunlight (A, B) and in the dark (C, D) reduced with HA at pH of 8.

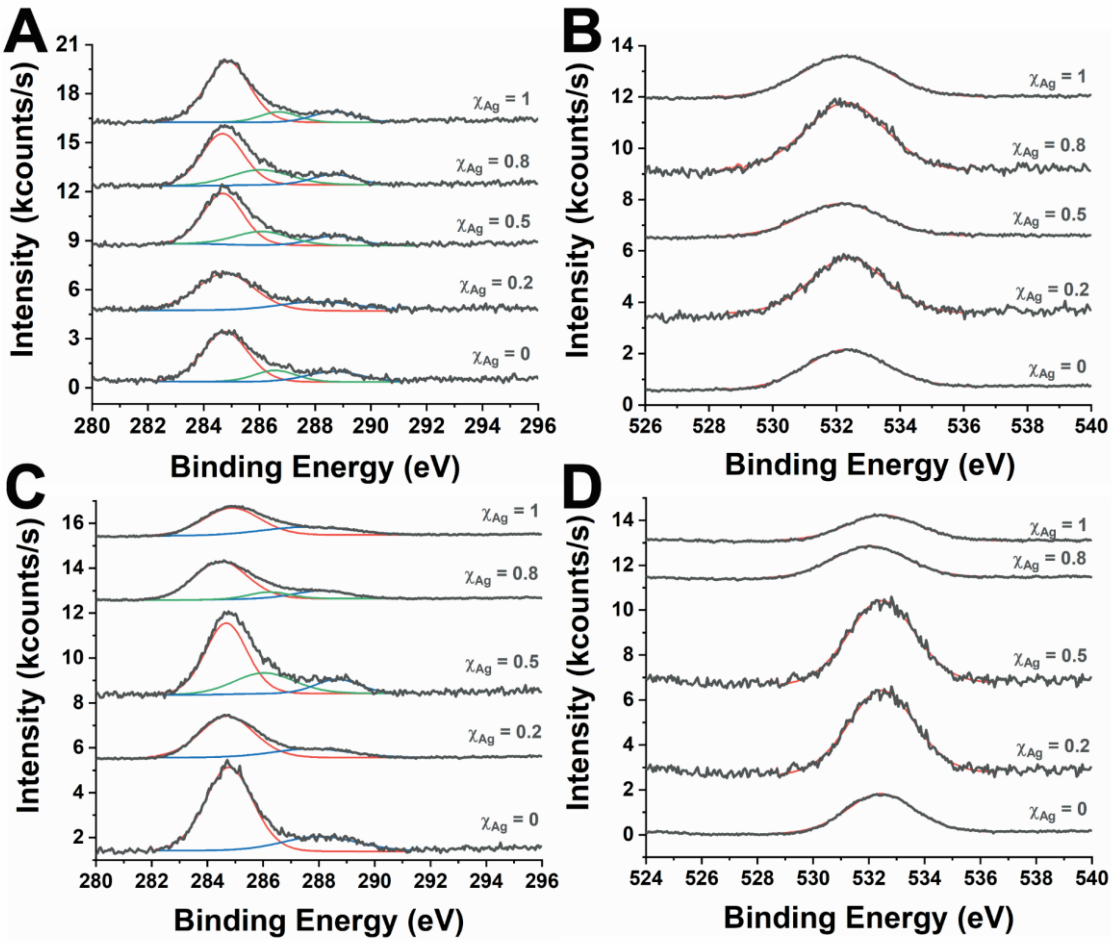

Figure 4.9: Fitted C 1s (A, C) and O 1s (B, D) high-resolution spectra of samples ran under sunlight (A, B) and in the dark (C, D) reduced with HA at pH of 8.

In order to mechanistically examine how natural sunlight promotes the growth of Ag, Au, and Ag-Au bimetallic alloy NPs, reactions were performed with a superoxide radical scavenger, SOD, at an external temperature of 28—32°C. **Figure 4.10** shows UV-vis spectra of sunlight-exposed samples ran at various concentrations of SOD (expressed in units/mL) at pH of 8, with HA as the reducing agent. Jiang and coworkers investigated the role of superoxide radicals in the reduction of Ag NPs. Their group narrowed down that photoactivation of DOMs results in the photooxidation of phenolic (or hydroquinone)

groups in DOMs. Once photoactivated, phenolic groups donate an electron to dissolved O_2 in aqueous solution, generating $O_2^{\bullet-}$ (mechanism ***c***).

Upon methylation of phenolic groups, the authors have noted a complete suppression of Ag NP formation, implying that dissolved O_2 in solution can only be formed upon the photoactivation of phenolic groups. In their work, they have only used one concentration of SOD (150 units/mL), which, while in excess, was enough to quench $O_2^{\bullet-}$ formation, and therefore, the reduction of Ag^+. In our study, we have noted that even a concentration of 50 units/mL (one-third of what was previously reported in literature[25]) was enough to prevent the production of Ag NPs (**Figure 4.10A**). This seems to imply that mechanism ***c*** is the dominant mechanism: HA is photoactivated, in turn reducing dissolved O_2 into $O_2^{\bullet-}$, which ultimately reduce Ag^+ in solution. A few studies have noted that the photoreduction of Ag^+ is kinetically slow[63,64] and requires the presence of ligands such as with ligands, such as citrate.[35] Reduction of Ag^+ with $O_2^{\bullet-}$ has been noted by Waite and coworkers to follow second-order kinetics.[63] Given that some studies, however, have noted that the presence of $O_2^{\bullet-}$ has minimal contribution to the reduction of Ag^+, another possibility for the decreased yield is the complexation of Ag^+ by Lewis basic sites in SOD. Behbehani *et al.* note that Ag-ions bind exothermically (association equilibrium constant of 5415.79±0.12 M^{-1} at 300 K) with Jack bean urease.[65] Specifically, Ag-ions are complexed at the thiol groups of the cysteine residue on ureases.[65,66]

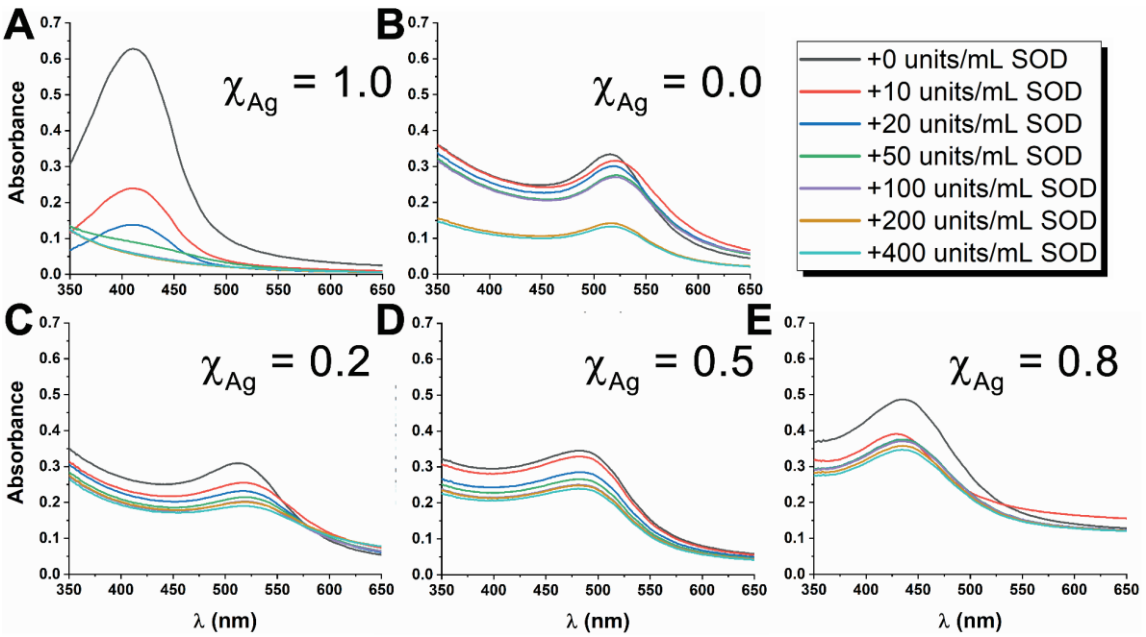

Figure 4.10: UV-vis spectra of SOD-treated χ_{Ag} = 1.0 (A), 0.0 (B), 0.2 (C), 0.5 (D), and 0.8 (E) NPs reduced with HA at a pH of 8 and exposed under natural sunlight. SOD is added at varying concentrations in order to determine which mechanism governs the growth of monometallic and bimetallic nanocrystals of Ag and Au.

On the other hand, for χ_{Ag} = 0.0, the generation of Au NPs is not quenched even with the addition of 400 units/mL SOD, which is around thrice what has been used in literature to capture $O_2^{\bullet-}$ in solution[25] (**Figure 4.10B**). Upon the addition of 10 units/mL SOD, the yield of Au NPs was minimally modulated, which is in stark contrast with the dramatic drop in the yield of Ag NPs (from an SPR intensity of *ca.* 0.62 to *ca.* 0.24) at the same concentration of SOD. At 50 units/mL SOD, the concentration at which Ag NPs ceased to form (**Figure 4.10A**), generation of Au NPs is still observed. For up to 100 units/mL SOD added, the formation of Au NPs monotonically decreased, albeit minimally. At 200 units/mL SOD, the yield of Au NPs significantly decreased, but plateaued at the same value at 400 units/mL SOD added. It is therefore likely that the

formation of Au NPs proceeds *via* mechanism ***b***. Wei and coworkers have previously reported that in the plasmon-mediated photoreduction of Au NPs, a sacrificial reagent such as methanol was needed in order to quickly scavenge photogenerated holes and isolate them from plasmon-generated electrons (methanol was irreversibly reduced to formaldehyde in the process).[67] Hydroxyl-containing groups in HA (phenols, hydroquinones, *etc*.) can serve as scavengers for the plasmon-generated holes. At higher concentrations of SOD (200 and 400 units/mL), the drop in yield of Au NPs can also be attributed to the formation of protein-Au NP conjugates with excess SOD in solution.[68]

Figures 4.10C, **D**, and **E** show UV-vis spectra of χ_{Ag} = 0.2, 0.5, and 0.8, respectively ran with the same range of SOD concentrations. For all cases, Ag-Au bimetallic alloy NP growth was still observed even with 400 units/mL SOD, suggesting that mechanism ***c*** is also the dominant reaction for alloy formation. Upon the initial formation of Ag and Au seeds *via* mechanisms ***a*** and/or ***b***, plasmon-mediated mechanism ***c*** takes over and promotes the growth of Ag and Au NPs. This is consistent with the mechanism proposed by Wiesner and coworkers.[47] Growing Ag and Au nanocrystals are subsequently alloyed to each other, given facile interdiffusion expected from their similar lattice constants. Galvanic replacement leads to the reduction of more Au^0 on the surface of HA—this reaction is indicative of preferential incorporation of Au over Ag.[23,69,70] Since there was preferential incorporation of Ag over Au in all bimetallic samples grown under photoillumination, it appears that galvanic replacement is not the likely mechanism which leads to the formation of Ag-Au bimetallic alloy NPs. Instead, Ag and Au NPs are alloyed to each other *via* the co-reduction[71] of Ag^+ and Au^{3+} by plasmon-generated electrons

(mechanism ***b***). Despite the fact that the reduction of Au^{3+} is more thermodynamically feasible than the reduction of Ag^{+} (E^0, (Au^{3+}) = 1.50 V *vs.* SHE, $E^0(Ag^{+})$ = 0.80 V *vs.* SHE), the plasmon-mediated reduction of Ag over Au is preferred given that only one electron is needed to reduce Ag-ions (compared to three for Au^{3+}). This explains the preferential incorporation of Ag over Au in all reactions conducted under photoillumination. The growth of Ag and Au seeds *via* mechanism ***c***, can be envisioned to play an initial role in the growth of NPs. Unlike Au NPs, the modulation of the yield of Ag-Au bimetallic alloy NP at 200 to 400 units/mL was very minimal, (most especially at χ_{Ag} = 0.8, which has the highest Ag at.% among all alloyed samples). **Figure 4.10C** shows that for χ_{Ag} = 0.2, a slight redshift towards the SPR of Au is also observed for all SOD-treated experiments. Since the Ag at.% is low at this molar fraction, formation of Ag seeds is suppressed with increasing concentrations of SOD, either because of the depletion of $O_2^{\bullet -}$ or by the complexation of Ag^{+} with SOD. At this point, the formation of Au NPs is more favored. On the other hand, while there is a decrease in absorbance intensity upon the addition of SOD, **Figure 4.10E** does not show any shifts in the SPR band position. The decrease in yield can be attributed to lesser [Ag^{+}] in solution upon the addition of SOD. Since the NP yield remained constant at any concentration of added SOD, mechanism ***c*** also appears to dictate the DOM-mediated formation of Ag-Au bimetallic alloy NPs under sunlight. The plasmon-induced mechanism is possible with the initial formation of Ag and Au nuclei *via* mechanisms ***a*** or ***b***. After the seeds are formed, the ions in solution are reduced by plasmon-generated electrons on the seed surface.

In order to determine whether superoxide anion radicals actually play a role in the formation of NPs, control experiments using a DSLR camera LED lamp as artificial white light source were performed. Particularly, monometallic Ag and Au NPs were grown with and without Ar-purging. While the process does not fully remove dissolved O_2 in solution, its concentration is substantially decreased. **Figure 4.11** shows UV-vis spectra of Ar-purged and unpurged samples after 24 h. Interestingly, both Ag and Au NPs showed a dramatic increase in NP yield upon purging the solutions with Ar (Ag NPs are actually *not* formed within the 24-hour range with the unpurged solution). Our control experiments show verify the work done by Adegboyega *et al.*[46] and Zepp and coworkers[45] that the reactive transient $O_2^{\bullet -}$ formed from the reduction of dissolved O_2 plays a minimal role in the formation of Ag and Au NPs. Indeed, the increased yield of Ag and Au NP upon Ar-purging underlines the dominant role of mechanism ***c***. Ag and Au nuclei are initially formed from reduction of Ag- and Au-ions with superoxide anion radicals in solution (mechanism ***b***) or by single-electron transfer events from redox-active quinone moieties in HA. After the formation of Ag and Au nuclei, NPs are further grown *via* the plasmon-induced pathway (mechanism ***c***), with HA serving as a scavenger of the plasmon-generated holes. Therefore, the previously observed decrease in NP yield can be attributed to the complexation of Ag- and Au-ions with SOD.

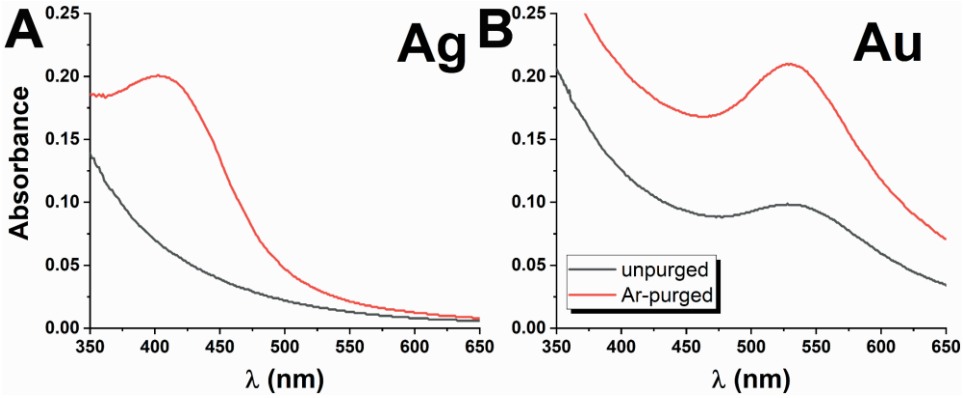

Figure 4.11: UV-vis spectra of monometallic Ag (A) and Au (B) NP grown under a DSLR camera white LED lamp. HA was used as the reducing agent at a pH of 8. Curves in black show unpurged solutions while red plots show Ar-purged solutions.

Figure 4.12 shows a schematic of the DOM-mediated formation of Ag, Au, and, Ag-Au bimetallic alloy NPs in the presence of natural sunlight. Overall, natural sunlight accelerates the DOM-mediated formation of Ag and Ag-Au bimetallic alloy NPs in aqueous media. Initially, Ag and Au nuclei are formed either by reduction with $O_2^{\bullet-}$ in solution[25] or by single-electron reduction events from quinone, hydroquinone, and semiquinone groups in the DOM.[23] Once formed, a surface plasmon is created on the surface of Ag and Au seeds, thereby promoting the generation of energetic charge-carriers on the seed surface.[35–37] DOMs behave as hole scavengers and abstract the plasmon-generated hole, leaving behind a build-up of negative charge on the metal surface. These plasmon-generated electrons subsequently reduce Ag- and Au-ions in solution, thereby furthering the growth of NPs. In the presence of both Ag^+ and Au^{3+}, Ag-Au bimetallic alloy NPs are formed by plasmon-induced co-reduction of Ag^+ and Au^{3+}. Preferential incorporation of Ag over Au is observed for the bimetallic samples given that only a single electron is needed to reduce Ag-ions.

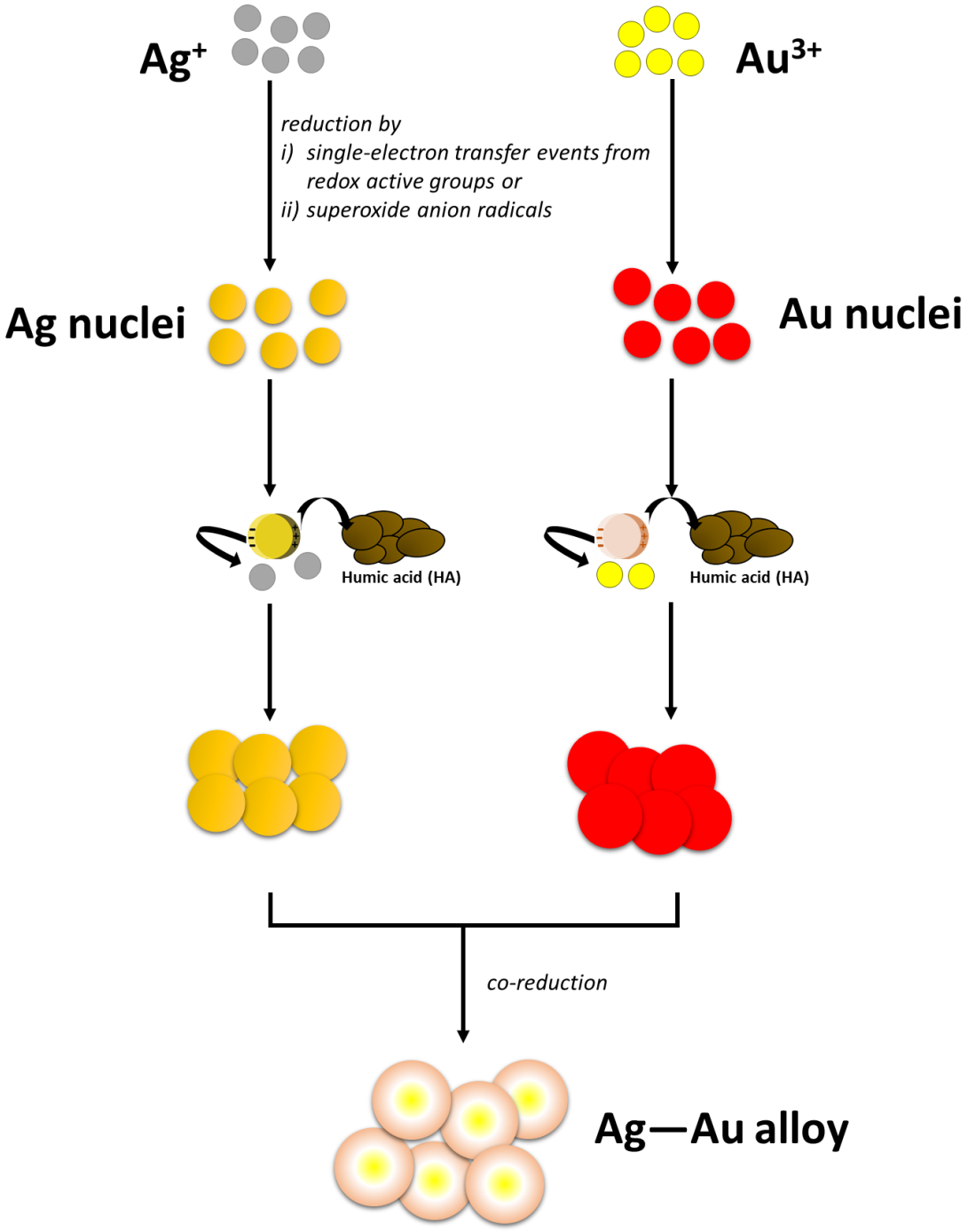

Figure 4.12: Schematic of the DOM-mediated formation of Ag, Au, and Ag-Au bimetallic alloy NPs under natural sunlight.

4.5 Conclusions and Environmental Significance

In this contribution, we have sought to understand the role of natural sunlight in the DOM-mediated reductive formation of Ag-Au bimetallic alloy NPs in aqueous media. In our previous work, we noted that DOMs such as HA and FA behave as reducing agents in the synthesis of monometallic Ag and Au NPs. In the presence of both Ag^{+} and Au^{3+} in aqueous media, Ag-Au bimetallic alloy NPs can be formed *via* galvanic replacement (the Ag-Au bimetallic alloy NPs were observed to be stable up to at least 120 days).[23] Superoxide anion radicals are formed from dissolved oxygen in water upon photoactivation of phenol and hydroquinone groups of HA.[25] These superoxide anion radicals in solution form Ag and Au nuclei, which exhibit characteristic surface plasmon resonances upon visible light illumination. Plasmon-generated holes are abstracted by HA leaving behind plasmon-generated electrons to reduce additional Ag^{+} and Au^{3+} in solution. In mixed aqueous solutions of Ag and Au ions, alloy formation under natural sunlight proceeds through a plasmon-induced pathway. Co-reduction of Ag^{+} and Au^{3+}[71] results in the DOM-mediated formation of Ag-Au bimetallic alloy NPs, with Ag as the dominant species; illumination with natural sunlight serves to accelerate the mineralization process and increases the predilection for Ag incorporation. The bimetallic species are stabilized by Au→Ag charge transfer as observed in high-resolution Ag 3d and Au 4f XPS. Knowledge of growth mechanisms of NPs under conditions emulative of natural aquatic media allows for better understanding of their transport and toxicological properties. While the toxicological properties of bulk metals are known, there is a knowledge gap on how their toxicity scales as a function of size. Given the high surface-area-to-volume ratio

of metallic nanocrystals, there has been considerable concern about their impact on aquatic fauna and on humans[72] (since these NPs can potentially be transported to potable water sources). The toxicological properties of Ag-Au bimetallic alloy NPs are a function of the elemental composition of Ag and Au, wherein greater toxicity is observed with greater Ag incorporation.[32]

4.6 References

(1) Benn, T. M.; Westerhoff, P. Nanoparticle Silver Released into Water from Commercially Available Sock Fabrics. *Environ. Sci. Technol.* **2008**, *42*, 4133–4139.

(2) Pourzahedi, L.; Vance, M.; Eckelman, M. J. Life Cycle Assessment and Release Studies for 15 Nanosilver-Enabled Consumer Products: Investigating Hotspots and Patterns of Contribution. *Environ. Sci. Technol.* **2017**, *51*, 7148–7158.

(3) Dubas, S. T.; Pimpan, V. Humic Acid Assisted Synthesis of Silver Nanoparticles and Its Application to Herbicide Detection. *Mater. Lett.* **2008**, *62*, 2661–2663.

(4) Fahimi-Kashani, N.; Hormozi-Nezhad, M. R. Gold-Nanoparticle-Based Colorimetric Sensor Array for Discrimination of Organophosphate Pesticides. *Anal. Chem.* **2016**, *88*, 8099–8106.

(5) Anker, J. N.; Hall, W. P.; Lyandres, O.; Shah, N. C.; Zhao, J.; Duyne, R. P. Van. Biosensing with Plasmonic Nanosensors. *Nat. Mater.* **2008**, *7*, 442–453.

(6) Amendola, V.; Pilot R.; Frasconi, M.; Maragò, O. M.; Iatì, V. A. Surface Plasmon Resonance in Gold Nanoparticles: A Review. *J. Phys. Condens. Matter* **2017**, *29*,

203002/1–48.

(7) Sharifi, S.; Behzadi, S.; Laurent, S.; Forrest, M. L.; Stroeve, P.; Mahmoudi, M. Toxicity of Nanomaterials. *Chem. Soc. Rev.* **2012**, *41*, 2323–2343.

(8) Pietroiusti, A.; Stockmann-Juvala, H.; Lucaroni, F.; Savolainen, K. Nanomaterial Exposure, Toxicity, and Impact on Human Health. *Nanomed. Nanobiotechnol.* **2018**, *10*, 1–21.

(9) Jia, J.; Li, F.; Zhou, H.; Bai, Y.; Liu, S.; Jiang, Y.; Jiang, G.; Yan, B. Oral Exposure to Silver Nanoparticles or Silver Ions May Aggravate Fatty Liver Disease in Overweight Mice. *Environ. Sci. Technol.* **2017**, *51*, 9334–9343.

(10) Yoshikawa, M. Sewage Yields More Gold than Top Mines https://www.reuters.com/article/2009/01/30/us-goldsewage-oddidUSTRE50T56120090130 (accessed Sep 1, 2017).

(11) Prichard, H. M.; Wedin, F.; Sampson, J.; Jackson, M. T.; Fisher, P. C. Precious Metals in Urban Waste. *Water Environ. J.* **2016**, *30* (1–2), 151–156.

(12) U. S. Environmental Protection Agency,. Ambient Water Quality Criteria for Silver https://nepis.epa.gov (accessed Sep 1, 2018).

(13) Furtado, L. M.; Norman, B. C.; Xenopoulos, M. A.; Frost, P. C.; Metcalfe, C. D.; Hintelmann, H. Environmental Fate of Silver Nanoparticles in Boreal Lake Ecosystems. *Environ. Sci. Technol.* **2015**, *49*, 8441–8450.

(14) Köser, J.; Engelke, M.; Hoppe, M.; Nogowski, A.; Filser, J.; Thöming, J. Predictability of Silver Nanoparticle Speciation and Toxicity in Ecotoxicological Media. *Environ. Sci. Nano* **2017**, *4*, 1470–1483.

(15) Iswarya, V.; Manivannan, J.; De, A.; Paul, S.; Roy, R.; Johnson, J. B.; Kundu, R.; Chandrasekaran, N.; Mukherjee, A.; Mukherjee, A. Surface Capping and Size-Dependent Toxicity of Gold Nanoparticles on Different Trophic Levels. *Environ. Sci. Pollut. Res.* **2016**, *23*, 4844–4858.

(16) Moreno-Garrido, I.; Pérez, S.; Blasco, J. Toxicity of Silver and Gold Nanoparticles on Marine Microalgae. *Mar. Environ. Res.* **2015**, *111*, 60–73.

(17) Sharma, V. K.; Filip, J.; Zboril, R.; Varma, R. S. Natural Inorganic Nanoparticles-Formation, Fate, and Toxicity in the Environment. *Chem. Soc. Rev.* **2015**, *44*, 8410–8423.

(18) Wagner, S.; Gondikas, A.; Neubauer, E.; Hofmann, T.; Von Der Kammer, F. Spot the Difference: Engineered and Natural Nanoparticles in the Environment-Release, Behavior, and Fate. *Angew. Chemie Int. Ed.* **2014**, *53*, 12398–12419.

(19) Zsolnay, Á. Dissolved Organic Matter: Artefacts, Definitions, and Functions. *Geoderma* **2003**, *113*, 187–209.

(20) Aiken, G. R.; Hsu-Kim, H.; Ryan, J. N. Influence of Dissolved Organic Matter on the Environmental Fate of Metals, Nanoparticles, and Colloids. *Environ. Sci. Technol.* **2011**, *45*, 3196–3201.

(21) Akaighe, N.; Depner, S. W.; Banerjee, S.; Sharma, V. K.; Sohn, M. The Effects of Monovalent and Divalent Cations on the Stability of Silver Nanoparticles Formed from Direct Reduction of Silver Ions by Suwannee River Humic Acid/Natural Organic Matter. *Sci. Total Environ.* **2012**, *441*, 277–289.

(22) Stenson, A. C.; Marshall, A. G.; Cooper, W. T. Exact Masses and Chemical

Formulas of Individual Suwannee River Fulvic Acids from Ultrahigh Resolution Electrospray Ionization Fourier Transform Ion Cyclotron Resonance Mass Spectra. *Anal. Chem.* **2003**, *75*, 1275–1284.

(23) Alivio, T. E. G.; Fleer, N. A.; Singh, J.; Nadadur, G.; Feng, M.; Banerjee, S.; Sharma, V. K. Stabilization of Ag-Au Bimetallic Nanocrystals in Aquatic Environments Mediated by Dissolved Organic Matter: A Mechanistic Perspective. *Environ. Sci. Technol.* **2018**, *52*, 7269–7278.

(24) Adegboyega, N. F.; Sharma, V. K.; Siskova, K.; Zbořil, R.; Sohn, M.; Schultz, B. J.; Banerjee, S. Interactions of Aqueous Ag+ with Fulvic Acids: Mechanisms of Silver Nanoparticle Formation and Investigation of Stability. *Environ. Sci. Technol.* **2013**, *47*, 757–764.

(25) Yin, Y.; Liu, J.; Jiang, G. Sunlight-Induced Reduction of Ionic Ag and Au to Metallic Nanoparticles by Dissolved Organic Matter. *ACS Nano* **2012**, *6*, 7910–7919.

(26) Thalmann, B.; Voegelin, A.; Von Gunten, U.; Behra, R.; Morgenroth, E.; Kaegi, R. Effect of Ozone Treatment on Nano-Sized Silver Sulfide in Wastewater Effluent. *Environ. Sci. Technol.* **2015**, *49*, 10911–10919.

(27) Thi Ngoc Anh, D.; Singh, P.; Shankar, C.; Mott, D.; Maenosono, S. Charge-Transfer-Induced Suppression of Galvanic Replacement and Synthesis of (Au@Ag)@Au Double Shell Nanoparticles for Highly Uniform, Robust and Sensitive Bioprobes. *Appl. Phys. Lett.* **2011**, *99*, 4–7.

(28) Nishimura, S.; Dao, A. T. N.; Mott, D.; Ebitani, K.; Maenosono, S. X-Ray

Absorption Near-Edge Structure and X-Ray Photoelectron Spectroscopy Studies of Interfacial Charge Transfer in Gold–Silver–Gold Double-Shell Nanoparticles. *J. Phys. Chem. C* **2012**, *116*, 4511–4516.

(29) Bzowski, A.; Yiu, Y. M.; Sham, T. K. Charge Redistribution in Au-Metalloid Intermetallics: A Au L2,3-Edge x-Ray-Absorption Study. *Phys. Rev. B.* **1995**, *51*, 9515−9520.

(30) Csapó, E.; Oszkó, A.; Varga, E.; Juhász, Á.; Buzás, N.; Korösi, L.; Majzik, A.; Dékány, I. Synthesis and Characterization of Ag/Au Alloy and Core(Ag)-Shell(Au) Nanoparticles. *Colloids Surfaces A Physicochem. Eng. Asp.* **2012**, *415*, 281–287.

(31) Yin, Z.; Wang, Y.; Song, C.; Zheng, L.; Ma, N.; Liu, X.; Li, S.; Lin, L.; Li, M.; Xu, Y.; Li, W.; Hu, G.; Fang, Z.; Ma, D.. Hybrid Au-Ag Nanostructures for Enhanced Plasmon-Driven Catalytic Selective Hydrogenation through Visible Light Irradiation and Surface-Enhanced Raman Scattering. *J. Am. Chem. Soc.* **2018**, *140*, 864–867.

(32) Li, T.; Albee, B.; Alemayehu, M.; Diaz, R.; Ingham, L.; Kamal, S.; Rodriguez, M.; Whaley Bishnoi, S. Comparative Toxicity Study of Ag, Au, and Ag-Au Bimetallic Nanoparticles on Daphnia Magna. *Anal. Bioanal. Chem.* **2010**, *398*, 689–700.

(33) Jin, R.; Cao, Y.; Mirkin, C. A.; Kelly, K. L.; Schatz, G. C.; Zheng, J. G. Photoinduced Conversion of Silver Nanospheres to Nanoprisms. *Science* **2001**, *294*, 1901–1903.

(34) Jin, R.; Cao, Y. C.; Hao, E.; Metraux, G. S.; Schatz, G. C.; Mirkin, C. A. Controlling Anisotripic Nanoparticle Growth Through Plasmon Excitation. *Nature.* **2003**, *425*,

487–490.

(35) Maillard, M.; Huang, P.; Brus, L. Silver Nanodisk Growth by Surface Plasmon Enhanced Photoreduction of Adsorbed [Ag^+]. *Nano Lett.* **2003**, *3*, 1611–1615.

(36) Linic, S.; Aslam, U.; Boerigter, C.; Morabito, M. Photochemical Transformations on Plasmonic Metal Nanoparticles. *Nat. Mater.* **2015**, *14*, 567–576.

(37) Brus, L. Plasmon-Driven Chemical Synthesis: Growing Gold Nanoprisms with Light. *Nat. Mater.* **2016**, *15*, 824–825.

(38) He, D.; Bligh, M. W.; Waite, T. D. Effects of Aggregate Structure on the Dissolution Kinetics of Citrate-Stabilized Silver Nanoparticles. *Environ. Sci. Technol.* **2013**, *47*, 9148–9156.

(39) Wu, X.; Thrall, E. S.; Liu, H.; Steigerwald, M.; Brus, L. Plasmon Induced Photovoltage and Charge Separation in Citrate-Stabilized Gold Nanoparticles. *J. Phys. Chem. C* **2010**, *114*, 12896–12899.

(40) Ratasuk, N.; Nanny, M. A. Characterization and Quantification of Reversible Redox Sites in Humic Substances. *Environ. Sci. Technol.* **2007**, *41*, 7844–7850.

(41) Zhou, S.; Chen, S.; Yuan, Y.; Lu, Q. Influence of Humic Acid Complexation with Metal Ions on Extracellular Electron Transfer Activity. *Sci. Rep.* **2015**, *5*, 1–9.

(42) Da Silva, A. G. M.; Rodrigues, T. S.; Haigh, S. J.; Camargo, P. H. C. Galvanic Replacement Reaction: Recent Developments for Engineering Metal Nanostructures towards Catalytic Applications. *Chem. Commun.* **2017**, *53*, 7135–7148.

(43) Sun, Y.; Xia, Y. Mechanistic Study on the Replacement Reaction between Silver

Nanostructures and Chloroauric Acid in Aqueous Medium. *J. Am. Chem. Soc.* **2004**, *126*, 3892–3901.

(44) Brus, L. Noble Metal Nanoparticles: Plasmon Electron Transfer Photochemistry and Single-Molecule Raman Spectroscopy. *Acc. Chem. Res.* **2008**, *41*, 1742–1749.

(45) Hou, W. C.; Stuart, B.; Howes, R.; Zepp, R. G. Sunlight-Driven Reduction of Silver Ions by Natural Organic Matter: Formation and Transformation of Silver Nanoparticles. *Environ. Sci. Technol.* **2013**, *47*, 7713–7721.

(46) Adegboyega, N. F.; Sharma, V. K.; Cizmas, L.; Sayes, C. M. UV Light Induces Ag Nanoparticle Formation: Roles of Natural Organic Matter, Iron, and Oxygen. *Environ. Chem. Lett.* **2016**, *14*, 353–357.

(47) Badireddy, A. R.; Farner Budarz, J.; Marinakos, S. M.; Chellam, S.; Wiesner, M. R. Formation of Silver Nanoparticles in Visible Light-Illuminated Waters: Mechanism and Possible Impacts on the Persistence of AgNPs and Bacterial Lysis. *Environ. Eng. Sci.* **2014**, *31*, 338–349.

(48) Xue, C.; Métraux, G. S.; Millstone, J. E.; Mirkin, C. A. Mechanistic Study of Photomediated Triangular Silver Nanoprism Growth. *J. Am. Chem. Soc.* **2008**, *130*, 8337–8344.

(49) Aeschbacher, M.; Graf, C.; Schwarzenbach, R. P.; Sander, M. Antioxidant Properties of Humic Substances. *Environ. Sci. Technol.* **2012**, *46*, 4916–4925.

(50) Jones, A. C.; Berweger, S.; Wei, J.; Cobden, D.; Raschke, M. B. Nano-Optical Investigations of the Metal-Insulator Phase Behavior of Individual VO_2 Microcrystals. *Nano Lett.* **2010**, *10*, 1574–1581.

(51) Rao, P. S.; Hayon, E. Redox Potentials of Free Radicals. IV. Superoxide and Hydroperoxy Radicals $^{\cdot}O_2^-$ and $^{\cdot}HO_2$. *J. Phys. Chem.* **1975**, *79*, 397–402.

(52) Casaletto, M. P.; Longo, A.; Martorana, A.; Prestianni, A.; Venezia, A. M. XPS Study of Supported Gold Catalysts: The Role of Au^0 and $Au^{+\delta}$ Species as Active Sites. *Surf. Interface Anal.* **2006**, *38*, 215–218.

(53) Uznanski, P.; Zakrzewska, J.; Favier, F.; Kazmierski, S.; Bryszewska, E. Synthesis and Characterization of Silver Nanoparticles from (Bis)Alkylamine Silver Carboxylate Precursors. *J. Nanoparticle Res.* **2017**, *19*, 121/1–20.

(54) Moulder, J. F.; Stickle, W. F.; Sobol, P. E.; Bomben, K. D. *Handbook of X-Ray Photoelectron Spectroscopy*; Chastain, J., King, R. C., Jr.: Eden Prairie, MN, 1995.

(55) National Institure of Science and Technology, X-Ray Photoelectron Spectroscopy Database http://srdata.nist.gov/xps/ (accessed Sep 1, 2017).

(56) Alves, L.; Ballesteros, B.; Boronat, M.; Cabrero-Antonino, J. R.; Concepcioén, P.; Corma, A.; Correa-Duarte, M. A.; Mendoza, E. Synthesis and Stabilization of Subnanometric Gold Oxide Nanoparticles on Multiwalled Carbon Nanotubes and Their Catalytic Activity. *J. Am. Chem. Soc.* **2011**, *133*, 10251–10261.

(57) Yin, Y.; Yu, S.; Liu, J.; Jiang, G. Thermal and Photoinduced Reduction of Ionic Au(III) to Elemental Au Nanoparticles by Dissolved Organic Matter in Water: Possible Source of Naturally Occurring Au Nanoparticles. *Environ. Sci. Technol.* **2014**, *48*, 2671–2679.

(58) Hammond, J. S.; Holubka, J. W.; deVries, J. E.; Dickie, R. A. The Application of X-Ray Photo-Electron Spectroscopy to a Study of Interfacial Composition in

Corrosion-Induced Paint de-Adhesion. *Corros. Sci.* **1981**, *21*, 239–253.

(59) Dong, T.-Y.; Chen, W.-T.; Wang, C.-W.; Chen, C.-P.; Chen, C.-N.; Lin, M.-C.; Song, J.-M.; Chen, I.-G.; Kao, T.-H. One-Step Synthesis of Uniform Silver Nanoparticles Capped by Saturated Decanoate: Direct Spray Printing Ink to Form Metallic Silver Films. *Phys. Chem. Chem. Phys.* **2009**, *11*, 6269.

(60) Chen, Z.; Campbell, P. G. C.; Fortin, C. Silver Binding by Humic Acid as Determined by Equilibrium Ion-Exchange and Dialysis. *J. Phys. Chem. A.* **2012**, *116*, 6532–6539.

(61) Bell, R. A.; Ogden, N.; Kramer, J. R. The Biotic Ligand Model and a Cellular Approach to Class B Metal Aquatic Toxicity. *Comp. Biochem. Physiol. C. Toxicol. Pharmacol.* **2002**, *133*, 175–188.

(62) Pensa, E.; Cortés, E.; Corthey, G.; Carro, P.; Vericat, C.; Fonticelli, M. H.; Benítez, G.; Rubert, A. A.; Salvarezza, R. C. The Chemistry of the Sulfur-Gold Interface: In Search of a Unified Model. *Acc. Chem. Res.* **2012**, *45*, 1183–1192.

(63) Jones, A. M.; Garg, S.; He, D.; Pham, A. N.; Waite, T. D. Superoxide-Mediated Formation and Charging of Silver Nanoparticles. *Environ. Sci. Technol.* **2011**, *45*, 1428–1434.

(64) Redmond, P. L.; Wu, X.; Brus, L. Photovoltage and Photocatalyzed Growth in Citrate-Stabilized Colloidal Silver Nanocrystals. *J. Phys. Chem. C.* **2007**, *111*, 8942–8947.

(65) Behbehani, G. R.; Saboury, A. A.; Taherkhani, A.; Barzegar, L.; Mollaagazade, A. A Thermodynamic Study on the Binding of Mercury and Silver Ions to Urease. *J.*

Therm. Anal. Calorim. **2011**, *105*, 1081–1086.

(66) Behbehani, G. R.; Saboury, A. A.; Baghery, A. F.; Abedini, A. Application of an Extended Solvation Theory to Study the Binding of Magnesium Ion with Myelin Basic Protein. *J. Therm. Anal. Calorim. Acta Biochim. Biophys. Sin.*. **2008**, *93*, 479–483.

(67) Zhai, Y.; DuChene, J. S.; Wang, Y. C.; Qiu, J.; Johnston-Peck, A. C.; You, B.; Guo, W.; Diciaccio, B.; Qian, K.; Zhao, E. W.; Ooi, F.; Hu, H.; Su, D.; Stach, E. A.; Zhu, Z.; Wei, W. D. . Polyvinylpyrrolidone-Induced Anisotropic Growth of Gold Nanoprisms in Plasmon-Driven Synthesis. *Nat. Mater.* **2016**, *15*, 889–895.

(68) Pudlarz, M., A.; Ranoszek-Soliwoda, K.; Czechowska, E.; Tomaszewska, E.; Celichowski, G.; Grobelny, J.; Szemraj, J. Study of the Activity of Recombinant Mn-Superoxide Dismutase in the Presence of Gold and Silver Nanoparticles. *Appl. Biochem. Technol.* **2018**, *186*, 1–18.

(69) Zhang, X.; Zhang, G.; Zhang, B.; Su, Z. Synthesis of Hollow Ag-Au Bimetallic Nanoparticles in Polyelectrolyte Multilayers. *Langmuir* **2013**, *29*, 6722–6727.

(70) Sun, X.; Yang, Y.; Zhang, Z.; Qin, D. Mechanistic Roles of Hydroxide in Controlling the Deposition of Gold on Colloidal Silver Nanocrystals. *Chem. Mater.* **2017**, *29*, 4014–4021.

(71) Link, S.; Wang, Z. L.; El-Sayed, M. A. Alloy Formation of Gold−Silver Nanoparticles and the Dependence of the Plasmon Absorption on Their Composition. *J. Phys. Chem. B* **1999**, *103* , 3529–3533.

(72) Kurwadkar, S.; Pugh, K.; Gupta, A.; Ingole, S. Nanoparticles in the Environment:

Occurrence, Distribution, and Risks. *J. Hazardous, Toxic, Radioact. Waste* **2015**, *19*, 04014039/1-9.

CHAPTER V

POSTSYNTHETIC ROUTE FOR MODIFYING THE METAL—INSULATOR TRANSITION OF VO_2 BY INTERSTITIAL DOPANT INCORPORATION[*]

5.1 Summary

The thermally driven orders-of-magnitude modulation of resistance and optical transmittance observed in VO_2 makes it an archetypal first-order phase transition material and underpins functional applications in logic and memory circuitry, electromagnetic cloaking, ballistic modulation, and thermochromic glazing to provide just a few representative examples. VO_2 can be reversibly switched from an insulating to a metallic state with an equilibrium transition temperature of 67°C. Tuning the phase diagram of VO_2 to bring the transition temperature closer to room temperature has been a longstanding objective and one that has tremendous practical relevance. Substitutional incorporation of dopants has been the most common strategy for modulating the metal—insulator transition temperature but requires that the dopants be incorporated during synthesis. Here we demonstrate a novel post-synthetic diffusive annealing approach for incorporating interstitial B dopants within VO_2. The post-synthetic method allows for the transition temperature to be programmed after synthesis and furthermore represents an entirely distinctive mode of modulating the phase diagram of VO_2. Local structure studies

[*] Reprinted with permission from "Postsynthetic Route for Modifying the Metal—Insulator Transition of VO_2 by Interstitial Dopant Incorporation" by Alivio, T. E. G.; Sellers, D. G.; Asayesh-Ardakani, H.; Braham, E. J.; Horrocks, G. A.; Pelcher, K. E.; Villareal, R.; Zuin, L.; Shamberger, P. J.; Arróyave, R.; Shahbazian-Yassar, R.; Banerjee, S. *Chem. Mater*. **2017**, *29*, 5401-5412.

in conjunction with density functional theory calculations point to the strong preference of B atoms for tetrahedral coordination within interstitial sites of VO_2; these tetrahedrally coordinated dopant atoms hinder the rutile → monoclinic transition by impeding the dimerization of V—V chains and decreasing the covalency of the lattice. The results suggest that interstitial dopant incorporation is a powerful method for modulating the transition temperature and electronic instabilities of VO_2 and provides a facile approach for post-synthetic dopant incorporation to reach a switching temperature required for a specific application.

5.2 Introduction

The binary vanadium(IV) oxide (VO_2), has been known for over five decades to be an archetypal metal—insulator transition material and exhibits an abrupt orders-of-magnitude first-order insulator → metal transition at *ca.* 67°C.[1–7] Considerable debate still exists as to whether the transition is underpinned by electron—phonon coupling (with an accompanying Peierls' distortion) or a modification of electron—electron correlation (as is characteristic of Mott insulators).[1,4,7,8] Below the transition temperature, the insulating phase of VO_2 has an optical bandgap estimated to be 600 meV, which is eliminated upon temperature-, voltage-, photoexcitation-, or strain-induced metallization.[9,10] Whether or not a specific crystal structure gives rise to a specific (insulating or metallic) electronic structure or is a consequence of such electronic structure, below the transition temperature, the monoclinic (M_1) phase ($P2_1/c$) of VO_2 is preferentially stabilized, whereas above the transition temperature, the tetragonal/rutile (R) phase ($P4_2/mnm$) represents the

thermodynamic minimum.[1,10–12] The M_1 phase of VO_2 has alternating V—V distances of 2.65Å and 3.12Å along the crystallographic *a* axis and presents a canted, zigzag configuration along the cation sublattice. In contrast, the R structure is a higher symmetry phase with a linear periodic arrangement of vanadium atoms along the cation sublattice characterized by uniform V—V lengths of 2.85Å (along the *c* axis).[1,11,13,14] The abrupt and massive switching of conductance and optical transmittance in close proximity of room temperature in response to external stimuli such as temperature (and also strain, photoexcitation, and voltage) makes this compound of great interest for functional applications in logic and memory circuitry, electromagnetic cloaking, ballistic modulation, and thermochromic glazing to provide just a few representative examples.[2,4,15–17]

A major challenge in studies of correlated systems, which also has widespread practical resonance for applications of these materials in devices requiring room-temperature operation, is to devise methods to modulate the transition temperature of the electronic instability. In VO_2, one approach for tuning the metal—insulator transition temperature involves scaling to finite size, wherein supercooling or superheating of the R and M_1 phases, respectively, is thought to arise from kinetic impediments to nucleating the phase transition as the volume density of potential nucleation sites is decreased with decreasing size.[18,19] Alternatively, the thermodynamic stabilities of the different phases can be altered by substitutional doping, resulting in elevation or depression of the transition temperature. The incorporation of early transition metals on the vanadium sublattice has been extensively explored as a means of modifying the phase transition

temperature using various synthetic methods spanning the range from hydrothermal reaction to chemical vapor deposition, sol—gel synthesis, and sputtering; the incorporation of tungsten, molybdenum, and titanium on the vanadium sublattice is particularly well explored and clear correlations between dopant incorporation and the depression of the transition temperature have been established for these homovalent and aliovalent species.[13,20–26] Trivalent dopants such as Al^{3+},[27] Cr^{3+},[28] and several lanthanide cations[29] have further been incorporated on the cation sublattice and allow for stabilization of M_2 and triclinic phases of VO_2 in addition to elevating the transition temperature of the M_1 to R transition. The introduction of oxygen vacancies by electrochemical reaction with ionic liquids (originally thought to be an electrostatic gating effect) has been developed recently as a means of modulating the phase transition temperature and has relevance for defining phase coexistence regimes wherein the conductance of the material provides a non-binary multistate variable.[30–33] Hydrogen incorporation through a catalytic spillover mechanism has also been explored as a means of modulating the transition temperature of VO_2.[7,34] Given the close-packed structure types involved, not much attention has focused on the use of interstitial dopants as a means of modulating the metal—insulator transition of VO_2. However, a computational study by Zhang *et al.* notes that small atoms such as B can be accommodated in tetrahedral holes of R-phase VO_2; these authors predict that selective stabilization of the R phase could result in as much as a 83 K/at.% decrease of the transition temperature, more than three-fold the value obtained for tungsten, the most widely explored substitutional dopant.[35] From a practical perspective, post-synthetic intercalation of dopants further holds promise as a means of adjusting the transition

temperature of highly crystalline VO_2 after synthesis, enabling unprecedented tunability of the phase diagram.

In this work, we have explored the incorporation of B within high-crystalline-quality VO_2 nanocrystals using a diffusive annealing approach. Ensemble and local structure methods suggest that B is indeed incorporated in interstitial sites wherein it strongly modifies the relative phase stabilities, thereby greatly decreasing the metal—insulator transition temperature. Diffusive doping of precursors initially deposited as surface ad-layers has proven to be successful for incorporation of dopants within Si, Ge, and complex III-V semiconductors and has emerged as a viable alternative to conventional ion-implantation and solid-state diffusion methods albeit, for the examples reported thus far, the dopants are still incorporated in substitutional sites.[36–39] The *ex situ* diffusive doping process developed here provides a robust and facile method for incorporating dopants and selectively tuning the transition temperature of VO_2. A linear correlation is established between dopant concentration and the critical transition temperature, T_{MIT}. The phase transformations of the B-incorporated VO_2 nanocrystals have been studied by temperature-dependent Raman spectroscopy and powder X-ray diffraction (XRD). The local structure of B within the VO_2 has been examined by X-ray photoelectron (XPS), electron energy loss (EELS), and X-ray absorption near-edge structure (XANES) spectroscopies.

5.3 Methods

5.3.1 Synthesis of VO_2 Nanobeams

VO_2 nanobeams with dimensions of 210±70 nm in width and 4.0±3.0 μm in length were prepared as reported in our previous work based on the hydrothermal reduction of V_2O_5 by small aliphatic molecules.[9,40] In brief, 2-propanol-reduced VO_2 (nanowires were synthesized hydrothermally in a 125 mL autoclave reactor (Parr Instrument Company, Moline, IL). 1.6000 g of V_2O_5 (Sigma-Aldrich, St. Louis, MO) was reduced to VO_2 with 10 mL of 2-propanol (Fisher, Fair Lawn, NJ) and 65 mL of deionized water (prepared with a Barnstead International NANOpure Diamond ultrapure water system $\rho = 18.2\ M\Omega\ cm^{-1}$), at 210°C for 72 h. The supernatant was discarded and the precipitates were rinsed with acetone (Macron Fine Chemicals, Center Valley, PA). The samples were then placed within a quartz tube, which in turn was annealed using a tube furnace at a temperature of 550°C (ramping at a rate of *ca.* 45°C/min) for 3 h under an ambient of Ar gas flowed at a rate of 800 mL/min.

Thinner and smaller VO_2 nanobeams with dimensions of 180±70 nm in width and 1.6±0.9 μm in length were also prepared hydrothermally in a 23 mL autoclave reactor (Parr Instrument Company). In brief, 0.3000 g of V_2O_5 was reduced to VO_2 with 9 mL of acetone (Macron, Center Valley, PA) and 7 mL of deionized water at 210°C for 18 h. The samples were washed with acetone and annealed at 550°C for 3 h as noted above.

VO_2 nanoparticles with dimensions of 100±50 nm (measured across the longest axis) were prepared by ball-milling. In a typical synthesis, 0.1000 g of the acetone-reduced

VO_2 was subjected to ball-milling with methacrylate polymer beads (Spex SamplePrep, St. Metuchen, NJ) for 2.5 h.

5.3.2 Incorporation of B by Diffusive Doping

2-Allyl-4,4,5,5-tetramethyl-1,3,2-dioxaborolane (97%) was purchased from Sigma-Aldrich (St. Louis, MO). In a typical reaction, 20 mg of VO_2 nanoparticles were dispersed in 1.00 mL of mesitylene (Sigma-Aldrich) by ultrasonication and 200 μL of 2-allyl-4,4,5,5-tetramethyl-1,3,2-dioxaborolane was added to the reaction mixture. The reactants were allowed to stir for 2.5 h at 120°C under an Ar ambient in a Schlenk flask. The VO_2 nanowires were then recovered by centrifugation then rinsed with toluene. Next, the nanowires were annealed using a 2-mL porcelain combustion boat (VWR, Sugar Land, TX) to a temperature of 900—950°C for 1 min under an Ar ambient in a quartz tube furnace (rapidly ramping at a rate of *ca.* 45°C/min). **Figure 5.1** plots the thermal profile used for the reaction. Control samples were prepared by subjecting unmodified VO_2 to annealing under the same conditions without addition of the boron precursor.

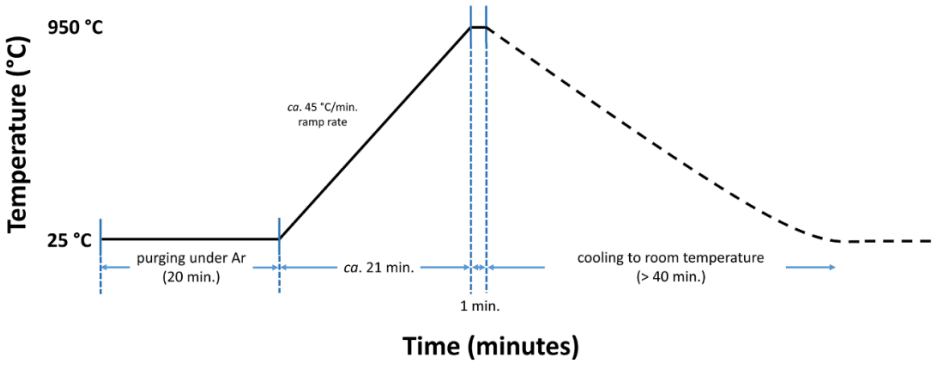

Figure 5.1: Rapid thermal annealing diagram for the diffusive doping process.

5.3.3 Characterization

5.3.3.1 Differential Scanning Calorimetry (DSC)

DSC measurements were performed using a Q2000 TA Instruments calorimeter. Measurements were performed under a flowing argon atmosphere in the temperature range from -20 to 100°C at a ramp rate of 15°C/min to examine the latent heat change given that the phase transition of VO_2 is first-order in nature.

5.3.3.2 Transmission Electron Microscopy (TEM)

The nanowire samples before and after dopant incorporation were imaged by high-resolution transmission electron microscopy (HRTEM) using a JEOL-2010 electron microscope at an operating voltage of 200 keV. Samples for HRTEM analysis were dispersed in ethanol (Koptec, King of Prussia, PA) drop-cast onto 400-mesh carbon-coated copper grids (Electron Microscopy Sciences, Hatfield, PA), and air-dried.

5.3.3.3 *In Situ* Temperature-Dependent Powder XRD

A Bruker-AXS D8 Vario X-ray powder diffractometer, using Cu Kα radiation (λ = 1.5418Å) and Ni filter was used for characterization of the samples by powder XRD. The samples were heated within a MTC oven mounted within the diffractometer; the samples were heated under a N_2 ambient from 30 to 100°C at a heating rate of 0.17°C/s. The sample was likewise cooled *in situ* from 100 to 30°C at the same ramp rate.

5.3.3.4 Variable Temperature Raman Spectroscopy

Raman spectra were acquired using a Jobin-Yvon Horiba Labram HR instrument coupled to an Olympus BX41 microscope using 514.5 nm laser excitation from an Ar-ion laser. Raman spectra were acquired using a 1800 lines/mm grating and an acquisition time of 300 s. The laser power was kept below 300 μW to minimize local heating and oxidation. A Linkam Scientific Instruments THMS 600 thermal stage was used for the *in situ* thermal cycling experiments, and the samples were allowed to equilibrate for at least 300 s, under a flowing N_2 ambient upon increasing/decreasing the temperature.

5.3.3.5 XPS

XPS analyses were performed on an Omicron XPS/UPS system with an Argus detector using Mg Kα X-rays (source energy of 1253.6 eV) and with charge neutralization of the samples (using a CN10 electron flood source). The instrument resolution was approximately 0.8 eV. All high-resolution spectra were collected at a pass energy of 100 eV (in constant analyzer energy (CAE) mode) and at an energy step size of 0.05 eV. All high-resolution spectra were calibrated using the C 1s line of adventitious carbon at 284.8 eV. Calculations of relative atomic concentrations were performed with the CasaXPS 2.3.16 software, using the Marquardt-Levenberg optimization algorithm.

5.3.3.6 High-Angle Annular Dark-Field Imaging (HAADF) and EELS

A probe-side aberration-corrected JEOL JEM ARM200CF with a cold field-emission gun and post-column Gatan Enfina spectrometer operated at 200 keV were used for HAADF

imaging and acquisition of EELS spectra, respectively. The collection angles for the HAADF detector were set to 90 mrad -370 mrad and the EELS spectra were acquired using a 45 mrad collection angle and 0.1 eV/channel dispersion.

5.3.3.7 XANES Spectroscopy

B K-edge XANES spectra were acquired in the energy range of 185—210 eV at the Variable Line Spacing-Plane Grating Monochromator (VLS-PGM) beamline ($E/\Delta E > 10{,}000$) of the Canadian Light Source in Saskatoon, SK. The samples were mounted in a UHV chamber at a pressure of at a pressure of 1×10^{-8} Torr. The XANES spectra were measured using the high-energy grating of the beamline yielding a spectral resolution of *ca.* 0.1 eV with entrance and exit slit widths of 100 μm. A microchannel plate detector was used to collect the fluorescence yield (FLY) signal. All spectra recorded were normalized to the intensity of the photon beam as measured by the drain current of a Ni mesh (transmission 90%) situated upstream of the sample.

5.3.4 DFT Calculations

First principles calculations were performed within the framework of density functional theory (DFT), as implemented in the Vienna ab initio simulation package (VASP),[41] applying the linear density approximation (LDA) exchange-correlation potential. The electronic configurations of the relevant elements were realized using the projector augmented wave (PAW) pseudo-potentials formalism.[42] All possible interstitial sites were identified using symmetry operations. Multiple structural relaxations were performed on

all the irreducible interstitial sites of the tetragonal cell. Convergence of the electronic structure was assumed, when changes between two consecutive steps fell below 10^{-7} eV. To assess the thermodynamic stability and obtain the formation enthalpies at infinite dilution, results obtained from calculations with supercells comprising 12, 24, 48, and 96 atoms were extrapolated.

5.4 Results and Discussion

The incorporation of B within tetrahedral holes of R-phase VO_2 has been explored using 2-allyl-4,4,5,5-tetramethyl-1,3,2-dioxaborolane as the precursor given previous reports of its ability to cleanly cleave B—C bonds at high temperatures, which has allowed for facile substitutional p-type doping of Si.[36] The diffusive annealing doping approach is a particularly attractive alternative to the *in situ* incorporation of dopants during synthesis since it allows for post-synthetic modification of previously prepared high-quality VO_2 crystals. In previous work, we have demonstrated that by controlling the reduction of V_2O_5 during hydrothermal growth by using the appropriate reducing agent in the correct concentration, the oxygen stoichiometry of the prepared VO_2 nanomaterials can be precisely controlled, yielding high crystalline quality materials that are unprecedented by other methods as characterized by the abruptness of the metal—insulator transition (within 1°C), the magnitude of the modulation of conductance (four orders of magnitude or greater), and the consistency of the electrical bandgap with the optical bandgap.[9,40] Using different reducing agents in hydrothermal synthesis allows for considerable control over the morphology and dimensions of the obtained nanomaterials.[13,40] Given that diffusive

doping is a surface-limited phenomenon, we have explored B-incorporation within three different size distributions of VO_2 nanocrystals.

The use of 2-propanol as the reducing agent yields VO_2 nanobeams that are 210±70 nm in width and 4.0±3.0 μm in length, whereas VO_2 nanobeams prepared using acetone are 180±70 nm in width and 1.6±0.9 μm in length.[43] To evaluate a further size distribution, acetone-reduced nanowires have been milled using polymer beads, which reduces the dimensions to 100±50 nm measured across the longest axis. **Figure 5.2A—C** depicts TEM images of as-prepared 2-propanol-reduced, acetone-reduced, and ball-milled acetone-reduced VO_2 nanobeams. Histograms of nanobeam and nanoparticle dimensions are shown in **Figure 5.3**. Overall, nanobeams synthesized with 2-propanol produce a large distribution of lengths spanning microns, whereas nanobeams synthesized with acetone are thinner and smaller. Ball-milling greatly reduces the dimensions of the nanowires, yielding nanorods. The DSC plots in **Figures 5.2D** and **E** illustrate heating and cooling transitions for each of these samples. As a first-order transition, the metal—insulator transition of VO_2 is characterized by a substantial latent heat and a pronounced discontinuity of the specific heat capacity. The latent heat has a lattice enthalpy component arising from the structural distortion induced as a result of the $M_1 \rightarrow R$ (or reverse) phase transition which is compensated for by a shift in phonon entropy and conduction entropy of the electrons induced as a result of charge ordering/delocalization.[44–46] The sharp and well-defined peaks observed for the heating and cooling transitions, respectively, attest to the high crystalline quality of the as-prepared VO_2 nanowires.[9,40] The observed elevation of the heating transition (to 73°C) and depression of the cooling transition (to 58°C) for

the ball-milled samples are thought to be derived from an extended kinetic stabilization of the phases induced as a result of a diminished density of nucleation sites available upon scaling to nanometer-sized dimensions.[18,19,47]

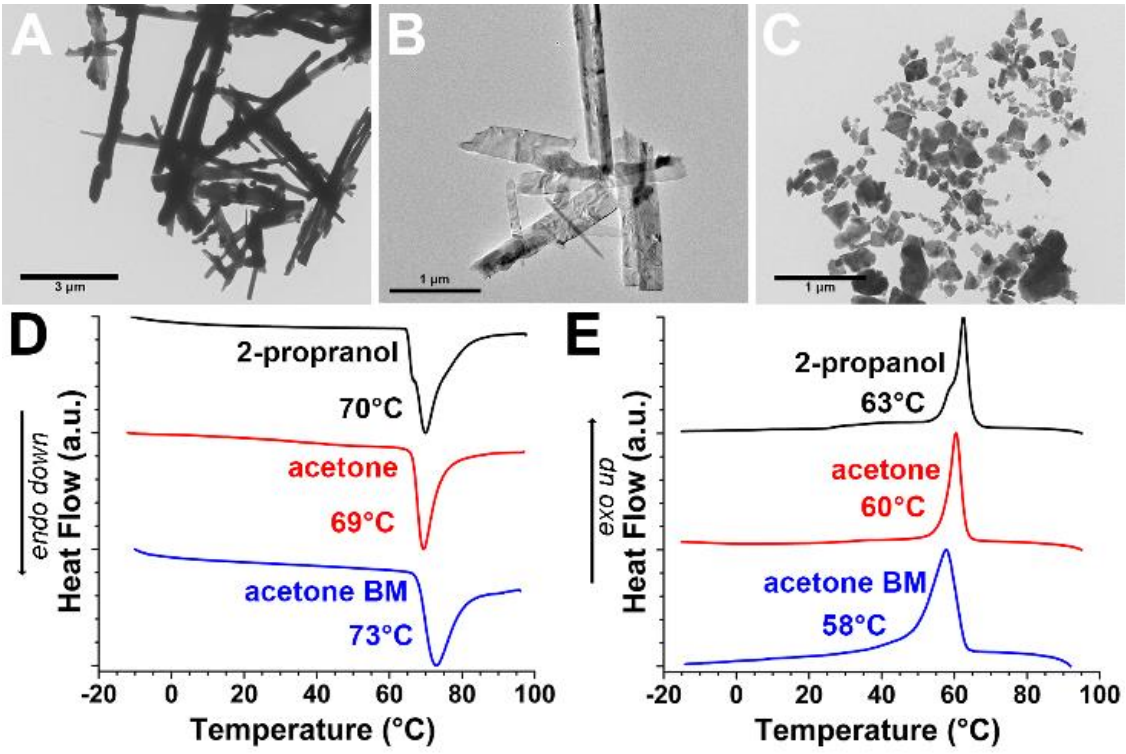

Figure 5.2: TEM micrographs of VO_2 nanobeams prepared by reduction of V_2O_5 by A) 2-propanol, B) acetone, and C) acetone, followed subsequently by ball-milling. The corresponding size distribution histograms are provided as **Figure 5.3**. DSC (D) heating and (E) cooling traces measured for the VO_2 nanobeams.

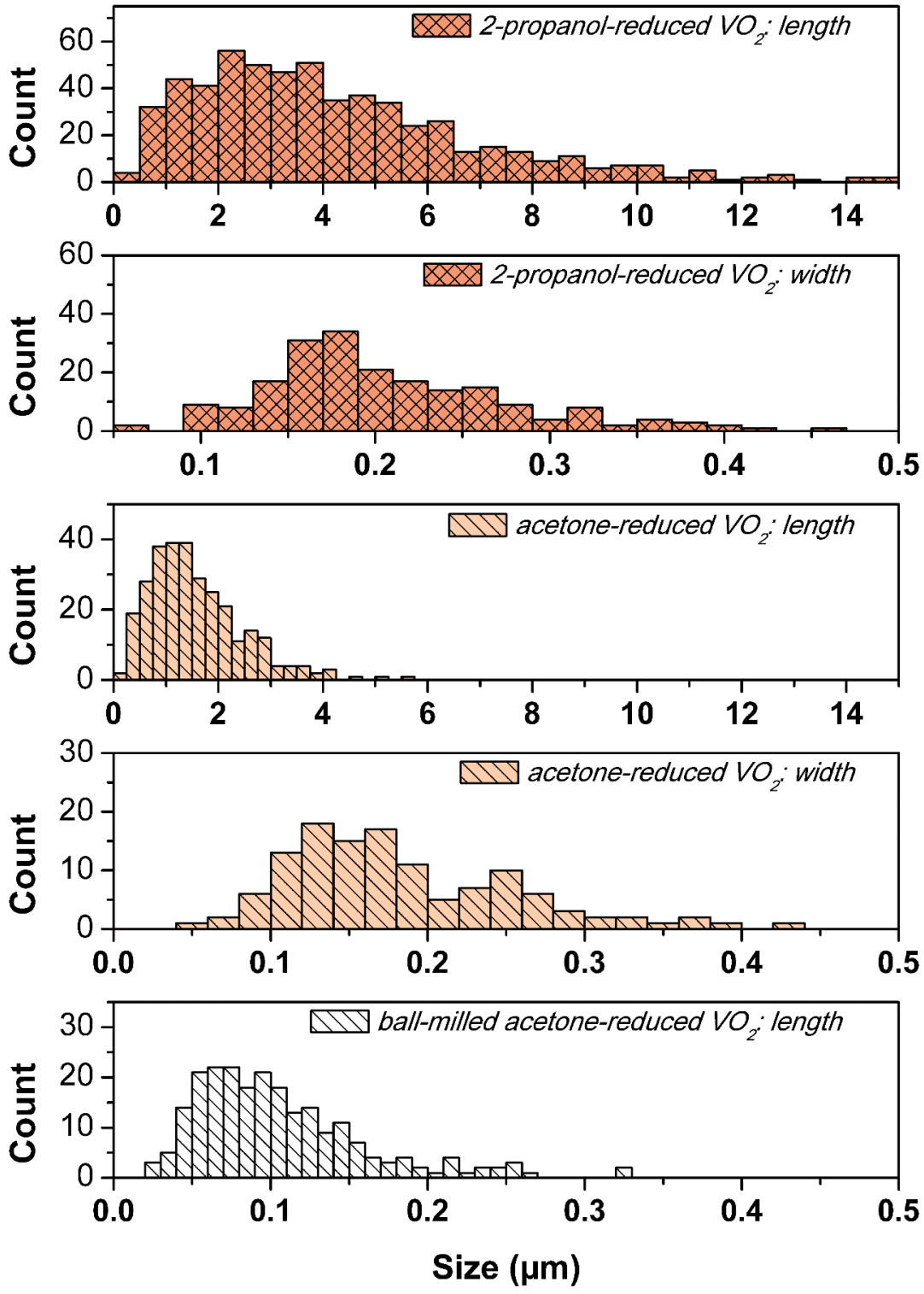

Figure 5.3: Size distribution histograms for 2-propanol-reduced, acetone-reduced, and acetone-reduced with ball-milled VO_2. The dimensions are derived from TEM images.

Figure 5.4 schematically illustrates the diffusive doping process adapted from monolayer doping of Si and III-V semiconductors.[36] As a surface-limited reaction, it is anticipated that the extent of doping will vary greatly with dimensions of the free-standing nanobeams.[36,38,39] An initial surface adsorption step is followed by diffusive annealing, which promotes the simultaneous cleavage of bonds within the anchored precursor and either 1) the thermal diffusion of dopant molecules (and residual products) into the substrate and 2) the removal of products with Ar flow. As the surface-area-to-volume ratio increases with decreasing particle size, it is expected that smaller particles will incorporate greater amounts of the dopant and that the dopant will be uniformly distributed within smaller particles. Infrared spectroscopy does not show establishment of covalent linkages; physisorption is the presumed adsorption process given the lack of functionality in 2-allyl-4,4,5,5-tetramethyl-1,3,2-dioxaborolane that can be grafted onto VO_2.

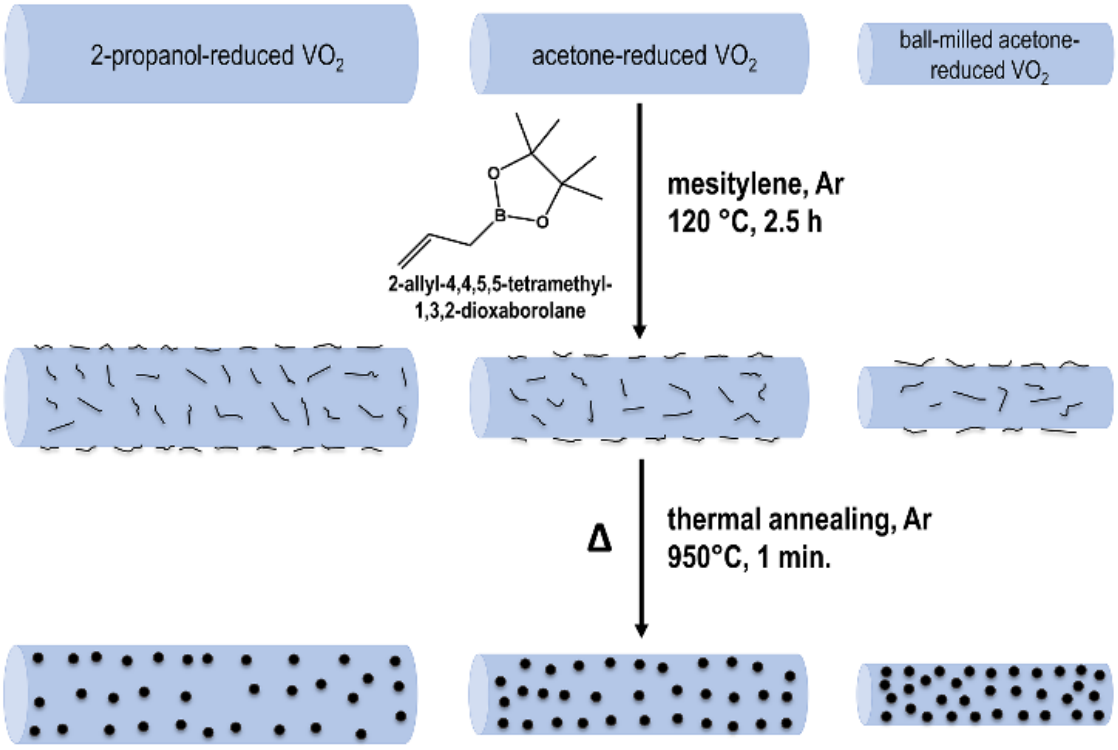

Figure 5.4: Schematic illustration of the diffusive boron doping of VO_2 nanobeams. Greater B incorporation is expected for smaller particles as a result of their greater surface-area-to-volume ratio.

The effect of substitutional incorporation on both the cation and the anion sublattices is to greatly modify the relative phase stabilities of the M_1 and R phases as well as to potentially stabilize the metastable M_2 and triclinic phases.[1,48] The close coupling of lattice, orbital, and spin degrees of freedom renders these polymorphs energetically quite accessible with minor perturbations. In the best studied case of W as a substitutional dopant, substitutional incorporation of hexavalent tungsten cations on the vanadium sublattice increases the stabilization of the R phase as a result of (a) an electronic effect arising from two electrons being added to the band structure per dopant cation (resulting in an increased carrier density); and (b) a structural effect involving a pronounced

anisotropic strain normal to $(12\bar{2})$ planes of the M_1 phase and an increase of local symmetry around the incorporated W atoms resulting in de-pairing of V—V dimers of the M_1 phase.[48–50]

Figure 5.5 examines the influence of diffusive B doping on the phase stabilities and metal—insulator transition temperatures of the three size distributions of VO_2 nanobeams noted above. **Figure 5.6** shows TEM images of the nanobeams suggesting substantial sintering upon diffusive annealing at 950°C. We have previously noted that annealing at temperatures greater than 600°C promotes the sintering of nanostructures into larger grains.[40] In each case, three DSC traces are depicted corresponding to the sample treated by diffusive annealing (labeled **1**), a control sample that is annealed under the same conditions without the B precursor (labeled **2**), and the as-prepared sample (labeled **3**). **Figure 5.7** suggests that the control samples have similarly been sintered into larger grains.

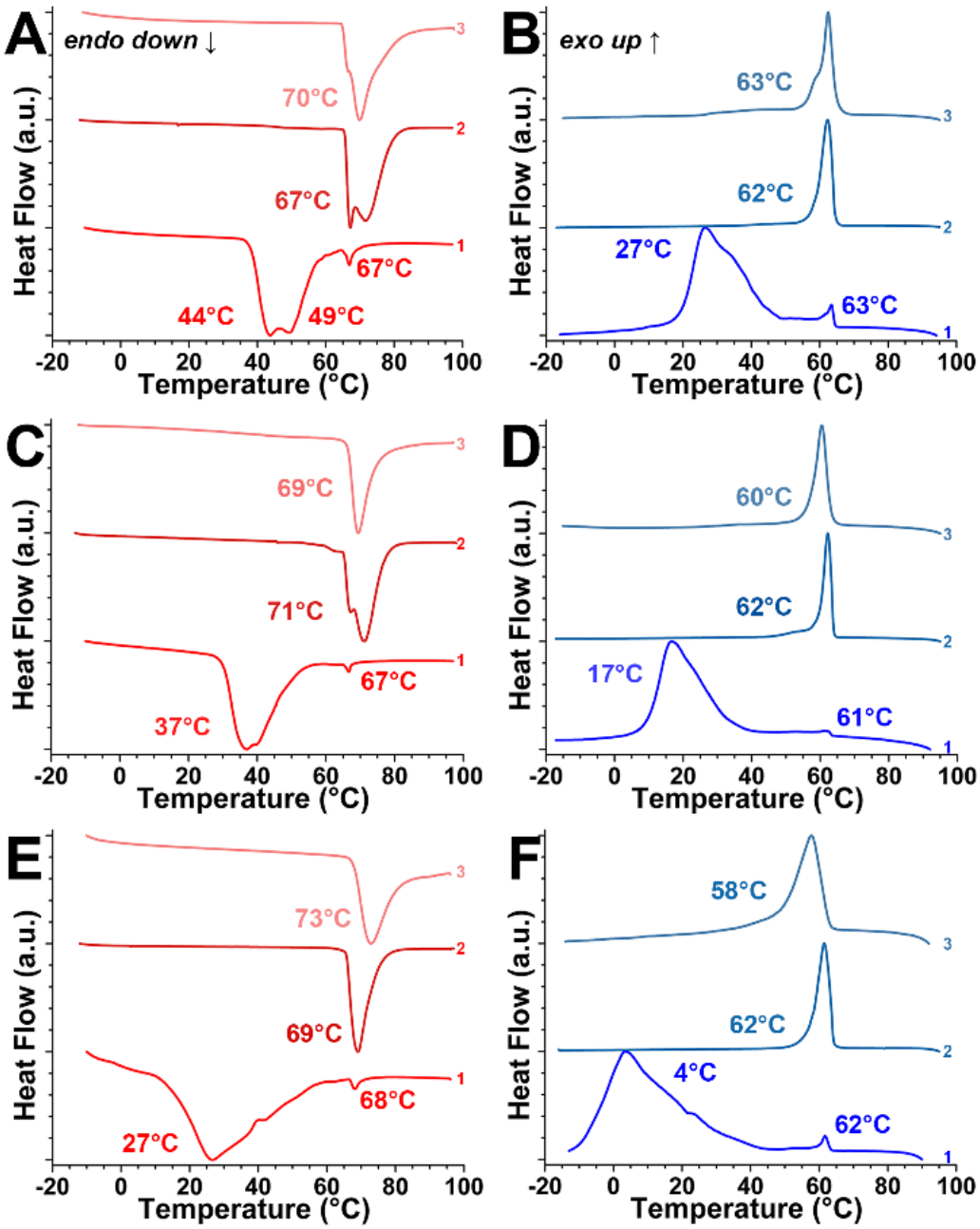

Figure 5.5: DSC traces acquired during a heating ramp for samples derived from A) reduction of V_2O_5 by 2-propanol; C) reduction of V_2O_5 by acetone, and E) reduction of V_2O_5 by acetone followed by ball-milling. Panels B, D, and F plot the cooling traces corresponding to A, C, and E, respectively. In each panel, the following samples are compared: 1: VO_2 sample prepared by diffusive B doping; 2: VO_2 sample annealed without exposure to the molecular B precursor; and 3: as-prepared samples.

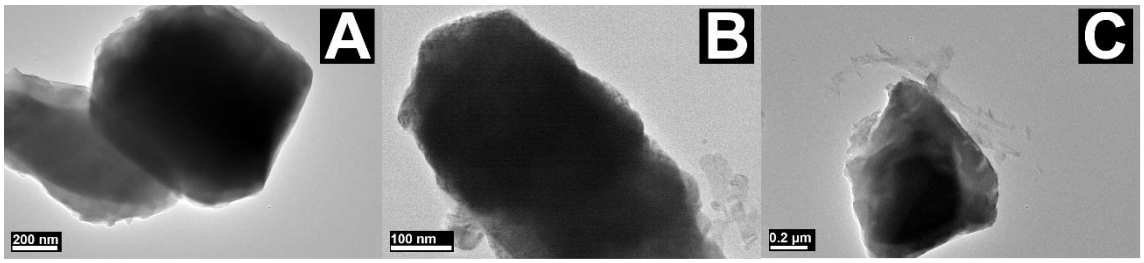

Figure 5.6: TEM images of B-incorporated samples of VO_2 nanowires reduced from A) 2-propanol, B) acetone, and C) acetone, subsequently ball-milled.

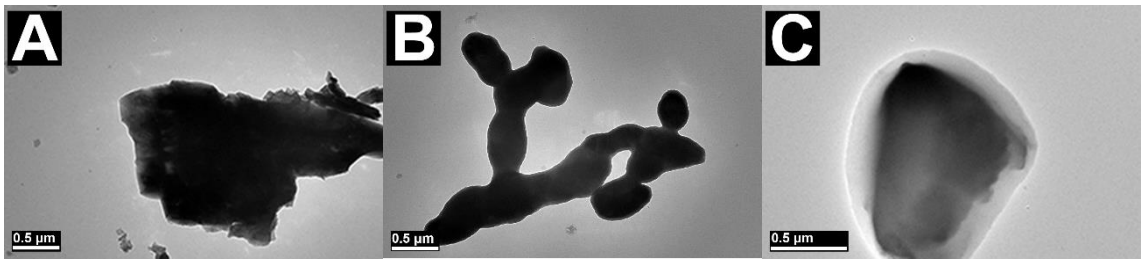

Figure 5.7: TEM images of VO_2 nanowires reduced from A) 2-propanol, B) acetone, and C) acetone, subsequently ball-milled annealed without exposure to the molecular B precursor.

Table 5.1 provides a summary of the transition temperature values derived from the DSC traces in **Figure 5.5**. For the samples prepared by hydrothermal reduction of V_2O_5 by 2-propanol and acetone, no substantial alteration of the transition temperatures is observed for the control samples that are annealed without first depositing the molecular B precursor. The observed hysteresis between the endothermic heating and exothermic cooling transition is indeed characteristic of first-order transitions. For the ball-milled sample with initial dimensions of 100±50 nm, the heating and cooling temperatures are decreased and increased, respectively, and become closer to the equilibrium transition temperatures of bulk VO_2. This behavior is thought be a result of sintering and grain growth (as evidenced in **Figure 5.7C**), which once again makes available a large density

of potential nucleation sites precluding kinetic stabilization of the M_1 and R phases beyond the equilibrium transition temperatures. Interestingly, upon B-incorporation by diffusive annealing, the large 2-propanol derived VO_2 samples are characterized by a substantial depression of both the heating and cooling transition temperatures. A bimodal distribution centered at 44 and 49°C is observed for the heating transition, whereas the cooling transition exhibits an anisotropic spread centered at *ca.* 27°C (**Figures 5.5A** and **B**). The bimodal spread is attributed to inhomogeneous or gradient incorporation of B as a result of the larger initial dimensions of these nanobeams. Indeed, for thinner acetone-derived nanobeams, a greater and relatively more homogeneous depression of the heating and cooling transition temperatures to 37 and 17°C, respectively, is observed (**Figures 5.5C** and **D**). For the smallest samples derived from ball-milling, the modulation of the heating and cooling temperatures is much more pronounced, down to 27 and 4°C, respectively, indicative of much greater B incorporation (**Figures 5.5E** and **F**). In both the heating and cooling plots, contributions from pristine VO_2 are still discernible (*ca.* 67 and 62°C), indicative of a small amount of undoped VO_2 within the sample. The increased homogeneity with smaller initial grain size is characteristic of diffusive doping or ion implantation processes and reflects a greater probability of dopant incorporation at shorter diffusion lengths.[38] It is also noteworthy to mention that all the B-incorporated samples exhibit an increased hysteresis, which has also been previously observed for W doping, as compared to the as-prepared and control samples (which have a value of *ca.* 7—15°C). In particular, the 2-propanol-derived doped sample has a hysteresis of 17—22°C, the acetone-derived doped sample has a hysteresis of 20°C, and the ball-milled acetone-

derived doped sample has a hysteresis of 23°C. Notably, dopant incorporation appears to be stable up to temperatures of 950°C unlike hydrogen incorporation where annealing to a temperature of 130°C results in elimination of interstitial hydrogen.[34]

Table 5.1: Transition temperatures of VO_2 samples doped by diffusive annealing contrasted to controls that are annealed without exposure to the molecular B precursor and the as-prepared VO_2 nanowires.

Dimensions of VO_2 Nanobeams and Mode of Processing		**Transition Temperature (°C)**	
		Heating ($M_1 \rightarrow R$)	**Cooling ($R \rightarrow M_1$)**
210±70 nm, 4.0±3.0 μm (*2-propanol)*	as-prepared	70	63
	control	67	62
	doped	44, 49	27
180±70 nm, 1.6±0.9 μm *(acetone)*	as-prepared	71	58
	control	71	62
	doped	37	17
100±50nm *(acetone, ball-milled)*	as-prepared	73	58
	control	69	61
	doped	27	4

Given the ability to tune the extent of incorporation of B based on dimensions of the particles and temperature, **Figure 5.8** depicts DSC traces acquired upon diffusive B incorporation within acetone-derived VO_2 nanobeams. **Table 5.2** lists atomic percentages for B as determined from high-resolution XPS scans by integrating the areas of spectral peaks assigned to V 2p, O 1s, and B 1s (assigned as per the NIST XPS Database).[51] **Figure 5.9** depicts high-resolution B 1s XPS spectra. The B 1s peaks are centered in the 191—192 eV range, which Quesada-González *et al*. have attributed to interstitial B in the case of doped TiO_2.[52] The spectra can be fitted to a single chemical species suggesting homogeneous incorporation at these concentrations. A clear monotonic correlation is evidenced between the amount of B incorporation and the depression of both the cooling

and heating transition temperatures. The concentration of B incorporated was primarily modulated by changing the surface-to-volume ratio of the initial VO_2 sample due to the surface limiting adsorption reaction of the B-precursor.

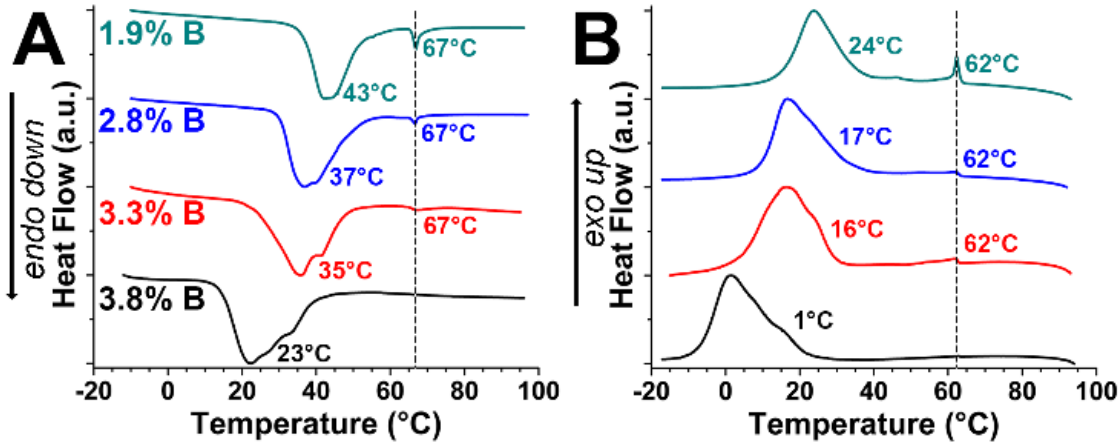

Figure 5.8: DSC (A) heating and (B) cooling traces for VO_2 samples with increasing B incorporation via diffusive doping. The B content is derived from XPS measurements shown in **Figure 5.9**.

Table 5.2: Correlation between atomic concentrations of B incorporated as determined from XPS studies and heating and cooling transition temperature as determined by DSC.

B at.% (at 95 % confidence level)	Transition Temperature (°C)	
	Heating	Cooling
3.8±2.0	23	1
3.3±1.6	35	16
2.8±1.4	37	17
1.9±1.0	43	24

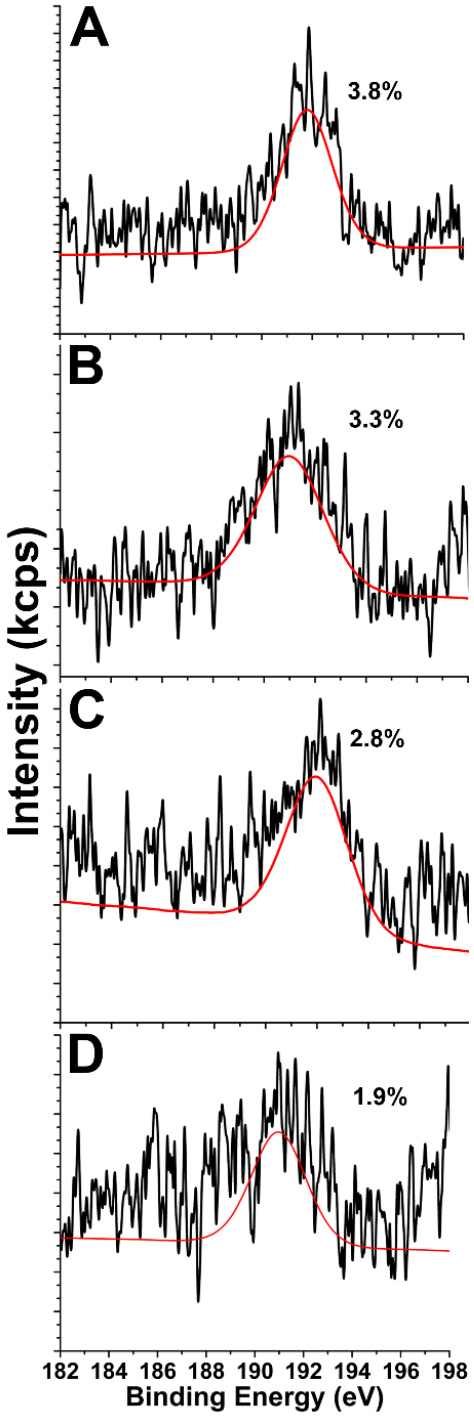

Figure 5.9: High-resolution B 1s XPS spectra of B-incorporated VO_2 samples with increasing B content. All fits (shown in red) are plotted as B-spline functions.

Figure 5.10 shows that an approximately linear correlation can be drawn between the depression of heating and cooling temperatures and the incorporation of B within this range of B concentrations. An approximately 10°C/at.% of B depression of the transition temperatures is observed. The linear correlation of the transition temperature with B content and the singular boron species suggests that B resides within a consistent local environment across these concentrations. Interestingly, the hysteresis is not strongly modified with increasing incorporation of B. Adventitious carbon detected by XPS did not notably increase upon B incorporation and no carbides were observed.

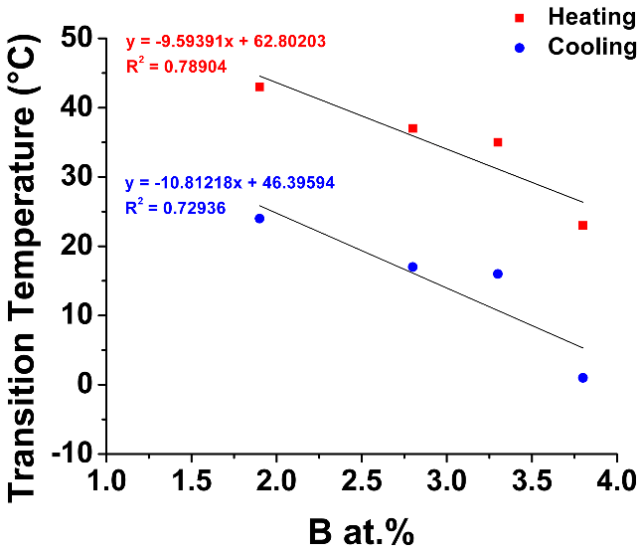

Figure 5.10: Linear relationship between B at.% and VO_2 transition temperatures.

The phase transition of B-incorporated VO_2 has been examined by temperature-dependent powder XRD and Raman spectroscopy in order to examine the influence of doping on the phase stabilities. **Figure 5.11** depicts *in situ* powder XRD patterns (**A, C**) and Raman spectra (**B, D**) of the 2.8 at.% B-doped VO_2 sample acquired upon heating and

cooling. The *in situ* heating and cooling XRD patterns shown in **Figures 5.11A** and **C**, respectively, have been collected in the temperature range from 30 to 100°C and are indexed to the M_1 (Joint Committee on Powder Diffraction Standards (JCPDS) 43-1051) and R (JCPDS 79-1655) phases of VO_2. A minority Magneli phase of V_8O_{15} (JCPDS 18-1448) is also detected at higher B concentrations and is thought to arise from increased VO_2 reduction (it does not however contribute to the observed metal—insulator transition since the transition temperature for this phase is 70 K).[53] No evidence is observed for the orthorhombic VO_2 phase stabilized by hydrogen incorporation.[7,54] **Figures 5.11A** and **C** highlight the 2θ range from 54—70°, which corresponds to reflections that are most greatly altered across the phase transition. **Figure 5.12** depicts the same powder XRD patterns across an extended 2θ range from 20 to 70°. **Figure 5.13** and **Table 5.3** present results of a Rietveld refinement to the room temperature pattern. Upon heating, **Figure 5.11A** indicates a pronounced splitting of the reflection indexed to the (013) planes of the M_1 polymorph at 2θ = 65° to reflections that can be indexed to the (310) and (002) planes of the R phase.[55] The splitting characteristic of the R phase is most clearly discernible at 50°C at which point the sample is predominately in the R phase. However, between 30—45°C the XRD patterns exhibit reflections associated with both M_1 and R phases, for instance, the (002) reflection (2θ = 65.2°) of the R phase appears alongside the broader reflections indexed to the ($\bar{4}02$) (2θ = 64.8°) and (013) (2θ = 65.0°) reflections of the M_1 phase. Similarly, between 30°C—45°C, broader reflections at 55° and 57° correspond to overlapping reflections attributed to the M_1 and R phases until 50°C, at which point the reflections shift and narrow to the characteristic reflections of the R phase. The

coexistence of the M_1 and R phases is in agreement with the dispersion of the phase transition temperature range shown in the DSC trace for the same sample in **Figure 5.8A**. In contrast, upon cooling **Figure 5.11C** depicts that the R phase is retained down to 30°C corresponding to the substantial hysteresis noted in **Figure 5.8** wherein the M_1 phase is not recovered until temperatures below 17°C.

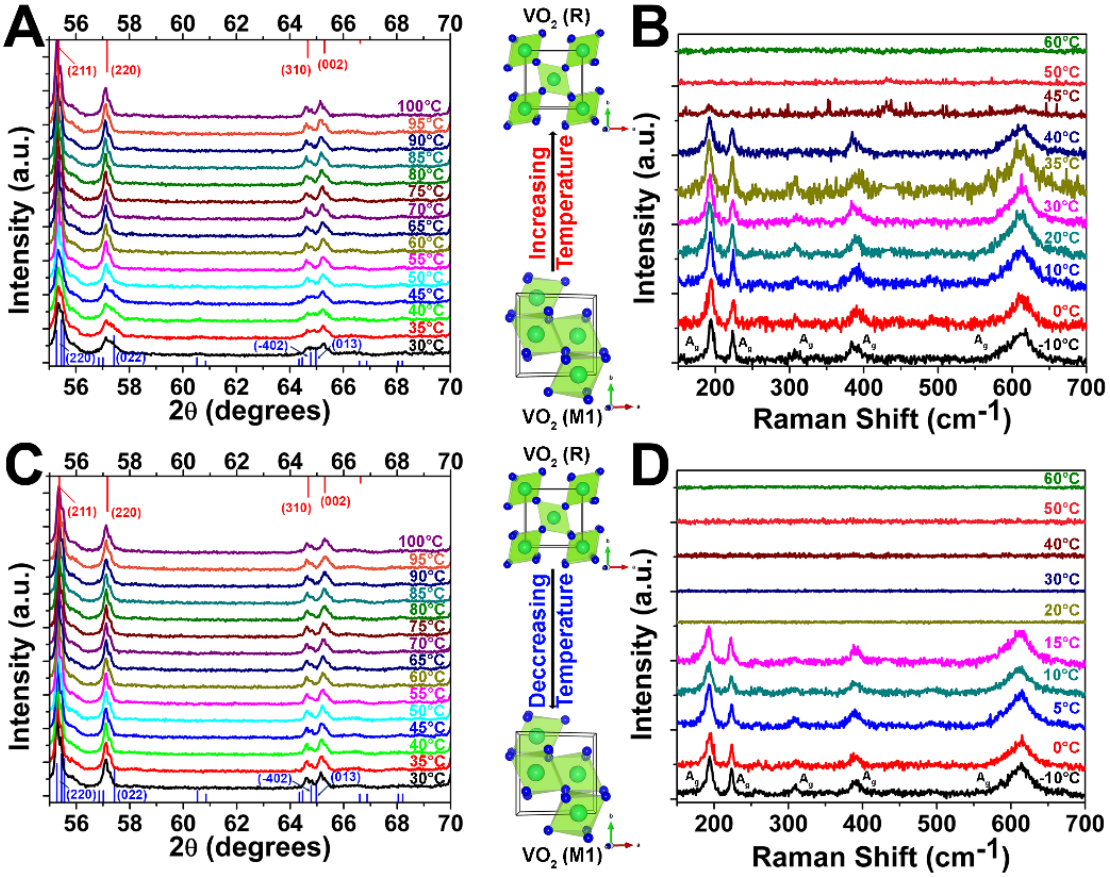

Figure 5.11: *In situ* heating (A) and cooling (C) powder XRD patterns measured for a VO_2 sample incorporating 2.8 at.% B collected at 5°C increments in the temperature range from 30 to 100°C. The vertical bars indicate positions and relative intensities of reflections derived from JCPDS XRD patterns. XRD patterns are shown in the 2θ range from 54—70°. Reflections of $VO_2(M_1)$ are indicated in blue (JCPDS # 43-1051) and VO_2(R) in red (JCPDS # 79-1655). *In situ* heating (B) and cooling (D) Raman spectra acquired for the same sample collected in the temperature range from -10 to 60°C. The crystal structures of the M_1 and R phases are depicted as insets; the green spheres represent V atoms whereas the blue spheres represent O atoms.

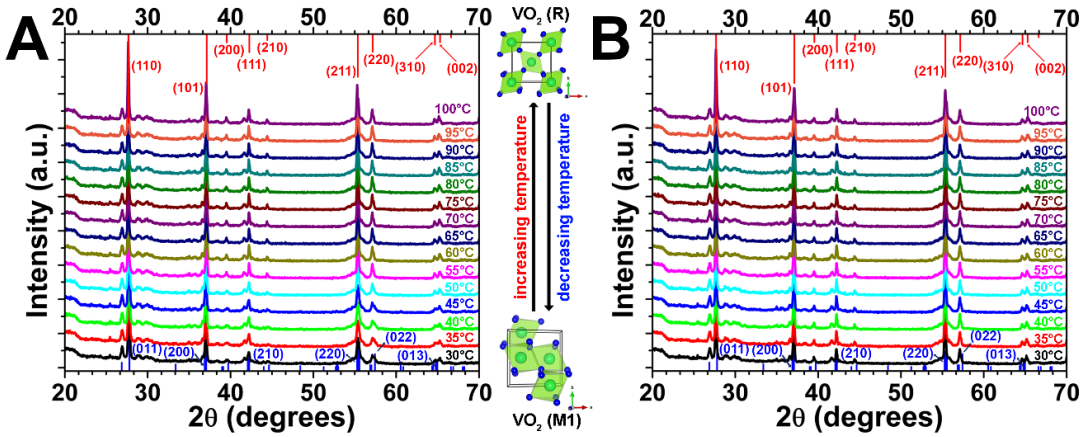

Figure 5.12: XRD patterns corresponding to *in situ* heating (a) and cooling (c) of a B-incorporated VO_2 sample collected at 5°C increments from 30 to 100°C. Vertical bars indicate positions and relative intensities of reflections derived from JCPDS XRD patterns. Reflections of $VO_2(M_1)$ are indicated in blue (JCPDS # 43-1051) and VO_2(R) in red (JCPDS # 79-1655).

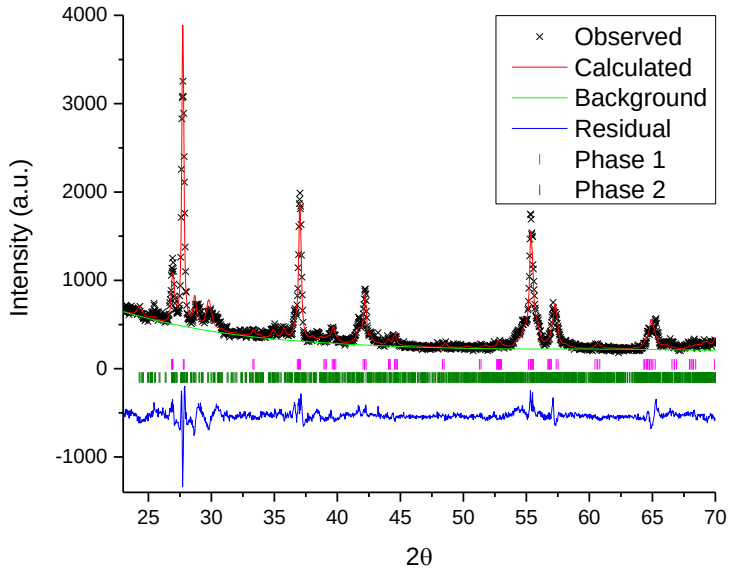

Figure 5.13: Rietveld refinement of powder XRD pattern of 2.8 at.% B-doped VO_2 nanocrystals acquired at 295 K (see **Table 5.3** for details). Pink tick marks indicate the position of reflections corresponding to the $P2_1/c$ monoclinic space group of VO_2 whereas green tick marks indicate the position of reflections corresponding to the $\mathbf{P\bar{1}}$ triclinic space group of V_8O_{15}.

Table 5.3: Tabulated parameters from a Rietveld refinement of 2.8 at.% B-doped VO_2 structure. Refinement statistics, including goodness of fit (χ^2), weighted goodness of fit (wRp) and the individual point residuals (Rp) show good agreement between the observed and calculated patterns.

Phase 1: VO_2 (M_1) // Space Group: $P2_1/c$ // Weight. Fraction: 0.55810 // Volume: 118.70(3)Å^3		
$\alpha = 90.000(0)°$	$\beta = 122.31(2)°$	$\gamma = 90.000(0)°$
a = 5.7424(8)	b = 4.539 (1)	c= 5.388(2)
$X^2 = 4.511$	wRp = 0.1040	Rp = 0.0834
Phase 2: V_8O_{15} (triclinic) // Space Group: $P\bar{1}$ // Weight Fraction: 0.44190 // Volume: 916.095(0)Å^3		
$\alpha = 98.90(4)°$	$\beta = 128.46(3)°$	$\gamma = 109.12(3)°$
a = 5.450(3)	b = 7.011(2)	c = 37.04(1)
$X^2 = 4.511$	wRp = 0.1040	Rp = 0.0834

Figures 5.11B and **D** show *in situ* Raman spectra of the same 2.8 at.% B-doped VO_2 sample collected at various temperatures upon heating and cooling. Based on symmetry considerations, the insulating M_1 phase has 18 Raman-allowed modes, nine of which are of A_g symmetry, whereas the other nine are of B_g symmetry.[56–59] In contrast, the metallic R phase exhibits a broad featureless spectrum, and does not show any Raman-allowed modes as a result of its highly reflective metallic character and high carrier density (which also greatly diminishes the laser penetration depth).[56,58] **Figure 5.11B** shows that the B-doped sample remains in the M_1 phase in the range from -10 to 40°C; the Raman signal is substantially attenuated at 40°C and then greatly diminished starting at 45°C indicating nucleation and substantial conversion to the R phase (these temperatures thus correspond to a phase coexistence regime as also observed by powder XRD);[55,56] complete conversion to the R phase is observed at temperatures beyond 50°C. The observed transition behavior is concordant with the DSC profile for this sample plotted in **Figure 5.8**. Analogously, **Figure 5.11D** indicates that upon cooling, modes corresponding to the

M_1 phase are recovered only at 15°C. Importantly, the Raman and XRD measurements indicate interconversion between M_1 and R phases without stabilization of the metastable M_2 phase, which is known to be stabilized by trivalent doping and upon the application of strain.[27,60] The M_2 polymorph of VO_2 is thrice more insulating than the M_1 phase and is characterized by distinctive Raman modes that are blue-shifted from the 189 and 607 cm^{-1} A_g modes of the M_1 phase (the 221 cm^{-1} A_g mode of the M_1 phase is further split into two distinct modes in the M_2 phase).[1,61–63] In other words, both Raman and powder XRD results suggest that the interconversion of M_1 and R phases (and the accompanying metal—insulator transition) is not mediated by stabilization of the M_2 phase despite the potential trivalency of the incorporated B atoms.

Further examination of the mode of dopant incorporation has been explored using HAADF STEM imaging (**Figure 5.14A—C**), EELS (**Figure 5.14D** and **E**), and XANES spectroscopy (**Figure 5.15**). **Figures 5.14A** and **B** indicate an atomic resolution HAADF STEM image and fast Fourier transform (FFT) acquired along the [111] zone axis for the same 2.8 at.% B-doped VO_2 doped sample. The atomic-resolution image and the FFT match well with a simulated diffraction patterns for VO_2(R) along the [111] zone axis (**Figure 5.14C** and **D**), suggesting stabilization of the R-phase. The stabilization of the R-phase is indeed concordant with the DSC traces shown in **Figure 5.8**, which indicate that as a result of the pronounced hysteresis (outside of the systematic temperature-controlled DSC experiment) samples at room temperature contain a mix of the M_1 and R phases as a result of the pronounced depression of the transition temperature brought about by B doping. While low-atomic-number B is not directly observed, the HAADF images do not

show any systematic intensity variations along the atomic columns and furthermore no evidence of strain is observed in these images. Notably, W atoms were distinguishable in substitutional sites and strong localized strain gradients were clearly discernible even at relatively low W concentrations in previous HAADF STEM studies of W-doped VO_2.[48]

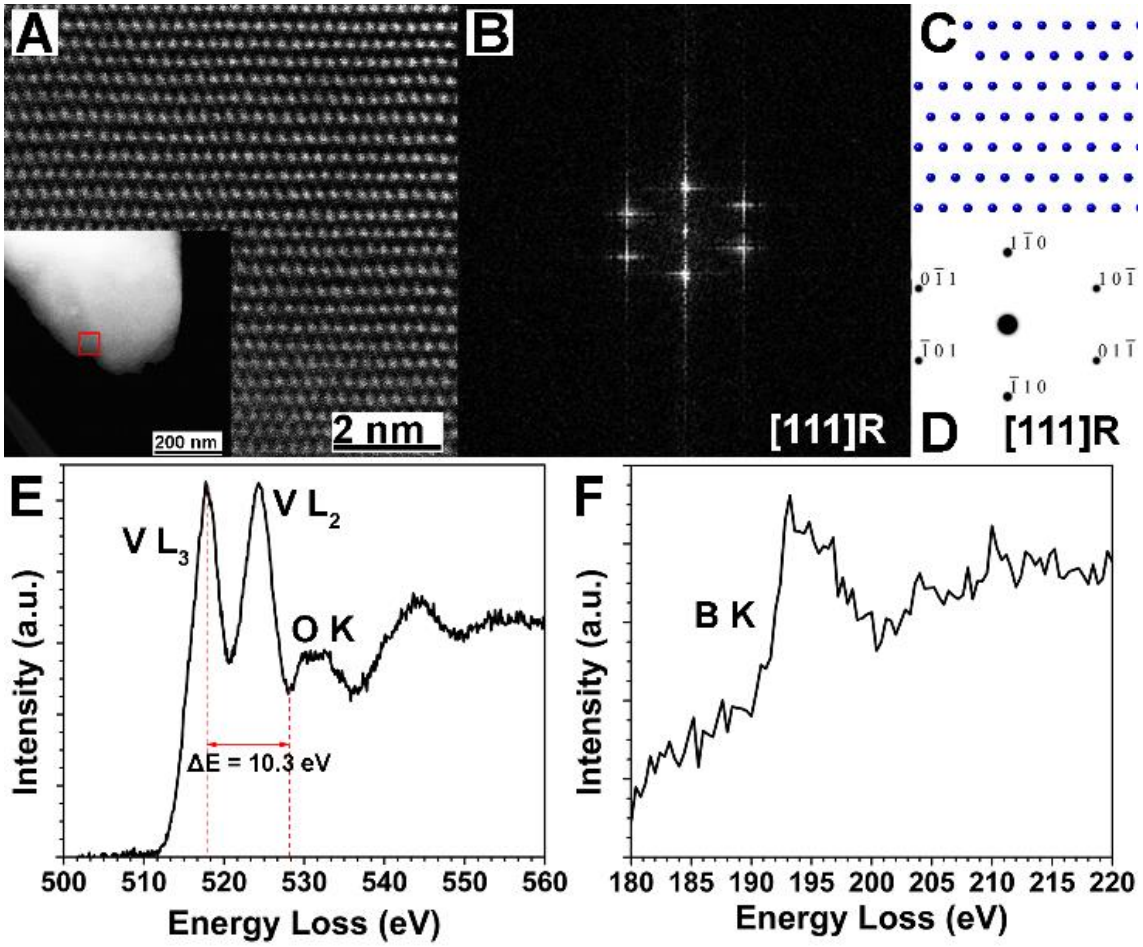

Figure 5.14: Scanning transmission electron microscopy (STEM) analysis of a VO_2 sample incorporating 2.8 at.% B. A) Atomic-resolution HAADF image (the inset shows a low-magnification view of the analysis area) and B) Fast-Fourier Transform (FFT) of (A) acquired along the [111] zone axis of the nanowire. C) Solid sphere reconstruction of the R structure corresponding to the [111] zone axis and D) simulated diffraction pattern based on (C), both confirming the R structure of the sample. E) V L-edge/O K-edge and F) B K-edge EELS spectra acquired for the B-doped VO_2 sample.

Figure 5.14F shows an averaged core-loss B K-edge EELS spectrum acquired for the same B-doped sample; a broad absorption centered at *ca.* 194 eV confirms the presence of B in VO_2. The presence of a singular B absorption feature further suggests homogeneity in terms of the mode of dopant incorporation. A core-loss EELS spectrum has also been collected at the V L- and O K-edges, as shown in **Figure 5.14E**. The oxidation state of V has been deduced from the V L_3- and O-K-edges,[64] by calculating the energy difference ΔE.[48] This value is found to be 10.3 eV, which corresponds to a vanadium oxidation state of +4. The overall retention of the oxidation state of vanadium is consistent with the retention of the VO_2 structure.[13,20,48] No interstitial carbon is detected in EELS measurements.

The local structure of the incorporated dopants has been further probed by B K-edge XANES spectroscopy. XANES involves the excitation of core-level electrons to partially occupied and/or unoccupied states and thus serves as a sensitive element-specific probe of the local electronic structure.[65,66] Fleet and Liu have extensively explored the electronic structure of tetrahedrally- and trigonally-coordinated boron in various compounds and have compiled a valuable and extensive compendium of B K-edge spectra.[67] **Figure 5.15A** shows the XANES B K-edge spectra of 3.3 at.% B-doped VO_2, along with spectra acquired for various B-containing compounds wherein the crystallography of the B sites is well established. Several prominent absorption features for the model compounds are labeled in the graph and are assigned to specific electronic transitions as listed in **Table 5.4**. The feature labeled *a* centered at 191.3 eV is assigned to excitation of a B 1s core electron to π^* states (derived primarily from unoccupied B $2p_z$

orbitals) of a C—B—C bond.[68] The absorption labeled *b* centered at 192.3 eV corresponds to the B 1s → π* transition of sp^2-hybridized planar boron compounds.[66,69] This peak is thus notably absent in tetrahedrally-bonded (sp^3) compounds of boron. The feature labeled *c* centered at 194.4 eV denotes the B 1s → π* transition to final states corresponding to anti-bonding B—O interactions in trigonally-coordinated boron compounds.[66,67,70] The feature labeled *d* centered at 198.0 eV corresponds to B 1s → σ* transitions of sp^3-hybridized tetrahedral geometries, usually associated with B—O bonds such as within the BO_4 group.[67] Finally, the feature labeled *e* centered at 203.0 eV corresponds to excitation of B 1s core electrons to σ* states of trigonal B—O bonds.[67,70]

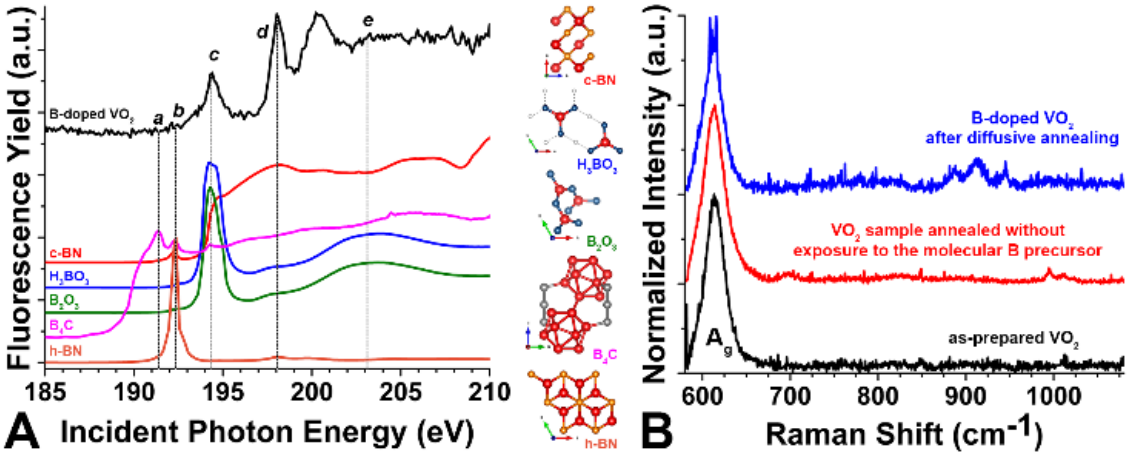

Figure 5.15: A) B K-edge XANES spectra of a VO_2 sample with *ca.* 3.3 at.% B incorporated by diffusive annealing alongside spectra acquired for various boron standards, cubic BN, hexagonal BN, rhombohedral B_4C, B_2O_3 and H_3BO_3. The crystal structures of these compounds are shown next to the plots and highlight the local bonding geometry of B atoms in each case; the colors of the spheres represent the following atoms: red: B, blue: O, white: H, gray: C, and orange: N. B) Raman spectra of B-doped VO_2 and two control samples, as-prepared VO_2 and VO_2 after diffusive annealing but in the absence of the B precursor. In this instance diffusive annealing led to incorporation of *ca.* 1.3 at.% B. The spectrum of as-prepared VO_2 is also shown.

Table 5.4: Assignment of spectral features in B K-edge XANES spectra to specific electronic transitions.

Label	Incident Photon Energy (eV)	Assignment
a	191.3	B 1s → π* C—B—C
b	192.3	B 1s → π* (planar)
c	194.4	B 1s → π* B—O (trigonal)
d	198.2	B 1s → σ* B—O (tetrahedral)
e	203.0	B 1s → σ* B—O (trigonal)

The absorption feature labeled *a* is only observed in the spectrum for B_4C, a rhombohedral compound. This compound has another feature at 192.3 eV, which can be attributed to excitation of B 1s electrons to anti-bonding states of inter-icosahedral B—B bonds within B_4C.[68] This feature is strongly overlapped with the 1s → π* transition of h-BN. The absorption labeled *c* is observed for H_3BO_3 and B_2O_3, which have a trigonally-coordinated B central atom. Peak *e* is likewise seen in these two compounds, characteristic of their sp^2 hybridization and corresponding to transitions to higher energy σ* B—O states. Finally, the spectrum for c-BN begins with a dominant absorption edge at *ca.* 193.8 eV, corresponding to transitions from B 1s to σ* continuum states in the conduction band.[66,69] A broad resonance at *d* observed for c-BN corresponds to transitions to B—N σ* states. Peak *b* is also present in the spectrum acquired for c-BN, and is likely due to the presence of h-BN impurities within the standard.

Figure 5.16 depicts the evolution of the B K-edge spectra for VO_2 with surface deposited 2-allyl-4,4,5,5-tetramethyl-1,3,2-dioxaborolane after diffusive annealing. The XANES spectrum for the B-doped VO_2 shows a prominent peak at 198.2 eV, which is well aligned with the featured labeled *d* (**Figure 5.15**); the prominence of this feature suggests tetrahedral coordination of B such as within BO_4 groups[67] of the mineral sinhalite

($MgAlBO_4$). The R phase of VO_2 does have tetrahedral sites that can accommodate B atoms wherein they can hybridize with four adjacent oxygen atoms, giving rise to B—O σ* states that serve as the final state for the absorption feature labeled *d*. The feature centered at *ca.* 194.2 eV observed for B-doped VO_2 can then be assigned to excitation of a B 1s electron to a hybrid B—O π* state. A broader feature centered at *ca.* 200 eV is also observed in the spectrum. Fleet and Liu note that additional bands within the 197—200 eV range are characteristic of tetrahedral B, as observed in their experiments with $MgAlBO_4$ and monoclinic metaboric acid (HBO_2(II)).[67] The relative intensities of the π* and σ* transitions confirm a strong distortion from trigonal symmetry for the X-ray excited B atom. These measurements and the assignment of B as being interstitially incorporated are further entirely consistent with preferred sites for B incorporation deduced from DFT calculations. The hybridization of the anion sublattice with the interstitial Lewis acidic B atoms suggests concomitantly decreased V—O hybridization, which further translates to stronger V—V interactions and a higher degree of ionicity and an increased predilection for metallicity.[71]

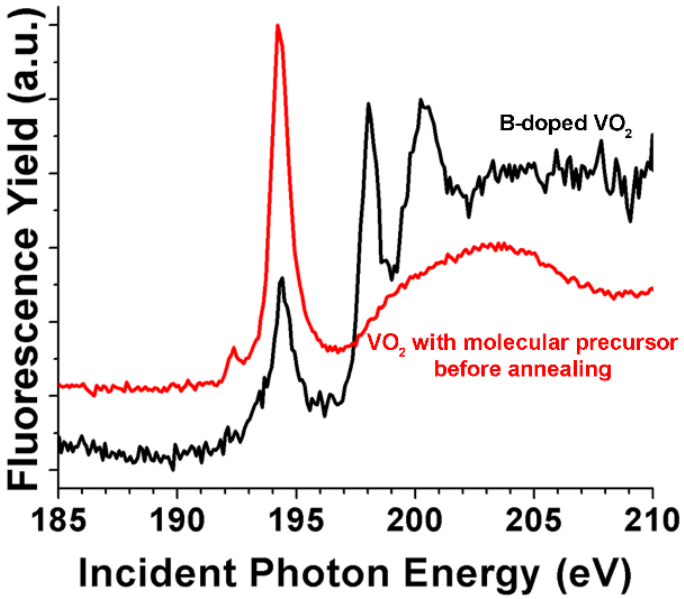

Figure 5.16: B K-edge XANES spectra of an acetone-reduced B-doped VO_2 sample before and after thermal annealing.

As another probe of dopant local structure, **Figure 5.15B** contrasts the Raman spectra of as-prepared and VO_2 annealed without exposure to the molecular B precursor with that of a sample that has been diffusively annealed with the molecular B precursor to incorporate 1.3 at.% B. Raman spectra have been acquired in the range from 580 to 1,080 cm^{-1}. For the diffusively annealed sample, we note the emergence of three additional modes at 888, 912, and 945 cm^{-1} that are not observed for as-prepared VO_2 and the sample annealed without reacting with the molecular B precursor. The appearance of these modes is intriguing especially since Pan and co-workers have suggested three possible interstitial sites in VO_2 that B can occupy after doping, each of which give rise to distinctive vibrational modes.[35] The peaks that we have observed in our Raman measurements are in close proximity with two of the calculated modes. The emergence of these modes in

Raman spectra of B-doped VO_2 thus provides compelling evidence for the B atoms being situated in interstitial sites after diffusive annealing.

In order to further examine the preferred location of B atoms, DFT calculations have been performed to determine the most thermodynamically favorable location of a B atom within the tetragonal VO_2 lattice. Formation energies (E_f) of all 10 possible interstitial sites (identified through symmetry operations) along with V and O substitutional sites were calculated using a 12-atom tetragonal supercell such that E_f is defined as:

$$E_f = E(BVO_2) - E(VO_2) - E(B) \qquad \textbf{Eq. 5.1}$$

where $E(BVO_2)$ is the total energy of a VO_2 supercell containing one B atom, $E(VO_2)$ is the energy of a pure VO_2 supercell, and $E(B)$ is the energy of a single B atom calculated to be -6.67713 eV based on a 36 atom unit cell. The three most thermodynamically viable interstitial locations are shown in **Figure 5.17A**, and are designated as *I1*, *I2*, and *I3*. All three sites are characterized by a tetrahedral coordination of the neighboring O atoms. Atomic positions of each of the interstitial sites are given in **Table 5.5**.

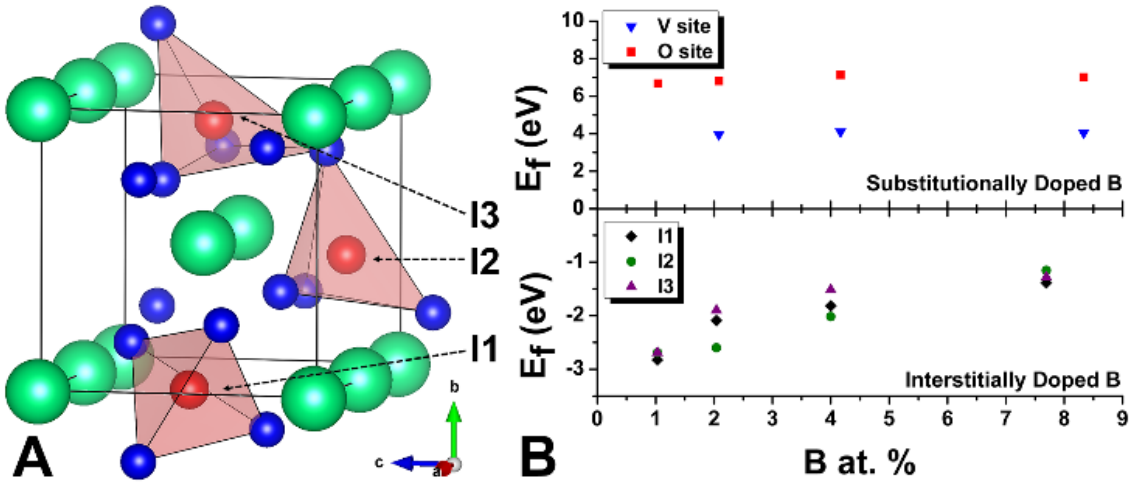

Figure 5.17: A) Calculated unit cell for B-doped VO_2, with the most thermodynamically favorable interstitial sites for B incorporation labeled *I1*, *I2*, and *I3*. All of the sites are characterized by a tetrahedral coordination of oxygen atoms. The colors of the spheres represent the following atoms: red: B, blue: O, green: O. B) Formation energy plotted as a function of B at.% for both substitutional and interstitial locations of VO_2.

Table 5.5: Fractional atomic coordinates of viable interstitial and substitutional sites for B placement within a tetragonal VO_2 assessed using DFT calculations.

Site	x	Y	z
I1	0.875000	0.000000	0.500000
I2	0.250001	0.411638	0.121699
I3	0.240321	0.875014	0.606839
V	0.500000	0.500000	0.250000
O	0.500000	0.779781	0.250000

In the high-symmetry tetragonal phase, V and O atoms each have one Wyckoff position possible for substitutional doping of a B atom, which was evaluated in conjunction with interstitial sites for comparison. Finite-size scaling using 12, 24, 48, and 96-atom supercells was employed in order to obtain E_f approaching infinite dilution for each interstitial and substitutional location and is plotted in **Figure 5.17B**. We find for a B atom substitutionally doped into a V or O site the change in E_f is positive, indicating thermodynamic instability of supercell, which does not change significantly when

extrapolating to infinite dilution. Conversely, for all three interstitial sites, E_f is negative indicating that B incorporation is thermodynamically favorable but is slightly decreased with increasing B content. The most stable interstitial locations *I1*, *I2*, and *I3* are quite similar in structure and energy. The calculations thus corroborate the pronounced energetic preference for the interstitial placement of B atoms within a tetrahedral geometry. The influence of B-doping on the transition temperature and relative phase stabilities is not reliably accessible from DFT calculations given the confounding effects of electron correlation.[8,72] Competing DMFT models can accurately predict the phase behavior of VO_2 but have yet to be extended to large supercells with low dopant concentrations.

The overall picture that emerges based on characterization of average and local structure and modification of the phase stabilities along with DFT calculations is that the molecular precursor is decomposed to yield B atoms that diffuse inwards from the surface of VO_2. Based on observation of distinctive Raman modes, B K-edge XANES measurements suggesting a tetrahedral local geometry for the B atoms, the constancy of electron density along vanadium columns in HAADF STEM images, and the strong thermodynamic preference deduced from DFT calculations, the B atoms are posited to occupy tetrahedral holes of R-phase VO_2, thereby forming interstitial dopants.[35] Such interstitial incorporation of B thermodynamically stabilizes the R phase of VO_2 based on the observed depression of the $M_1 \rightarrow R$ and $R \rightarrow M_1$ phase transitions (**Figures 5.5** and **5.8**). The increased stabilization of the R phase is explicable based on both structural and electronic arguments. In the former case, in R-phase VO_2 corner-sharing VO_6 octahedra

align linearly (with slight Jahn-Teller distortions) along the crystallographic *c*-axis with uniform V—V distances of 2.85Å.[1] When the structure transitions from R → M_1, the VO_6 octahedra dimerize and tilt along the *c*-axis resulting in alternating short and long V—V bond distances of 2.65Å and 3.12Å, respectively.[1,11] The canting of the VO_6 octahedra would reduce the volume of some interstitial sites while increasing the volume of others. The filling of interstitial sites with B atoms can thus destabilize dimerization of pairs of VO_6 polyhedra required for stabilization of the M_1 phase. Such an "obstructed volume" results in stabilization of the R-phase to substantially lower temperatures as compared to undoped VO_2. From an electronic structure perspective, B incorporation induces renormalization of electron density within the VO_2 lattice as a result of B—O interactions evidenced in B K-edge XANES spectroscopy. While the precise bonding geometry of B is unknown, B—O σ and π hybridization results in increased electron density on B, which in turn will reduce V 3d—O 2p hybridization. The subsequent weakening of V—O bonds results in decreased covalency and improved V—V overlap along the *c*-axis of the crystal structure making the lattice more metallic, and thereby stabilizing the R phase of VO_2.

5.5 Conclusions

In this contribution, we introduce a novel method for post-synthetic introduction of dopants within VO_2 based on diffusive annealing of surface-deposited molecular species. As a surface-limited method, the concentration of the dopant is controllable by tuning particle size of the VO_2 precursor. Local structure tools indicate that B is incorporated within interstitial sites, specifically the tetrahedral holes of the R phase of VO_2. The

preference for interstitial rather than substitutional incorporation is further corroborated by DFT calculations. The incorporation of B stabilizes the R phase preferentially to the M_1 phase and thereby decreases the phase transition temperature. A linear, *ca.* 10°C/at.%, depression of the transition temperature is observed with increasing B content. The thermodynamic stabilization of the R polymorph is attributed to the incorporation of B atoms impeding the 1D dimerization of [VO_6] octahedra required to stabilize the M_1 phase and the reduced covalency of V—O bonds and increased metallicity induced by B—O hybridization. The developed method provides a means to precisely "dial in" the transition temperature for pre-synthesized VO_2 as required for specific functional applications. The ability to access interstitial sites of VO_2 further provides a new structural and electronic tool for modulating the properties of this canonical metal—insulator transition material. Future work will focus on exploring a broader palette of interstitial dopants.

5.6 References

(1) Whittaker, L.; Patridge, C. J.; Banerjee, S. Microscopic and Nanoscale Perspective of the Metal-Insulator Phase Transitions of VO_2: Some New Twists to an Old Tale. *J. Phys. Chem. Lett.* **2011**, *2*, 745–758.

(2) Wang, S.; Liu, M.; Kong, L.; Long, Y.; Jiang, X.; Yu, A. Recent Progress in VO_2 Smart Coatings: Strategies to Improve the Thermochromic Properties. *Prog. Mater. Sci.* **2016**, *81*, 1–54.

(3) Morin, F. J. Oxides Which Show a Metal-to-Insulator Transition at the Neel Temperature. *Phys. Rev. Lett.* **1959**, *3*, 34–36.

(4) Imada, M.; Fujimori, A.; Tokura, Y. Metal-Insulator Transitions. *Rev. Mod. Phys.* **1998**, *70*, 1039–1263.

(5) Yang, Z.; Ko, C.; Ramanathan, S. Oxide Electronics Utilizing Ultrafast Metal-Insulator Transitions. *Annu. Rev. Mater. Res.* **2011**, *41*, 337–367.

(6) Guiton, B. S.; Gu, Q.; Prieto, A. L.; Gudiksen, M. S.; Park, H. Single-Crystalline Vanadium Dioxide Nanowires with Rectangular Cross Sections. *J. Am. Chem. Soc.* **2005**, *127*, 498–499.

(7) Wei, J.; Ji, H.; Guo, W.; Nevidomskyy, A. H.; Natelson, D. Hydrogen Stabilization of Metallic Vanadium Dioxide in Single-Crystal Nanobeams. *Nat. Nanotechnol.* **2012**, *7*, 357–362.

(8) Brito, W. H.; Aguiar, M. C. O.; Haule, K.; Kotliar, G. Metal-Insulator Transition in VO_2: A DFT + DMFT Perspective. *Phys. Rev. Lett.* **2016**, *117*, 1–6.

(9) Horrocks, G. A.; Singh, S.; Likely, M. F.; Sambandamurthy, G.; Banerjee, S. Scalable Hydrothermal Synthesis of Free-Standing VO_2 Nanowires in the M1 Phase. *ACS Appl. Mater. Interfaces* **2014**, *6*, 15726–15732.

(10) Wei, J.; Wang, Z.; Chen, W.; Cobden, D. H. New Aspects of the Metal-Insulator Transition in Single-Domain Vanadium Dioxide Nanobeams. *Nat. Nanotechnol.* **2009**, *4*, 420–424.

(11) Goodenough, J. B. The Two Components of the Crystallographic Transition in VO_2. *J. Solid State Chem.* **1971**, *3*, 490–500.

(12) Baum, P.; Yang, D.-S.; Zewail, A. H. 4D Visualization of Transitional Structures in Phase Transformations by Electron Diffraction. *Science* **2007**, *318*, 788–792.

(13) Whittaker, L.; Wu, T.-L.; Patridge, C. J.; Sambandamurthy, G.; Banerjee, S. Distinctive Finite Size Effects on the Phase Diagram and Metal–Insulator Transitions of Tungsten-Doped Vanadium(IV) Oxide. *J. Mater. Chem.* **2011**, *21*, 5580–5592.

(14) Pelcher, K. E.; Crawley, M. R.; Banerjee, S. Silica-Shell Encapsulation and Adhesion of VO_2 Nanowires to Glass Substrates: Integrating Solution-Derived VO_2 Nanowires within Thermally Responsive Coatings. *Mater. Res. Express* **2014**, *1*, 035014/1–12.

(15) Driscoll, T.; Kim, H.-T.; Chae, B.-G.; Kim, B.-J.; Lee, Y.-W.; Jokerst, N. M.; Palit, S.; Smith, D. R.; Di Ventra, M.; Basov, D. N. Memory Metamaterials. *Science* **2009**, *325*, 1518–1521.

(16) Jo, S. H.; Chang, T.; Ebong, I.; Bhadviya, B. B.; Mazumder, P.; Lu, W. Nanoscale Memristor Device as Synapse in Neuromorphic Systems. *Nano Lett.* **2010**, *10*, 1297–1301.

(17) Wu, C.; Feng, F.; Xie, Y. Design of Vanadium Oxide Structures with Controllable Electrical Properties for Energy Applications. *Chem. Soc. Rev.* **2013**, *42*, 5157–5183.

(18) Whittaker, L.; Jaye, C.; Fu, Z.; Fischer, D. A.; Banerjee, S. Depressed Phase Transition in Solution-Grown VO_2 Nanostructures. *J. Am. Chem. Soc.* **2009**, *131*, 8884–8894.

(19) Lopez, R.; Feldman, L. C.; Haglund, R. F. Size-Dependent Optical Properties of VO_2 Nanoparticle Arrays. *Phys. Rev. Lett.* **2004**, *93*, 20–23.

(20) Patridge, C. J.; Whittaker, L.; Ravel, B.; Banerjee, S. Elucidating the Influence of Local Structure Perturbations on the Metal-Insulator Transitions of $V_{1-x}Mo_xO_2$ Nanowires: Mechanistic Insights from an X-Ray Absorption Spectroscopy Study. *J. Phys. Chem. C* **2012**, *116*, 3728–3736.

(21) Wang, N.; Duchamp, M.; Xue, C.; Dunin-Borkowski, R. E.; Liu, G.; Long, Y. Single-Crystalline W-Doped VO_2 Nanobeams with Highly Reversible Electrical and Plasmonic Responses Near Room Temperature. *Adv. Mater. Interfaces* **2016**, *3*, 1600164/1–9.

(22) Zhou, J.; Gao, Y.; Liu, X.; Chen, Z.; Dai, L.; Cao, C.; Luo, H.; Kanahira, M.; Sun, C.; Yan, L. Mg-Doped VO_2 Nanoparticles: Hydrothermal Synthesis, Enhanced Visible Transmittance and Decreased Metal-Insulator Transition Temperature. *Phys. Chem. Chem. Phys.* **2013**, *15*, 7505–7511.

(23) Lee, S.; Cheng, C.; Guo, H.; Hippalgaonkar, K.; Wang, K.; Suh, J.; Liu, K.; Wu, J. Axially Engineered Metal-Insulator Phase Transition by Graded Doping VO_2 Nanowires. *J. Am. Chem. Soc.* **2013**, *135*, 4850–4855.

(24) Manning, T. D.; Parkin, I. P.; Blackman, C.; Qureshi, U. APCVD of Thermochromic Vanadium Dioxide Thin Films - Solid Solutions $V_{2-x}M_xO_2$ (M = Mo, Nb) or Composites VO_2: SnO_2. *J. Mater. Chem.* **2005**, *15*, 4560–4566.

(25) Manning, T. D.; Parkin, I. P.; Pemble, M. E.; Sheel, D.; Vernardou, D. Intelligent Window Coatings: Atmospheric Pressure Chemical Vapor Deposition of Tungsten-Doped Vanadium Dioxide. *Chem. Mater.* **2004**, *16*, 744–749.

(26) Peng, Z.; Jiang, W.; Liu, H. Synthesis and Electrical Properties of Tungsten-Doped

Vanadium Dioxide Nanopowders by Thermolysis. *J. Phys. Chem. C* **2007**, *111*, 1119–1122.

(27) Strelcov, E.; Tselev, A.; Ivanov, I.; Budai, J. D.; Zhang, J.; Tischler, J. Z.; Kravchenko, I.; Kalinin, S. V.; Kolmakov, A. Doping-Based Stabilization of the M2 Phase in Free-Standing VO_2 Nanostructures at Room Temperature. *Nano Lett.* **2012**, *12*, 6198–6205.

(28) Marezio, M.; McWhan, D. B.; Remeika, J. P.; Dernier, P. D. Structural Aspects of the Metal-Insulator Transitions in Cr-Doped VO_2. *Phys. Rev. B* **1972**, *5*, 2541–2551.

(29) Wang, N.; Duchamp, M.; E. Dunin-Borkowski, R.; Liu, S.; Ting Zeng, X.; Cao, X.; Long, Y. Terbium-Doped VO_2 Thin Films: Reduced Phase Transition Temperature and Largely Enhanced Luminous Transmittance. *Langmuir* **2016**, *32*, 759–764.

(30) Jeong, J.; Aetukuri, N.; Graf, T.; Schladt, T. D.; Samant, M. G.; Parkin, S. S. P. Suppression of Metal-Insulator Transition. *Science* **2013**, *339*, 1402–1405.

(31) Singh, S.; Abtew, T. A.; Horrocks, G. A.; Kilcoyne, C.; Marley, P. M.; Stabile, A. A.; Banerjee, S.; Zhang, P.; Sambandamurthy, G. Selective Electrochemical Reactivity of Rutile VO_2 Towards the Suppression of Metal-Insulator Transition. *Phys. Rev. B* **2016**, *93*, 125132/1–8.

(32) Ji, H.; Wei, J.; Natelson, D. Modulation of the Electrical Properties of VO_2 Nanobeams Using an Ionic Liquid as a Gating Medium. *Nano Lett.* **2012**, *12*, 2988–2992.

(33) Dahlman, C. J.; LeBlanc, G.; Bergerud, A.; Staller, C.; Adair, J.; Milliron, D. J.

Electrochemically Induced Transformations of Vanadium Dioxide Nanocrystals. *Nano Lett.* **2016**, *16*, 6021–6027.

(34) Filinchuk, Y.; Tumanov, N. A.; Ban, V.; Ji, H.; Wei, J.; Swift, M. W.; Nevidomskyy, A. H.; Natelson, D. In Situ Diffraction Study of Catalytic Hydrogenation of VO_2: Stable Phases and Origins of Metallicity. *J. Am. Chem. Soc.* **2014**, *136*, 8100–8109.

(35) Zhang, J. J.; He, H. Y.; Xie, Y.; Pan, B. C. Boron-Tuning Transition Temperature of Vanadium Dioxide from Rutile to Monoclinic Phase. *J. Chem. Phys.* **2014**, *141*, 194707/1–5.

(36) Ho, J. C.; Yerushalmi, R.; Jacobson, Z. A.; Fan, Z.; Alley, R. L.; Javey, A. Controlled Nanoscale Doping of Semiconductors via Molecular Monolayers. *Nat. Mater.* **2008**, *7*, 62–67.

(37) Ho, J. C.; Ford, A. C.; Chueh, Y. L.; Leu, P. W.; Ergen, O.; Takei, K.; Smith, G.; Majhi, P.; Bennett, J.; Javey, A. Nanoscale Doping of InAs via Sulfur Monolayers. *Appl. Phys. Lett.* **2009**, *95*, 8–11.

(38) O'Connell, J.; Biswas, S.; Duffy, R.; Holmes, J. D. Chemical Approaches for Doping Nanodevice Architectures. *Nanotechnology* **2016**, *27*, 342002/1–19.

(39) Kort, K. R.; Hung, P. Y.; Lysaght, P. D.; Loh, W.-Y.; Bersuker, G.; Banerjee, S. Raman Spectroscopy Studies of Dopant Activation and Free Electron Density of $In_{0.53}Ga_{0.47}As$ via Sulfur Monolayer Doping. *Phys. Chem. Chem. Phys.* **2014**, *16*, 6539–6543.

(40) Whittaker, L.; Zhang, H.; Banerjee, S. VO_2 Nanosheets Exhibiting a Well-Defined

Metal-Insulator Phase Transition. *J. Mater. Chem.* **2009**, *19*, 2968–2974.

(41) Kresse, G.; Furthmüller, J. Efficient Iterative Schemes for Ab Initio Total-Energy Calculations Using a Plane-Wave Basis Set. *Phys. Rev. B* **1996**, *54*, 11169–11186.

(42) Blöchl, P. E. Projector Augmented-Wave Method. *Phys. Rev. B* **1994**, *50*, 17953–17979.

(43) Farley, K. E. Electron-Phonon Coupling and Structural Phase Transitions in Early Transition Metal Oxides and Chalcogenides. Ph.D. Thesis, University at Buffalo: The State University of New York, Buffalo, New York, United States, 2016.

(44) Berglund, C. N.; Guggenheim, H. J. Electronic Properties of VO_2 near the Semiconductor-Metal Transition. *Phys. Rev.* **1969**, *185*, 1022–1033.

(45) Salker, A. V.; Seshan, K.; Keer, H. V. Phase Transition Behaviour of VO_2. *Phys. Status Solidi* **1983**, *75*, K37–K40.

(46) Budai, J. D.; Hong, J.; Manley, M. E.; Specht, E. D.; Li, C. W.; Tischler, J. Z.; Abernathy, D. L.; Said, A. H.; Leu, B. M.; Boatner, L. A.; McQueeney, R. J.; Delaire, O. Metallization of Vanadium Dioxide Driven by Large Phonon Entropy. *Nature* **2014**, *515*, 535–539.

(47) Lopez, R.; Haynes, T. E.; Boatner, L. A.; Feldman, L. C.; Haglund, R. F. Size Effects in the Structural Phase Transition of VO_2 Nanoparticles. *Phys. Rev. B* **2002**, *65*, 224113/1–5.

(48) Asayesh-Ardakani, H.; Nie, A.; Marley, P. M.; Zhu, Y.; Phillips, P. J.; Singh, S.; Mashayek, F.; Sambandamurthy, G.; Low, K.; Klie, R. F.; Banerjee, S.; Odegard, G. M.; Shahbazian-Yassar, R. Atomic Origins of Monoclinic-Tetragonal (Rutile)

Phase Transition in Doped VO_2 Nanowires. *Nano Lett.* **2015**, *15*, 7179–7188.

(49) Tang, C.; Georgopoulos, M.; Fine, M. E.; Cohen, J. B. Local Atomic and Electronic Arrangements in $W_xV_{1-x}O_2$. *Phys. Rev. B* **1985**, *31*, 1000–1011.

(50) Booth, J. M.; Casey, P. S. Anisotropic Structure Deformation in the VO_2 Metal-Insulator Transition. *Phys. Rev. Lett.* **2009**, *103*, 1–4.

(51) National Institute of Standards and Technology. NIST X-ray Photoelectron Spectroscopy Database: NIST Standard Reference Database 20, Version 4.1 http://srdata.nist.gov/xps/Default.aspx (accessed Apr 18, 2016).

(52) Quesada-González, M.; Boscher, N. D.; Carmalt, C. J.; Parkin, I. P. Interstitial Boron-Doped TiO_2 Thin Films: The Significant Effect of Boron on TiO_2 Coatings Grown by Atmospheric Pressure Chemical Vapor Deposition. *ACS Appl. Mater. Interfaces* **2016**, *8*, 25024–25029.

(53) Kachi, S.; Kosuge, K.; Okinaka, H. Metal-Insulator Transition in V_nO_{2n-1}. *J. Solid State Chem.* **1973**, *6*, 258–270.

(54) Yoon, H.; Choi, M.; Lim, T. W.; Kwon, H.; Ihm, K.; Kim, J. K.; Choi, S. Y.; Son, J. Reversible Phase Modulation and Hydrogen Storage in Multivalent VO_2 Epitaxial Thin Films. *Nat. Mater.* **2016**, *15*, 1113–1119.

(55) Corr, S. A.; Shoemaker, D. P.; Melot, B. C.; Seshadri, R. Real-Space Investigation of Structural Changes at the Metal-Insulator Transition in VO_2. *Phys. Rev. Lett.* **2010**, *105*, 1–4.

(56) Whittaker, L.; Wu, T. L.; Stabile, A.; Sambandamurthy, G.; Banerjee, S. Single-Nanowire Raman Microprobe Studies of Doping-, Temperature-, and Voltage-

Induced Metal-Insulator Transitions of $W_xV_{1-x}O_2$ Nanowires. *ACS Nano* **2011**, *5*, 8861–8867.

(57) Schilbe, P. Raman Scattering in VO_2. *Phys. B* **2002**, *316–317*, 600–602.

(58) Jones, A. C.; Berweger, S.; Wei, J.; Cobden, D.; Raschke, M. B. Nano-Optical Investigations of the Metal-Insulator Phase Behavior of Individual VO_2 Microcrystals. *Nano Lett.* **2010**, *10*, 1574–1581.

(59) Petrov, G. I.; Yakovlev, V. V.; Squier, J. Raman Microscopy Analysis of Phase Transformation Mechanisms in Vanadium Dioxide. *Appl. Phys. Lett.* **2002**, *81*, 1023–1025.

(60) Zhang, S.; Chou, J. Y.; Lauhon, L. J. Direct Correlation of Structural Domain Formation with the Metal Insulator Transition in a VO_2 Nanobeam. *Nano Lett.* **2009**, *9*, 4527–4532.

(61) Cao, J.; Gu, Y.; Fan, W.; Chen, L. Q.; Ogletree, D. F.; Chen, K.; Tamura, N.; Kunz, M.; Barrett, C.; Seidel, J.; Wu, J. Extended Mapping and Exploration of the Vanadium Dioxide Stress-Temperature Phase Diagram. *Nano Lett.* **2010**, *10*, 2667–2673.

(62) Ghedira, M.; Vincent, H.; Marezio, M.; Launay, J. C. Structural Aspects of the Metal-Insulator Transitions in $V_{0.985}Al_{0.015}O_2$. *J. Solid State Chem.* **1977**, *22*, 423–438.

(63) Tselev, A.; Luk'yanchuk, I. A.; Ivanov, I. N.; Budai, J. D.; Tischler, J. Z.; Strelcov, E.; Kolmakov, A.; Kalinin, S. V. Symmetry Relationship and Strain-Induced Transitions between Insulating M1 and M2 and Metallic R Phases of Vanadium

Dioxide. *Nano Lett.* **2010**, *10*, 4409–4416.

(64) Gallasch, T.; Baither, D.; Schmitz, G. V_2O_5 Thin Film Electrodes in Rechargeable Li-Ion Batteries – Sample Characterization by EELS. In *MC2009*; 2009; Vol. 3, pp 493–494.

(65) Chen, J. G. NEXAFS Investigations of Transition Metal Oxides, Nitrides, Carbides, Sulfides and Other Interstitial Compounds. *Surf. Sci. Rep.* **1997**, *30*, 1–152.

(66) Hemraj-Benny, T.; Banerjee, S.; Sambasivan, S.; Fischer, D. A.; Han, W.; Misewich, J. A.; Wong, S. S. Investigating the Structure of Boron Nitride Nanotubes by Near-Edge X-Ray Absorption Fine Structure (NEXAFS) Spectroscopy. *Phys. Chem. Chem. Phys.* **2005**, *7*, 1103–1106.

(67) Fleet, M. E.; Liu, X. Boron K-Edge XANES of Boron Oxides: Tetrahedral B-O Distances and Near-Surface Alteration. *Phys. Chem. Miner.* **2001**, *28*, 421–427.

(68) Jiménez, I.; Terminello, L. J.; Himpsel, F. J.; Grush, M.; Callcot, T. A. Photoemission, X-Ray Absorption and X-Ray Emission Study of Boron Carbides. *J. Electron Spectros. Relat. Phenomena* **1999**, *101–103*, 611–615.

(69) Terminello, L. J.; Chaiken, A.; Lapiano-Smith, D. A.; Doll, G. L.; Sato, T. Morphology and Bonding Measured from Boron-Nitride Powders and Films Using Near-Edge X-Ray Absorption Fine Structure. *J. Vac. Sci. Technol. A Vacuum, Surfaces, Film.* **1994**, *12*, 2462–2466.

(70) Li, D.; Bancroft, G. M.; Fleet, M. E. B K-Edge XANES of Crystalline and Amorphous Inorganic Materials. *J. Electron Spectros. Relat. Phenomena* **1996**, *79*, 71–73.

(71) Tolhurst, T. M.; Leedahl, B.; Andrews, J. L.; Marley, P. M.; Banerjee, S.; Moewes, A. Contrasting 1D Tunnel-Structured and 2D Layered Polymorphs of V_2O_5: Relating Crystal Structure and Bonding to Band Gaps and Electronic Structure. *Phys. Chem. Chem. Phys.* **2016**, *18*, 15798–15806.

(72) Nájera, O.; Civelli, M.; Dobrosavljević, V.; Rozenberg, M. J. Resolving the VO_2 Controversy: Mott Mechanism Dominates the Insulator-to-Metal Transition. *Phys. Rev. B* **2017**, *95*, 035113/1-6.

CHAPTER VI

CONCLUSIONS AND FUTURE OUTLOOK

6.1 General Remarks

In three disparate examples delineated in **Chapters II—V**, my dissertation research demonstrates that the surface chemistry of nanomaterials profoundly influences their properties and reactivity. When materials are confined to the nanoscale, surface energy contributions outweigh the bulk free energy, providing the thermodynamic basis for the observed amplification of surface control.[1,2] Tuning these properties allows for the design of materials which can be useful for specific applications; the examples delineated in this dissertation suggest a myriad of applications such as for a) tunability of the electronic structure of graphene upon interfacing with gate dielectrics, for use in the semiconductor industry, b) knowledge of surface properties of nanomaterials for e design of effective environmental remediation strategies, and c) programmability of the metal—insulator transition temperature of VO_2 for thermochromic fenestration. In these concluding remarks, important findings from each of our studies are again highlighted, and potential future research directions are outlined.

6.2 Towards the Programmable Design of Metal Oxide/Graphene Heterostructures

In **Chapter II**, the electronic structure evolution of graphene oxide as an atomic layer deposition (ALD) substrate was monitored during the early stages of HfO_2 growth. Both X-ray photoelectron (XPS) and near-edge X-ray absorption fine structure (NEXAFS)

spectroscopies show that in the initial ALD step, water-treatment results in the elimination of basal hydroxyl and epoxide groups, which can be attributed to the reaction of these functional groups with water and mobile carbonyl groups, liberating CO_2.[3] The removal of these functional groups on the surface of graphene oxide results in the partial restoration of the π-conjugated network of graphene. Upon treatment with *tetrakis*(dimethylamido)hafnium(IV) (TDMH), pendant carboxylic acid groups on the edges of graphene oxide play a more prominent role in the ALD process by serving as nucleation sites for the growth of amorphous HfO_2. The growth is accompanied by the sharing of electron density from the carboxylic acid groups of graphene oxide to Hf^{4+}, forming Hf-carboxylates in the process.[3] Hole-doping, which was previously reported following the plasma vapor deposition (PVD) of HfO_2 on graphene[4] is not observed, thus suggesting an entirely different mechanism when the said dielectric is grown by ALD on the surface of graphene oxide.

Our results for the ALD of HfO_2 on graphene oxide underline the importance of how surface functionalization can be used to tailor the electronic properties of materials. Understanding the mechanism of interfacing HfO_2 with graphene oxide finds immediate significance in the design of metal oxide/graphene heterostructures which can be used for graphene-based field-effect transistors (FETs). Graphene has been reported to be a good candidate in replacing Si as an active element in FETs.[5] However, it is imperative to modulate its semimetallic properties with high-κ gate dielectrics. The imminent issue in interfacing metal oxides on graphene is the lack of functional groups, which can serve as nucleation sites for the growth of these oxides. On the other hand, introducing functional

groups by the simultaneous oxidation and exfoliation of graphite renders graphene insulating. Our work on the ALD of HfO_2 on graphene oxide addresses both fundamental issues: a) graphene oxide is partially reduced during the early stages of the ALD process through the removal of basal hydroxyl and epoxide groups and b) carboxylic acid groups serve as anchoring points for the growth of HfO_2. Fundamental knowledge of the roles of these functional groups at the interface of metal oxides and graphene oxide serves as an important guide in the rational construction of such graphene-based FETs and similar devices. Graphene-based FETs are reported to have a cutoff frequency greater than 100 GHz, which remarkably outperforms traditional Si/SiO_2 FETs.[6–8] **Figure 6.1** shows a schematic cross-section of a graphene-based FET fabricated by IBM in 2008. In this device, Al_2O_3 is deposited by ALD onto graphene/SiO_2/Si to serve as the gate insulator for the FET. The use of graphene oxide (over unfunctionalized graphene) introduces multiple nucleation sites (carboxylic acid groups) for the ALD of gate dielectrics such as Al_2O_3 and HfO_2. Moreover, the ALD of dielectrics on graphene oxide simultaneously restores the π-conjugated network of graphene by thermal defunctionalization.[3]

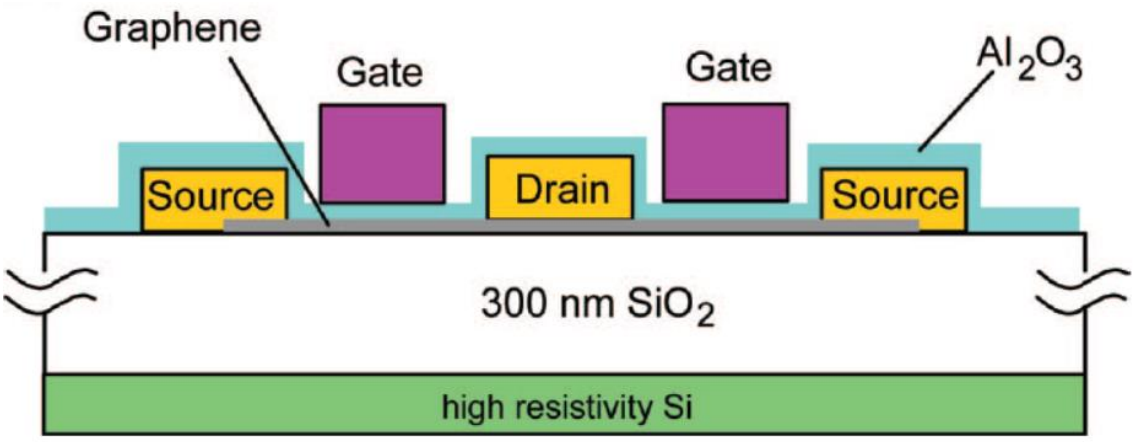

Figure 6.1: Cross-section schematic of a graphene-based FET. The device fabricated by IBM in 2008 was noted to have a cutoff frequency of 26 GHz. Image from reference 5. Reprinted with permission from reference 5. Copyright 2009 American Chemical Society.

Metal oxide/graphene assemblies can likewise be used as cocatalysts in the photodegradation of persistent organic compounds (POPs).[9] Among POPs, pharmaceutical compounds (as non-metabolized parent compounds or metabolites after digestion and secretion[10]) like antibiotics, anticonvulsives, and endocrine disruptors, to name a few representative examples, are released into the environment through effluents from wastewater treatment plants (WWTPs) [11,12] and hospitals.[13] Alarming concentrations of pharmaceutical compounds have been reported, for example in 2011, Ventura and coworkers have measured 1,200 ng/L of valsartan, an antihypertensive drug, in surface water from the Llobregat River in Spain.[14] These pharmaceuticals can eventually find their way into drinking water and back into the human body. Unintentional intake of exogenous drugs poses various human health risks—Jones *et al.* note that pharmaceuticals of sufficient quantity interfere with the regulation of metabolic systems (and can be fatal).[12] Antibiotics, such as amoxycillin and penicillin, have been reported to promote the

development of resistant bacteria.[11,15] Another important concern is the synergistic adverse effects of these pharmaceutical compounds.[15] Conventional water treatment processes such as filtration, chlorination, and in some cases, ozonization, have been reported to be inefficient in the removal and degradation of these persistent pharmaceutical compounds.[14] Research studies have been developed into looking for alternative methods to degrade these persistent compounds. Wide-band gap semiconductors, including TiO_2 and ZnO, have been studied as catalysts for the degradation of various organic compounds such as dyes and pesticides.[16,17] In past work, we have used ZnO tetrapods as catalysts for the photodegradation of PFOA and fluorotelomer carboxylic 5:3 acid in aqueous solutions.[18] TiO_2 and ZnO have been used as catalysts in the photodegradation of pharmaceutical compounds.[19,20] An issue however, is that the insulating/semiconducting nature of wide-band gap transition metal oxides limits the mobility of photogenerated charge carriers. By using transition metal oxide/graphene interfaces, graphene—a highly conductive semimetal—can behave as a "non-innocent" catalyst support to mitigate the poor ionic and electronic conductivity of transition metal oxides.[4,21] Graphene not only serves as an electron reservoir/shuttle for preventing charge carrier recombination[22] (thereby driving direct and indirect hole-mediated photooxidation forward[16]), but it can likewise provide a high surface area for the local accumulation of organic compounds near active sites. The mechanism we have derived from understanding the atomic layer growth of HfO_2 on the surface of graphene oxide serves as an important model in interfacing commonly used transition metal oxide catalysts, such as ZnO and TiO_2, with graphene. Various studies in literature reporting the hydrothermal growth of ZnO and TiO_2 in the

presence of graphene oxide observed an increase in catalytic activity from using as-prepared ZnO and TiO_2.[23] For example, Balkus and coworkers report *ca.* 75% degradation of malachite green with TiO_2 nanotubes after 60 minutes which increased to a value of *ca.* 90% with TiO_2/graphene oxide composites.[24] Zhou *et al* note *ca.* 80% degradation of methylene blue with ZnO/N-doped graphene oxide composites after 130 minutes *versus ca.* 10% degradation with just ZnO nanorods within the same time.[25] In the hydrothermal syntheses of these heterostructures, graphene oxide is partially reduced as the metal oxide subsequently nucleates and grows its surface. The study of such heterostructures has so far been limited to dyes and pesticides and therefore, it should be noteworthy if these materials can be used with various persistent pharmaceutical compounds in surface and drinking as well. As a literature precedent, the photocatalytic activity towards caffeine and carbamezepine of P25 TiO_2/reduced graphene oxide heterostructures developed by Linley *et al.* exceeded that of commercial P25 TiO_2 by a factor of 1.2.[10]

6.3 Towards Understanding the Surficial Properties of Natural Nanomaterials for Environmental Remediation Efforts

In **Chapters III** and **IV**, we turn our attention to the surface-mediated growth of natural nanoparticles in the environment. Herein, we note that in the presence of dissolved organic matter (DOMs) such as fulvic or humic acids, Ag-Au bimetallic alloy nanoparticles can be formed and stabilized in natural aqueous media. Previous studies have investigated the growth and stabilization of monometallic Ag and Au nanoparticles in aquatic systems,[26,27] but it is only now that the mechanism of DOM-mediated Ag-Au bimetallic alloy

nanoparticle formation has been elucidated. The growth of Ag-Au bimetallic alloy nanoparticles is highly dependent on the solution pH and the molar mass of the DOM. In the absence of sunlight, there is a preferential reduction of Au over Ag due to the former having a higher redox potential over the latter. Ag- and Au-ions are first complexed by Lewis basic groups (carbonyls, carboxyls, thiols, *etc*.) in fulvic and humic acids, after which they are reduced to their zerovalent form by single-electron transfer events mediated by quinone, hydroquinone, and semiquinone groups in the DOM. Ag^0 on the surface of the DOM reacts with $AuCl_4^-$ in solution *via* galvanic replacement reactions, depositing Au^0 on the DOM surface and releasing Ag^+ back into the aqueous solution. The newly formed Au^0 reacts with unreacted Ag^0 on the surface of DOMs, initiating the growth through interdiffusion of Ag-Au bimetallic alloys, given that both face-centered cubic metals have well-matched lattice constants. In general, the yield of Ag-Au bimetallic alloy nanoparticles increases with increasing solution pH. The bimetallic alloys are stabilized by a charge transfer from Au to Ag, as seen in shifts to lower and higher binding energies in XPS for Ag and Au, respectively.[28] Agglomeration and twinning are observed in the crystalline samples, which appear to more prominent for humic acid-grown alloys, given that this DOM has a higher molar mass and therefore more functional groups for ion-complexation than fulvic acid. On the other hand, natural sunlight seems to play a role in the preferential photoreduction of Ag over Au, given that only one electron is needed for Ag^+ to be reduced to its zerovalent form. In the presence of sunlight, superoxide anion radicals (formed upon the photoactivation of DOMs) in solution reduce Ag-and Au-ions initially form Ag and Au seeds in solution, respectively, after which, the nanocrystals are

further grown *via* plasmon-induced reduction The same surficial interactions (complexation of metals with Lewis basic groups and Au→Ag charge transfer) are also observed for the Ag-Au bimetallic alloy nanoparticles grown upon visible light photoexcitation.

As previously emphasized, another important task at hand is determining the toxicity of the Ag-Au bimetallic alloy nanoparticles. It has been noted in a previous lead study that the toxicity of citrate-reduced Ag-Au bimetallic alloy nanoparticles in *Daphnia magna* is dependent on the alloy elemental compisition.[29] In our work, we have noted that fulvic and humic acids not only serve as reducing agents, but also act as surface-passivating ligands on Ag-Au bimetallic alloy nanoparticles, which promotes their colloidal stability in aquatic systems for at least 120 days. Studies on Group 1B monometallic nanoparticles show that their toxicity is a function of their size and the type of the passivating ligand,[30,31] thereby underscoring the importance of understanding the interfacial chemistry and mechanistic formation of these natural nanomaterials. Surface-capping ligands have been reported to dictate the size and morphologies not just of metallic nanoparticles,[32] but also of oxychloride nanoplatelets,[33,34] quantum dots,[35] and many others. Moving forward, it is equally important to determine the fate of these bimetallic alloy nanoparticles when they are further transported into aqueous systems with a different chemistry, given that their colloidal stability can result in long-range transport. In past work, our group in collaboration with the group of Dr. Virender Sharma and Dr. Mary Sohn has noted that in hard water systems such as hot springs, estuarine ecosystems, and other areas with high limestone deposits, the presence of other metal cations, including

Na^+, K^+, Mg^{2+}, and Ca^{2+}, promotes the aggregation, agglomeration, and eventual sedimentation and removal of Ag nanoparticles. This effect is more pronounced for Ca^{2+}, which is a divalent ion with a larger ionic radius than Mg^{2+}.[36] In particular, Ca^{2+} can form stable complexes with the carboxylic acid groups in DOMs,[37] which leads to the destabilization and sedimentation of Ag nanoparticles. This suggests that Ag nanoparticles are strategically easier to remove in harder water streams than in freshwater systems. It will be imperative to extend this study to our Ag-Au bimetallic alloy nanoparticles. Understanding the chemistry at the surface of DOMs and nanomaterials opens up possibilities for the design of careful remediation efforts not only of Ag and Ag-Au bimetallic alloy nanoparticles but also for other precious metals polluting aquatic environments. A recent phytoremediative process developed by Olkhovych *et al* reports partial (30%) to total (100%) removal of Mn, Cu, Zn, and Ag nanoparticles with various submerged and free-floating aquatic plants.[38]

Our mechanistic studies discussed in **Chapters III** and **IV** also provide insight on the DOM-mediated reductive mineralization of other precious metal ions in aquatic systems. Examples of precious metals that have been detected at overwhelming concentrations in groundwater are Pt and Pd. In 2012, 602,000 μg/L Pt and 710,000 μg/L Pd were detected in sewage ash from incinerators in the United Kingdom.[39] Under relevant conditions, silver bi- and trimetallic alloys, such as Ag—Pt, Ag-Au—Pd, Ag-Au—Pt, and Ag—Pd—Pt, can be synthesized *via* single and/or sequential galvanic replacement reactions.[40] Mechanistic understanding derived from our studies with Ag-Au bimetallic alloy nanoparticle stabilization and formation in aqueous media will guide understanding

of the toxicity of other precious monometallic and alloyed nanoparticles released in the environment. Zimmermann *et al.* note that Pd and Pt are significantly more toxic to *Daphnia magna* than other metals such as Rh, and the effect is magnified considerably when Pd and Pt are both present in solution.[41] It is therefore important to determine whether or not other alloyed metal systems can be formed naturally in the presence of DOMs in aquatic systems *via* the mechanism we have outlined. Elucidating the mechanism behind alloy formation and identifying surficial interactions on the metallic nanoparticles are integral in determining the stabilization and toxicity of these nanomaterials in natural aquatic media.

6.4 Towards Temperature Tunability of Close-Packed Systems for Memory and Thermochromic Applications

In **Chapter V**, we developed a novel two-step surface-limiting technique for introducing dopant atoms into the VO_2 lattice, which leads to the stabilization of its R phase at lower temperatures. The first step includes the physisorption of the molecular precursor, 2-allyl-4,4,5,5-tetramethyl-1,3,2-dioxaborolane, onto the surface of freestanding VO_2 nanowires. In the second step, the precursor/VO_2 assembly is subsequently annealed at 900—950°C temperatures to promote the decomposition of 2-allyl-4,4,5,5-tetramethyl-1,3,2-dioxaborolane as well as the diffusion of B atoms into the VO_2 lattice. We note a linear correlation between dopant concentration and the extent of modulation of the metal—insulator transition temperature (T_{MIT}). In other words, the greater the amount of B atoms incorporated, the lower the temperature of the metal—insulator transition. This is evident

in decreasing particle size of VO_2 nanowires, wherein more B dopant atoms are incorporated as a result of increasing surface-area-to-volume ratio, further emphasizing the surface-limiting nature of the diffusive doping process. In stabilizing VO_2(R) at lower temperatures, the novel *ex situ* diffusive doping process developed shows a more tunable route for the modification of the phase diagram of VO_2 by introduction of diffusive dopants into the VO_2 lattice. Aside from the R phase, the introduction of B atoms into the VO_2 lattice does not promote the stabilization of other metastable phases of VO_2. We observe no evidence of strains along the crystallographic columns of VO_2 and overall retention of the +4 oxidation state of V. X-ray absorption near-edge spectroscopy (XANES) and density functional theory (DFT) calculations show that B atoms reside in tetrahedral interstitial sites of VO_2.[42] Two arguments can be posited for the stabilization of the R phase as a consequence of B-doping. First, from a structural perspective, the dimerization of V—V pairs as VO_2 undergoes the R→M_1 transition causes some interstitial sites in the lattice to expand and some to contract. With B atoms residing in interstitial sites, there is an obstruction to the phase transition owing to the decrease in volume of some of the interstitial holes, thereby stabilizing the R phase below the T_{MIT} of undoped VO_2. Second, from an electronic structure perspective, B—O bonds are formed upon the introduction of B atoms in the interstitial sites of VO_2. This causes a shift of electron density towards B, thus weakening V—O bonds and subsequently strengthening V—V bonds, rendering the material more metallic. In contrast, for W- and Mo-doped VO_2, the strain which arises from dopant substitution at a V site and the donation of electrons (two for W^{6+} and one for Mo^{5+}) to the electronic structure of VO_2 stabilize the R

phase at lower temperatures.[43,44] Diffusive annealing provides the ability to "dial in" the T_{MIT} of VO_2 after first synthesizing high-quality materials. This programmable doping feature offers a greater advantage over hydrothermal syntheses, which are prone to "trial-and-error." Diffusive doping in close-packed systems, such as VO_2, has hitherto been relatively underexplored. It is envisioned that this technique can be extended to other close-packed metal oxides in which the metal—insulator transition is fairly accessible, such as NbO_2, which transitions from a body-center tetragonal distorted rutile structure to a regular undistorted rutile structure at 807°C.[45] Other *ex situ* doping methods can likewise be used with other diffusive dopants. For example, it has been calculated that Be-doping can likewise stabilize VO_2(R) at lower temperatures.[46]. H-doping has been shown to stabilize the orthorhombic and metallic O1 and O2 phases of VO_2, which will be useful for applications requiring cryogenic conditions.[47] Moreover, the *ex situ* diffusive doping process also opens opportunities for co-doping of VO_2 and other close-packed structures.[48]

We note that aside from lowering the T_{MIT} of VO_2 as a function of dopant concentration, the introduction of B atoms into its lattice also increases its hysteresis (*ca.* 19—23°C). The emergence of such large hysteresis values can be useful for designing hybrid memory devices. Metamaterials undergo changes in electromagnetic properties in response to the introduction of external stimuli, such as heat and voltage.[49] However, in order to retain these altered properties, the external stimulus must be continuously supplied, otherwise its removal causes the metamaterial to revert back to its original properties. Such metamaterials can be more beneficial if the altered properties were to be retained after the removal of the stimulus. Given that the metal—insulator transition of

VO_2 can be triggered by the introduction of heat, voltage, or an external electric field, VO_2 can be interfaced with metamaterials for memory devices in various switching applications. Driscoll *et al* have designed a hybrid architecture of a gold spin-ring resonator array, patterned over a thin film of VO_2 in which, upon application of voltage, local heating of VO_2 is promoted. In effect, the resonance frequency of the gold spin-ring resonator array redshifts by *ca.* 20%, which is retained even after the removal of the voltage.[49] It is important to note that the VO_2 used by the authors are undoped films which a) have a smaller hysteresis (*ca.* 5°C) *versus* W-, Mo-, and B- doped VO_2 and b) may not be practical for ambient applications. The introduction of B-dopants into VO_2 *via* diffusive annealing therefore not only allows for the generation of a large hysteresis, but it also promotes the operation of hybrid memory devices at other highly specific working temperatures.

It was also envisioned that B-doped VO_2 could be used for thermochromic glazing. However, the annealing process that promotes the diffusion of dopant atoms into the VO_2 lattice results in the inevitable sintering of nanowires. Optical studies have noted that particle sizes less than 50 nm are ideal for thermochromic glazings[50,51] (larger nanoparticles promote Mie scattering[52]). Therefore, post-processing, such as ball-milling, is necessary in order for the doped samples to be useful for thermochromic applications, after which, further assessment of their optical properties can be performed.

6.5 References

(1) Depner, S. W.; Cultrara, N. D.; Farley, K. E.; Qin, Y.; Banerjee, S. Ferroelastic

Domain Organization and Precursor Control of Size in Solution-Grown Hafnium Dioxide Nanorods. *ACS Nano* **2014**, *8*, 4678–4688.

(2) Waetzig, G. R.; Depner, S. W.; Asayesh-Ardakani, H.; Cultrara, N. D.; Shahbazian-Yassar, R.; Banerjee, S. Stabilizing Metastable Tetragonal HfO_2 Using a Non-Hydrolytic Solution-Phase Route: Ligand Exchange as a Means of Controlling Particle Size. *Chem. Sci.* **2016**, *7*, 4930–4939.

(3) Alivio, T. E. G.; De Jesus, L. R.; Dennis, R. V.; Jia, Y.; Jaye, C.; Fischer, D. A.; Singisetti, U.; Banerjee, S. Atomic Layer Deposition of Hafnium(IV) Oxide on Graphene Oxide: Probing Interfacial Chemistry and Nucleation by Using X-Ray Absorption and Photoelectron Spectroscopies. *ChemPhysChem* **2015**, *16*, 2842–2848.

(4) Schultz, B. J.; Dennis, R. V.; Lee, V.; Banerjee, S. An Electronic Structure Perspective of Graphene Interfaces. *Nanoscale* **2014**, *6*, 3444–3466.

(5) Lin, Y.-M.; Jenkins, K. A.; Valdes-Garcia, A.; Small, J. P.; Farmer, D. B.; Avouris, P. Operation of Graphene Transistors at Gigahertz Frequencies. *Nano Lett.* **2009**, *9*, 422–426.

(6) Lin, Y.-M.; Dimitrakopoulos, C.; Jenkins, K. A.; Farmer, D. B.; Chiu, H.; Grill, A.; Avouris, P. 100-GHz Transistors From. *Science* **2010**, *327*, 100.

(7) Lin, Y.-M.; Valedes-Garcia, A.; Han, S.-J.; Farmer, D. B.; Meric, I.; Sun, Y.; Wu, Y.; Dimitrakopoulos, C.; Grill, A.; Avouris, P.; Jenkins, K. E. Wafer-Scale Graphene Integrated Circuit. *Science* **2011**, *332*, 1294–1298.

(8) Moon, J. S.; Seo, H. C.; Yang, B.; Antcliffe, M.; Son, K. A.; Wong, D.; Schmitz,

A.; Fung, H.; Le, D.; McGuire, C.; Kang, J.-C.; Song, H. J.. Graphene and Lateral Heterostructure for THz Imaging. *IEEE Trans. Terahertz Sci. Technol.* **2015**, *5*, 344–350.

(9) Muir, D. C. G.; Howard, P. H. Are There Other Persistent Organic Pollutants? A Challenge for Environmental Chemists. *Environ. Sci. Technol.* **2006**, *40*, 7157–7166.

(10) Linley, S.; Liu, Y.; Ptacek, C. J.; Blowes, D. W.; Gu, F. X. Recyclable Graphene Oxide-Supported Titanium Dioxide Photocatalysts with Tunable Properties. *ACS Appl. Mater. Interfaces* **2014**, *6*, 4658–4668.

(11) Kim, S.; Aga, D. S. Potential Ecological and Human Health Impacts of Antibiotics and Antibiotic-Resistant Bacteria from Wastewater Treatment Plants. *J. Toxicol. Environ. Heal. Part B Crit. Rev.* **2007**, *10*, 559–573.

(12) Jones, O. A.; Voulvoulis, N.; Lester, J. N. Potential Ecological and Human Health Risks Associated with the Presence of Pharmaceutically Active Compounds in the Aquatic Environment. *Crit. Rev. Toxicol.* **2004**, *34*, 335–350.

(13) Kümmerer, K. Drugs in the Environment: Emission of Drugs, Diagnostic Aids and Disinfectants into Wastewater by Hospitals in Relation to Other Sources - a Review. *Chemosphere* **2001**, *45*, 957–969.

(14) Huerta-Fontela, M.; Galceran, M. T.; Ventura, F. Occurrence and Removal of Pharmaceuticals and Hormones through Drinking Water Treatment. *Water Res.* **2011**, *45*, 1432–1442.

(15) Jones, O. A.; Lester, J. N.; Voulvoulis, N. Pharmaceuticals: A Threat to Drinking

Water? *Trends Biotechnol.* **2005**, *23*, 163–167.

(16) Hoffmann, M. R.; Martin, S.; Choi, W.; Bahnemann, D. W. Environmental Applications of Semiconductor Photocatalysis. *Chem. Rev.* **1995**, *95*, 69–96.

(17) Schneider, J.; Matsuoka, M.; Takeuchi, M.; Zhang, J.; Horiuchi, Y.; Anpo, M.; Bahnemann, D. W. Understanding TiO_2 Photocatalysis : Mechanisms and Materials. *Chem. Rev.* **2014**, *114*, 9919–9986.

(18) Abada, B.; Alivio, T. E. G.; Shao, Y.; O'Loughlin, T. E.; Klemashevich, C.; Banerjee, S.; Jayaraman, A.; Chu, K. H. Photodegradation of Fluorotelomer Carboxylic 5:3 Acid and Perfluorooctanoic Acid Using Zinc Oxide. *Environ. Pollut.* **2018**, *243*, 637–644.

(19) Das, R.; Sarkar, S.; Chakraborty, S.; Choi, H.; Bhattacharjee, C. Remediation of Antiseptic Components in Wastewater by Photocatalysis Using TiO_2 Nanoparticles. *Ind. Eng. Chem. Res.* **2014**, *53*, 3012–3020.

(20) Mohapatra, D. P.; Brar, S. K.; Daghrir, R.; Tyagi, R. D.; Picard, P.; Surampalli, R. Y.; Drogui, P. Photocatalytic Degradation of Carbamazepine in Wastewater by Using a New Class of Whey-Stabilized Nanocrystalline TiO_2 and ZnO. *Sci. Total Environ.* **2014**, *485–486*, 263–269.

(21) Xiang, Q.; Yu, J.; Jaroniec, M. Synergetic Effect of MoS_2 and Graphene as Cocatalysts for Enhanced Photocatalytic H_2 Production Activity of TiO_2 Nanoparticles. *J. Am. Chem. Soc.* **2012**, *134*, 6575–6578.

(22) Lightcap, I. V.; Kosel, T. H.; Kamat, P. V. Anchoring Semiconductor and Metal Nanoparticles on a Two-Dimensional Catalyst Mat. Storing and Shuttling Electrons

with Reduced Graphene Oxide. *Nano Lett.* **2010**, *10*, 577–583.

(23) Machado, B. F.; Serp, P. Graphene-Based Materials for Catalysis. *Catal. Sci. Technol.* **2012**, *2*, 54–75.

(24) Perera, S. D.; Mariano, R. G.; Vu, K.; Nour, N.; Seitz, O.; Chabal, Y.; Balkus, K. J. Hydrothermal Synthesis of Graphene-TiO_2 Nanotube Composites with Enhanced Photocatalytic Activity. *ACS Catal.* **2012**, *2*, 949–956.

(25) Zhou, X.; Shi, T.; Zhou, H. Hydrothermal Preparation of ZnO-Reduced Graphene Oxide Hybrid with High Performance in Photocatalytic Degradation. *Appl. Surf. Sci.* **2012**, *258*, 6204–6211.

(26) Adegboyega, N. F.; Sharma, V. K.; Siskova, K.; Zbořil, R.; Sohn, M.; Schultz, B. J.; Banerjee, S. Interactions of Aqueous Ag^+ with Fulvic Acids: Mechanisms of Silver Nanoparticle Formation and Investigation of Stability. *Environ. Sci. Technol.* **2013**, *47*, 757–764.

(27) Yin, Y.; Yu, S.; Liu, J.; Jiang, G. Thermal and Photoinduced Reduction of Ionic Au(III) to Elemental Au Nanoparticles by Dissolved Organic Matter in Water: Possible Source of Naturally Occurring Au Nanoparticles. *Environ. Sci. Technol.* **2014**, *48*, 2671–2679.

(28) Alivio, T. E. G.; Fleer, N. A.; Singh, J.; Nadadur, G.; Feng, M.; Banerjee, S.; Sharma, V. K. Stabilization of Ag-Au Bimetallic Nanocrystals in Aquatic Environments Mediated by Dissolved Organic Matter: A Mechanistic Perspective. *Environ. Sci. Technol.* **2018**, *52*, 7269–7278.

(29) Li, T.; Albee, B.; Alemayehu, M.; Diaz, R.; Ingham, L.; Kamal, S.; Rodriguez, M.;

Whaley Bishnoi, S. Comparative Toxicity Study of Ag, Au, and Ag-Au Bimetallic Nanoparticles on *Daphnia magna*. *Anal. Bioanal. Chem.* **2010**, *398*, 689–700.

(30) Moreno-Garrido, I.; Pérez, S.; Blasco, J. Toxicity of Silver and Gold Nanoparticles on Marine Microalgae. *Mar. Environ. Res.* **2015**, *111*, 60–73.

(31) Iswarya, V.; Manivannan, J.; De, A.; Paul, S.; Roy, R.; Johnson, J. B.; Kundu, R.; Chandrasekaran, N.; Mukherjee, A.; Mukherjee, A. Surface Capping and Size-Dependent Toxicity of Gold Nanoparticles on Different Trophic Levels. *Environ. Sci. Pollut. Res.* **2016**, *23*, 4844–4858.

(32) Maillard, M.; Huang, P.; Brus, L. Silver Nanodisk Growth by Surface Plasmon Enhanced Photoreduction of Adsorbed [Ag^+]. *Nano Lett.* **2003**, *3*, 1611–1615.

(33) Kort, K. R.; Banerjee, S. Oriented Electrophoretic Deposition of GdOCl Nanoplatelets. *J. Phys. Chem. B* **2013**, *117*, 1585–1591.

(34) Waetzig, G. R.; Horrocks, G. A.; Jude, J. W.; Villalpando, G. V.; Zuin, L.; Banerjee, S. Ligand-Mediated Control of Dopant Oxidation State and X-Ray Excited Optical Luminescence in Eu-Doped LaOCl. *Inorg. Chem*. **2018**, *57*, pp 5842–5849.

(35) Bailey, R. E.; Smith, A. M.; Nie, S. Quantum Dots in Biology and Medicine. *Phys. E* **2004**, *25*, 1–12.

(36) Akaighe, N.; Depner, S. W.; Banerjee, S.; Sharma, V. K.; Sohn, M. The Effects of Monovalent and Divalent Cations on the Stability of Silver Nanoparticles Formed from Direct Reduction of Silver Ions by Suwannee River Humic Acid/Natural Organic Matter. *Sci. Total Environ.* **2012**, *441*, 277–289.

(37) Ouatmane, A.; Hafidi, M.; Gharous, M. El. Complexation of Calcium Ions by Humic and Fulvic Acids. *Analusis* **1999**, *27*, 428–432.

(38) Olkhovych, O.; Svietlova, N.; Konotop, Y.; Karaushu, O.; Hrechishkina, S. Removal of Metal Nanoparticles Colloidal Solutions by Water Plants. *Nanoscale. Res. Lett.* **2016**, *11*,1–7.

(39) Prichard, H. M.; Wedin, F.; Sampson, J.; Jackson, M. T.; Fisher, P. C. Precious Metals in Urban Waste. *Water Environ. J.* **2016**, *30*, 151–156.

(40) Da Silva, A. G. M.; Rodrigues, T. S.; Haigh, S. J.; Camargo, P. H. C. Galvanic Replacement Reaction: Recent Developments for Engineering Metal Nanostructures towards Catalytic Applications. *Chem. Commun.* **2017**, *53*, 7135–7148.

(41) Zimmermann, S.; Wolff, C.; Sures, B. Toxicity of Platinum, Palladium and Rhodium to Daphnia Magna in Single and Binary Metal Exposure Experiments. *Environ. Pollut.* **2017**, *224*, 368–376.

(42) Alivio, T. E. G.; Sellers, D. G.; Asayesh-Ardakani, H.; Braham, E. J.; Horrocks, G. A.; Pelcher, K. E.; Villareal, R.; Zuin, L.; Shamberger, P. J.; Arroyave, R.; Shahbazian-Yassar, R.; Banerjee, S. Postsynthetic Route for Modifying the Metal—Insulator Transition of VO_2 by Interstitial Dopant Incorporation. *Chem. Mater*. **2017**, *29*, 5401–5412.

(43) Whittaker, L.; Wu, T.-L.; Patridge, C. J.; Sambandamurthy, G.; Banerjee, S. Distinctive Finite Size Effects on the Phase Diagram and Metal–Insulator Transitions of Tungsten-Doped Vanadium(IV) Oxide. *J. Mater. Chem.* **2011**, *21*,

5580–5592.

(44) Patridge, C. J.; Whittaker, L.; Ravel, B.; Banerjee, S. Elucidating the Influence of Local Structure Perturbations on the Metal-Insulator Transitions of $V_{1-x}Mo_xO_2$ Nanowires: Mechanistic Insights from an X-Ray Absorption Spectroscopy Study. *J. Phys. Chem. C* **2012**, *116*, 3728–3736.

(45) O'Hara, A.; Demkov, A. A. Nature of the Metal-Insulator Transition in NbO_2. *Phys. Rev. B* **2015**, *91*, 094305.

(46) Zhang, J.; He, H.; Xie, Y.; Pan, B. Giant Reduction of the Phase Transition Temperature for Beryllium Doped VO_2. *Phys. Chem. Chem. Phys.* **2013**, *15*, 4687–4690.

(47) Filinchuk, Y.; Tumanov, N. A.; Ban, V.; Ji, H.; Wei, J.; Swift, M. W.; Nevidomskyy, A. H.; Natelson, D. In Situ Diffraction Study of Catalytic Hydrogenation of VO_2: Stable Phases and Origins of Metallicity. *J. Am. Chem. Soc.* **2014**, *136*, 8100–8109.

(48) Burkhardt, W.; Christmann, T.; Meyer, B. K.; Niessner, W.; Schalch, D.; Scharmann, A. W-and F-Doped VO_2 Films Studied by Photoelectron Spectrometry. *Thin Solid Films* **1999**, *345*, 229–235.

(49) Driscoll, T.; Kim, H.-T.; Chae, B.-G.; Kim, B.-J.; Lee, Y.-W.; Jokerst, N. M.; Palit, S.; Smith, D. R.; Di Ventra, M.; Basov, D. N. Memory Metamaterials. *Science* **2009**, *325*, 1518–1521.

(50) Fleer, N. A.; Pelcher, K. E.; Zou, J.; Nieto, K.; Douglas, L. D.; Sellers, D. G.; Banerjee, S. Hybrid Nanocomposite Films Comprising Dispersed VO_2

Nanocrystals: A Scalable Aqueous-Phase Route to Thermochromic Fenestration. *ACS Appl. Mater. Interfaces* **2017**, *9*, 38887–38900.

(51) Naoi, Y.; Amano, J. Optimization of VO_2 Nanowire Polymer Composite Thermochromic Films by Optical Simulation. *J. Appl. Phys.* **2016**, *120*, 235301/1–7.

(52) Fleer, N. A.; Pelcher, K. E.; Nieto, K.; Braham, E. J.; Zou, J.; Horrocks, G. A.; Naoi, Y.; Depner, S. W.; Schultz, B. J.; Amano, J.; Sellers, D. G.; Banerjee, S. Elucidating the Crystallite Size Dependence of the Thermochromic Properties of Nanocomposite VO_2 Thin Films. *ACS Omega* **2018**, *3*, 14280–14293.